THIN FILM DIAMOND DEVICES AS PHOTON AND IONISING RADIATION DETECTORS

Robert David McKeag

A thesis submitted for the degree of Doctor of Philosophy

Department of Electronic and Electrical Engineering
UNIVERSITY COLLEGE
UNIVERSITY OF LONDON

July 2002

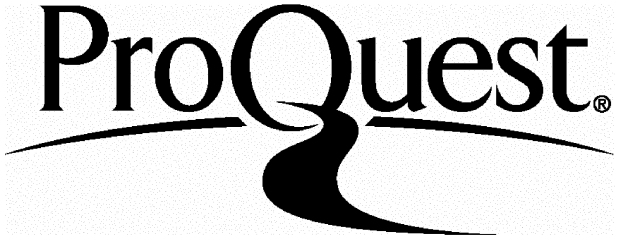

ABSTRACT

Thin Film Diamond Devices as Photon and Ionising Radiation Detectors

The emergence over the past decade of new techniques for the synthesis of high quality diamond films having a range of unique properties which include a wide bandgap, high carrier mobilities, high electric field breakdown strength and radiation hardness, has created the opportunity to exploit this material in the fabrication of microelectronic sensors. New insight is offered into the electronic and electro-optic properties of thin polycrystalline diamond films in respect to the processing and performance of devices for the detection of deep ultraviolet light and ionising radiation.

The known properties of natural and synthetic diamond are reviewed and evaluated in the context of previous studies which have sought to develop diamond electronic devices. A design philosophy and experimental methods are identified by which high performance ultraviolet photodetector structures may be fabricated to overcome the limitations of contemporary films, and prototype devices are presented and evaluated. Vacuum and gas ambient processes are proposed and undertaken which act to optimise specific aspects of detector performance such as speed or sensitivity and the mechanisms by which such processes operate are discussed. Further engineering of the optical detection capabilities of thin film diamond devices is explored with the aim of effecting modifications to the spectral profile of the detector's sensitivity. The detection of alpha particles is undertaken and evaluated with a view to optimisation and the hardness of the detectors to gamma radiation is explored.

Finally, in view of the current advanced state of commercial exploitation of the devices described, a brief review is undertaken to identify the realistic market impact of diamond electronic devices.

TABLE OF CONTENTS

ACKNOWLEDGEMENTS

Thin Film Diamond Devices as Photon and Ionising Radiation Detectors

Since my initial involvement in thin film diamond technology at a time when the required background reading consisted of around half a dozen papers, I have had the relatively uncommon good luck to have been involved in a series of experiments which have been successful beyond our reasonable expectations. Consequently, I now find myself working for the industrial licencee of the resulting device technology, charged with helping to implement a programme of full scale exploitation for the world's first commercial diamond UV photodetectors.

One of the greatest pleasures of scientific research is the extended community in which the modern student operates. Whilst rivals and colleagues alike provide the ebb and flow of ideas, insights and that unique laboratory humour which has no parallel in other disciplines, the work of previous generations in the form of dusty volumes drawn from the library reserve collection frequently offer a welcome sense of context and continuity to apparently disparate ideas; the phrase "...shoulders of giants..." comes to mind. The main piece of equipment which underpinned the work presented in this thesis was a monochromated xenon light source, and it has been particularly satisfying to reflect from time to time on the coincidence that our research has to some extent been enabled by the work of Prof. William Ramsay who discovered xenon during his tenure here at UCL almost exactly one hundred years before our own experiments took place.

Returning to the present, it is clear that a project of the type described herein cannot (unlike the experiments themselves) take place in a vacuum and the credit for successful completion of the programme must be spread amongst a great many people. My wife Angélique's permission to embark upon a PhD was of course a prerequisite for the programme to take place and her subsequent support, encouragement, patience and good-natured poverty over the ensuing six years are what have enabled me to complete the work. On a practical level my parents' generous financial support, particularly

during the first year of the programme must at times have seemed like a waste of a good stair carpet: as usual you were right, but thank you for letting me do what I wanted to anyway. My grandmothers Alice and Zer have both been very kind in their assistance with the expenses of study, and my whole and extended family have been generous in their support, advice and gentle pressure as required over the past few years.

Within the department at UCL many people have helped in many different ways. The cleanroom staff of Fred, Kevin, David and Chris (in chronological order of arrival - I think) have unquestionably all done their bit whilst Alan, Trevor and Jim in the workshop have made things for me against drawings which most people would decline to feed to the average cat. The Group which has variously consisted of Judith, Duncan, Lye Hing, Simon, Bhaswar, Lisa, Mike, Hui Jin, Stuart, Olivier and most recently Ollie would like me to say something humorous and insightful about them, but we have libel laws in this country. Of many essential MSc and 3rd year project students who have contributed to the work, Ian Davies and Kyaw Kyaw Soe deserve particular mention. Of Richard-The-Boss-Jackman I could say many embarrassingly complimentary things, however his constant stream of ideas, suggestions and increasingly audacious abstract writing has left me too exhausted to eulogise extensively: it will be years before I have fully absorbed everything you have taught me.

Beyond College the involvement of Centronic Ltd. and Rod Barnes' stewardship of this relationship have been essential aspects of our work and have frequently guided our decisions and motivation. At Centronic Bob Angel, Brendon Fahy and Brendan Bilton have shown a courage and insight that is all too rare in British industry by sticking with a long term development project through bad times as well as good. During my studentship Chris Farnworth provided an essential introduction to the ways of industry.

Further afield Philippe Bergonzo and his colleagues (including Duncan Marshall again) at CEA Saclay have been invaluable collaborators and generous hosts: the work we conducted together in their laboratories forms the backbone of chapter ten. This arrangement was made possible by an EU grant under the Alliance programme. Additional recognition is due to Paul Chalker and Colin Johnston with whom we collaborated at AEA Technology on electrical contact work (published elsewhere) which preceded the studies presented in this thesis.

The Institute of Physics kindly provided assistance with the costs of attending and presenting at the 1998 Congress and the Rank Prize Fund generously enabled me to attend their mini symposium on "Optoelectronic Materials for the New Millenium".

1 INTRODUCTION

The microelectronics industry and the associated fields of modern communications and information technology have grown to their present social and economic significance over the relatively short period of fifty years since the first laboratory demonstrations of early transistor structures. Most of this progress has taken place by means of devices engineered from silicon, and it is inevitable when one attempts to discuss a new electronic material that the performance, versatility, availability, processability and economics of the new contender will be judged against the standards set by silicon.

In the early days of synthetic thin diamond film becoming available to electronic device engineers, many commentators were tempted to insert the known properties of diamond into established design equations and figures of merit normally used to describe the performance of silicon devices. This euphoric activity (reviewed in §3.4.1) was particularly prevalent in the United States and led to a number of dramatic claims being made for putative diamond devices which would significantly outperform their silicon counterparts, particularly in terms of speed and power handling. The successful genesis of a new electronic material technology is not however contingent upon the demonstration of enhanced performance alone, and the unconfined initial enthusiasm described above turned in many cases to bitter disillusionment when economic and manufacturability issues were taken into account.

It has been a specific aim of the work presented in this thesis to investigate the electronic sensor opportunities offered by contemporary, commercially available diamond film with a view to informing industry of the relative merits of working with this material. Enhancements in material quality and growth techniques can be

anticipated to offer future potential, however the key question which this thesis aims to address is whether today's affordable diamond films can form the basis of a manufacturable and commercially viable device technology.

With reference to the preceding paragraphs, it is unlikely that the limitations of contemporary diamond films will allow the material to compete favourably in a head-on comparison with silicon. Instead it has been our policy to identify application areas in which diamond may be anticipated to represent an enabling technology; helpfully such fields are often subject to less stringent economic demands than would-be competitor technologies can expect to face when entering an established discipline.

Although thin film diamond is a relatively new material, natural diamond has of course been available for many hundreds of years and is consequently reasonably well understood. Chapter 1 reviews the relevant existing information and models available which describe the structure and properties of diamond, and attempts where possible to comment upon the relationship between the properties of the natural and synthetic forms of the material. Because of the long history of experiments undertaken using natural diamond, many suggestions have been made historically for possible applications of diamond if suitable material should sometime become available. This body of work is reviewed in chapter 3 and discussed in the context of more recent studies which have taken place using thin film diamond.

Our decision to develop a thin film diamond detector for deep ultraviolet light, and the various factors which influenced the design process are discussed in chapter 5. Chapters 6 to 9 build upon the work of chapter 5 by exploring possible processes which may be used to manage or engineer the properties and performance of the original devices. Functionality is addressed in terms of sensitivity, speed of response, wavelength selectivity and durability of the detectors, whilst the mechanisms behind the processes developed are investigated in an effort to establish an understanding of the scope and limitations of these processes which will be required for future device engineering. In a slight departure from the general theme of photon detection, chapter 10 investigates the performance of the diamond devices as alpha particle detectors as this has been identified as another field in need of an enabling semiconductor device technology.

The results presented in these experimental chapters support the idea that contemporary diamond films can be processed into useful electronic sensors. In particular high sensitivity, low dark current, radiation hard deep UV detectors are demonstrated which

can be engineered to optimise either sensitivity (by means of photoconductive gain) or speed of response. Such detectors are anticipated to find immediate industrial applications in processes which include 193nm excimer laser based photolithography systems, high intensity UV sterilisation lamp monitoring and a range of combustion control systems which encompass incinerators, furnaces and high performance aero-engines.

Commercial diamond UV detectors based closely upon the processes developed in chapter 6 are now being manufactured under licence by our industrial collaborator, Centronic Ltd. and a new business unit has been created within the company to develop further technical and commercial opportunities from this initial product.

In rereading the chapters which follow, I am reminded of the extent to which this thesis reports, quite properly in my view, a series of engineering projects supported by scientific explanation as opposed to a science project dressed up in an engineering context. Many more questions are raised than are answered and it is satisfying to note that two PhD students who have followed me into this work and are now undertaking extensive studies using equipment and collaborative links which are certain to assist with cracking some of the questions left behind by this thesis.

2 THE STRUCTURE, SYNTHESIS AND PROPERTIES OF DIAMOND

2.1 Introduction

This chapter reviews and draws direction from a selected subset of the literature relating to the known properties of diamond. A brief overview of the structure and bonding of the material, and the means by which it may be obtained, is followed by more detailed discussions of the properties which are most relevant to the exploitation of diamond in microelectronics. Specific attention is given to the roles of defects and impurities and the ways in which they are known to modify the characteristics of ideal diamond; the black art of electrical contact formation is also discussed. It has not been the intention of the author to undertake a definitive review of the entire field but instead to explore

more fully those insights which directly inform or underpin the device technologies which are experimentally investigated in subsequent chapters.

2.2 Carbon Bonding

The carbon atom is composed of a nucleus of six protons and six, seven or eight neutrons surrounded by six electrons occupying the ground state orbitals $1s^2 2s^2 2p^2$. In molecular carbon, such as diamond and graphite, this structure is hybridised by the promotion of one 2s electron either into the vacant 2p orbital (sp^3 hybrid) or into a combination with the two half filled 2p orbitals (sp^2 hybrid) to facilitate the tetravalent bonding of the various alletropes discussed below.

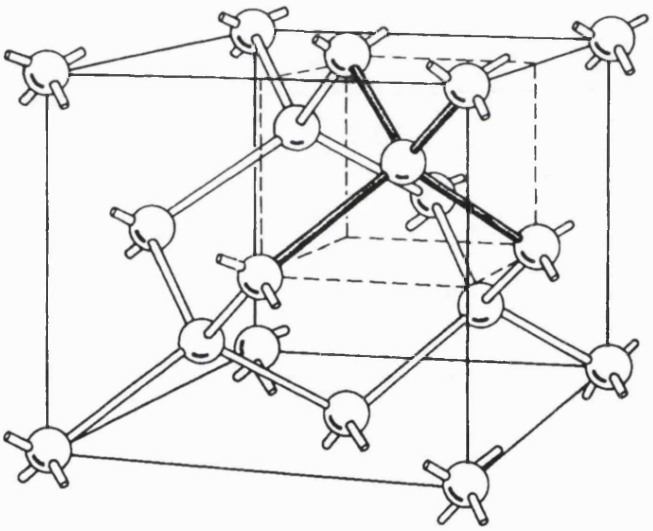

Figure 2.1: A unit cell of the diamond lattice, highlighting the four tetrahedral bonds of a single carbon atom. [Reproduced from 2.1].

Diamond is well known as the tetrahedrally sp^3 bonded cubic polytype of molecular carbon, occupying the characteristic crystal lattice structure to which it lends its name. The classic view of this structure, a pair of interpenetrating face centred cubes displaced from one another by one quarter of the cube diagonal is sketched in figure (2.1). Another perspective of the same crystal is presented in figure (2.2(a)), where the (111) plane is regarded as consisting of a set of basic building blocks having the form of six member carbon rings in the 'chair' configuration, which are stacked according to the

ABC ABC pattern illustrated. The four covalent directed (σ) bonds formed by each atom are 1.5445Å long [2.2] and are separated from one another by an angle of 109°28' with a bond energy of 711KJ/mol [2.3].

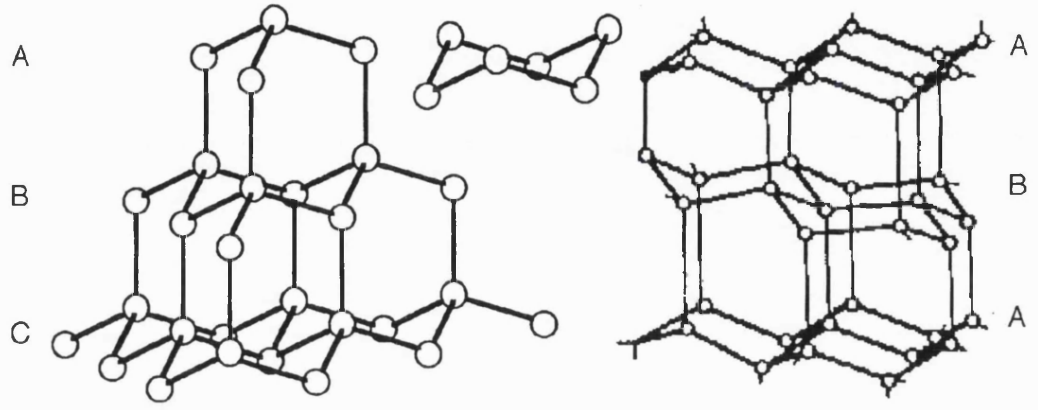

Figure 2.2: (a) left: the ABC stacking pattern of diamond as is constructed from the 'chair' prototype shown floating. (b) right: the AB AB stacking pattern of lonsdaleite. [Reproduced from 2.3]

An alternative stacking pattern of AB AB can be realised as shown in figure (2.2(b)) which results in the creation of lonsdaleite, also known as hexagonal (6-H) diamond. This structure has a slightly shorter bond length of 1.54Å resulting in an even tighter, stronger material than cubic diamond. The additional bonding energy required for the formation of hexagonal diamond means however that the cubic polytype is preferentially formed under most conditions. Lonsdaleite is rare to the extent that for the purpose of this thesis it can realistically be regarded as a fault system within cubic diamond rather than as a separately available material, however its strength and stability should be noted.

Graphite is familar as the product of sp^2 bonded carbon atoms and can be perceived as consisting of planar rings of six carbon atoms as shown in figure (2.3(a)) where each atom forms three strong covalent σ bonds of length 1.41Å separated from one another by 120° in the x-z plane. The fourth (π) bond is perpendicular to the σ bonding plane and the valence electron orbitals are 'time shared' in the positive and negative y direction resulting in much weaker bonding between parallel planes. As in the case of diamond, two stacking patterns can occur giving rise to either the more common hexagonal graphite of figure (2.3(a)) with an AB AB pattern, or the thermodynamically

less stable rhombohedral graphite with an ABC ABC pattern as shown in figure (2.3(b)).

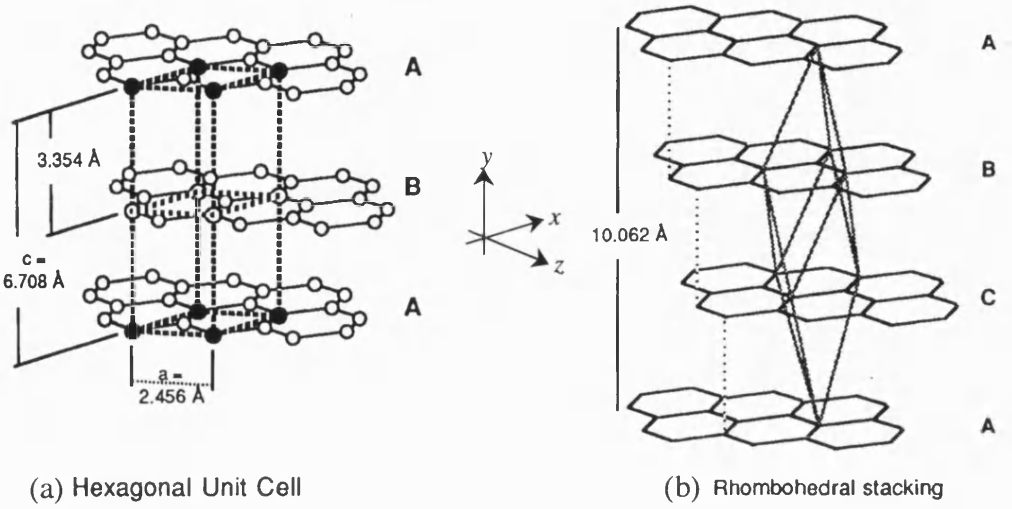

Figure 2.3 Schematics representing the stacking patterns of graphite polymorphs: (a) the common hexagonal form having an alternating ABAB pattern, (b) the very rare rhombohedral form with an ABC stacking pattern. [Reproduced from 2.4].

The particular polymorph which can be expected to form under a given set of conditions of pressure and temperature can be anticipated from the phase diagram of carbon, reproduced in figure (2.4). The significant feature of this system is the fact that diamond can exist as a metastable phase under conditions of low pressure and temperature which are calculated to favour the graphite phase. The reason for this is that although the bonding energy of graphite is 2.1 KJ/mol lower than that for diamond [2.4], the strong covalent bonds of the diamond structure must first be broken, requiring 711 KJ/mol, before reconstruction can occur. This required transformation energy equates to a temperature of ≈1620°C at atmospheric pressure and so enables diamond, once formed, to persist indefinitely in the metastable phase under normal conditions [2.4].

An example of modified sp^2 bonding is found in the new classes of carbon materials which encompass buckminsterfullerines [2.3] and carbon nanotubes [2.5]. These materials, which lie well beyond the scope of the present work, consist of sheets of hexagonally bonded carbon atoms which in the case of nanotubes are 'wrapped around' in the manner of a sausage roll which is then capped with half a 'buckyball' at each end, the buckyballs themselves being similar hexagonal sheets interspersed with a dozen

pentagons to accomodate complete closure into a 'football-like' sphere. It has been speculated that applications for these new alletropic families could eventually include single-molecule transistors, fuel cells and superconductors.

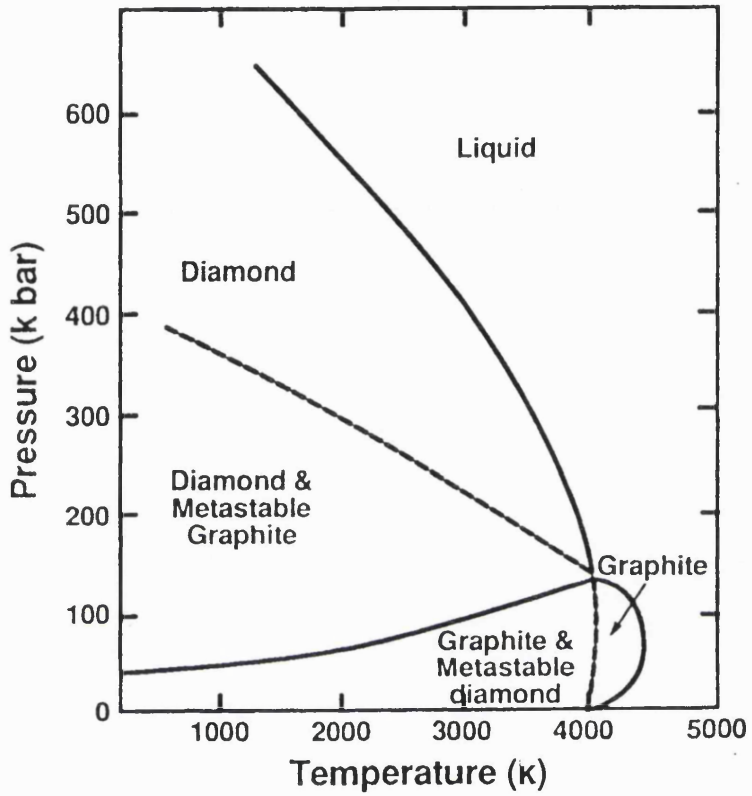

Figure 2.4 The phase diagram of carbon over a range of temperature and pressure conditions. [Reproduced from 2.3].

2.3 Synthesis of Diamond

2.3.1 Natural Diamond

Natural diamond is believed to form over a period ranging from milllions to billions of years ago at between 140 and 200km beneath the surface of the earth where the temperature ranges between 900 and 1400°C and the pressure between 45 and 60 Kbar [2.6, 2.7]. The precise means and mechanism of geological diamond formation are unclear and remain the subject of ongoing research, however commercial interest in the mining of natural stones has led to a comprehensive understanding of the location and extraction of these deposits. Although not in itself a volcanic material, natural diamond is transported to accessible regions within the earth's crust by volcanic eruptions and

primary deposits are therefore found embedded within kimberlite, a form of solidified lava, inside extinct volcanic pipes [2.8]. Glacial and alluvial erosion have subsequently distributed these deposits over wider geographical areas.

Extraction of natural diamond entails mining large quantities of the kimberlite carrier, which is then crushed to a slurry and refined by a series of physical separation techniques to extract the target stones at a yield of around 0.2g per tonne of raw extract.

Naturally occurring diamonds of extraterrestrial origin have occasionally been found in small quantities within meteorites [2.8], which are believed to be remnants of the supernova disintegration of dying stars.

2.3.2 HPHT Synthesis of Diamond

The earliest success in synthesising diamond replicated the assumed conditions of geological formation by applying a high pressure, high temperature (HPHT) process which was reported in 1955 by Bundy *et al.* [2.9]. There were and remain substantial technological challenges associated with creating a regime in which the conversion of graphitic species to diamond is thermodynamically favoured; in particular it has not been possible to design equipment which is capable of steady state maintenance of such conditions. Instead either a shock (explosion) is used to achieve a fleeting period of extremely high pressure, or a 'Hall Belt' cell is used which first maximises the pressure and then uses resistive heating to melt both the solid precursor and the metallic cell walls which act as a catalyst, facilitating creation of diamonds at a lower combined temperature and pressure than that indicated thermodynamically in figure (2.4) for the uncatalysed system.

HPHT synthesis is now an established technology for the preparation of diamond crystallites and grit particles up to a diameter of $\approx$10μm, accounting for around 90% of the world-wide market in diamond for industrial applications [2.10]. The primary limitations of this mode of synthesis can be summarised as following from a lack of facility for detailed process control. This is manifested as: an inability to form crystals in a planar geometry or as a coating on shaped surfaces, a lack of ability to control the ultimate lattice location of any impurities introduced and in most cases an upper limit on crystallite size of $\approx$10μm due to the rapid cooling inherent in the process which precludes long range ordering of the constituent atoms.

2.3.3 Chemical Vapour Deposition of Diamond

Modern growth of diamond from the vapour phase stems directly from the work of Spitsyn, Bouilov and Derjaguin [2.11] who in 1981 reported the successful nucleation and uninterrupted growth of polycrystalline diamond on non-diamond substrates including copper, tungsten and, crucially for the semiconductor industry, silicon. This was achieved by a chemical vapour deposition (CVD) process in which a precursor gas mixture of ≈0.5-5% methane (CH_4) in hydrogen (H_2) had been dissociated either thermally with a filament (HFCVD) or by an electric discharge (d plasma) over a substrate in the remarkably moderate temperature range of 600-1000°C.

The achievements of Spitsyn *et al.* built upon work by Eversole [2.12, 2.13] in 1958 and Angus [2.14] in 1968 which had established that diamond could be grown on a diamond seed crystal by pyrolysis of CH_4 at <1 bar or carbon monoxide (CO) at around 10 bar, however these processes had been limited by the unwanted deposition of non-diamond carbon phases which blackened both the seed material and the reaction vessel and inhibited further diamond growth. The success of the modern technique is due to the presence of sufficient atomic hydrogen during the entire growth process to ensure that any non-sp^3 (diamond) bonded carbon deposits are rapidly removed, thereby suppressing the thermodynamically preferred nucleation and growth of graphite in favour of metastable diamond.

Following the publication of these results, a substantial and on-going international research effort has yielded many improvements upon the original process. In addition to the techniques of hot filament and dc discharge deposition discussed above, a fuel-rich acetylene torch was shown by Hirose et.al. [2.15] to be viable as a low-cost method for nucleation and rapid growth of low grade films. The most important development however, was the demonstration by Kamo *et al.* [2.16] that dissociation of the precursor gases could be readily achieved using 2.45GHz microwave energy [MPACVD]. As the microwaves could be transmitted into the reaction chamber through a quartz plate, this development removed the need for a heating filament or set of electrodes to be placed within the highly reactive growth environment and so permitted diamond films to be grown with much lower impurity levels than could be achieved using a hot filament or electric discharge. Furthermore, the skilful application of established microwave engineering techniques enabled much more accurate process control over factors including plasma shape, size and energy, which in turn led to nucleation of better quality, more uniform films over larger areas [2.17, 2.18].

Although homoepitaxial growth is possible on diamond seed crystals, it should be noted that all of the above techniques give rise to the growth of polycrystalline films when nucleated on non-diamond substrates; this can readily be related to the random orientations of the individual crystallites which nucleate and subsequently coalesce to form a continuous film. The detailed mechanisms of nucleation remain the subject of extensive debate: early observations that nucleation tended to occur at defects on the substrate surface led to the widespread practice of scratching substrates prior to film growth. More recent research [2.19] has shown that electrically biasing the substrate with respect to the plasma during the early stages of MPACVD causes the crystallites to nucleate in a uniform orientation and with a high degree of alignment. These oriented, aligned hetero-grown films represent the current state of the art in terms of overall film quality, however this does not necessarily make them the material of choice for all applications, as will be discussed later in this thesis (§5).

Further variants of the basic MPACVD process include the use of different substrate temperatures, excitation frequencies, precursor gases/ratios and run times to control film properties such as morphology, thickness and purity. As examples of the types of film which are currently available, figure (2.5(a)) is an electron micrograph of a very low grade small grain film on a silicon substrate, this texture incorporates many defects/non-diamond carbon phases and has been nicknamed 'cauliflower growth'. Figure (2.5(b)) shows a reasonable quality film on silicon which has good crystallinity and a predominantly (111) crystallite orientation, whilst figure (2.5(c)) shows a large grain freestanding film which has been grown to a thickness of $\approx$100μm, making it strong enough to withstand being separated from the substrate after growth. Figure (2.5(d)) shows a state of the art oriented aligned film; although this too is polycrystalline, it can be seen that the crystallites have started to coalesce offering the prospect that continued growth could lead to a single crystalline film. A limit on this effect arises however, due to the strain that is created within such coalesced material.

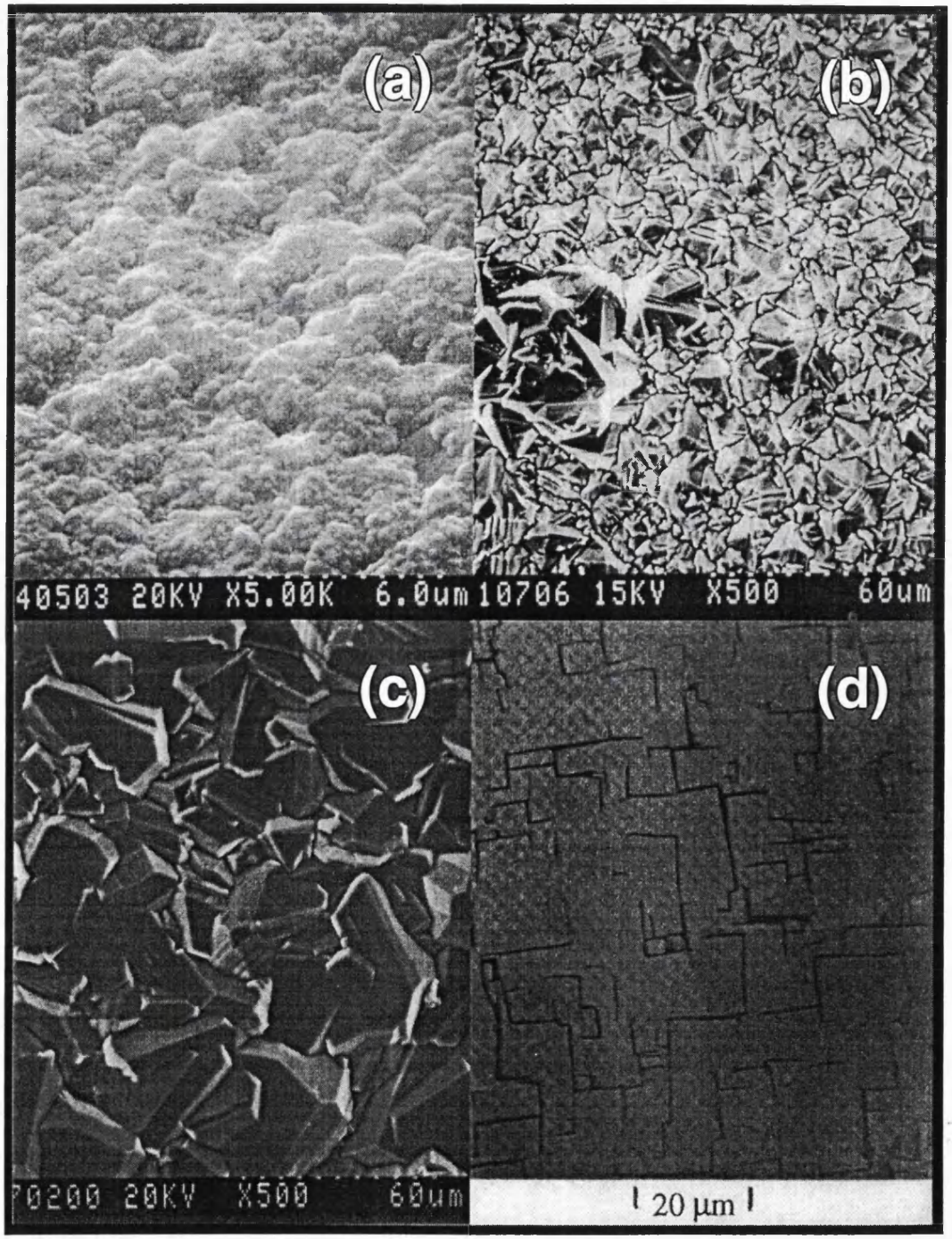

Figure 2.5: The growth surfaces of typical MPACVD diamond films (a) low quality 'cauliflour' texture with no discernable crystallinity, (b) small grain, predominantly (111) faceted thin film, (c) large grain randomly oriented freestanding film and (d) oriented aligned film grown by biased enhanced nucleation showing coallescence of crystallites. [Image (d) reproduced from ref. 2.20].

2.4 Electronic Properties of Ideal Diamond

Many of the properties of diamond, which arise from its composition and structure, have been calculated or derived from fundamental principles by a number of researchers with the dual intentions of achieving a reliable understanding of the material and an indication of the characteristics which could be expected of a perfectly pure, perfectly crystalline sample. The well known limits on the ability of theory to anticipate empirical results apply particularly strongly in the case of diamond: the need to simplify inputs to render a model comprehensible, and the requirement of most models to operate upon empirically determined constants, leads either to over generalisation and a prediction with no practical analogue, or to over specification with a different description offered for each sample analysed.

This section (§2.4) summarises the general case of ideal diamond and is followed in later sections by a review of empirically observed variations caused by impurities (§2.5.1) and structural defects (§2.5.5).

2.4.1 The Band Structure of Diamond

The band structure of a bulk crystalline material, which arises from the effect of the Pauli exclusion principle upon the overlapping wavefunctions of each electron of each atom in a sample, provides an insight into the fundamental relationship between the composition of that material and many of its properties. Band structure calculations are based upon a quantum mechanical analysis of the effects on a free electron of the periodic potential which it experiences due to interactions with atom nuclei, core electrons and valence electrons. Of the many models which have been employed to calculate semiconductor band structures this century [2.21], the Linear Combination of Atomic Orbitals (LCAO) [2.22] is regarded as the most valid for diamond because it lends appropriate weight to the Tight Binding of core electrons to the atomic nuclei and reflects the strong covalent bonding discussed above (§2.2).

Painter *et al.* [2.23] derived the diamond band structure by *ab initio* calculation using the Discrete Variational Method based on the LCAO approach. The diagram they generated is reproduced in figure (2.6) and anticipates a wide indirect bandgap between the valence band maximum at Γ and the conduction band minimum at $\Gamma X \approx (0.7, 0, 0)$. The degeneracy (co-incidence of bands at a single energy level and a single point in k space) which is indicated at the valence band maximum is an approximation by the model as the bands are actually known to be separated by 5, 6 or 7 meV [2.24]. The

calculated value of the bandgap, E_g, at 5.40eV agrees well with empirical results reported elsewhere of 5.47 and 5.49eV [2.24]; for practical calculations E_g is generally stated as 5.5eV.

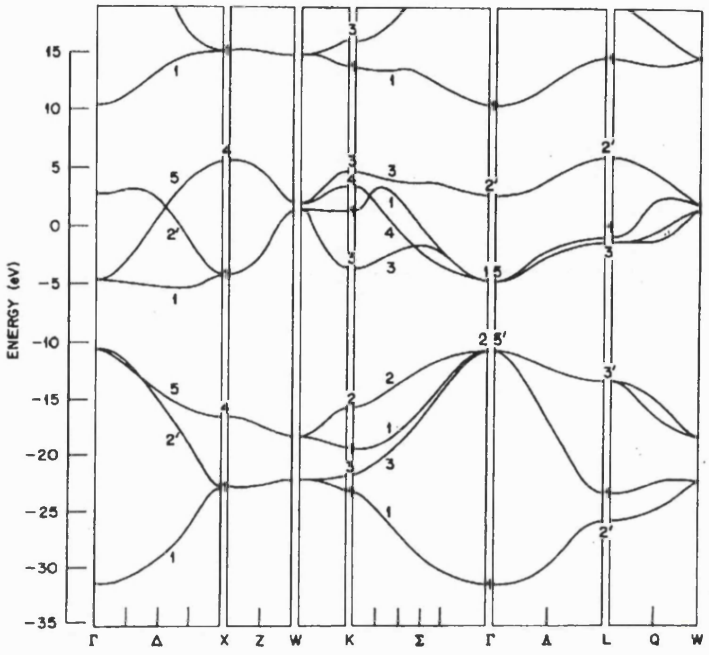

Figure 2.6: The energy band structure of diamond. [Reproduced from 2.23]

2.4.2 Effective Carrier Masses

The effective mass m^* of the carriers in a particular band of the energy structure of a semiconductor is an important construct: the influence of the periodic lattice potential on a mobile carrier is incorporated parametrically into the effective mass which can then be applied as a prescaler to the free space carrier mass m_0. This enables mobile carriers within the solid to be analysed in terms of classical electrodynamics [2.22].

To a first approximation, the energy of a carrier in the region of a valence band maximum (or conduction band minimum) is treated as being parabolic in k and expressed as [2.25]:

$$E(k) = \left(\frac{\hbar^2}{2m^*}\right)k^2 \tag{2.1}$$

where ħ is the modified Planck constant. From this, the effective carrier mass is given at the band maximum/minimum by the E, k relationship [2.25]:

$$m^* = \frac{\hbar^2}{\partial^2 E / \partial k^2 \big|_{k=k_0}} \tag{2.2}$$

From this equation it follows that carriers in bands having different radii of curvature, such as the nearly degenerate valence band maxima at Γ, will have different values of effective mass. A shallower curve has a smaller $\partial^2E/\partial k^2$ and hence a larger m^* giving rise to the terminology of light and heavy holes. This description has a logical interpretation in that 'lighter' carriers are more mobile.

In practice an accurate calculation of m^* must reflect the fact that the equipotential surfaces of the conduction band of diamond are ellipsoidal rather than parabolic, so that m^* is composed of the longitudinal and transverse components m_{el}^* and m_{et}^*. These two parameters can be combined to express the electron density of states effective mass $m_{e,dos}^*$ [2.26]:

$$m_{e,dos}^* = \left(m_{el}^* m_{et}^{*2}\right)^{1/3} \tag{2.3}$$

Correspondingly, the hole density of states effective mass $m_{h,dos}^*$ is calculated from the heavy and light hole effective mass components m_{hh}^* and m_{lh}^* as [2.26]:

$$m_{h,dos}^* = \left(m_{hh}^{*3/2} + m_{lh}^{*3/2}\right)^{2/3} \tag{2.4}$$

A detailed review of the current state-of-the-art with regard to both theoretically derived and experimentally observed effective mass data for diamond has been presented by Chan [2.26], from which it may be concluded that contemporary models show a reasonable correlation with experimental results obtained from natural stones, although little comparison with thin film diamond has yet been undertaken. A summary comparison of effective carrier masses in diamond and a number of other widely used semiconductor materials is presented in table (2.1).

Material	m_{el}^*/m_0	m_{et}^*/m_0	m_e^*/m_0	m_{hh}^*/m_0	m_{lh}^*/m_0
Diamond theory	1.24 / 1.665	0.25 / 0.290	-	0.614 / 0.40	0.208 / 0.28
Diamond expt.	1.4	0.36	-	1.1	0.3 / 1.1 / 0.75
Si	0.98	0.19	-	0.53	0.16
Ge	1.64	0.082	-	0.35	0.43
GaAs	-	-	0.067	0.62	0.074
InP	-	-	0.08	0.85	0.089
InSb	-	-	0.014	0.47	0.015

Table (2.1): The effective carrier masses of diamond and a selection of other semiconductors, wherein the subscripts denote el: electrons longitudinal, et electrons transverse, e: electrons in a material having spherical conduction band minima, hh: heavy holes, lh: light holes and m_0 is the free space electron mass. [Reproduced from 2.26].

2.4.3 Carrier Mobility

The mobility μ of a charge carrier describes the ease with which it can move through a semiconductor under the force arising from the application of an electric field. It is related to the effective mass of the carrier by [2.25]:

$$\mu_{n,p} = \frac{q\langle \tau_m \rangle}{m^*_{n,p}} \tag{2.5}$$

where q is the electronic charge and $<\tau_m>$ the mean free time between scattering collisions. The carrier mobility is of fundamental importance in device design and analysis as it determines the conductivity σ of a sample according to the equation [2.25]:

$$\sigma = q\left(n\mu_n + p\mu_p\right) \tag{2.6}$$

where n and p are the respective electron and hole densities. In a structurally perfect semiconductor the carrier scattering probability will be determined exclusively by collisions with dopant atoms and phonon interactions (lattice vibrations) such that impurity scattering will be the dominant influence on $<\tau_m>$ at lower temperatures leading to an impurity controlled mobility μ_i whilst at higher temperatures the lattice scattering controlled mobility μ_l becomes more important. The overall mobility is expressed by summing these components, and in imperfect material any additional components due to other scattering mechanisms, according to the Mathiesson rule[2.27]:

$$\mu^{-1} = \mu_i^{-1} + \mu_l^{-1} \tag{2.7}$$

Mobility values determined theoretically and experimentally for diamond are compared with those of other semiconductor materials in table (2.2). It can be seen that diamond not only has a higher electron mobility than silicon, but that the electron and hole mobilities are more closely matched than for any of the other materials listed. It has been suggested that this property could be particularly useful in the design of high power devices exhibiting low losses [2.28].

Material	μ_n ($cm^2V^{-1}s^{-1}$)	μ_p($cm^2V^{-1}s^{-1}$)
Diamond theory	2000	2100
Diamond expt.	2300 / 2000 / 1850	1850 / 1200
Si	1350	450
GaAs	8500	400
Ge	3900	1900
InSb	78000	750
InP	4600	150
InAs	33000	450

Table (2.2): The electron and hole low field mobilities (300K) of diamond and a selection of other semiconductors [Reproduced from 2.26].

2.4.4 Saturated Carrier Velocity

Under high bias potentials the drift velocity of carriers in a semiconductor can become comparable to their thermal velocity at which point any additional energy imparted to the carriers by the field will be lost to the lattice as heat in increased scattering events [2.25]. This situation, which is known as a 'hot carrier' effect, defines a saturation velocity for carriers in a given material and thereby sets an upper limit on the speed of devices which can be fabricated under that regime. The velocity-field characteristics for electrons and holes in diamond have been calculated by Trew *et al.* [2.29] and are reproduced as figure (2.7). It can be seen that the maximum carrier velocities of both electrons and holes in diamond are higher than those of silicon and that the high-field velocity of carriers in diamond saturates in contrast to the high-field hole velocity in gallium arsenide; this is potentially useful for high-speed, high power device applications as will be discussed in a later section (§3.4).

Concomitant with the attainment and maintenance of high saturated carrier velocities is the requirement for a sample to be capable of sustaining a high electric field without breakdown. This parameter has not been definitively determined for diamond but is known the exceed $4*10^6 Vcm^{-1}$ and is believed to be as high as $2*10^7 Vcm^{-1}$, both of which values compare well with figures for silicon and gallium arsenide which lie in the range $2\text{-}4*10^5 Vcm^{-1}$ [2.30].

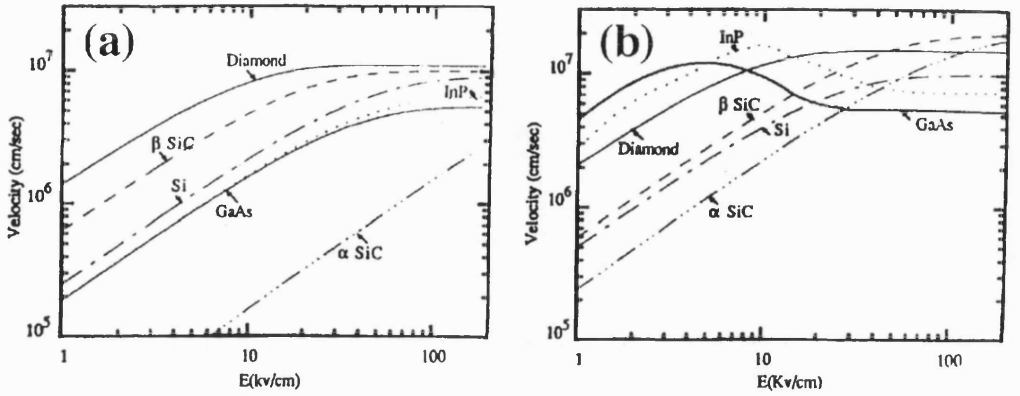

Figure 2.7: The calculated carrier velocities with respect to applied field in diamond and other semiconductors for (a) electrons and (b) holes. [Reproduced from 2.29].

2.5 Impurities in Diamond

The characteristics above (§2.4) aim to describe perfect diamond: a material which for most practical purposes does not exist. This section reviews the ways in which imperfections consisting of impurities (§2.5.1) and structural faults (§2.5.5) modify the ideal characteristics of diamond to present an empirically based description of a real material. It is important in this context to avoid the pejorative connotations of the term 'imperfect': the utility of any semiconductor material lies primarily in the ability of defects and impurities to modify its characteristics, and the success of any device engineering project is substantially contingent upon the degree of control which can be exerted over these features. The various means by which impurities are introduced into the diamond lattice are discussed in a later chapter (§9.2, §9.3), whilst the following paragraphs review the nature and influence of these centres. For reference, the ultraviolet and visible absorption of ultra-pure IIa material shown in figure (2.8(a)).

2.5.1 The Type Classification

Nitrogen and boron are the most commonly found contaminants in natural diamond, indeed stones without one or both of these impurities are extremely rare and correspondingly expensive. To meet the requirements of the gem trade, a classification system has developed over the past half century which assigns diamonds to one of a number of 'types' according to properties, primarily colour, which can be related to the content and nature of the above impurities. Although much modern research on thin

film diamond conforms to the conventions of the semiconductor industry by stating impurity levels as a doping density and lattice location, the use of the type classification system is still sufficiently widespread to warrant a brief description.

Robertson *et al.* [2.31] noted in 1934 that based upon deep ultraviolet absorption spectra, there appeared to be 'two types of diamond', which led to the notation that stones with an absorption cut-off at wavelengths greater than 300nm were of type I as this was the most prevalent behaviour observed amongst the 2-300 stones investigated, whilst those having a 225nm threshold were designated type II. It has subsequently emerged that type I stones contain nitrogen and can be subdivided into class Ia (colourless→yellow) containing either or both of the 'A' and 'B' impurity centres and Ib (yellow→green) which contain the 'C' impurity; type II is also subdivided with IIa (colourless) being the very rare ultra-pure stones and IIb (colourless→blue) containing detectable levels of boron [2.8]. This scheme is summarised in table (2.3).

Type	Impurity	Concentration
Ia	Nitrogen: A or B centres	≈3000ppm
Ib	Nitrogen: C centre	≈40ppm
IIa	Nitrogen: A or B centres	<10ppm
IIb	Boron > nitrogen	B<1ppm

Table (2.3): A summary of the classification scheme used for natural diamond, indicating typical impurity concentrations for each type of stone [Data abstracted from 2.8, 2.32].

2.5.2 Nitrogen in Diamond

Nitrogen, as the group V element adjacent to carbon, might be expected to act as an n-type electrical dopant for diamond by analogy to phosphorous in silicon, however the activation energy required to ionise even the most shallow of the nitrogen impurity states is such as to render nitrogen doped diamond insulating at room temperature [2.33]. Despite this inactivity as a donor dopant, the presence or absence of nitrogen has an important effect on many of the optical and electronic properties of diamond due both to its role in the creation of photon absorption and carrier recombination centres and to its effects in compensating acceptors [2.34]. As the influence exerted by an impurity is intimately linked to its lattice location, the following terminology has

evolved to identify the various forms of nitrogen impurity centre which have been observed in diamond.

2.5.2.1 The A centre

The A aggregate consists of two substitutional nitrogen atoms on adjacent lattice sites [2.8] and is the most commonly found form of nitrogen in natural diamond. Typical ultraviolet/visible and infra red absorption spectra for a stone in which the A centre is the main impurity are reproduced as figure (2.8(b)): in comparison to figure (2.8(a)) these show additional infra red absorption between $1000cm^{-1}$ and $1400cm^{-1}$ and a shift in the high energy ultraviolet absorption threshold from the 5.5eV bandgap position of pure diamond to ≈4eV (≈300nm). Although it cannot always be assumed that optical absorption events will lead to the creation of mobile charge carriers, the A centre absorption spectrum correlates well with the onset of sub-bandgap photoconductivity observed by Denham *et al.* [2.35] in 'intermediate' (nitrogen containing) stones, as will be discussed in more detail in a later chapter (§3.2). It is understood that the apparent shift in the onset of ultraviolet absorption is not due simply to the effective narrowing of the bandgap by the presence of a thermally ionised impurity atom, but that distortions in the symmetry of the diamond lattice due to the presence of the nitrogen pair give rise to three direct transition energies of 3.757, 3.901 and 3.928eV which are then broadened by an additional set of indirect transitions involving phonons of 113meV and 159meV [2.8, 2.36]. It is worth noting that the A centre should not be confused with the well known 'band A' luminescence phenomenon which is believed to be due to donor-acceptor pairs or dislocations and is discussed later in this thesis (§8).

2.5.2.2 The B centre

The B centre is known to consist of an even number of aggregated substitutional nitrogen atoms, and although it has been much less intensively researched than the A centre, a consensus is emerging that it probably takes the form of four substitutional nitrogens arranged around a vacancy [2.8, 2.37]. The optical absorption spectra representing a stone dominated by the B centre are reproduced as figure (2.8(c)), which shows stronger and broader infra red absorption features than occur due to the A centre. The fact that the ultraviolet absorption is very similar to that observed in a pure stone is qualitatively consistent with the concept that A centre absorption is due to a disruption of symmetry in the diamond lattice caused by the two-atom nitrogen impurity, whilst the four-atom plus vacancy B centre has a shorter range effect on the bulk of the diamond, and so causes only a low level of sub-bandgap absorption.

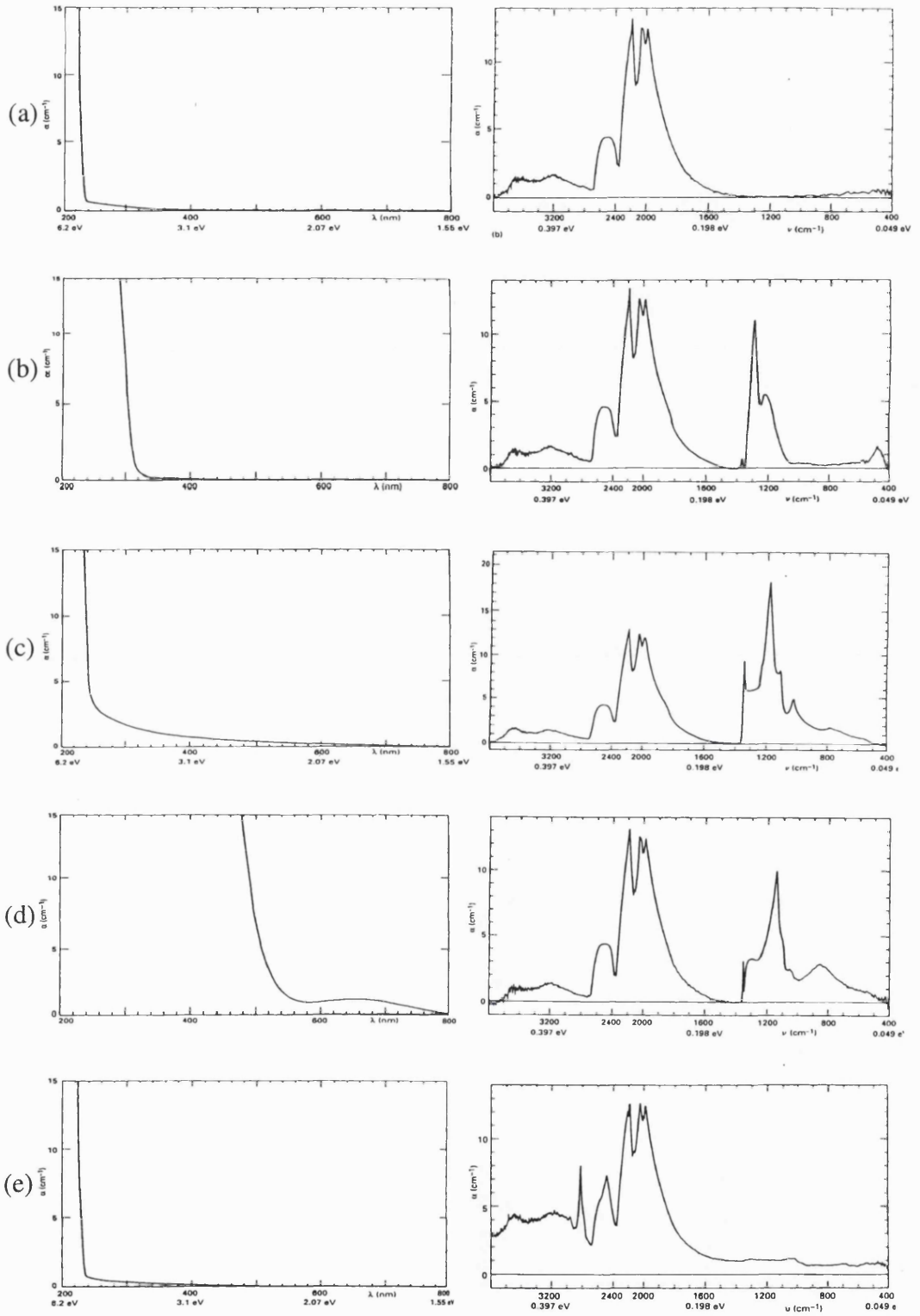

Figure 2.8: Typical ultraviolet and infra red absorption spectra of natural diamonds exhibiting the following impurity related characteristics (a) pure diamond, (b) the A centre, (c) the B centre, (d) the single N centre and (e) boron . [Adapted from ref. 159]

2.5.2.3 The C centre

The C centre [2.38] is also described eponymously as the 'single substitutional nitrogen centre' [2.8, 2.36]. The optical absorption spectra attributable to the C centre are reproduced as figure (2.8(d)) and indicate extensive, but less intense, infra red absorption than exhibited by the A and B centres accompanied by a substantial and intense visible absorption continuum occurring at ≈1.7eV (≈720nm) and extending into the intrinsic deep ultraviolet. Theory [2.39] and experiments [2.40] both indicate that the (111) carbon-nitrogen bond is distorted by a mutual repulsion leading to a displacement of both atoms from their specified lattice sites and a consequent increase in bond length of 25-35% . As a combined consequence of the impurity and the lattice distortion, two states are believed to occur within the bandgap: one at ≈1.7 eV below the conduction band is singly occupied, the ionisation of which leads to the 1.7eV absorption threshold and the other is doubly occupied and occurs just above the valence band.

2.5.2.4 The N3 centre

The N3 centre occurs only in stones which also contain the A or B centres [2.8] but is physically distinct from its co-defects. Its presence is indicated by an additional optical absorption peak at ≈2.9eV (≈415nm) [2.41] accompanied by a broad absorption band at 360-400nm and a smaller feature at 450-480nm; this is illustrated by figure (2.9) in which the N3 absorption spectrum is seen to co-exist with a characteristic A centre spectrum. The N3 centre is believed to take the form of three adjacent substitutional nitrogen atoms in a {111} plane, each having a bond to a common vacancy [2.41].

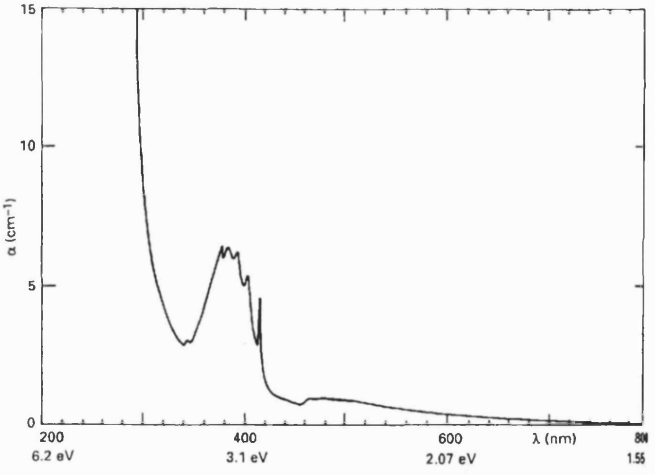

Figure 2.9: Optical absorption spectrum showing the additional absorption due to the N3 centre in co-existence with the A centre. [Reproduced from 2.8]

2.5.3 Boron in Diamond

The incorporation of boron as a substitutional impurity renders diamond p-type semiconducting, as might be expected from its position in group III next to carbon [2.8]. In natural IIb stones which have very low impurity concentrations, the energy required to activate the boron acceptor level at ≈0.37eV above the valence band edge results in only ≈0.2% ionisation at room temperature (≈20°C) [2.42]. Optical absorption spectra typical of a IIb diamond are reproduced in figure (2.8(e)) and indicate that in this stone, absorption occurs only in the infra-red region. As commented above (§2.5.1), a visible blue colouration is typically seen in a IIb material with a sufficiently high boron content: an HPHT synthesised stone exhibiting this property is represented by the *transmission* spectrum reproduced as figure (2.10).

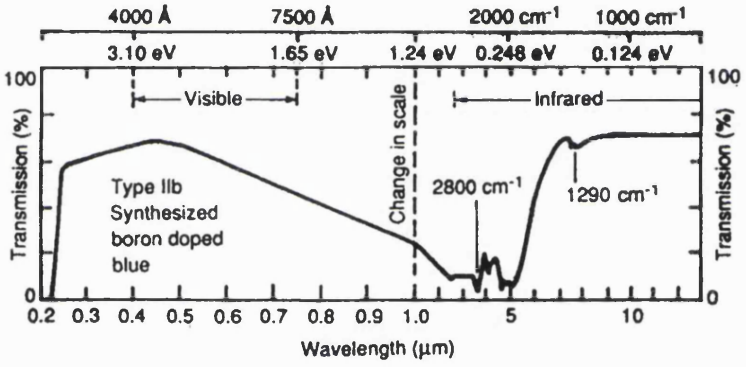

Figure 2.10: Transmission of a synthetic diamond containing boron. [Reproduced from 2.116].

The use of boron doping to achieve n-type electrical conductivity is a key capability underpinning many of the applications envisaged for active electronic devices made from CVD diamond films (§3). Most examples of such doping rely upon incorporation of the boron during film growth from solid or vapour sources including a boron rod [2.43] and, more normally, gaseous borane (B_2H_6) [2.44, 2.45]. Several studies have also demonstrated the viability of ion implantation as a doping technique [2.46, 2.47] although the problem of minimising implantation damage remains an issue. The enhanced process control, uniformity and patterning capabilities of implantation make it far more versatile than grown-in doping, however the high bonding energy and low-pressure metastability of diamond preclude the use of normal thermal annealing techniques to repair the ensuing damage, as will be discussed in a later chapter (§8.1).

Despite the generally poor carrier transport properties of contemporary polycrystalline diamond films (§2.6.2), and the wide variations in material which limited the generality of many early observations, the technology of boron doped p-type diamond has reached a point of relative maturity [2.44, 2.48, 2.49, 2.50]. Werner *et al.* [2.51] have examined the temperature dependent conductivity of samples with a range of doping levels to demonstrate that *in situ* doped polycrystalline films with boron concentrations up to $7x10^{20}cm^{-3}$ conform to theoretical expectations (Fermi-Dirac statistics), whilst heavily doped samples ($N_A>8x10^{20}cm^{-3}$) exhibit metallic (degenerate) conduction with potential applications in contact formation. These results were in good agreement with previous studies using boron doped HPHT diamond [2.52].

2.5.4 Hydrogen in Diamond

Hydrogen is found in many natural diamonds [2.8] and is present to some extent in all CVD material due to its ubiquity for the processes of metastable growth [2.53] (§2.3.3). It has been widely observed that hydrogenation decreases the resistivity of diamond through increased hole conduction leading to a p-type characteristic in the surface region, however the origin of this effect remains controversial. It has been proposed that the carriers arise through the formation of shallow acceptor states beneath the surface when hydrogen is present [2.54, 2.55, 2.56, 2.57], however other studies suggest that surface bound hydrogen causes band bending leading to an accumulation of holes in this region [2.58, 2.59]. In the case of polycrystalline diamond it has also been claimed that changes to the sp^2 (non-diamond) carbon may be responsible for variations in surface conductivity, rather than the hydrogen itself [2.60, 2.61, 2.62]. Recent results [2.63] support the incorporated hydrogen model, however surface hydrogen is known to have a separate role in the prevention of a Fermi level pinning effect [2.64, 2.65, 2.66] (§2.6.1).

2.5.4 Other Impurities in Diamond

Other impurities which can occur in, or be introduced into, diamond include phosphorous, sodium and lithium . Although distinct optical and electrical effects have been observed in some such samples, it has been commented that nitrogen and boron are the only substitutional impurities which have been shown to influence the electrical properties of natural diamond [2.42]. It therefore remains a matter of intense debate whether n-type characteristics observed in material which has been doped with phosphorous, sodium or lithium are due to the donation of carriers by the impurity atom, or disruption of the lattice which itself could be attributed either to the presence of the interstitial, or implantation damage when ion implantation has been used.

Phosphorous in believed to occupy a substitutional lattice location in diamond and is expected to form a donor level 0.2eV below the conduction band edge, however the substantially larger covalent radius of phosphorous (1.13Å) compared to carbon (0.77Å) leads to a large formation energy and low solubility which mitigate against efficient incorporation either during growth or by subsequent implant-and-anneal processes [2.39]. *In situ* phosphorous doping of CVD diamond has been reported using both powdered [2.67] and gaseous [2.68] diphosphorous pentoxide (P_2O_2) as well as tri-n-butylphosphine [2.69] and phosphine (PH_3) [2.70] however carrier densities, confirmed by Hall measurements to be n-type, were low, typically in the order of $10^{15}cm^{-3}$ and mobility where reported was also poor at $\approx 50cm^2V^{-1}s^{-1}$ [2.68].

Lithium and sodium have been proposed as interstitial donor dopants with activation energies 0.1eV and 0.3eV respectively [2.39] however efficient incorporation remains problematic. Ion implantation of both species into natural IIa diamond has been demonstrated, however the authors acknowledge that the low values of conductivity obtained could be attributed to implantation damage rather than ionised dopant atoms. Interstitial lithium is known to relatively mobile in diamond at moderate temperatures [2.39] and recent studies have reported high concentrations of lithium incorporation (in the order of $10^{21}cm^{-3}$) into Ia and IIa crystals by in-diffusion under a 400-600°C temperature regime [2.71]. The fact that no n-type behavior was observed after this processing was attributed to clustering of the lithium atoms in the near surface region.

2.6 Structural Defects in Diamond

In addition to lattice damage caused by the presence or incorporation of impurities as discussed above, structural defects can occur in diamond due to damage such as high energy particle irradiation or as a result of the conditions under which the material formed. In the case of polycrystalline CVD diamond the point defects, stacking faults and dislocations which occur in any crystal growth regime are compounded by the effects of grain boundaries and secondary nucleation sites to further deteriorate the carrier transport and optical properties of the ideal material.

2.6.1 Surface Reconstruction

Unless terminated by hydrogen (§2.5.4), the (111) and (100) diamond surfaces are known to relax such that the top two layers of carbon atoms are rearranged into a zig-zag structure described as a 'π-bonded chain' [2.72]; crystallographically this can be stated in terms of Low Energy Electron Diffraction (LEED) patterns using Wood

notation [2.73] as a (2x2)/(2x1) reconstruction of the (1x1) surface. In the case where hydrogen termination has prevented this re-ordering, the surface is described as 'unreconstructed'.

It is now well established that reconstruction gives rise to both occupied and empty surface states which act to pin the diamond Fermi level at a higher position in the bandgap than for the unreconstructed surface [2.72]. It has also been widely demonstrated that the surface hydrogenation can be removed by annealing in the temperature range 400-780°C in a nitrogen ambient and restored by processing in a hydrogen plasma [2.53].

2.6.2 Damage Induced Defects

Although diamond is regarded as a particularly 'radiation hard' semiconductor on account of its strong covalent bonding and wide bandgap (§3.8.2), it is nonetheless susceptible to damage caused by sufficiently high energy radiation or particle bombardment. Radiation damage is used in the gem trade to modify the appearance of diamonds to be sold for jewellery, as a result of which a number of specific defect mechanisms have been studied extensively.

The two primary radiation induced defects are known as GR1 ('general radiation') and ND1 and are typically formed under high energy electron (1-2MeV) [2.8] or neutron (0.1 -7MeV) [2.73] radiation. Both arise from the creation of a vacancy and an interstitial when a carbon atom is displaced from the lattice, a process which has been calculated to have a threshold energy of 35±5eV [2.8]. In both cases however the characteristic of the resulting defect has been found most closely to resemble a vacancy, with GR1 being neutral and ND1 having a negative charge. Both defects modify the optical absorption of a sample but in very different ways. ND1 is essentially a photoconducting system [2.74] in which the spectral absorption due to the centre is reproduced in the photoconductive photocurrent spectra obtained from the sample reproduced as figure (2.11(a)), whilst the GR1 system has been labelled luminescent and exhibits an inverse correlation between the additional absorption components and the photoconductivity of the modified material, figure (2.11(b)).

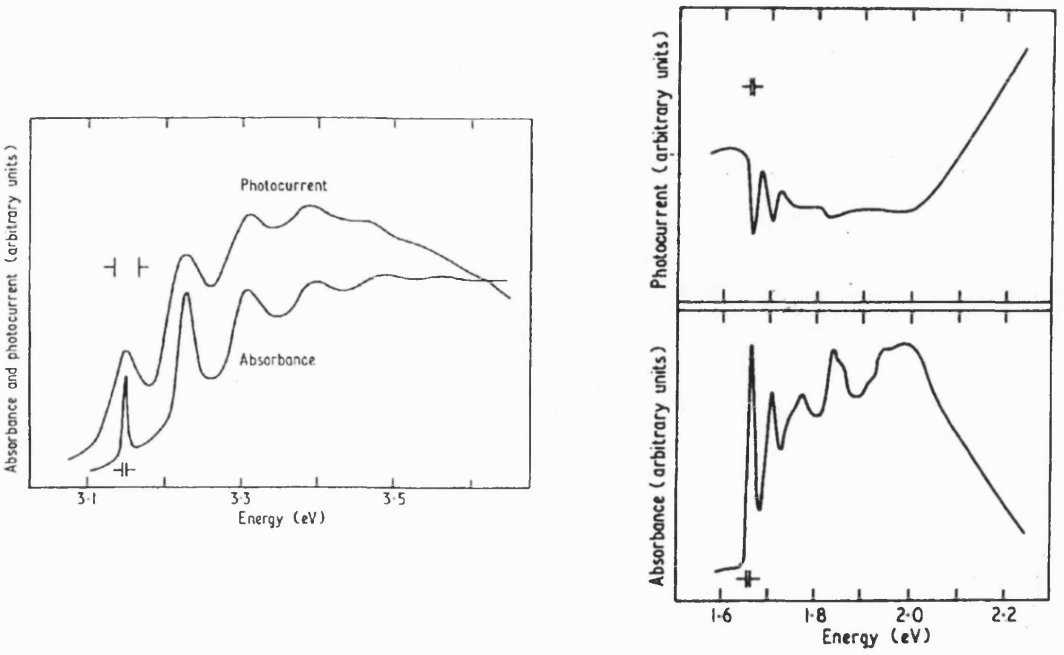

Figure 2.11: radiation induced defect centres (a) left: the absorption and photoconduction spectra caused by the ND1 centre. (b) right: the absorption and photocondution spectra caused by the GR1 centre. [Reproduced from 2.74].

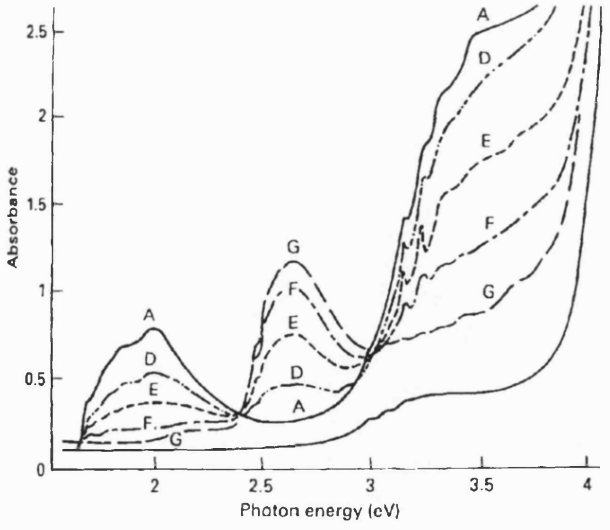

Figure 2.12: The effect of annealing at a range of temperatures up to 930°C (increasing A-D) on the optical absorption of radiation damaged diamond. [Reproduced from 2.8].

Further modification of the optical absorption properties of radiation damaged diamond can be effected by annealing the sample, as indicated by figure (2.12) which shows dramatic changes occurring in the 1-4eV (310nm-1.24μm) spectral region of a sample annealed at temperatures up to 930°C after 1MeV electron irradiation. It has been suggested that interstitials may become mobile at ≈50K whilst vacancies remain immobile to ≈600°C [2.8] which may explain why defects in the region of original damage tend to exhibit vacancy-like characteristics. Annealing at temperatures >600°C is believed to cause a migration of vacancies towards A and B centres when present, resulting in a new set of defects labelled H3 and H4 having the characteristics outlined in table (2.4).

Centre	Peak energy (eV) / wavelength (nm)	Structure
GR1	1.673 / 741	Neutral vacancy
ND1	3.150 / 393	Negative vacancy
After Annealing		
H3	2.463 / 503	Vacancy plus A
H4	2.498 / 496	Vacancy plus B
1.945	1.945 / 595	Vacancy plus C

Table (2.4): Optical centres produced by irradiation and subsequent annealing [Reproduced from 2.8].

2.6.2 Defects in Polycrystalline Diamond

The grain boundaries in polycrystalline diamond films can clearly be expected to modify the characteristics of CVD material from those of a good quality single crystal, however such regions are by their nature difficult to analyse because they consist of inhomogeneous regions of random disorder. The formation and hence the structure of grain boundaries can be influenced by factors including the orientation of the adjoining crystallites, stress and strain arising from the disordered lattice, the presence of impurities which typically diffuse towards grain boundaries and the thermodynamic regime under which the film was formed. It is therefore expected that grain boundaries will contain dangling bonds, interstitials, vacancies and localised regions typical of all the possible carbon phases. Because of the difficulty in identifying individual phases in such a region, and the question of how many atoms in a given arrangement are necessary to constitute a region of a particular phase, the term 'non-diamond carbon' (NDC) is widely used to describe such material.

Whilst it has been speculated that conduction in specific diamond films may be linked to interstitial carbon donor levels and vacancy acceptor levels [2.75], the mechanisms which govern electrical conduction in polycrystalline diamond have been subject to extensive debate. In separate studies Sugino *et al.* [2.76] and Fiegl *et al.* [2.77] have examined the d.c. current-voltage (I-V) characteristics of MPACVD films and attributed the observed conductivity to grain boundary effects whilst an investigation by Ashok *et al.* [2.78] found evidence of space charge limited conduction (carrier injection) (§2.7.1) within crystallites having a high density of traps. The conclusions of Sugino *et al.* differ from those of Fiegl *et al.* in that the latter work attributes all conduction to grain boundary hopping whilst the former identifies two distinct regions of the I-V behaviour: at fields of up to $\approx 4 \times 10^6 Vcm^{-1}$ an ohmic ($I \propto V$) characteristic was observed whilst at higher fields the current was seen to exhibit a dependence on the square root of the bias potential consistent with Poole-Frenkel conduction. This mechanism consists of field enhanced thermal excitation of trapped electrons into the conduction band and is entirely expected above the electric field breakdown strength of a semiconductor [2.79] (§2.4.4).

At fields below $4 \times 10^6 Vcm^{-1}$ Sugino *et al.* found different conduction mechanisms to operate according to the processing experienced by the sample. As-grown samples which had been rapidly cooled in vacuum after deposition, and which were therefore believed to be non-hydrogen terminated, were relatively conductive having a conductivity $\sigma_a \approx 10^{-6} Scm^{-1}$. This was attributed to surface and grain boundary conduction through non-diamond carbon material, the presence of which was confirmed by the detection of a broad Raman peak (§4.4.3) around $1500cm^{-1}$ which is indicative of disordered sp^2 bonded graphitic carbon. Annealing in flowing nitrogen at 570 K and 670 K resulted in progressive reductions in the conductivity to $\sigma_b \approx 10^{-8} Scm^{-1}$ and $\sigma_c \approx 10^{-13} Scm^{-1}$ respectively, after which further heating yielded no additional reduction in conductivity. The greatly improved resistivity of annealed samples was attributed to removal of non-diamond carbon material, a postulate supported by a Raman spectrum of an annealed film which contained only the $1333cm^{-1}$ diamond signature and lacked the $1500cm^{-1}$ NDC component. Further confirmation of NDC removal was provided by etching a sample in a hot CrO_3-H_2SO_4 solution which is known to oxidise diamond and attack non-diamond material (§4.2.2); this sample generated similar I-V and Raman results to the annealed samples. Analysis of the weak $T^{-1/4}$ temperature dependence of the conductivity under this regime indicated variable range hopping to be the dominant conduction mechanism. The conductivity of the annealed samples had a stronger temperature dependence and was found to be governed by traps with an activation energy of $\approx 0.93eV$ attributed to small levels of residual NDC material .

Pan *et al.* [2.80, 2.81] and Jany *et al.* [2.82] have identified the effective mean carrier collection distance d within a sample as being a key parameter indicating film quality for device applications such as ionising radiation detectors. Incorporated in d are the effective carrier mobility μ_{eff} and lifetime $\tau_{l[eff]}$ which, as a product with the applied field $E=V_B/l$ indicate the average distance which the carriers created within a crystallite can be expected to travel before being lost to recombination:

$$d = \mu_{eff}\tau_{l[eff]}E \tag{2.8}$$

The value of d as a parameter is that it has both a good physical interpretation and can be determined empirically by insertion of measured values for μ and τ, subject to the limitation that it is often impossible to separate the electron and hole components of the input data which must therefore be expressed as 'effective' values.

Studies by Pan *et al.* [2.27] and Plano [2.83] have investigated the transport characteristics of carriers within diamond films at the growth surface and in the nanocrystalline region at the nucleation surface. Reference to the electron micrograph in figure (4.3) suggests intuitively that larger crystallite dimensions should yield better performance. This is supported by the above studies in which Pan *et al.* working on 360μm thick MPACVD film found that mobility on the growth (large grain) surface was 50 times greater than on the nucleation surface as indicated in figure (2.13(a)). Plano *et al.* working on 500μm thick MPACVD and flame grown material compared the surface collection distance d_s for planar electrode structures with the bulk collection distance d_b for 'sandwich' electrodes on the growth and nucleation surfaces. The results reproduced as figure (2.13(b)) clearly show that $d_s \approx 2d_b$ for both types of film.

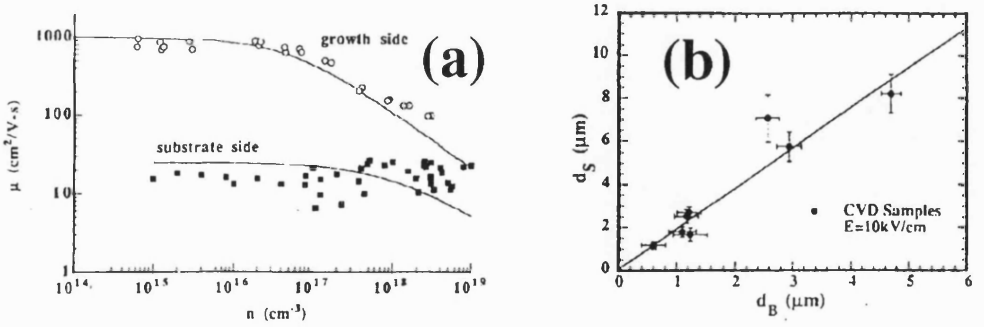

Figure 2.13: (a) A comparison of the carrier mobilities on the nucleation and growth surfaces of a 360μm thick MPACVD diamond film. (b) A comparison of the surface and bulk carrier collection distances in CVD diamond films of different thicknesses. [Reproduced from 2.27, 2.83]

An observation by Pan *et al.* [2.27] in 1993 was that collection distances at the time of writing (d_{CVD}<0.1μm, d_{IIa}≤30μm) were substantially less than the average crystallite size in the samples under investigation (≈1μm diameter). This led to the conclusion that charge centre scattering within crystallites was the primary limit on mobility in such CVD films for all carrier densities in contrast to natural IIa material, wherein mobility is limited by phonon scattering at low carrier densities and by carrier scattering at high densities. More recently reported collection distances in CVD material have been in the range 60-80μm [2.84].

2.7 Electrical Contacts to Diamond

The provision of reliable electrical contacts to the semiconductor surface is a fundamental requirement common to all microelectronic device technologies. Contacts are required variously to bias, remove carriers from and inject carriers into the active regions of a device and can be designed to fulfil their specific functions according to a combination of theoretical and empirical insight.

2.7.1 Metal-Semiconductor Contacts

Under ideal conditions the electrical behaviour of an intimate metal-semiconductor contact is determined by the relative magnitudes of the metal workfunction $q\phi_M$ and the semiconductor workfunction† $q\phi_s$. In the case of a p-type semiconductor, such as most doped diamond films (§2.5), a rectifying contact is obtained if $q\phi_M < q\phi_s$ and an ohmic contact results if $q\phi_M > q\phi_s$. This description is however qualified by the comment that surface states frequently modify the interface properties of such systems, leading to electrical characteristics substantially different to those which might be anticipated based the nature of the bulk material. Further complexity arises because an evaporated metal contact will be polycrystalline causing ϕ_M to deviate from the ideal value quoted for a single crystalline vacuum-metal interface as illustrated by table (2.5).

The energy band structure of a rectifying contact between a metal and a p-type semiconductor meeting the requirement $q\phi_M < q\phi_s$ is outlined schematically in figure (2.14). At thermal equilibrium the surface band bending required to match the Fermi

† The term 'semiconductor workfunction' may not strictly be correct, but lends clarity to the description and is used in several authoritative texts including those of Rhoderick [2.86] and Bube [2.85]. More properly, one could define $q\phi_s \equiv q(\chi + V_b)$ where $q\chi$ is the electron affinity of the semiconductor measured from the bottom of the conduction band to the vacuum level, and qV_b is the energy difference between the Fermi level and the bottom of the conduction band [2.79].

levels of the metal and the semiconductor results in a diffusion potential $\phi_D = (\phi_s - \phi_M)$ and a barrier height given by $q\phi_B = E_g - q(\phi_M - \chi)$, where $q\chi$ is the electron affinity of the semiconductor as shown in figure (2.14(a)) [2.79, 2.85].

Metal	ϕ_M (C-V)	ϕ_M (Photoresponse)	ϕ_M (Vacuum Work Function)
Mg	3.35	3.15	3.7
Al	4.1	4.1	4.25
Ni	4.55	4.6	4.5
Cu	4.7	4.7	4.25
Ag	5.0	5.0	4.8
Ag	5.1	5.05	4.3

Table (2.5): The work functions of a number of contact metals obtained experimentally for the polycrystalline case using an Si-SiO_2 MOS diode (capacitance-voltage and photoemission techniques) and for single crystal samples (in vacuum) [Reproduced from 2.79].

When a forward bias is applied, in the sense that the semiconductor is made positive with respect to the metal, ϕ_D is reduced by the bias potential V_B enabling a hole current to flow into the metal (figure (2.14(b)). Under a reverse bias the band bending is increased and the current becomes independent of the bias, being controlled instead by the unchanging barrier height ϕ_B as sketched in figure (2.14(c)).

The current density J through the contact is given by [2.85]:

$$J = J_0\left(\exp\left(\frac{qV_B}{nkT}\right) - 1\right) \tag{2.9}$$

in which k is the Boltzmann constant, T the temperature in kelvin and n the ideality factor. The exponential term in equation (2.9) describes the influence of the bias on the band bending and J_0 accounts for the thermionic emission component such that [2.86]:

$$J_0 = A^{**}T^2 \exp\left(\frac{-q\phi_B}{kT}\right) \tag{2.10}$$

where A^{**} is the modified Richardson constant, reduced from its free carrier value of 12×10^5 $Am^{-2}K^{-2}$ due to factors including the effective mass of the carriers (§2.4.2). It is possible to this explore these expressions more closely, particularly by breaking A^{**}

into more fundamental components and including the series resistance of the device in J, however the above description is more than sufficiently detailed for the predominantly qualitative analysis appropriate to contemporary rectifying contacts on diamond.

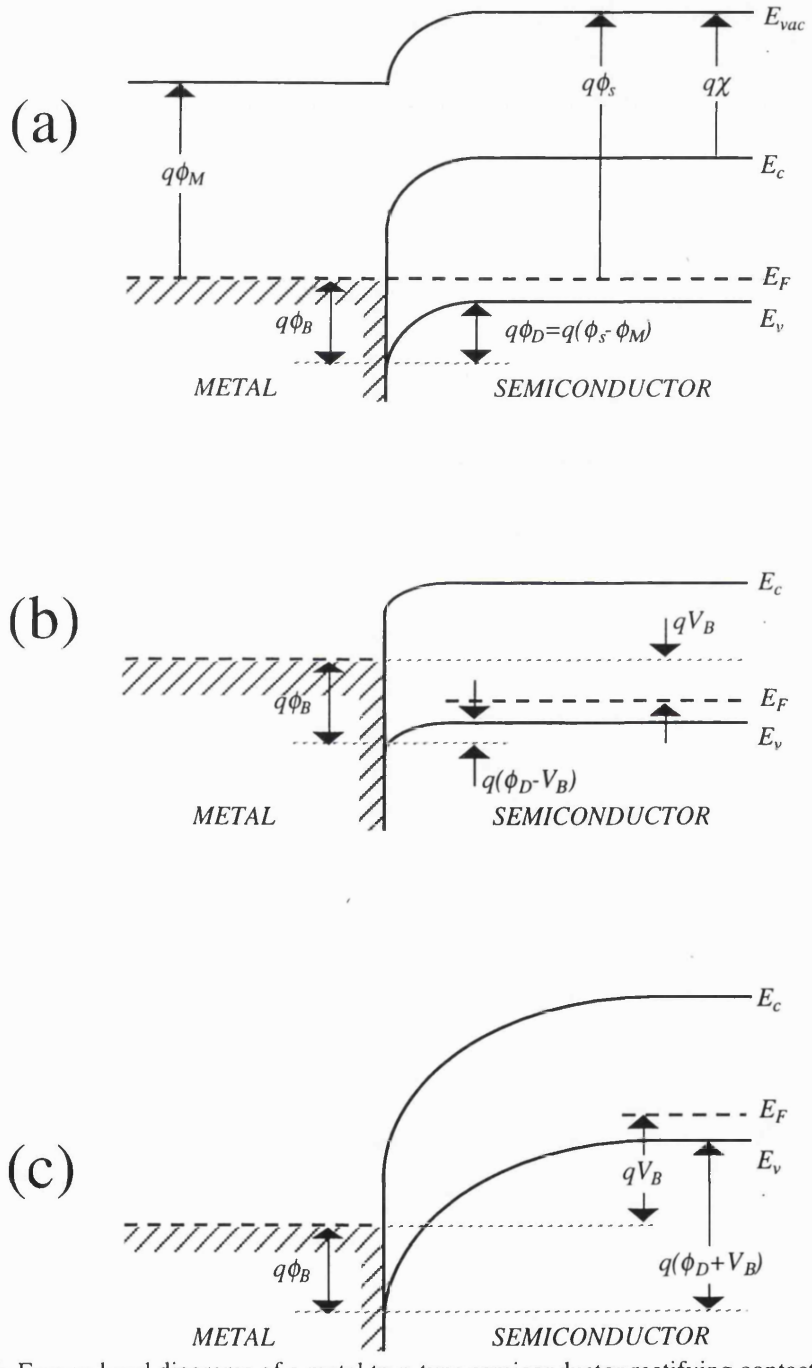

Figure 2.14: Energy band diagrams of a metal to p-type semiconductor rectifying contact (a) thermal equilibrium (b) forward bias (c) reverse bias.

As a prelude to the following paragraphs it should be noted that the term 'ohmic' is used very loosely when applied to contact technologies. A linear relationship between current passed and voltage applied is not necessarily the defining factor of what is regarded as a good ohmic contact: an interface which obeys Ohm's law but has substantial contact resistance R_c is of little practical use. Instead, the accepted meaning of the term is given by Rhoderick [2.86] as a contact which has a very small resistance compared to the device or structure it services.

The theoretical approach to forming an ohmic contact to a p-type semiconductor is outlined in figure (2.15(a)) in which it can be seen that because the Fermi levels have been aligned by the transfer of majority carriers, the near surface of the semiconductor is an accumulation region rather than a depletion region and there is negligible impediment to carriers traversing the interface in either direction.

If the bias applied to an ohmic contact becomes sufficiently large, then carriers injected from the contact may become the dominant component of the current flowing in the semiconductor. In this situation the semiconductor could be viewed as a dielectric of permittivity $\varepsilon_r\varepsilon_0$ between two capacitor plates of spacing d; the current is then described as being 'space-charge-limited' with the current density J_{SLC} approximated by [2.85]:

$$J_{SLC} \approx \frac{\varepsilon_r \varepsilon_0 \mu V_B^2}{d^3} \tag{2.11}$$

where μ is the carrier mobility in the semiconductor.

In practice it is often unrealistic to use a metal satisfying the $q\phi_M > q\phi_s$ criterion for ohmic contacts, so one of two highly effective but less analytically elegant approaches is usually used. Figure (2.15(b)) illustrates the band structure arising when a rectifying contact is made to the surface of a very highly doped region of semiconductor: the high density of mobile carriers results in a very narrow depletion region which facilitates bi-directional carrier transport across the interface by tunnelling through the barrier, regardless of its height [2.79]. An alternative and highly empirical technique is to create a high density of surface defects leading to a large number of sub-bandgap states [2.86]; these reduce the effective barrier height by pinning the Fermi level at a higher energy than would occur in the unpinned condition (allowing that for p-type material hole energy increases in the direction *away* from the vacuum level). Appropriate 'damage' can be caused chemically by selecting a contact metal that will react with the semiconductor, or physically by milling or ion implantation.

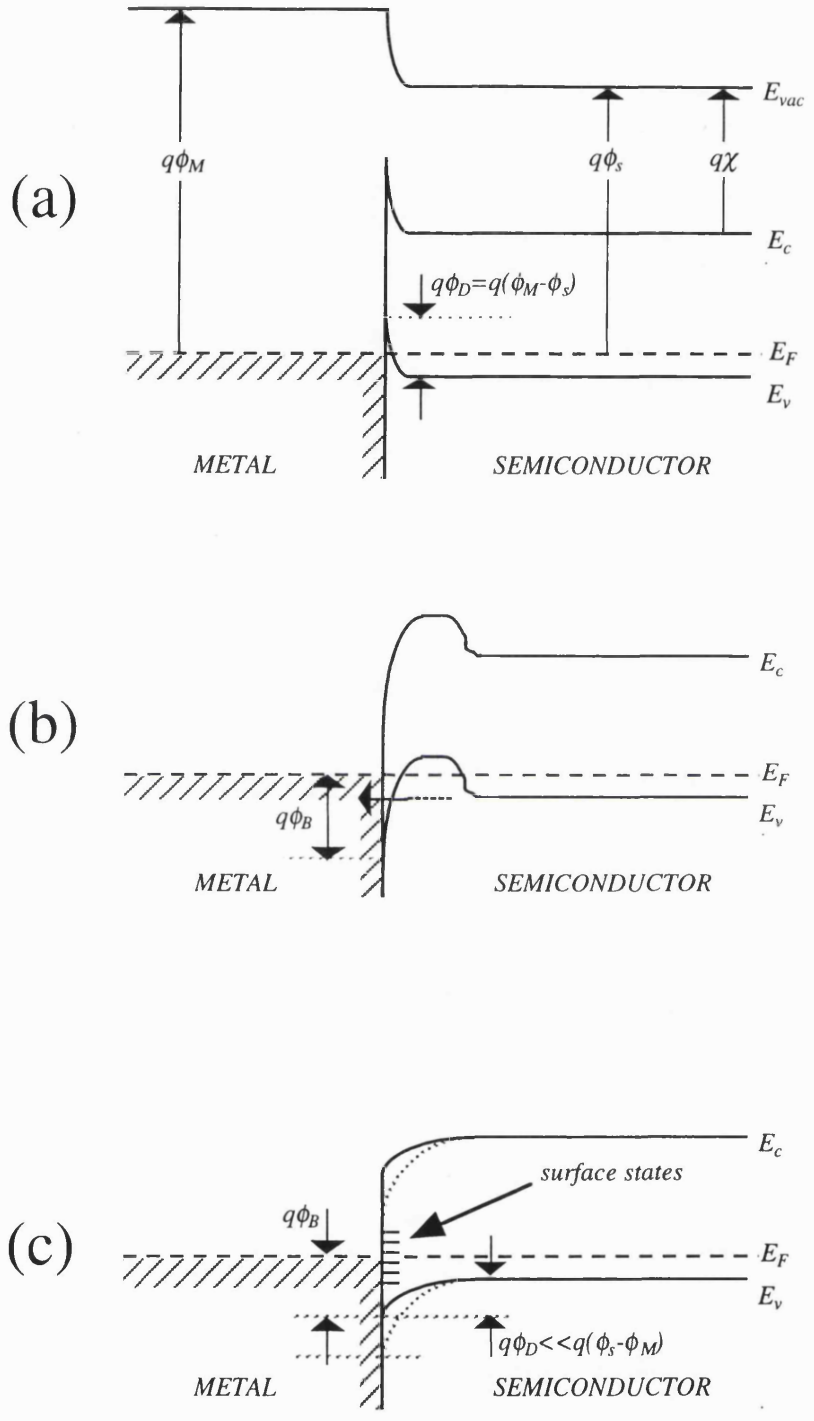

Figure 2.15: Standard methods of ohmic contact formation to a p-type semiconductor (a) metalisation selected such that $q\phi_M > q\phi_M$ (b) degenerately doped contact region (c) reduced barrier height due to surface defects which pin Fermi level.

2.7.2 Metal-Diamond Contacts

In the formation of contacts to diamond, the presence or absence of hydrogen is of critical importance. If device designs require rectifying contacts to be made then they must tolerate either the Fermi level pinning of the reconstructed diamond surface (§2.6.1), or near surface conductivity due to the hydrogen which is required to stabilise the unreconstructed surface (§2.5.4). The situation is further complicated by the variation in the work function $q\phi_d$ which has been measured for diamond samples having supposedly similar surface termination. Table (2.6) lists values ranging from 7eV down to the negative electron affinity (NEA) condition in which the vacuum level is less than the conduction band minimum. Against this background it is clear that selecting a metalisation regime according to the work function criteria alone is unlikely to produce the desired results, and it can be of little surprise that formation of both ohmic and rectifying contacts on diamond, and particularly CVD diamond, is primarily an empirical discipline.

Surface condition	Work Function, (eV)
Unreconstructed, calculation	7±0.7
Hydrogenated	NEA
Reconstructed	4.4
Reconstructed	<5

Table (2.6): The workfunction of the diamond surface reported by a number of studies on samples having different termination [Data abstracted from 2.87].

2.6.1 Ohmic Contacts to Diamond

Silver dag is the simplest reported contact to diamond and has found extensive use in the electrical and electro-optic study of natural material [2.88]. The silver particles in the dag are literally glued onto the surface of the sample, from which it is clear that a truly intimate contact is unlikely to result: this indicates that injection is the likely transport mechanism in such experiments, a view which is supported by the high bias potentials employed in many of these studies.

Properly formed ohmic contacts to CVD diamond have been reviewed by van Enckevort [2.89] who notes that by far the most widely used technique involves the application of a thin layer of a carbide forming metal to the diamond surface; this is

then covered with a less reactive metal to form a structure which is both robust and electrically efficient. Metals which form a conductive carbide on diamond include titanium, tantalum [2.90] and molybdenum [2.91, 2.92, 2.93] of which titanium is the most commonly used, in combination with gold as the protective cap.

Although the formation of titanium carbide is thermodynamically favoured at room temperature (ΔH=-44kcal/mol at 25°C) [2.94], it has been found that reduced resistance and improved linearity can be obtained from Ti/Au contacts after annealing for 20-30 minutes at temperatures in the range 430-850°C [2.94, 2.95, 2.96, 2.97]. Tachibana et.al. [2.98] confirmed experimentally that the ohmic characteristic of Ti based contacts is due to the reaction in which TiC is formed, rather than the presence of TiC. TiC contacts on a B doped MPACVD sample were demonstrated to be temperature-stable rectifiers, whilst Ti contacts on the same sample exhibited a poor diode characteristic in the as-deposited condition and became low-resistivity ohmics after annealing. A specific resistivity of $2x10^{-6}\Omega.cm^2$ has been reported for Ti/Au contacts deposited on MPACVD material where the host surface had been rendered highly p-type conductive by B ion implantation to a density of $\approx 7x10^2 cm^{-3}$ [2.96].

The high diffusivity of Ti in Au can result in long term contact deterioration, especially when operated at high temperatures [2.99, 2.100]. To address this problem a number of tri-layer schemes have been investigated in which a 'barrier' metal is introduced between the Au and the Ti, examples of this approach include the use of Ti/Pt/Au [2.101] and Ti/Ag/Au [2.102].

Non-carbide forming schemes which have been reported as offering ohmic contact behaviour include Pt, In, Al, Au , Mg, Pd, Al/Si and TiWN-Au [2.89, 2.91, 2.100, 2.103], although in several of these cases ohmic characteristics were only obtained on heavily doped regions whilst rectification occurred on low conductivity samples [2.91, 2.103]. The Al/Si system on $5x10^{21}cm^{-3}$ *in situ* B doped MPACVD material resulted in a specific contact resistivity of $2.3x10^{-7}\Omega.cm^2$, which is in the order specified by Rhoderick [2.86] for a good general purpose ohmic contact. A further area of research has been to create physical surface damage as opposed to the chemical 'damage' of carbide formation. Kr^+ ion implantation at a dose of $2x10^{16}cm^{-2}$ has been used to 'mix' Si contacts into the surface of natural IIb diamond resulting in a specific contact resistivity of $\approx 7x10^{-4}\Omega.cm^2$ [290].

2.6.2 Rectifying Contacts to Diamond

The ability to create rectifying contacts on diamond, and the characteristics of such contacts as have been demonstrated, continues to be highly dependant upon the qualities of the diamond to which the contact is made. Rectifying characteristics have been demonstrated using Au [2.95, 2.104, 2.105], Al [2.55, 2.105, 2.106, 2.107], Ag [2.108], W [2.109], Ni [2.110], Cu [2.111], Hg [2.105], Pt [2.112], Ti [2.113], TiC [2.98, 2.114] and P-Si [2.112, 2.115] to offer a small but representative representative sub-set of the results which are in the public domain. From the above list it can be inferred that under appropriate conditions almost any metal contact to diamond will be rectifying, which tends to support the higher values of $q\phi_d$ presented in table(2.6). In order to establish a reliable baseline for comparisons, it is useful to consider methods by which a diamond surface may be standardised, or at least processed into a known starting condition. There two most intuitive techniques for this are either to oxidise the surface thereby removing hydrogen or to hydrogenate the surface and exploit the resulting p-type conductivity for device fabrication.

Diode formation on an oxidised surface has been demonstrated by Ebert *et al.* [2.117], who used *in situ* B doped (10^{16}-10^{19}cm^{-3}) homoepitaxial single crystalline MPACVD films on highly doped (N_A>10^{20}cm^{-3}) commercial synthetic substrates. After growth the samples were cleaned in an oxygen plasma process prior to device fabrication. Ohmic contacts were provided through the substrate and the Schottkys were lithographically defined in sputtered Au on the oxidised growth surface of each sample. At room temperature a device on highly doped (N_A≈10^{18}cm^{-3}) material exhibited poor rectification and fitted an ideality factor of 2.0 which conforms to the expectation that thermionic emission should dominate at high doping densities. Samples with a lower doping density (N_A≈3x10^{16}cm^{-3}) had ideality factors of ≈1.2 and a rectification ratio of more than eight orders of magnitude at ±5V with breakdown at ≈90V and a pre-breakdown reverse current density of ≈5μA. The Schottky barrier height for the lower doped devices was in the range 1.6-1.8eV although this is likely to have been determined by the Fermi level pinning rather than by the choice of Au as the contact metal. An unrelated study of Schottky barrier heights on oxidised (600°C, 20 minutes) *in situ* B doped (N_A≈2.5x10^{18}cm^{-3}) polycrystalline CVD material [2.118] found a $q\phi_B$ value of ≈0.5eV for Ti, Mo, Cr, Co and Pt providing clear evidence of Fermi level pinning. The difference in the pinned values obtained in these two carefully executed studies indicates how much more remains to be learned about the intimate metal-diamond interface on oxidised surfaces.

Using MPACVD on Ib substrates, Hayashi *et al.* [2.66] deposited homoepitaxial undoped and B doped diamond films which were fully hydrogenated by being allowed to cool in a hydrogen ambient after deposition whilst control samples underwent hydrogen removal by wet oxidation in an acidic H_2SO_4/HNO_3 solution. Al Schottky contacts and unannealed Ti/Au ohmics were formed and found to offer a rectification ratio of over six orders of magnitude at ±1V and a reverse leakage current of less than 0.01pA on the hydrogenated samples. The oxidised controls exhibited no rectification and were highly resistive, passing a current of ≈0.5pA at all bias levels. On subsequent rehydrogenation however, after fifteen minutes at 750°C in a hydrogen plasma, the undoped sample exhibited excellent diode characteristics which were comparable to those of the original hydrogen terminated device. Further evaluation by Hall effect measurements indicated that both the doped and undoped hydrogenated samples had near surface region carrier concentrations in the order of $10^{12}cm^{-2}$ which was four orders of magnitude more than the oxygenated, doped sample. Such results lay the groundwork for more sophisticated devices such as the recently announced field effect device employing the excellent carrier transport properties offered by hydrogen related conductivity to demonstrate the potential for exceptionally high speed, high power devices [2.119].

2.9 References

2.1 S.M. Sze, "Semiconductor Devices: physics and technology", Wiley, New York, 1985.

2.2 D.F. Shriver, P.W. Atkins and C.H. Langford, "Inorganic Chemistry", 2nd Edition, Oxford University Press, Oxford (1996).

2.3 H.O. Pierson, "Handbook of Carbon, Graphite, Diamond and Fullerenes: properties, processing and applications", Noyes Publications, New Jersey (1993)

2.4 I.A.S. Edwards, " Structure in Carbon and Carbon Forms" in "Introduction to Carbon Science", Ed. H. Marsh, Butterworth, London, 1989.

2.5 M. Dresselhaus, G. Dresselhaus, P. Eklund and R. Saito, Physics World, pp33, January (1998).

2.6 G.S. Woods in "Properties and Growth of Diamond", Ed. G. Davies, INSPEC, London , UK, pp98, 1994.

2.7 J. Banfield "Diamonds and Diamond Simulants", Lecture notes for "Geology 306" at University of Wisconsin-Madison, USA, available at http://www.geology.wisc.edu/~jill/Lect6.html, (1997).

2.8 J. Wilks and E. Wilks, "Properties and Applications of Diamond", Butterworth-Heinemann, Oxford (1991).

2.9 F.P. Bundy, H.T. Hall, H.M. Strong and R.H. Wentorf Jr., Nature Lond. 176, 51 (1955)

2.10 National Materials Advisory Board, "Status and Applications of Diamond and Diamond-Like Materials: An Emerging Technology", NMAB-445, National Academy Press, Washington USA (1990).

2.11 B.V. Spitsyn, L.L. Bouilov and B.V. Derjaguin, Journal of Crystal Growth 52, 219 (1981).

2.12 W.G. Eversole, United States Patent Specification 3,030,187 (1962).

2.13 W.G. Eversole, United States Patent Specification 3,030,188 (1962).

2.14 J Angus, H.A. Will and W.S. Stanko, Journal of Applied Physics 39, 2915 (1968).
2.15 Y. Hirose, S. Amanuma and K. Komaki, Journal of Applied Physics 68, 6401 (1990; 1988).
2.16 M. Kamo, Y. Sato, S. Matsumoto and N. Setaka, Journal of Crystal Growth 62, 642 (1983).
2.17 W. Zhu, B.R. Stoner, B. E. Williams and J.T. Glass, Proceedings of the IEEE 79, 621 (1991).
2.18 C. Wild, M. Füner, E. Wörner, R. Locher, W. Muller-Sebert and P. Koidl, at Diamond 1997 Conference, Heriot-Watt University, Edinburgh 3-8 Aug. 1997, proceedings in press as Diamond and Related Materials.
2.19 B.R. Stoner, G.-H.M. Ma, S.D. Wolter and J.T. Glass, Physical Review B 45, 11067 (1992).
2.20 D.K. Milne, P.G. Roberts, P. John, M.G. Jubber, M. Liehr and J.I.B. Wilson, Diamond and Related Materials 4, 394 (1995).
2.21 C.Y. Fong and B.M. Klein, "Electronic and Vibrational Properties of Bulk Diamond" in "Diamond: Electronic properties and Applications", Ed. L.S. Pan and D.R. Kania, Kluwer Academic Press, Massachusetts, USA, 1995.
2.22 C.M. Wolfe, N. Holonyak Jr. and G.E. Stillman, "Physical Properties of Semiconductors", Prentice-Hall, New Jersey (1989).
2.23 G.S. Painter, D.E. Ellis and A.R. Lubinsky, Physical Review B4, 3610 (1971).
2.24 A. Mainwood, in "Properties and Growth of Diamond", Ed. G. Davies, INSPEC, London , UK, pp3, 1994.
2.25 B.G. Streetman, "Solid State Electronic Devices", Prentice-Hall, New Jersey, 1990.
2.26 S.S.M. Chan, "Electronic Device Fabrication from Thin Film Diamond: surface preparation, patterning, metallisation and characterisation", PhD Thesis, University College, University of London, 1996.
2.27 L.S. Pan, D.R. Kania, P. Pianetta, J.W. Ager III, M.I. Landstrass and S. Han, Journal of Applied Physics 73, 2888 (1993).
2.28 K. Shenai, R.S. Scott and B.J. Baliga, IEEE Transactions on Electron Devices 36, 1811 (1989).
2.29 R.J. Trew, J-B. Yan and P.M. Mock, Proceedings of the IEEE 79, 598 (1991).
2.30 M.W. Geis, Proceedings of the IEEE 79, 669 (1991).
2.31 R. Robertson, J.J. Fox and A.E. Martin, Philosophical Transactions of the Royal Society of London A232, 463 (1934).
2.32 A.T. Collins in "Properties and Growth of Diamond", Ed. G. Davies, INSPEC, London , UK, pp263, 1994.
2.33 A.T. Collins, in "Properties and Growth of Diamond", Ed. G. Davies, INSPEC, London , UK, pp284, 1994.
2.34 S. Sonoda, J.H. Won, H. Yagi, A. Hatta, T. Ito and A. Hiraki, Appl. Phys. Lett. 70, 2574 (1997).
2.35 P. Denham, E.C. Lightowlers and P.J. Dean, Physical Review 161, 762 (1967).
2.36 M.H. Nazaré in "Properties and Growth of Diamond", Ed. G. Davies, INSPEC, London , UK, pp88, 1994.
2.37 M.H. Nazaré in "Properties and Growth of Diamond", Ed. G. Davies, INSPEC, London , UK, pp90, 1994.
2.38 I. Kiflawi, H. Kanda, D. Fisher and S.C. Lawson, Diamond and Related Materials 6, 1643 (1997).
2.39 S.A. Kajihara, A. Antonelli, J. Bernholc and R. Car, Physical Review Letters 66, 2010 (1991).
2.40 M.H. Nazaré in "Properties and Growth of Diamond", Ed. G. Davies, INSPEC, London , UK, pp85, 1994.
2.41 M.H. Nazaré in "Properties and Growth of Diamond", Ed. G. Davies, INSPEC, London , UK, pp92, 1994.
2.42 A.T. Collins, Semiconductor Science and Technology 4, 605 (1989).
2.43 H. Opyrchal, K.K. Chin, E. Kohn and W. Ebert, Diamond and Related Materials 6, 940 (1997).

2.44 R.E. Harper, C. Johnston, N.G. Blamires, P.R. Chalker and I.M. Buckley-Golder, Surface and Coatings Technology 47, 344 (1991).

2.45 H. Sternschulte, S. wahl, K. Thonke, R. Sauer, M. Dalmer, C. Ronning and H. Hofsäss, Applied Physics Letters 71, 2668 (1997).

2.46 J. F. Prins, "Modification, Doping and Devices in Ion Implanted diamond" in "The Properties of Natural and Synthetic Diamond", Ed. J.E. Field, Academic Press, London, 1992.

2.47 R. Kalish, C. Uzan-Saguy, A. Samoiloff, R. Locher and P. Koidl, Applied Physics Letters 64, 2532 (1994).

2.48 K. Miyata and D.L. Dreifus, Japanese Journal of Applied Physics 33, 4526 (1994).

2.49 D.M. Malta, J.A. von Windheim and B.A. Fox, Applied Physics Letters 62, 2926 (1993).

2.50 A.T. Collins in "Properties and Growth of Diamond", Ed. G. Davies, INSPEC, London , UK, pp280, 1994.

2.51 M. Werner, O. Dorsch, H.U. Baerwind, E. Obermier, L. Haase, W. Seifert, A. Ringhandt, C. Johnston, S. Romani, H. Bishop and P.R. Chalker, Applied Physics Letters 64, 595 (1994).

2.52 A.S. Vishnevskii, A.G. Gontar, V.I. Torishnii and A.A. Shul'zhenko, Soviet Physics and Semiconductors 15, 659 (1981).

2.53 K. Das, V. Venkatesan, K. Miyata, D.L. Dreifus and J.T. Glass, Thin Solid Films 212, 19 (1992).

2.54 M.I. Landstrass and K.V. Ravi, Applied Physics Letters 55, 1391 (1989).

2.55 H. Shiomi, Y. Nishibayashi and N. Fujimori, Japanese Journal of Applied Physics 29, L2163 (1990).

2.56 T. Maki, S. Shikama, M. Komori, Y. Sakaguchi, K. Sakuta and T. Kobayashi, Japanese Journal of Applied Physics 31, 1363 (1992).

2.57 K. Hayashi, S. Yamanaka, H. Okushi and K. Kajimura, Applied Physics Letters 68, 376 (1996).

2.58 J. Shirafuji and T. Sugino, Diamond and Related Materials 5, 706 (1996).

2.59 H. Kawarada, H. Sasaki and A. Sato, Physical Review B 52, 11351 (1995).

2.60 Y. Mori, Y. Show, M. Deguchi, H. Yagi, H. Yagyu, N. Eimori, T. Okada, A. Hatta, K. Nishimura, M. Kitabatake, T. Ito, T. Hirao, T. Izumi, T. Sasaki and A. Hiraki, Japanese Journal of Applied Physics 32, L987 (1993).

2.61 Y. Muto, T. Sugino, J. Shirafuji and K. Kobashi, Applied Physics Letters 59, 843 (1991).

2.62 A.K. Kulkarni, A. Shrotriya, P. Cheng, H. Rodrigo, R. Bashyam and D.J. Keeble, Thin Solid Films 253, 141 (1994).

2.63 H.J. Looi, L.Y.S. Pang, Y. Wang, M.D. Whitfield and R.B. Jackman, Diamond and Related Materials 7, 565 (1998).

2.64 H. Kawarada, M. Aoki, H. Sasaki and T. Tsugawa, Diamond and Related Materials 4, 961 (1994)

2.65 H. Kiyota, H. Okushi, T. Ando, M. Kamo and Y. Sato, Diamond and Related Materials 5, 718 (1996).

2.66 K. Hayashi, H. Watanabe, S. Yamanaka, T. Sekiguchi, H. Okushi and K. Kajimura, Diamond and Related Materials 6, 303 (1997).

2.67 T.H. Borst and O. Weis, Diamond Films 1994, Il Ciocco, Italy (Elsevier), Pre-print: not published in conferenceproceedings, filed under Diamond & Related Materials 4 (1994).

2.68 K. Okano, H. Kiyota, T. Iwasaki, Y. Nakamura, Y. Akiba, T. Kurosu, M. Iida and T. Nakamura, Applied Physics A 51, 344 (1990).

2.69 T. Nishimori, K. Nakano, H. Sakamoto, Y. Takakuwa and S. Kono, Applied Physics Letters 71, 945 (1997).

2.70 S. Koizumi, M. Kamo, Y. Sato, H. Ozaki and T. Inzuka, Applied Physics Letters 71, 1065 (1997).

2.71 J. te Nijenhuis, G.Z. Cao, P.C.H.J. Smits, W.J.P. van Enckevort, L.J. Giling, P.F.A. Alkemade, M. Nesládek and Z. Remes, Diamond and Related Materials 6, 1726 (1997).
2.72 T.Tachibana, J.T. Glass and R.J. Nemanich, Journal of Applied Physics 73, 835 (1993).
2.73 D.P. Woodruff and T.A. Delchar, "Modern Techniques of Surface Science", Cambridge University Press, U.K., 1986.
2.74 R.G. Farrer and L.A. Vermeulen, Jourcal of Physics C: Solid State Physics 5, 2762 (1972).
2.75 J.W. Vandersande and L.D. Zoltan, Surface and Coatings Technology 47, 392 (1991).
2.76 T. Sugino, Y. Muto, J. Shirafuji and K. Kobashi, Diamond and Related Materials 2, 797 (1993).
2.77 B. Fiegl, R. Kuhnert, M.Ben-Chorin and F. Koch, Applied Physics Letters 65, 371 (1994).
2.78 S. Ashok, S. Srikanth, A. Badzian, T. Badzian and R. Messier, Applied Physics Letters 50, 763 (1987).
2.79 S.M. Sze, "Physics of Semiconductor Devices", Wiley, New York, 1981.
2.80 L.S. Pan, D.R. Kania, S. Han, J.W. Ager III, M. Landstrass, O.L. Landen and P. Pianetta, Science 255, 830 (1992).
2.81 L.S. Pan, S. Han, D.R. Kania, M.A. Plano and M.I. Landstrass, Diamond and Related Materials 2, 820 (1993).
2.82 C. Jany, F. Foulon, P. Bergonzo, A. Brambilla, F. Silva, A. Gicquel and T. Pochet, Diamond and Related Materials Preprint (1996).
2.83 M.A. Plano, S. Zhao, C.F. Gardinier, M.I. Landstrass, D.R. Kania, H. Kagan, K.K. Gan, R. Kass, L.S. Pan, S. Han, S. Schnetzer and R. Stone, Applied Physics Letters 64, 193 (1994).
2.84 C. Manfredotti, F. Fizzotti, K. Mirri, P. Polesello, E. Vittone, M. Jaksic, T. Tadic, I. Bodganovic and T. Pochet, Diamond and Related Materials 6, 320 (1997).
2.85 R.H. Bube, "Photoelectronic Properties of Semiconductors", Cambridge University Press, U.K., 1992.
2.86 E.H. Rhoderick, "Metal-Semiconductor Contacts", Clarendon Press, U.K., 1978.
2.87 S. Evans, "Surface properties of diamond" in "The Properties of Natural and Synthetic Diamond" Ed. J.E. Field pp259-290, Academic Press, London, 1992.
2.88 J. Nahum and A. Halperin, J. Phys. Chem. Solids. 23, 345 (1962).
2.89 W.J.P. van Enckevort in "Properties and Growth of Diamond", Ed. G. Davies, INSPEC, London , UK, pp316, 1994.
2.90 F. Fang, C.A. Hewett, M.G. Fernandes & S.S. Lau, IEEE Transactions on Electron Devices 36, 1783 (1989).
2.91 C.A. Hewett and J.R. Zeidler, Diamond and Related Materials 2, 1319 (1993).
2.92 J. Nakanishi, A. Otsuki, T. Oku, O. Ishiwata and M. Murakami, Journal of Applied Physics 76, 2293 (1994).
2.93 G. Kawaguchi, J. Nakanishi, A. Otsuki, T. Oku and M. Murakami, Journal of Applied Physics 75, 5165 (1994).
2.94 T. Tachibana, B.E. Williams and J.T. Glass, Physical Review B 45, 11975 (1992).
2.95 G.S. Gildenblat, S.A. Grot, C.W. Hatfield, A.R. Badzian and T. Badzian, IEEE Electron Device Letters 11, 371 (1990).
2.96 V. Venkatesan and K. Das, IEE Electron Device Letters 13, 126 (1992).
2.97 V. Venkatesan, D.M. Malta, K. Das and A.M. Belu, Journal of Applied Physics 74, 1179 (1993).
2.98 T. Tachibana, J.T. Glass and D.G. Thompson, Diamond and Related Materials 2, 37 (1993).
2.99 R.E. Harper, C. Johnson, P.R. Chalker, D. Totterdell, I.M. Buckley-Golder, M. Werner, E. Obermier and M. Van Rossum, Diamond and Related Materials 1, 692 (1992).
2.100 M. Werner, O. Dorsch, H.U. Baerwind, E. Obermeier, C. Johnston, P.R. Chalker and S. Romani, IEEE Transactions on Electron Devices 42 (7), 1344 (1995).
2.101 H.A. Hoff, G.L. Waytena, C.L. Vold, J.S. Suehle, I.P. Isaacson, M.L. Rebbert, D.I. Ma and K. Harris, Diamond and Related Materials 5, 1450 (1996).

2.102 R.D. Mckeag, S.S.M. Chan, C. Johnson, P.R. Chalker and R.B. Jackman, Materials Science and Engineering B29, 223 (1995).

2.103 T. Iwasaki, K. Okano, Y. Matsumae, E. Matsushima, H. Maekawa, H. Kiyota, T. Kurosu and M. Iida, Diamond and Related Materials 3, 30 (1993).

2.104 S.A. Grot, S. Lee, G.Sh. Gildenblat, C.W. Hatfield, C.R. Wronski, A.R. Badzian, T. Badzian and R. Messier, Journal of Materials Research 5, 2497 (1990).

2.105 M.W. Geis, N.N. Efremow and J.A. von Windheim, Applied Physics Letters 63, 952 (1993).

2.106 D.G. Jeng, H.S. Tuan, R.F. Salat and G.J. Fricano, Journal of Applied Physics 68, 5902 (1990).

2.107 C. Gomez-Yanez and M. Alam, Journal of Applied Physics 71, 2303 (1992).

2.108 G. Zhao, T. Stacey, E.J. Charlson, C.H. Chao, M. Hajsaid, J. Meese, G. Popovici and M. Prelas, Applied Physics Letters 61, 1119 (1992).

2.109 H. Shiomi, H. Nakahata, T. Imai, Y. Nishibayashi and N. Fujimori, Japanese Journal of Applied Physics 28, 758 (1989).

2.110 T.P Humphreys, J.V. LaBrasca, R.J. Nemanich, K. Das and J.B. Posthill, Japanese Journal of Appled Physics 30, L1409 (1991).

2.111 P.K. Baumann, T.P. Humphreys, R.J. Nemanich, K. Ishibashi, N.R. Parikh, L.M. Porter and R.F. Davis, Diamond and Related Materials 3, 883 (1994).

2.112 V. Venkatesan, J.A. von Windheim and K. Das, IEEE Transactions on Electron Devices 40, 1556 (1993).

2.113 J. van der Weide and R.J. Nemanich, Journal of Vacuum Science and Technology B 10, 1940 (1992).

2.114 T.P. Humphreys, J.V. Labrasca, R.J. Nemanich, K.Das and J.B. Posthill, Electronics Letters 27, 1516 (1991).

2.115 V. Venkatesan, D.G. Thompson and K. Das, Materials Research Society Symposium Proceedings 270, (1992).

2.116 J.I. Pankove and C-H. Qiu, "Synthetic Diamond: Emerging CVD Science and Technology" Ed. K.E. Spear and J.P. Dismukes, John Wiley & Sons, 1994.

2.117 W. Ebert, A. Vescan, P. Gluche, T. Borst and E. Kohn, Diamond and Related Materials 6, 329 (1997).

2.118 Y. Koide, M. Yokoba, A. Otsuki, F. Oku and M. Murakami, Diamond and Related Materials 6, 847 (1997).

2.119 H.J. Looi , L.Y.S. Pang, J.S. Foord and R.B. Jackman, Solid State Electronics 42, 2215 (1998).

3 THE APPLICATIONS OF DIAMOND

3.1 Introduction

Diamond is not primarily an electronic material: approximately 80 tonnes of the material is sold for industrial use annually (1990) of which around 90% is manufactured synthetically [3.1, 3.2]. Of this it has been suggested that the total quantity of material used for non-abrasive applications is probably in the order of 2kg per annum, with a small but profitable sideline operating in the market of natural stones for engagement rings. Diamond grit in the form of a paste is used for polishing and lapping operations, whilst diamond saws find application in the cutting and finishing of masonry and the texturing of road and runway surfaces. Polycrystalline diamond composites (PCDs) consisting of a cluster or random array of stones set into a host material or sintered together with a metal binder are used extensively for drilling and machining in sectors ranging from woodworking to gas and oil extraction.

The scale and profitability of the activities outlined above has led to a considerable degree of research being undertaken into the nature and properties of diamond over the past century, and has provided the motivation for the genesis of CVD diamond growth processes. Whilst the semiconductor industry could never have justified the investment costs of developing thin film diamond as an electronic material, these costs have been willingly borne by parties to the abrasives market. As a result, electronic grade diamond films are now available for development into products, unencumbered by the overheads which might usually accompany a new materials technology.

As a consequence of the substantial degree of research undertaken into natural diamond, there presently exist many leads and suggestions for applications of the material which have been explored provisionally or proved in principle, but which were never developed into products due to the economic realities of working with infinitely differing natural stones. The electronic and optical properties of diamond are first reported to have been studied systematically in the 1930's by Robertson et. al [3.3] whilst research in the 1960's explored in more detail the role of impurities in the extrinsic photoconductivity of diamond [3.4, 3.5, 3.6] and the detection of ionising radiation was investigated in the 1970's [3.7, 3.8, 3.9, 3.10].

The advent of thin film diamond has refocused attention on many of the possible applications suggested by the above studies, particularly in the field of high performance electronic sensors, which is one of the areas in which existing semiconductor systems such as silicon offer restricted scope for innovation due to the same material properties which make them so ideal for mass market applications. It is against this background that the rest of the chapter explores the ability of diamond to detect ultraviolet and ionising radiation as a starting point for the author's own research, followed by an overview of the device technologies being investigated by other researchers for applications including high performance transistors and field emitting displays.

3.2 Photodetection

3.2.1 Photoconductivity

Photoconductivity is the process in which the absorption of a suitably energetic photon of wavelength λ_i by a semiconductor of bandgap E_g results in the creation of an electron-hole pair, thereby increasing the conductivity of the sample for the lifetime of the carriers τ_l due to the increase in n and p in equation (2.4) [3.11]. Absorption can be

either intrinsic, involving the excitation of an electron across the bandgap, or extrinsic involving one or more impurity states within the bandgap as indicated in figure (2.6). For a bandgap expressed in eV, the low energy cut-off wavelength λ_c for intrinsic photoconductivity is given in nanometers by:

$$\lambda_c \leq \frac{hc}{E_g} = \frac{1239}{E_g(eV)} \tag{3.1}$$

where h is the Planck constant and c is the speed of light. For diamond having a bandgap of ≈5.5eV (§2.4.1) this corresponds to a threshold wavelength of ≈225nm. If $\lambda_i > \lambda_c$ then the incident photons will be insufficiently energetic to excite an electron into the conduction band and will pass unabsorbed through the crystal, hence diamond's optical transparency at visible wavelengths. If $\lambda_i \leq \lambda_c$ then the photons will be absorbed strongly and photoconductivity will occur with the absorption being described at its simplest by Beer's law [3.12]:

$$I_{(x)} = I_0 \exp(-\alpha x) \tag{3.2}$$

where $I_{(x)}$ is the intensity of light at a given depth x beneath the surface of a material with absorption coefficient α when I_0 is the intensity of light on that surface.

3.2.2 Photoconductivity in Diamond

The modern study of photoconductivity in natural diamond was initiated by Nahum and Halperin in the early 1960's [3.4]. Analysis of a stone described as 'intermediate', meaning that it had properties between types I and II, yielded a strong photoconductive response with a threshold of ≈225nm corresponding to intrinsic absorption. Sub-bandgap photoconductive peaks were also observed and found to be strongly temperature dependent, appearing in spectra obtained at 300K but not at 80K. This characteristic was attributed to indirect transitions involving phonon interaction and thermally ionised carriers from states within the bandgap.

Denham et. al. [3.5] investigated the influence of nitrogen content on photoconductivity. The low temperature (90K) photocurrent spectra for samples of types Ia, IIb and 'intermediate' are reproduced as figure (3.1). A single, strong photoconductivity threshold corresponding to the bandgap is evident for the low nitrogen type IIb sample as expected, whilst the two nitrogen containing stones exhibit a considerable sub-bandgap response. The low energy threshold of the nitrogen related feature occurs at ≈300nm, from which it may be deduced that the dominant impurity

based absorption mechanism is likely to be the presence of single substitutional 'C' centres (§2.5.2.4). Additional studies have investigated the photoconductivity associated with the population of states by longer wavelength light in the range 3.5μm-350nm [3.6, 3.13, 3.14]. Photoconductivity spectra exhibiting sharp sub-bandgap peaks in the range 440-364nm have been widely reported for samples following high energy electron irradiation [3.15, 3.16, 3.17] and is believed to be caused by the presence of vacancies.

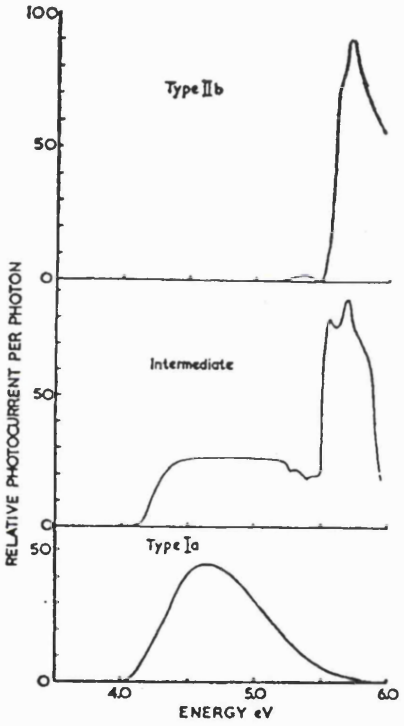

Figure 3.1: The photoconductivity spectra of three natural diamonds having differing nitrogen contents (a) Type IIb (b) 'Intermediate' (c) Type Ia. [Reproduced from 3.5].

The spectral photoconductivity of freestanding 190-500μm thick MPACVD polycrystalline films from four independent sources has been studied by Allers and Collins [3.18] who identified a defect believed to be unique to CVD material which appeared as a broad band in the infra red at ≈825nm (1.5eV). A similar observation was reported for 10μm thick films by Gonon et. al. [3.19, 3.20] who recorded peaks at 1127nm (1.1eV), 886nm (1.4eV) and 653nm (1.9eV) and attributed the low energy response to acceptor states due to the grain boundaries and the highest energy feature to acceptor states in the bulk diamond.

In a study of 15μm thick MPACVD material Vaitkus et. al. [3.21] observed a marked increase in the sub-bandgap photoconductivity following exposure to deep ultraviolet radiation from a deuterium lamp. The ultraviolet photoresponse current, reproduced as figure (3.2) was found to evolve slowly, taking almost $1^1/_2$ hours to approach saturation in the 'on' condition. After removal of the ultraviolet source the current decayed slowly to approximately 10% of the saturated value and remained at that level during exposure to sub-bandgap (550nm) green light. The state of persistent conductivity was 'reset' by exposure to a bright white light. A similar condition of persistent conductivity was observed by Gonon et. al. [3.22] and attributed to electron trapping at an ionised donor level 1.9eV below the conduction band.

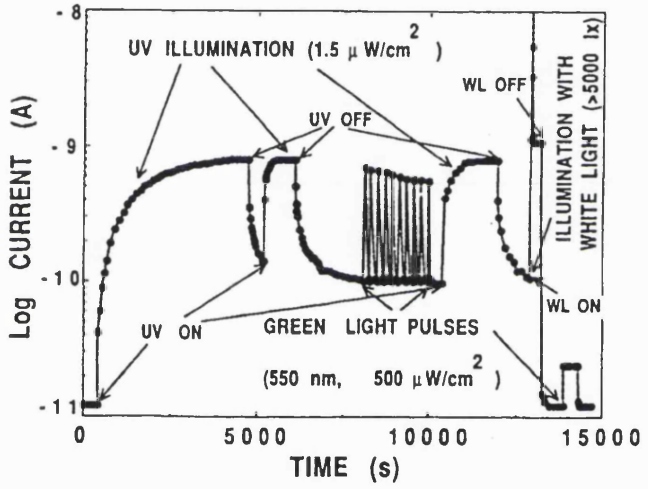

Figure 3.2: The temporal evolution of the photocurrent excited in a 15μm thick MPACVD diamond film by light of various wavelengths as indicated. [Reproduced from 3.21].

3.2.3 Diamond Photoconducting Devices

Kania et.al. [3.23] discussed the potential application of thin film diamond as a visible blind photoconductor. The effective mean carrier collection distance *d* (§2.6.2) was again identified as an important figure of merit, particularly as it was stated that optical carrier generation could be expected only within the first 2μm of the illuminated surface. A planar device structure consisting of a pair of surface electrodes was proposed as a means of achieving efficient collection of photoexcited carriers, with the active device area being maximised my interdigitating the two electrodes. A device on homoepitaxial diamond with an electrode spacing of 35μm based on these principles was presented in a subsequent paper [3.24] and exhibited a dark current in the order of

≈60pA at 10V bias. Under illumination from an unfiltered deuterium lamp the device current increased by around three orders of magnitude, and it was commented that the response to intense visible light was around 250 times less than the UV response, however no spectral discrimination data was presented.

A contemporaneous study by Binari et. al. [3.25] compared the DUV-visible spectral response of simple devices made on natural IIa, synthetic Ib and polycrystalline CVD diamond (of unstated thickness and grain size). The device format was a basic structure of two Al electrodes 2.5mm long, 300μm wide and separated by a gap L of 350μm, with the external quantum efficiency (EQE) (§5.3.2) being adopted as the figure of merit. The results obtained are reproduced as figure (3.3) and show the natural IIa stone to achieve the best DUV-visible discrimination of 2-3 orders of magnitude with an EQE at 200nm of 26%, although the small number of data points presented makes it difficult to assess the extent of sub-bandgap absorption which may occur in the 200-300nm region. The substantially lower EQE of 0.09% recorded for the thin film device was attributed to the smaller d (not quantified) for that material, to which it can be added that the condition $L \leq d$ is assumed not be have been met, although this too was not specifically stated.

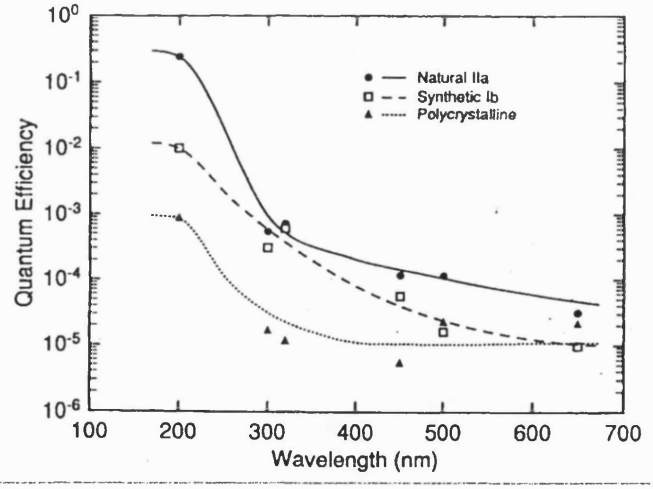

spectra obtained by Pace et. al. [3.26] and Salvatori et. al. [3.27] reproduced as figure (3.4 (a) and (b)) respectively. The device presented by Pace et. al. is made from 10-20μm thick polycrystalline diamond on silicon and has 5μm spaced interdigitated electrodes, whilst Salvatori et. al. described the device characterised in figure (3.4(b)) simply as consisting of polycrystalline HFCVD diamond and employing lithography to a resolution of 5μm, from which it is assumed that 5μm is the pitch of the electrode structure.

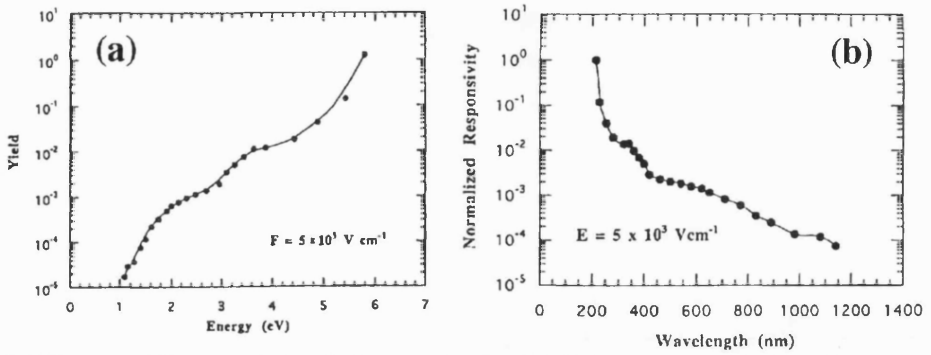

Figure 3.4 The spectral responsivity of photoconducting DUV detectors on thin film diamond recently published by (a) Pace et. al. [3.26] and (b) Salvatori et.al. [3.27].

One recurrent difficulty which is arises when attempting to compare the results of different studies is the lack of a common set of performance descriptors. In consequence it is usually most informative to evaluate published spectral response curves qualitatively in terms of the relative sensitivity of a particular device to a range of wavelengths, and particularly to note the *shape* of the spectral characteristic.

In addition to wavelength selectivity, speed of response is an important detector characteristic. Response times in the range 100-300ps to sub-bandgap laser pulses have been reported for photoconductive detectors made of IIb natural diamond [3.28] and responses in the order of 20ns under 193nm and 222nm excitation have been claimed for IIa devices [3.29]. Gain-bandwidth product arguments (§5.3) however would suggest that such rapid photoconductive response characteristics can only arise in material having a substantial density of defects which act as recombination centres, a view which is supported by the sensitivity of the IIb device to sub-bandgap wavelengths.

It has been commented that because carrier lifetimes in polycrystalline diamond are reduced by defects and grain boundary phenomena, it should be possible to fabricate ultra-high speed devices from intentionally defective material [3.30]. Consistent with the arguments of Kania et. al. [3.23] regarding carrier collection efficiency and photon penetration depth, fast photoconducting detectors are expected to be surface or near-surface devices, however the high potentials required to accelerate carriers to saturation velocity (§2.2.4) have been found under some circumstances to result in surface flashover [3.31]. To avoid this problem, several examples have been presented of buried electrode near-surface planar photoconductors [3.30, 3.31] in which a surface electrode pattern defined in Pt is overgrowth with a thin encapsulation of additional CVD diamond. Surprisingly, it is claimed that the quality of the overgrowth is identical to that of the underlying film, however even if this were not be be achievable, any defects would probably further reduce carrier lifetimes and improve the speed of the device.

The sub-nanosecond response of such a device to a sub-bandgap 248nm laser (KrF) pulse is reproduced as figure (3.5). The applied field was $1.5 \times 10^4 Vcm^{-1}$ which is substantially below anticipated breakdown (§2.2.4) and the resolution of the test system was stated to be 20ns.

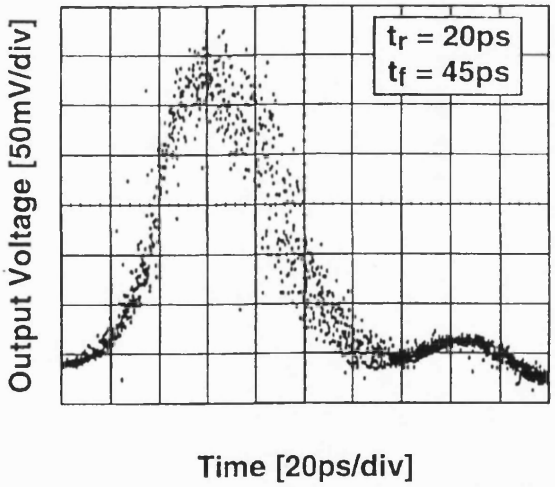

Figure 3.5: The sub-nanosecond response of a buried electrode photoconductor to a laser (KrF, 248nm) pulse of unspecified duration. [Reproduced from 3.30].

It is important to note that the characteristic presented in figure (3.5) represents a response to sub-bandgap absorption which is likely to lead to a low excited carrier density and hence a very high carrier mobility. The sub-bandgap sensitivity is likely to be due in part to the very small grain size of the material employed (≈0.5μm) and it will be a feature of devices which employ such defects to reduce carrier lifetimes that they are unlikely to exhibit the visible blindness expected of good quality diamond.

3.2.4 Other Photodetecting Devices

Although the photodiode is the most widely used photodetecting structure implemented in silicon, the difficulties involved in establishing reliable, reproducible rectifying contacts to diamond (§2.6.2) have restricted the development of equivalent devices in CVD diamond. The development of diamond photodiodes remains of longer term interest however, due to the prospect of wavelength selectivity by choice of metal workfunction once the surfaces and interfaces involved have been more reliably characterised. Marchywka et. al. [3.32] demonstrated three promising photodiode based UV detectors using p-type diamond (implied to be natural) and aluminium Schottky contacts. Of the three structures one was a conventional photodiode whilst the other two contained interface regions which had been damaged by ion implantation (undisclosed species) and were tentatively labelled n-type between the diamond and the aluminium. The spectral characteristics reproduced as figure (3.6) were obtained for reverse bias of up to 4.5V and can be seen to be radically altered by processing.

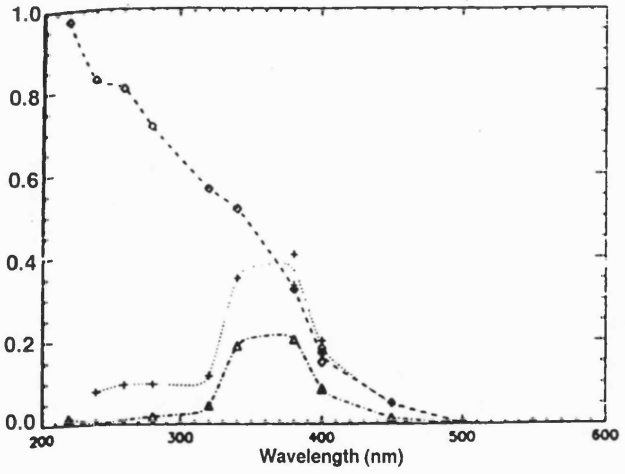

Figure 3.6: The 'arbitrarily normalised' photoresponse spectra of three diode based detector structures. Dashed: Al Schottky diode. Dotted: diode containing layers of graphitic and ion damaged diamond. Dot-dashed: diode similar to 'dotted' but etched to remove graphitic layer. [Reproduced from 3.32].

MIS capacitor based structures are another important type of photodetector element, forming the fundamental building blocks of charge-coupled devices (CCDs) as used in imaging array technologies [3.33]. CVD diamond MIS capacitors using a SiO_2 dielectric have been demonstrated [3.34, 3.35] and shown to behave as integrating photodetectors at wavelengths shorter than 400nm, however successful operation was understandably found to be strongly dependant on the condition of the diamond surface.

Polyakov et. al. [3.36] demonstrated prototype photovoltaic devices using HFCVD films. The structures exploited the difference in built-in potential between two different rectifying contacts and developed photovoltages of 0.7-1V under illumination described only as a "flash lamp". Unfortunately a useful evaluation of this approach must await a more explicit report on the structures and the test conditions applied.

3.3 Diamond and Ionising Radiation

The properties of diamond recommend it for a number applications pertaining to ionising radiation, most of which derive from the fact that the material is structurally strong but electronically sensitive.

3.3.1 Solid State Radiation Detectors

In contrast to a photoconduction event (§3.2.1) in which a single absorbed photon creates a single electron-hole pair, a charged particle such as a proton or alpha particle on passing through a detector material will lose energy through many ionising collisions with bound electrons. These 'knock-on electrons', termed δ-rays, will acquire kinetic energy in the impact and will themselves continue to traverse the detector causing further ionising collisions and creating further δ-rays until their energy falls below the ionisation threshold of the material, at which point the electron will yield its remaining energy to the target material as heat [3.37]. In this way the absorption of a single ionising particle can create within the target a large number of electrons and ions, to use the terminology of a nuclear physicist, or alternatively a 'charge cloud' of electrons and holes as perceived by an electronics engineer.

In a detector application the charge cloud can be monitored by one of two methods. The simpler but less useful method is to make a current measurement in the manner of a photoconductivity experiment (§4.5.3), however this simply offers an indication of whether or not an ionising signal is present: because of photoconductive gain and carrier lifetime effects it is not generally practical to determine the energy or arrival rate

of the ionising particles from raw current data. The more usual and accurate technique is to use the 'pulse counting' mode of operation, whereby a charge sensitive pre-amplifier is connected through a shaping amplifier to a computer controlled multi-channel analyser (MCA) which generates a counts/energy plot accompanied by accurate arrival rate data.

The term 'Ionisation Chamber' is sometimes used to describe solid state radiation detectors in an effort to underline the fact that they employ similar operating principles to the argon containing metal/mica 'chambers' of tube based detectors [3.38].

3.3.2 Radiation Hardness

Diamond is frequently described as having potential as a 'Radiation Hard' detector or device material in reference to its resistance to physical damage when exposed to a flux of energetic or massive particles. This is because the strong covalent bonding of its lattice and the consequently large activation energy required to break these bonds (§2.2) mean that it can sustain exposure to much more energetic particles than other semiconductor materials, including silicon. It should be noted however that the deliberate modification of diamond by certain types of irradiation is a well established practice in the gemstone industry [3.39] as was commented upon previously (§2.6.2) and that radiation hardness should therefore be viewed as an enhanced tolerance of harsh environments and not as a measure of invincibility. As an indication of the resilience required of a modern detector, it is informative to note a that hardness to neutron doses of up to $2x10^{15}n/cm^2$ would be sufficient to permit a device to operate for ten years in the proposed LHC beampipe at CERN [3.40].

In an early experiment to quantify the radiation hardness of diamond, Kozlov et. al. [3.7] compared the counting amplitude and energy resolution of silicon and natural diamond (type IIa) α detectors in the pulse counting mode when exposed to increasing doses of neutrons having energy of up to 0.5MeV. Their results, reproduced as figure (3.7), indicate diamond (solid line) to be capable of operation at up to 100 times the neutron dose at which silicon deteriorated, offering stable and reliable performance at exposures of up to 10^{14}neutrons/cm^2. Regarding the amplitude scale of figure (3.7), it should be noted that the data was normalised by the original authors: on an absolute scale the signal response of silicon would be larger than that for diamond because the ionisation energy required to create each δ-ray in diamond is $\approx$13.25eV [3.10] compared to $\approx$3.62eV in silicon [3.7].

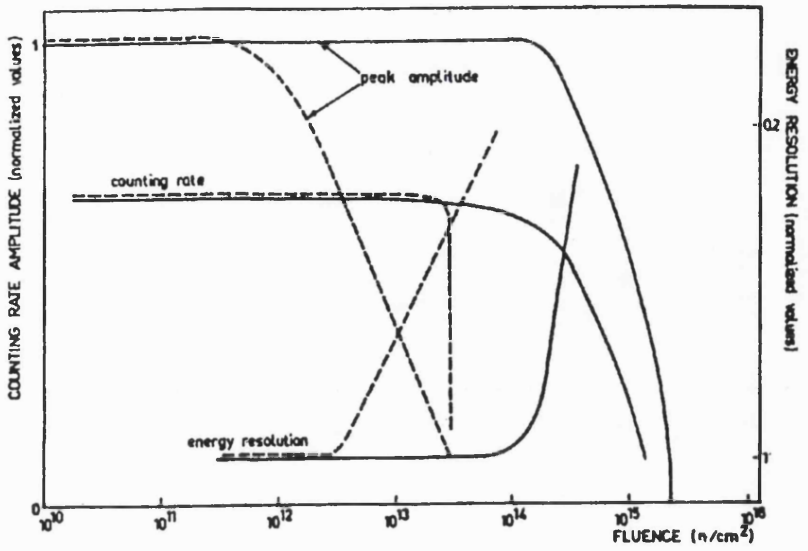

Figure 3.7: The relative hardness to fast neutrons of a Type IIa diamond (solid line) and silicon (dotted line) as α particle detectors. [Reproduced from 3.7].

A substantial body of more recent work on the neutron hardness of CVD diamond has reported that contrary to initial expectations, doses of 1MeV neutrons up to 10^{14}n/cm^2 [3.41, 3.42] or 10^{15}n/cm^2 [3.43, 3.40] can routinely improve the electronic performance of β vertex detectors, resulting in lower dark current, stronger signal response and 30-40% better charge collection distance than could be achieved with the same detectors prior to irradiation. Control experiments indicate that this effect is not observed in natural stones but is unique to thin film material. The authors have postulated that point defects and impurities in the CVD diamond, acting as shallow donors and acceptors, are thermally activated at room temperature leading to an increased carrier population which contributes to the dark current, whilst the ionised defects themselves trap carriers from the δ-ray induced charge cloud and thereby reduce the amplitude of the signal response. They argue that deep defect centres created by mild neutron damage act to compensate the shallow imperfections inherent in the material to yield the reported improvement. The same studies however have indicated that higher neutron doses of ≈6x10^{15}n/cm^2 [3.40] can lead to the onset of deterioration in the performance parameters discussed above.

Although this neutron induced improvement, or 'priming', is presented as a potentially useful phenomenon, it should be remembered that stability and uniformity of response are fundamental requirements of almost all sensor technologies, and that a detector which improves with continued operation can be as unwelcome as one which

deteriorates over a similar timescale. It might therefore be constructive to regard neutron priming as a means of improving the performance of imperfect CVD diamond for electro-optic applications in non-ionising environments, whereas better quality material should be sought for applications requiring non-varying operation under heavy neutron fluences.

An investigation into the effects on CVD diamond of irradiation with ^{60}Co photons (γ-rays), 300MeV/*c* pions, 500MeV protons and 5MeV alpha particles has been reported by Bauer et. al. [3.44]. The detectors were fabricated using 700μm thick freestanding undoped tiles with Cr/Au electrical contacts on the front and rear surfaces of each device, except for the α particle experiments which used a planar geometry with a pair of adjacent contacts on the growth surface of a single tile. The benchmark performance indicator adopted was the carrier collection distance measured in response to a β particle flux from a ^{90}Sr source. After a priming effect, similar to that discussed above, stable performance was observed after exposure to γ-rays up to 10MRad, protons to $5x10^{13}cm^{-2}$ and pions to $8x10^{13}$pions/cm^2. A steady deterioration of response amplitude was observed with respect to an increasing dose of 5MeV α particles such that the amplitude response after a total fluence of $\approx 10^{15}$ α/cm^2 (dose $\approx$1MGy) was half that for a fluence of 10^{10} α/cm^2 (dose $<10^{-3}$ Gy).

3.3.3 Alpha Particle Detection

The primary demand for alpha particle detection is in process and safety monitoring for the nuclear power industry. Specifically, plutonium in the reactor core emits both alpha particles and fission induced neutrons, whilst waste products containing transuranic elements such as americium are also alpha emitters [3.45]. Detectors for use in these environments must be capable of operation at elevated temperatures and in contact with the strong acids which are used as solvents and can carry radioactive waste. A further application for sensitive large area devices arises in the context of decommissioning work, where very low concentrations of emitting particulate contamination must be detected. From these specifications it emerges that two distinct resolutions of detector output may be required: in some cases it is sufficient simply to indicate the presence or absence of emitting material, whilst in other spectroscopic contexts it is necessary to determine the energy of the detected particles in order to identify the isotopic species from which the emission emanates.

Kozlov et. al. [3.7] investigated the α detection capability of a natural IIa diamond operating in the current measuring mode and observed a linear amplitude response with respect to both energy and bias voltage for α particle irradiation in the range 5-8.8MeV

and bias potential of 50-300V across a detector thickness of 100-300μm. Problems of detector deterioration over periods of sustained operation were attributed to polarisation of the diamond by the creation of space charge regions due to electrically activated defect centres; this was addressed using a combination of rectifying and ohmic contacts to inject carriers, thereby compensating the ionised defects. In a subsequent experiment Kozlov et. al. [3.46] mounted a diamond detector in a teflon capsule which was then immersed in a range of bimolar nitrate solutions containing plutonium (^{239}Pu is an α emitter) in concentrations of ≈10-100mg/litre. The counts/energy curve obtained showed only a broad central feature indicating little spectroscopic resolution, however an excellent linearity was observed in the relationship between the count rate and the plutonium concentration in the liquid. This work established the viability of using good quality diamond to detect α emission within a corrosive solvent.

A related study, again using natural stones but employing the pulse counting mode of operation, demonstrated excellent energy discrimination in 150μm thick diamond detectors at 300V bias [3.10]. This data indicated that diamond detectors could offer spectroscopic response and resolution that was broadly comparable to that of a silicon device as illustrated by the counts/energy curves reproduced here as figure (3.8(a)) for the silicon control and figure (3.8(b)) for the diamond detector. The slightly degraded resolution of the diamond spectrum due to broadening of the low energy side of each peak was attributed to an inhomogeneous energy distribution of trapping centres.

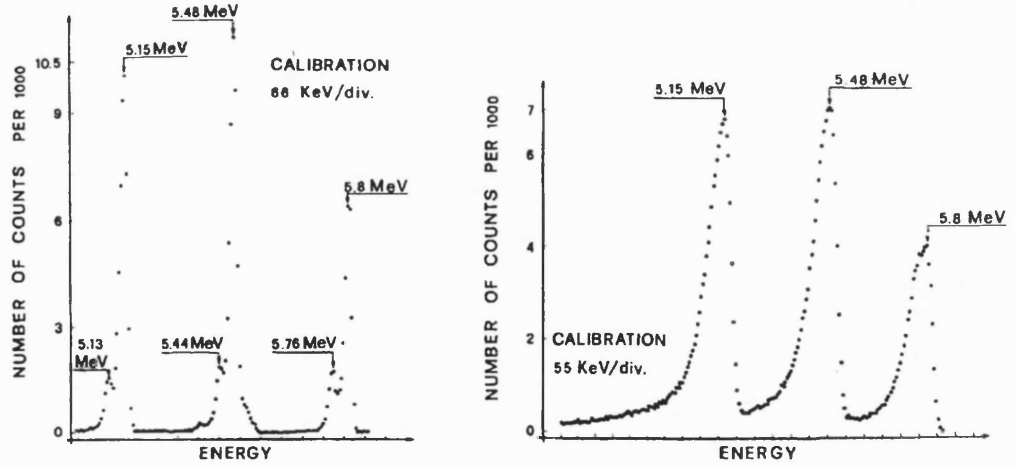

Figure 3.8: Alpha spectra from a source containing a mixture of ^{241}Am, ^{239}Pu and ^{244}Cm emitting at 5.15MeV, 5.48MeV and 5.8MeV respectively. (a) LEFT spectrum obtained from a commercial Ortec surface barrier Si detector. (b) RIGHT spectrum obtained from a natural diamond detector. [Reproduced from 3.10].

When the response of figure (3.8(b)) is viewed in combination with the radiation hardness indicated by figure (3.7), it can be seen that a compelling argument for radiation hard diamond α detectors has existed since these results were published in the late 1970's, although it has required the advent of CVD diamond deposition to make such detectors an economically viable proposition.

Although many α detectors have recently been made using thin film diamond [3.47, 3.48, 3.49, 3.45, 3.50], none have yet been reported to approach the spectroscopic performance of the natural device discussed above. Pochet et. al. [3.45] recently compared the performance of devices made from 180μm thick undoped freestanding MPACVD diamond, 6-19μm thick silicon backed undoped MPACVD diamond and 200μm thick slices taken from a type IIa natural stone. All devices took the form of 'sandwich' detectors, having thermally evaporated gold electrical contacts on the front and rear faces with the α particles being incident upon the growth surface of the CVD samples. The counts/energy curves obtained from these samples are reproduced in figure (3.9) as labelled and show a single sharp peak for the natural device and broader, flatter responses from the CVD devices. It is clear from this work that good natural material continues to offer better spectroscopic resolution than contemporary thin diamond films, however it was calculated in this experiment that the natural samples achieved only a 15% efficiency in the collection of the δ-ray induced charge cloud, whilst the silicon backed diamond achieved 10%, indicating that none of the detectors prototyped to date remotely approach the levels of performance which are anticipated for optimally used good quality diamond.

The authors of the above report attempted to calculate d for the devices investigated, although they, like Manfredotti et. al. [3.49], acknowledged that any value they obtained was likely to be somewhat misleading due to the combined effects in polycrystalline material of carrier trapping and recombination at grain boundaries and the consequent emergence of bias reducing space charge regions. The 'apparent' collection distances obtained for each type of material represented a small fraction of the respective device thicknesses, from which it might be deduced that matching device dimensions to material properties could yield substantial improvements in detector efficiency. It is this approach which forms the foundations of the experimental α particle detector work presented in this thesis (§10).

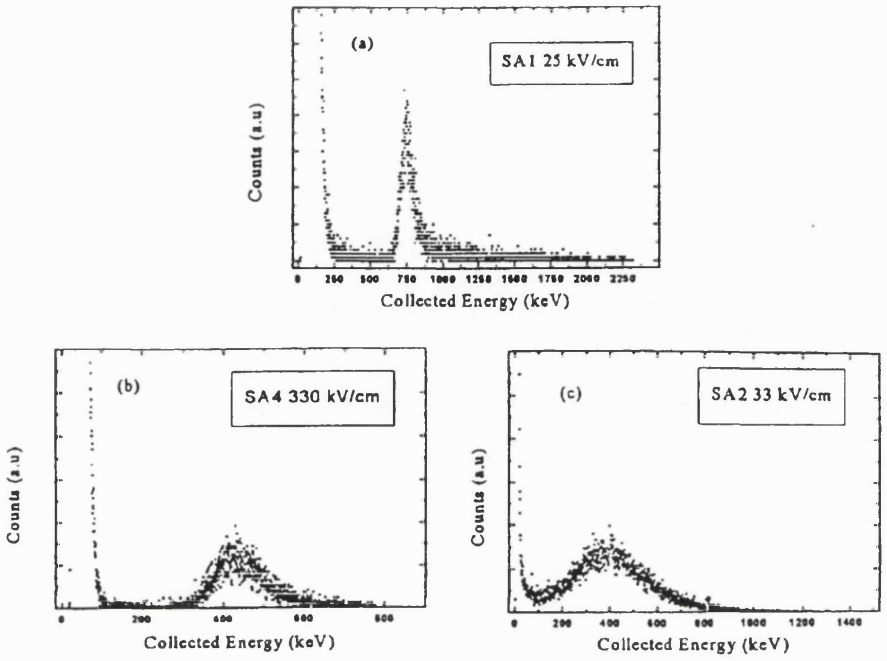

Figure 3.9: The 241Am (5.15MeV) alpha spectra obtained from natural and CVD diamond 'sandwich' detectors. (a) natural IIa diamond 200μm thick. (b) CVD diamond 6-19μm thick. (c) CVD diamond 180μm thick. [Reproduced from 3.45].

3.3.4 Beta Particle Detection

In terms of applications, beta particle detectors are of greatest interest to particle physicists who seek to track the reaction products emanating from high energy physics experiments. By determining the energy and trajectory of such particles, it is possible to develop an insight into the reactions and interactions occurring at the site of, for example, a proton-proton collision experiment. One of the main participants in contemporary research into thin film diamond β particle detectors is a large international collaboration known as "RD42" which is seeking to develop devices for the LHC, ATLAS and CMS research programmes at CERN [3.51].

A more fundamental reason for studying β particle detection in diamond is that the β particle is a prototype for other forms of low mass, high energy species so that experiments performed with β irradiation can provide a degree of generic knowledge about charged particle interaction with the detector material. This arises because β particles having an appropriate velocity ($\approx^{9}/_{10}$ speed of light) [3.37] experience a minimum energy loss during transit through a material and therefore cause a minimum degree of ionisation in the detector. Because they lose so little of their energy to ionisation events, MIPs travel further into, or even through, the target material, which is

one reason why they are useful in tracking experiments: a 5.5MeV alpha particle which deposits all its energy into the first 17μm of a detector provides much less spatial information than a MIP which can travel several millimeters through diamond, traversing several orthogonal vertexing detectors as sketched in figure (3.10).

Early work on β particle detection using natural diamond was reported by Kozlov et. al. [3.7, 3.8, 3.53] and included the use of the same structure as described above for α particle detection (§2.8.3). This device yielded an electron energy spectrum under ^{207}Bi β particle irradiation for which the authors claimed better resolution of the 500keV peak than was offered by a silicon detector, however little further data or discussion was presented.

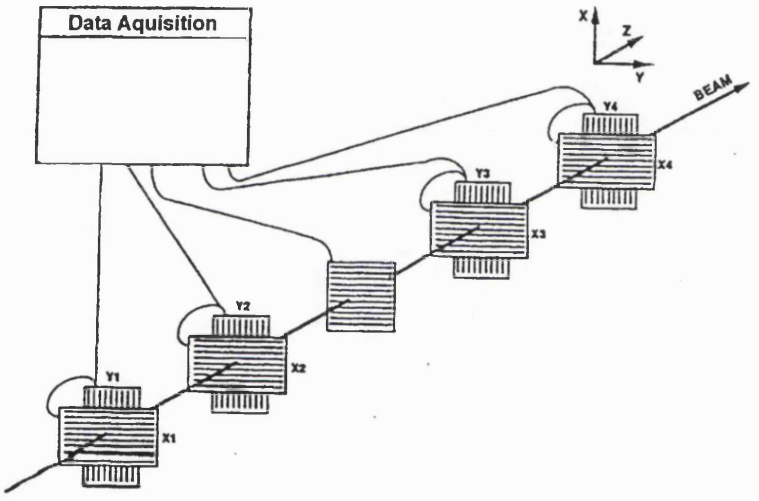

Figure 3.10: Schematic diagram outlining the principle of a tracking vertexing detector arrangement. [Reproduced from 3.52].

Beta detector work using CVD diamond has been dominated since 1994 by the RD42 investigations [3.51, 3.54, 3.52, 3.55, 3.44, 3.56]. The fundamental device format used for these experiments is an 8x8mm tile of ≈300μm thick freestanding undoped MPACVD diamond which has been backside thinned to remove the nanocrystalline nucleation region and metalised with Cr/Au bilayer (or in later work Ti/Pt/Au trilayer) contacts on the front and rear surfaces in a classic bulk 'sandwich' structure. Spatial resolution of the ionising event is achieved by the standard technique of patterning the top (growth surface) electrode into a series of sixty-four 50μm wide parallel strips on a 100μm pitch. Each strip is read out to a separate detector/amplifier channel on a

dedicated integrated circuit, so that when a 'telescope' of such devices is cascaded as per figure (3.10), the signal arising from the charge cloud of ≈36 electron-hole pairs per micron of diamond traversed [3.51] can be interpolated between strips and plates and thereby tracked. Following initial results in which a simplified (non-strip) 'sandwich' detector exhibited a linear response to an electron beam in the energy range 0.5-5GeV[3.51], work has progressed to the detection and tracking of other minimum ionising particles, including most recently a 100GeV pion beam [3.54] for which satisfactory tracking was achieved (91% track reconstruction efficiency), although carrier collection distance continues to be an inherent limitation of existing material.

In pursuit of fast, ultrahigh dose-rate detectors to operate beyond the limits of linearity which apply to existing silicon devices, Han et. al. [3.57] fabricated both sandwich and planar structures which were then exposed to 25ps (nominal) 16MeV electron pulses from a linear accelerator. The planar devices consisted of two 1mm^2 Ti/Au electron-beam evaporated contact pads separated by a 1mm gap, whilst the bulk devices had end contacts of 0.4x1.5mm^2 of the same type and were separated by 4mm of diamond. Both detectors achieved similar levels of performance, having response times of <45ps and linear dose rate response up to 10^{13}Rad/s, however sensitivity was disappointingly low at 10^{-5}-10^{-6} A/W.

3.3.5 X and Gamma Ray Detection

In addition to applictions in the previously mentioned fields of nuclear plant monitoring and particle physics, there is a strong motivation to use diamond as a detector of x-rays and γ rays for medical and industrial dosimetry due to the material's property of 'tissue equivalence'. Because the atomic number (6) is comparable to that for human tissue (7.1) the penetration and effect of high energy photon radiation in a diamond detector will be similar to that in the human body [3.58, 3.59].

Of the many studies into high energy photon detection with diamond, the most diligent must surely be that undertaken by Cotty [3.58] who demonstrated pulse counting under ^{60}Co γ rays but succinctly anticipated the unfavourable economics of natural diamond devices when he wrote in Nature in 1956 that:

> "I therefore sorted through approximately a hundred thousand diamonds to test this possibility ....".

Two decades later, Kozlov et. al. [3.9] studied the response of natural single crystal diamond (type unspecified) to γ and x-rays, working in the current mode as the small

absorption coefficient of diamond in the energy range 20-1250keV made pulse counting impractical. Silver and gold metallisations were used as rectifying contacts, or non-rectifying when deposited onto boron implanted regions at opposing ends of the selected crystals, having a surface collection area 10-15mm^2 and a thickness 200-400μm. The x-ray response (22keV) was linear with dose up to a dose of 500μrad/s (≈0.018Gy/h in SI units) beyond which the sensitivity of the detector decreased; a similarly linear response was obtained for gamma irradiation of 661keV and 1250keV. Over a range of devices the dark current was found to be in the order of picoamps and the typical sensitivity was around 1.1x10^{-14}As/μrad (≈0.306nA/(Gy/h) in SI units).

Keddy et. al. [3.59] evaluated the ^{60}Co response of synthetic diamond detectors containing very low levels of nitrogen. These devices were operated in the current mode and achieved linearity only up to doses of ≈60Gy/h with a sensitivity of ≈1.7pA/(Gy/h), however it was observed from luminescence experiments that the presence of very low levels of boron (≈1ppm) could increase the region of linearity up to an absolute dose of 10Gy. Subsequent studies using synthetic Ib stones [3.60, 3.61] led to the development of a battery operated handheld probe with an LCD readout for dose rates 10μGy/h to 10Gy/h.

Several studies of freestanding polycrystalline diamond film detectors have been reported [3.47, 3.48, 3.45, 3.62, 3.63, 3.64]. Beetz et. al. [3.62] investigated the use of *in situ* nitrogen doped 10μm thick freestanding films configured in a sandwich structure with an ohmic and Schottky electrode pair. Against a 0.01pA dark current, a response of 30nA was generated under 30keV x-ray excitation (copper target, 50μA tube), with the carrier collection efficiency estimated to be at least 25%.

The response of polycrystalline CVD detectors to 40keV x-rays has been studied by Foulon et. al. [3.63] and compared to structures formed from natural IIa material. Sandwich electrodes were formed on three types of material: 6μm thick diamond on silicon, 480μm thick freestanding diamond film and 200μm thick natural (IIa) diamond. The sensitivity of the CVD device was found to be 1nA/(Gy/h) exceeding that of the natural sample which yielded 0.9nA/(Gy/h); this difference was attributed to the greater thickness of the CVD detector.

3.3.6 Neutron Detection

Although not strictly ionising, neutron radiation is intimately related to the various emissions discussed above. Because of their high energy and lack of charge, neutrons cannot interact directly with detector materials to create an electrical signal; typically

neutron detection is therefore achieved by means of secondary, or related effects such as the emission of an alpha particle or the radioactive decay of the detector material caused by a neutron impact.

Kovalchuck et. al. [3.65] described the use of diamond (type unspecified) to detect fast neutrons. The nuclear reaction ^{12}C (n, α) ^{9}Be was promoted by 14.6MeV neutrons within the volume of a detector having a thickness 200-400μm, with a multi-peaked spectrum being obtained from the detection of the resulting charged particles. The charge collected due to the alpha particle and the recoiling Be nucleus could be clearly attributed to a single peak, in contrast to the case of a silicon detector where the reactions ^{28}Si (n, p) ^{28}Al, ^{28}Si (n, α) ^{25}Mg gave a more complex spectrum; this led the authors to conclude that diamond was of significant interest as a neutron detecting medium.

Pochet et. al. [3.45] have discussed the detection of neutrons using CVD diamond in combination with the standard converter ^{10}B; the reaction ^{10}B (n, α) ^{7}Li yields an energetic α particle signal to which the diamond detector can respond. On this basis the authors identify the development of the underlying high performance CVD diamond α detectors as a research priority.

3.4 Active Electronic Devices

3.4.1 Figures of Merit

The unique properties of diamond have been evaluated by several authors in terms of standard figures of merit which are intended to indicate the suitability of a semiconductor material for specific device application [3.66, 3.67, 3.68, 3.69, 3.70]. A drawback to the figure of merit approach is that such parameters are inevitably devised and weighted to reflect established materials systems and device structures. It is possible as a result that when the characteristics of a radically different material such as diamond are substituted into the relevant expressions, the outcome may lack the subtlety which the originator of the equation intended to express. Nonetheless the following figures of merit indicate the extent to which good quality electronic grade diamond might be suitable for certain types of application.

In a detailed comparison of optimum semiconductors for high power electronics, Shenai et. al. [3.66] evaluated the Johnson (JFM) and Keyes (KFM) figures of merit for a range of materials normalised to the values obtained for silicon. The JFM assesses the

suitability of a material for high frequency, high power applications such as microwave and millimeter-wave devices and is calculated as:

$$JFM = \left(\frac{E_{\max} v_s}{2\pi}\right)^2 \tag{3.3}$$

where E_{max} is the electric field breakdown strength and v_s the carrier saturation velocity (§2.4.4). In which the power handling capability is represented by the breakdown strength because of the fundamental relationship $P=V^2/R$ and the saturation velocity determines how rapidly carriers can transit the device.

The KFM expresses the suitability of a material for use in densely packed integrated circuit applications by taking into account the thermal conductivity σ_c as a limiting factor on packing density and the dielectric constant ε_r as an indication of minimum device dimension which would be electrically viable. The KFM is expressed as:

$$KFM = \sigma_c \sqrt{\frac{c v_s}{4\pi\varepsilon_r}} \tag{3.4}$$

where c is the speed of light. The calculated values of the JFM and the KFM along with the main parameter valued used by Shenai et. al. [3.66] are reproduced as table (3.1) from which is can be seen that diamond outscores the other materials by a substantial margin in both parameters.

Material	ε_r	E_{max}	v_s	σ_c	*JFM*	*KFM*
Si	1	1	1	1	1	1
Ge	1.36	0.54	0.6	0.40	0.1	0.27
GaAs	1.09	1.08	2.0	0.31	4.67	0.41
GaP	0.94	1.89	2.0	0.33	14.3	0.49
6H-SiC	0.85	8.1	2.0	3.3	262	5.1
Diamond	0.47	18.9	2.7	13.3	2601	32

Table (3.1): The Johnson and Keyes figures of merit and their primary constituent parameters for a selection of semiconductors normalised to the values for silicon. [Reproduced from 3.66].

In another comprehensive analysis Trew et. al. [3.71] have inserted parameter values for diamond into RF power device simulation models which have been verified as accurate by comparing predicted and experimental results for GaAs devices. The simulation of metal semiconductor field effect transistor (MESFET) devices is of particular interest as primitive implementations of this structure have now been demonstrated by a number of laboratories as discussed in the following section (§3.4.2). The anticipated high frequency performance of GaAs, SiC and diamond MESFETS is reproduced as figure (3.11), which has been generated by a sophisticated model in which the devices are redesigned and scaled for different frequencies. The calculations predict that at 100GHz about 1W and 300mW of RF power can potentially be obtained from diamond and SiC MESFETs respectively, which is significantly better that possible with comparable GaAs devices.

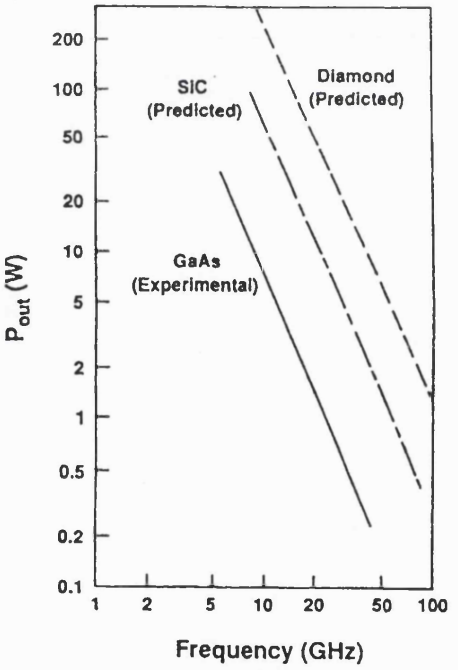

Figure 3.11: The anticipated RF power performance w.r.t. frequency for diamond, SiC and GaAs MESFETs. [Reproduced from 3.71].

3.4.2 Prototype Transistors

Diodes fabricated on diamond have generally been reported from a material properties perspective (§2.6.2) or as an aspect of a sensor application (§3.4.3); in contrast to this

transistor structures have been described which provide proof-of-principle evidence of the viability of active diamond electronic devices [3.72, 3.73, 3.74, 3.75, 3.76, 3.77, 3.78, 3.79].

Geis et. al [3.73] using boron doped HPHT stones demonstrated point-contact transistors which were claimed to be the first such structures on diamond to exhibit power gain. The devices were operated up to 510°C at which temperature a power gain of 4.5 was calculated for the best samples. Field Effect Transistors (FETs) on polycrystalline MPACVD film were demonstrated by Tessmer et. al. [3.75]. The devices employed SiO_2 as the gate insulator and exhibited a saturated drain current and a peak transconductance of 65nS/mm at 150°C which increased to 300nS/mm at 250°C.

More recently Pang et. al. [3.78] have presented a polycrystalline MISFET in which intrinsic diamond was used as the gate electrode. This device was successfully operated at up to 300°C and exhibited complete channel current pinch-off and modulation with a peak transconductance of 174μS/mm. A parallel technology to the development of conventional FET structures is the emergence of transistor designs which exploit the near-surface hydrogen related p-type conductivity of the unreconstructed diamond surface [3.79, 3.80] (§2.5.4). Hokazono et. al. [3.79] created NOT NAND and NOR logic gates from a combination of enhancement and depletion mode MESFETs on hydrogenated homoepitaxial diamond films. Looi et. al. [3.80] have demonstrated the potential for high power devices on hydrogenated polycrystalline material using Al as a gate electrode.

3.4.3 Other Potential Devices

It has previously been commented that under some circumstances the diamond surface can exhibit negative electron affinity (NEA) such that the vacuum level is less than the conduction band minimum [3.81] (§2.7.2). Controllable low-field electron emission from a readily patternable surface is a primary requirement of flat panel display technology [3.82] and is therefore an important area of diamond research. Although it is known that modification of the surface by various techniques can lower the conduction band minimum, much remains to be discovered. Bachmann et. al. [3.81] have reported that polycrystalline CVD diamond films exhibit NEA after exposure to a hydrogen plasma whilst Baral et. al. [3.82] demonstrated relatively stable levels of electron emission at modest electric fields of 20-45V/μm after argon bombardment or heat treatment in hydrocarbon gas ambients.

Many other device structures which exploit diamond's unique properties have been demonstrated or proposed. Pressure sensors exploiting the material's strength and resistance to chemical attack have been fabricated based on a piezoresistor [3.83] or the effect of stress on a diode structure [3.84]. Polycrystalline diamond diodes have also been used as a hydrogen sensor [3.85] whilst resistor structures have been operated as thermistors [3.86]. Despite diamond's indirect bandgap proposals have also arisen for light emitting structures [3.87, 3.88] although the recent commercialisation of high intensity GaN LEDs has served to reduce the motivation to develop such devices further.

3.5 Conclusions

The review presented in this chapter has demonstrated that whilst thin film diamond deposition techniques were not specifically developed to aid the introduction of new electronic device technologies, there exists substantial potential to exploit the material for this purpose. The extreme nature of the properties of diamond render it highly suitable for deployment in harsh environments and other unusually demanding applications such as ultra high speed or power devices. Extensive preliminary evidence exists to suggest that sensor applications such as deep ultraviolet and ionising radiation detectors fabricated from good quality thin film diamond could outperform all other material systems in terms of both primary operating function and resistance to damage. Active electronic devices have also been demonstrated to be viable, but are likely to require further improvements in the quality of material available at affordable prices before truly outstanding performance can become an economically realistic target.

On the basis of the evidence presented it can be concluded that there is a sound basis on which to undertake a diamond electronic device development programme, with the greatest prospect of imminent success arising in the area of optimised device structures for the detection of deep ultraviolet and ionising radiation.

3.6 References

3.1 M. Seal, "High Technology Applications of Diamond" in "The Properties of Natural and Synthetic Diamond" Ed. J.E. Field pp607, Academic Press, London, 1992.

3.2 P.N. Tomlinson, "Applications of Diamond Grits and Composites" in "The Properties of Natural and Synthetic Diamond" Ed. J.E. Field pp637, Academic Press, London, 1992.

3.3 R. Robertson, J.J. Fox and A.E. Martin, Philosophical Transactions of the Royal Society of London A232, 463 (1934).

3.4 J. Nahum and A. Halperin, J. Phys. Chem. Solids. 23, 345 (1962).
3.5 P. Denham, E.C. Lightowlers and P.J. Dean, Physical Review 161, 762 (1967).
3.6 A.T. Collins and E.C. Lightowlers, Physical Review 171, 843 (1968).
3.7 S.F. Kozlov, R. Stuck, M. Hage-Ali and P. Siffert, IEEE Transactions on Nuclear Science 22, 160 (1975).
3.8 S.F. Kozlov, V.P. Katkov and A.J. Krupman, IEEE Transactions on Nuclear Science 22, 901 (1975).
3.9 S.F. Kozlov, E.A. Konorova, Y.A. Kuznetsov, Y.A. Salikov, V.I. Redko, V.R. Grinberg and M.L. Meilman, IEEE Transactions on Nuclear Science 24, 235 (1977).
3.10 C. Canali, E. Gatti, S.F. Kozlov, P.F. Manfredi, C. Manfredotti, F. Nava and A. Quirini, Nuclear Instruments and Methods 160, 73 (1979).
3.11 S.M. Sze, "Physics of Semiconductor Devices", Wiley, New York, 1981.
3.12 R.H. Bube, "Photoelectronic Properties of Semiconductors", Cambridge University Press, U.K., 1992.
3.13 A.T. Collins, E.C. Lightowlers and P.J. Dean, Physical Review 183, 725 (1969).
3.14 E. Pereira and L. Santos, Diamond and Related Materials 4, 688 (1995) Pre-Print.
3.15 R.G. Farrer and L.A. Vermeulen, Journal of Physics C: Solid State Physics 5, 2762 (1972).
3.16 A. Halperin and L.A. Vermeulen, J. Phys. Chem. Solids. 43, 691 (1982).
3.17 L.A. Vermeulen and A. Halperin, Journal of Physics and Chemistry of Solids 45, 771 (1984).
3.18 L. Allers and A.T. Collins, Journal of Applied Physics 77, 3879 (1995).
3.19 P. Gonon, A. Deneuville, E. Gheeraert and F. Fontaine, Diamond and Related Materials 3, 836 (1994).
3.20 P. Gonon, A. Deneuville, F. Fontaine and E. Gheeraert, Journal of Applied Physics 78, 6633 (1995).
3.21 R. Vaitkus, T. Inushima and S. Yamazaki, Applied Physics Letters 62, 2384 (1993).
3.22 P. Gonon, S. Prawer, Y. Boiko and D.N. Jamieson, Diamond and Related Materials 6, 860 (1997).
3.23 D.R. Kania, M.I. Landstrass, M.A. Plano, L.S. Pan and S. Han, Diamond and Related Materials 2, 1012 (1993).
3.24 M.I. Landstrass, M.A. Plano, M.A. Moreno, S. McWilliams, L.S. Pan, D.R. Kania and S. Han, Diamond and Related Materials 2, 1033 (1993).
3.25 S.C. Binari, M. Marchywka, D.A. Koolbeck, H.B. Dietrich and D. Moses, Diamond and Related Materials 2, 1020 (1993).
3.26 E. Pace, F. Galluzzi, M.C. Rossi, S. Salvatori, M. Marinelli and P. Paroli, Nuclear Instruments and Methods in Physics Research A 387, 255 (1997).
3.27 S. Salvatori, E. Pace, M.C. Rossi and F. Galluzzi, Diamond and Related Materials 6, 361 (1997).
3.28 J.F. Young, L.A. Vermeulen, D.J. Moss and H.M. van Driel, Applied Physics Letters 42, 434 (1983).
3.29 Y.S. Huo, X.J. Gu, R.F. Code and Y.G. Fuh, Journal of Applied Physics 59, 2060 (1986).
3.30 Y. Aikawa, K. Bab, N. Shohata, H. Yoneda and K. Ueda, Preprint presented at "Diamond Films '95", Albufiera, Portugal, proceedings published as Diamond and Related Materials (1996).
3.31 H. Yoneda, K. Ueda, Y. Aikawa, K. Baba and N. Shohata, Applied Physics Letters 66, 460 (1995).
3.32 M. Marchywka, J.F. Hochedez, M.W. Geis, D.G. Socker, D. Moses and R.T. Goldberg, Applied Optics 30, 5011 (1991).
3.33 J. Singh, "Optoelectronics - an introduction to materials and devices", McGraw-Hill, New York, 1996.
3.34 M. Marchywka, S.C. Binari and D. Moses, Electronics Letters 30, 365 (1994).
3.35 M. Marchywka and D. Moses, IEEE Transactions on Electron Devices 41, 1265 (1994).

3.36 V.I. Polyakov, N.M. Rossukanyi, P.I. Perov, A.I. Rukovishnikov, A.V. Khomich, V.P. Varnin and I.G. Teremetskaya, Diamond and Related Materials 4, 1061 (1995).

3.37 W.S.C. Williams, "Nuclear and Particle Physics", Oxford University Press, U.K. 1991, 1994.

3.38 K. Kleinknecht, "Detectors for Particle Radiation", Cambridge University Press, Cambridge, U.K., 1987.

3.39 H.B. Dyer and L. du Preez, The Journal of Chemical Physics 42, 1898 (1965).

3.40 L. Allers, A.S. Howard, J.F. Hassard and A. Mainwood, Diamond and Related Materials 6, 353 (1997).

3.41 A. Mainwood, L. Allers, J.F. Hassard, A.S Howard and A. Mahon, Proceedings of 187th Meeting of the Electrochemical Society, Reno, Nevada, USA, May 1995.

3.42 A. Mainwood, L. Allers, A.T. Collins, J.F. Hassard, A.S. Howard, A.R. Mahon, H.L. Parsons, T. Sumner, J.L. Collins, G.A. Scarsbrook, R.S. Sussmann and A.J. Whitehead, Journal of Physics D: Applied Physics 28, 1279 (1995).

3.43 J. Hassard, Nuclear Instruments and Methods in Physics Research A 368, 217 (1995).

3.44 C. Bauer, I. Baumann, C.Colledani, J. Conway, P. Delpierre, F. Djama, W. Dulinski, A. Fallou, K.K. Gan, R.S. Gilmore, E. Grigoriev, G. Hallewell, S. Han, T. Hessing, K. Honschied, J. Hrubec, D. Husson, H. Kagen, D. Kania, R. Kass, W. Kinnison, K.T. Knopfle, M. Krammer, T.J. Llewellyn, P.F. Manfredi, L.S. Pan, H. Pernegger, M. Pernicka, R. Plano, V. Re, S. Roe, A. Rudge, M. Schaffer, S. Schnetzer, S. Somalwar, V. Speziali, R. Stone, R.J. Tapper, R. Tesarek, W. Trischuk, R. Turchetta, G.B. Thomson, R. Wagner, P. Weilhammer, C. White, H. Ziock and M. Zoeller, Nuclear Instruments and Methods in Physics Research A 367, 207 (1995).

3.45 T. Pochet, A. Brambilla, P. Bergonzo, F. Foulon, C. Jany and A. Gicquel, Italian Physical Society Conf. Proc. (Eurodiamond '96) 52, 111 (1996).

3.46 S.F. Kozlov, E.A. Konorova, M.I. Krapivin, V.A. Nadein and V.G. Yudina, IEEE Transactions on Nuclear Science 24, 242 (1977).

3.47 F. Foulon, T. Pochet, E. Gheeraert and A. Deneuville, Materials Research Society Symposium Procedings 339, 185 (1994).

3.48 F. Foulon, T. Pochet, E. Gheeraert and A. Denueville, IEEE Transactions on Nuclear Science 41, 927 (1994).

3.49 C. Manfredotti, F. Fizzotti, E. Vittone, S. Bistolfi, M. Boero and P. Polesello, Nuclear Instruments and Methods in Physics Research B 93, 516 (1994).

3.50 A. Brambilla, P. Bergonzo, F.Foulon, C. Jany, B. Guizard and T. Pochet, unspecified conference proceeding / Personal communication, 363 (≈1996).

3.51 C. White, Nuclear Instruments and Methods in Physics Research A 351, 217 (1994).

3.52 F. Borchelt, W. Dulinski, K.K. Gan, S. Han, J. Hassard, A. Howard, H. Kagan, D.R. Kania, R. Kass, G. Lu, E. Nygard, L.S. Pan, S. Schnetzer, R. Stone, J. Straver, R.J. Tesarek, W. Trischuk, P. Weilhammer, C. White, R.L. Woodin and S. Zhao, Nuclear Instruments and Methods in Physics Research A 354, 318 (1995).

3.53 S.F. Kozlov, A.V. Bachurin, S.S. Petrusev and Y.P. Fedorovsky, IEEE Transactions on Nuclear Science 24, 240 (1977).

3.54 C. Bauer, I. Baumann, C.Colledani, J. Conway, P. Delpierre, F. Djama, W. Dulinski, A. Fallou, K.K. Gan, R.S. Gilmore, E. Grigoriev, G. Hallewell, S. Han, T. Hessing, J. Hrubec, D. Husson, H. Kagen, D. Kania, R. Kass, W. Kinnison, K.T. Knopfle, M. Krammer, T.J. Llewellyn, P.F. Manfredi, L.S. Pan, H. Pernegger, M. Pernicka, V. Re, S. Roe, A. Rudge, M. Schaffer, S. Schnetzer, S. Somalwar, V. Speziali, R. Stone, R.J. Tapper, R. Tesarek, W. Trischuk, R. Turchetta, G.B. Thomson, R. Wagner, P. Weilhammer, C. White and M.M. Zoeller, Nuclear Instruments and Methods in Physics Research A 367, 202 (1995).

3.55 C. Bauer, I. Baumann, C.Colledani, J. Conway, P. Delpierre, F. Djama, W. Dulinski, A. Fallou, K.K. Gan, R.S. Gilmore, E. Grigoriev, G. Hallewell, S. Han, T. Hessing, K. Honscheid, J.

Hrubec, D. Husson, R. James, H. Kagen, D. Kania, R. Kass, K.T. Knopfle, M. Krammer, T.J. Llewellyn, P.F. Manfredi, D. Meier, L.S. Pan, H. Pernegger, M. Pernicka, V. Re, S. Roe, D. Roff, A. Rudge, M. Schaeffer, M. Schieber, S. Schnetzer, S. Somalwar, V. Speziali, R. Stone, R.J. Tapper, R. Tesarek, W. Trischuk, R. Turchetta, G.B. Thomson, R. Wagner, P. Weilhammer, C. White, H. Ziock and M.M. Zoeller, Nuclear Instruments and Methods in Physics Research A 383, 64 (1996).

3.56 C. Bauer, I. Baumann, C.Colledani, J. Conway, P. Delpierre, F. Djama, W. Dulinski, A. Fallou, K.K. Gan, R.S. Gilmore, E. Grigoriev, G. Hallewell, S. Han, T. Hessing, J. Hubec, D. Husson, H. Kagen, D. Kania, R. Kass, W. Kinnison, K.T. Knopfle, M. Krammer, T.J. Llewellyn, P.F. Manfredi, L.S. Pan, H. Pernegger, M. Pernicka, V. Re, S. Roe, A. Rudge, M. Schaeffer, S. Schnetzer, S. Somalwar, V. Speziali, R. Stone, R.J. Trapper, R. Tesarek, W. Trischuk, R. Turchetta, G.B. Thomson, R. Wagner, P. Weilhammer, C. White, H. Ziock and M.M. Zoeller, Nuclear Instruments and Methods in Physics Research A 380, 183 (1996).

3.57 S. Han, R.S. Wagner, J. Joseph, M.A. Plano and M. Dale Moyer, Review of Scientific Instruments 66, 5516 (1995).

3.58 W.F. Cotty, Nature 177, 1075 (1956).

3.59 R.J. Keddy, T.L. Nam and R.C. Burns, Carbon 26, 345 (1988).

3.60 P.J. Fallon, T.L. Nam, R.J. Keddy, R.C. Burns & J.H. Grobbelaar, Applied Radiation Isotopes 41, 35 (1990).

3.61 J.H. Grobbelaar, R.C. Burns, T.L. Nam and R.J. Keddy, Nuclear Instruments and Methods in Physics Research B 61, 553 (1991).

3.62 C.P. Beetz, B. Lincoln, D.R. Winn, K. Segall, M. Vasas and D. Wall, IEEE Transactions on Nuclear Science 38, 107 (1991).

3.63 S. Han, R.S. Wagner and E. Gullikson, Nuclear Instruments and Methods in Physics Research A 380, 205 (1996).

3.64 A. Brambilla, P. Bergonzo, F. Foulon, C. Jany and T. Pochet, Nuclear Instruments and Methods in Physics Research A 380, 446 (1996).

3.65 V.D. Kovalchuck, V.I. Trotsik and V.D. Kovalchuck, Nuclear Instruments and Methods in Physics Research A 351, 590 (1994).

3.66 K. Shenai, R.S. Scott and B.J. Baliga, IEEE Transactions on Electron Devices 36, 1811 (1989).

3.67 B.J. Baliga, IEEE Electron Device Letters 10, 455 (1989).

3.68 K. Shenai, IEEE Electron Device Letters 11, 520 (1990).

3.69 G.S. Gildenblat, S.A. Grot and A. Badzian, Proceedings of the IEEE 79, 647 (1991).

3.70 T.P. Chow and R. Tyagi, IEEE Transactions on Electron Devices 41, 1481 (1994).

3.71 R.J. Trew, J-B. Yan and P.M. Mock, Proceedings of the IEEE 79, 598 (1991).

3.72 J.F. Prins, Applied Physics Letters 41, 950 (1982).

3.73 M.W. Geis, D.D. Rathman, D.J. Erlich, R.A. Murphy and W.T. Lindley, IEEE Electron Device Letters 8, 341 (1987).

3.74 H. Kiyota, K. Okano, T. Iwasaki, H. Izumiya, Y. Akiba, T. Kurosu and M. Iida, Japanese Journal of Applied Physics 30, L2015 (1991).

3.75 A.J. Tessmer, L.S. Plano and D.L. Dreifus, IEEE Electron Device Letters 14, 66 (1993).

3.76 S.A. Grot, G. Sh. Gildenblat and A.R. Badzian, IEEE Electron Device Letters 13, 462 (1992).

3.77 H. Kawarada, M. Aoki and M. Ito, Applied Physics Letters 65, 1563 (1994).

3.78 L.Y.S. Pang, S.S.M. Chan, C. Johnston, P.R. Chalker and R.B. Jackman, Diamond and Related Materials 6, 333 (1997).

3.79 A. Hokazono, T. Ishikura, K. Nakamura, S. Yamashita and H. Kawarada, Diamond and Related Materials 6, 339 91997).

3.80 H.J. Looi, L.Y.S. Pang, Y. Wang, M.D. Whitfield and R.B. Jackman, Diamond and Related Materials 7, 565 (1998).

3.81 P.K. Bachmann, W. Eberhardt, B. Kessler, H. Lade, K. Radermacher, D.U. Wiecher and H. Wilson, Diamond and Related Materials 5, 1378 (1996).

3.82 B. Baral, J.S. Foorde and R.B. Jackman, Diamond and Related Materials 6, 869 (1997).

3.83 J.L. Davidson, D.R. Wur, W.P. Kang, D.L. Kinser and D.V. Kerns, Diamond and Related Materials 5, 86 (1996).

3.84 G. Zhao, E.M. Charlson, E.J. Charlson, T. Stacey, J. Meese, G. Popovici and M. Prelas, Journal of Applied Physics 73, 1832 (1993).

3.85 W.P. Kang, Y. Gurbuz, J.L. Davidson and D.V. Kerns, Journal of the Electrochemical Society 141, 2231 (1994).

3.86 K. Miyata, K. Saito, K. Nishimura and K. Kobashi, Review of Scientific Instruments 65, 3799 (1994).

3.87 N. Fujimori, Y. Nishibayashi and H. Shiomi, Japanese Journal of Applied Physics 30, 1728 (1991).

3.88 B. Burchard, A.M. Zaitsev, W.R. Fahrner, A.A. Melnikov, A.V. Denisenko and V.S. Varichenko, Diamond and Related Materials 3, 947 (1994).

4 EXPERIMENTAL METHODS

4.1 Introduction

A range of experimental systems and methods encompassing material analysis, material modification, microelectronic device fabrication and evaluation have been employed in the course of the investigations presented in subsequent chapters. Some processes are specific to, or constitute an integral part of, the results to which they relate, in which case they are more appropriately discussed in detail as part of the relevant results chapter, an example being the work on α particle detection (§10). Presented in this chapter are the techniques which have a broader relevance underpinning the fundamental ability to fabricate and assess devices in terms of their structure, composition and performance. The function of the chapter is in part to prevent repetition in later sections, in which light it can be regarded as a toolbox from which instruments will subsequently be drawn and used as appropriate.

4.2 Cleanroom Processing

For the purposes of this project, work described as having been carried out in a Clean Room, refers to a particle, temperature and humidity controlled environment specified to Class 1000 with laminar flow workspaces locally Class 100 and yellow light throughout. Unless stated otherwise, all other work was carried out in open laboratory space under normal ambient room temperature and white working light.

4.2.1 Surface Degrease

Every sample used in the course of this project has been subjected to an initial degrease as summarised below:

warm Trichloroethylene → Acteone → IPA → DI → N_2

The trichloroethylene and the acetone serve as general purpose solvents to loosen or remove grease, moisture and particulate contamination, IPA follows the acetone as it is the purest of the electronic grade organic solvents [4.1] and is readily miscible in DI water, which completes the sequence as the purest solvent available. A rapid blow-dry in N_2 is followed by a 20 minute bake at 85°C to yield a uniformly clean, dry surface.

Some samples were received with visible evidence of substantial particulate surface contamination, such as powdered graphite residue from laser dicing operations. In these cases the degrease was preceded by a brief rinse in DI water under ultrasonic agitation.

4.2.2 Oxidising Etches

It has been established by [4.2] that the as-grown surface of a CVD diamond film can be expected to carry a substantial degree of contamination in the form of amorphous, or other non-diamond, carbon. The polished surface of natural diamond is also known to be similarly contaminated [4.3], and a number of strongly oxidising processes have been proposed to remove this material [4.2, 4.3, 4.4, 4.5, 4.6]. For the purposes of this project, the following hybridised regime was derived from the published literature and found to be effective; the process was subsequently evaluated in more detail elsewhere [4.7].

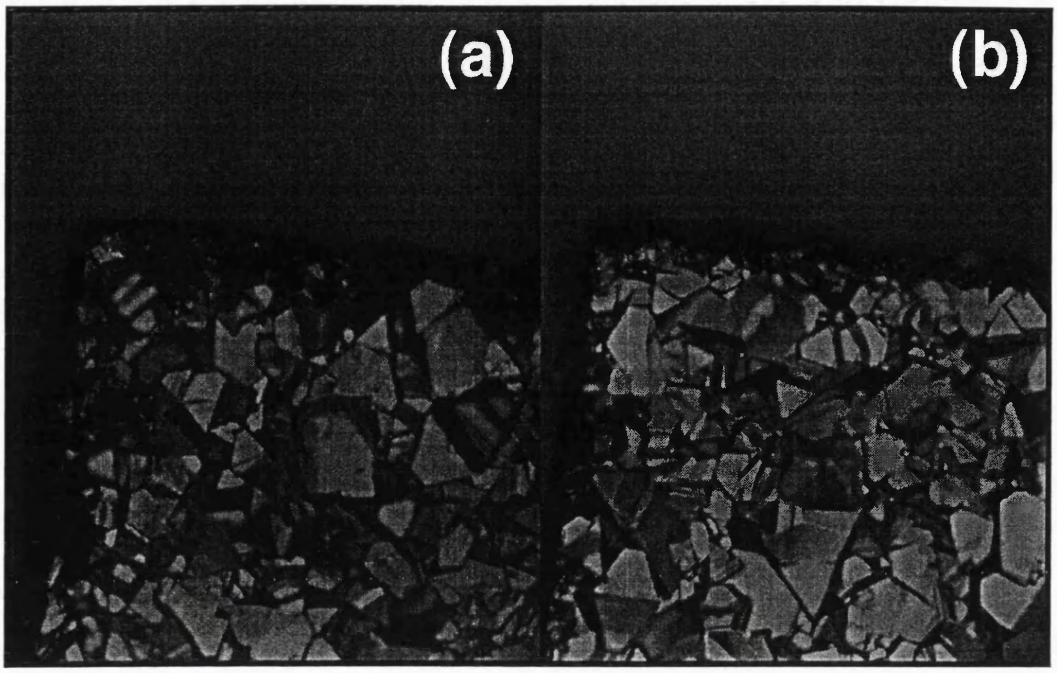

Figure 4.1: Optical micrographs indicating the effect of acid treatment on a typical freestanding CVD diamond tile (a) untreated - extensive non-diamond carbon deposits can be seen along laser-cut edges, sample lacks lustre (b) after acid treatment - the cutting debris has been removed and the tile appears generally brighter and clearer.

The sample is placed in a saturated solution of ammonium persulphate ($(NH_4)_2S_2O_8$) in sulphuric acid (H_2SO_4) which is then heated to around 230°C, being maintained above 170°C for 20 minutes. The sample is then transferred to a solution of hydrogen peroxide (H_2O_2) (70%) and ammonium hydroxide (NH_4OH) (30%) combined in equal quantities by volume. The first stage specifically attacks non-diamond carbon [4.2] whilst the second stage is identical to the industry standard RCA clean, SC-1 which is widely employed to effect wet oxidation of organic surface films and expose the surface for desorption of trace metals including gold, silver, copper, nickel, zinc and chrome [4.1]. The effectiveness of this cleaning regime is illustrated in figure (4.1) which shows the contaminated edge and surface of a laser cut tile of freestanding CVD diamond before and after cleaning, in which the extent of material removal is clearly visible. Baral et. al. [4.7] have used auger electron spectroscopy to confirm that the process effectively removes graphitic and non-diamond carbon material and surface hydrogen, but commented that it leaves some residual surface contamination in the form of sulphur and oxide complexes. This contamination has not been found to be a problem for the majority of devices of interest. Given the wide range of sample types investigated and the variety of conditions in which they were received, this cleaning

regime has been essential in asserting a baseline condition against which differences can be measured for different samples and different forms of processing.

4.2.3 Photolithography on Rough Surfaces

Standard photolithographic methods for defining device geometries on a smooth, flat semiconductor surface are a well developed and characterised technology [4.8]. Films of photoresist are deposited on the sample surface either by spraying or by dripping a pool of resist onto the centre of the wafer and then spinning it with a speed and duration specified by the manufacturer to achieve the desired thickness, typically in the order of ≈1.3 to 1.8μm. The coverage and uniformity of such films are generally excellent and the device image is then created by exposing the resist to a patterned light source of the appropriate UV wavelength, typically ≈300 to 400nm. Developing the resist will remove either the illuminated or the unilluminated regions depending upon the chosen regime, so that the sample surface is then left exposed though a pattern of 'windows' in a protective film of resist. The exposed surface can be selectively etched away, or an overlayer can be deposited through the 'windows' so that when the resist is subsequently removed, only the exposed regions of the sample surface have been coated, (this latter process is known as 'lift off').

The main challenge in processing the randomly oriented 4.2x4.2mm^2 polycrystalline CVD diamond tiles, as used predominantly in this project, is the difficulty in achieving total and reasonably uniform coverage of the very rough surface. This problem has resonances in other fields of small-dimension manufacturing such as micromechanics and optoelectronic interconnects, so thick photoresist technologies are commercially available. Even with specialised resists however, the nature of the work undertaken required that they be used at and beyond the limits of their data sheet specifications. To achieve this, extensive iterative optimisation was carried out to establish a feasible regime of spin speed, spin time, exposure intensity and exposure time that was capable of yielding successful device definition on a range of substrates.

Hoechst AZ4620A is a viscous positive photoresist specifically designed for thick coating of semiconductor surfaces [4.9]: manufacturer's spin speed/time parameters to achieve a given film thickness on a smooth surface are reproduced in figure (4.2). Figure (4.3) shows a cross-sectional electron micrograph of a typical freestanding CVD diamond film used in this project with an inset indicating the surface roughness to have a peak-to-trough height of around 15μm.

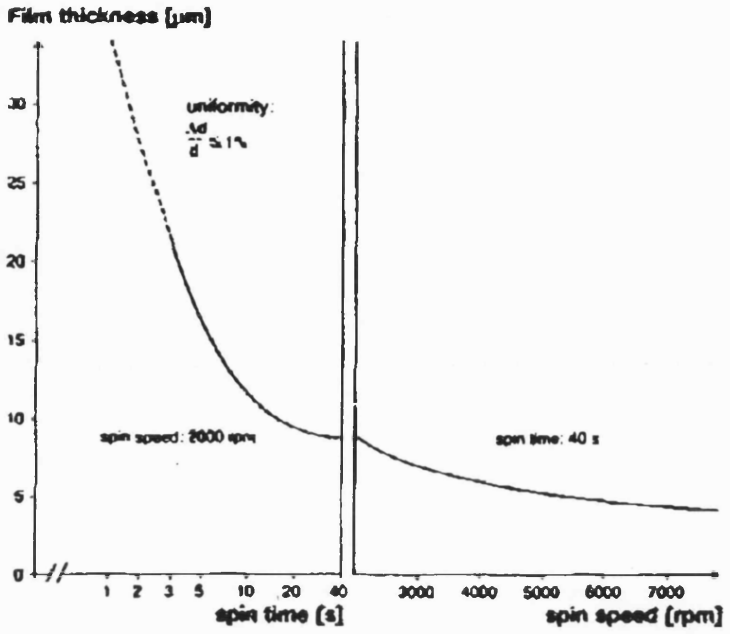

Figure 4.2: Manufacturer's recommended spin parameters to achieve a given thickness of AZ4620P photoresist on a smooth surface. [Reproduced from 4.9].

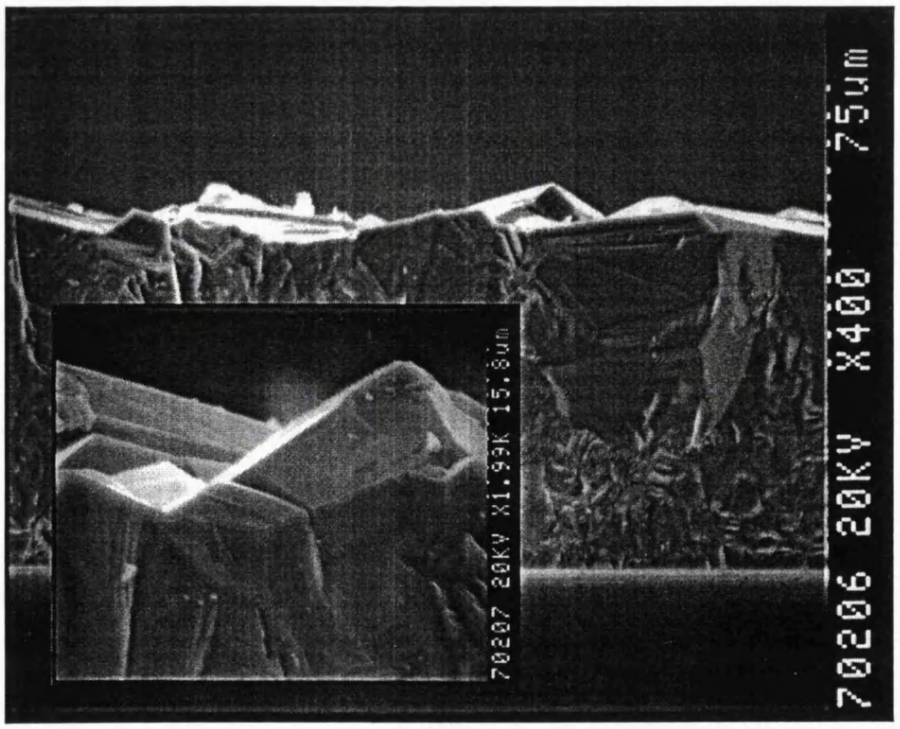

Figure 4.3: Cross sectional electron micrograph of typical CVD diamond tile with inset indicating a peak-to-trough surface roughness of ≈15µm.

The surface roughness gives rise to two primary problems: complete and effective coating of the surface requires that a substantial thickness of resist be employed, placing the parameter selection in the 2000rpm region of figure (4.2), whilst the flow of the viscous resist across the non-smooth surface serves to undermine the applicability of these data sheet parameters. Under these circumstances the use of data sheet parameters to achieve adequate coverage at the centre of the tile results in an extensive occurrence of the 'edge-bead effect' [4.10] whereby excess resist fails to be expelled by centripetal force during spinning and collects instead at the perimeter of the sample, leading to both a substantial inhomogeneity in resist thickness across the sample and extensive spreading of this usually minor effect across a significant proportion of the surface of the tile.

It was found that a spin of 2000rpm for 20 seconds followed immediately by a second spin at 5000rpm for 20 seconds yielded a tile-centre resist thickness sufficient to achieve unpenetrated coverage with an edge bead width <1mm. Exposing this resist for 720 seconds to 400nm, 7.3mW/cm^2 followed by a develop of ≈50 seconds in a formulation of dilute commercial 351 developer (351:DI, 1:2) achieved satisfactory reproduction of device features in the order of 25μm. It was noted that this regime operates substantially in the tolerance region of the photoresist, beyond the conditions recommended by the manufacturer, with the result that very little latitude remains for variations in the process parameters or the nature of the sample surface before critical failure of the process will occur. Some low-grade 10μm device features were also achieved on a one-off basis, however this work was highly irreproducible and could not be regarded as a reliably characterised system.

4.3 Laboratory Processing

4.3.1 Vacuum and Gas Ambient Annealing

High temperature processing of samples under either vacuum or a range of laboratory grade gas ambients was carried out using the system represented schematically in figure (4.4). The system comprised a single reaction chamber evacuated by a series combination of a turbomolecular pump and a rotary vane pump. Chamber pressure was monitored using either a Pirani gauge at low vacuum or an ionisation gauge at high vacuum; an additional Pirani gauge was fitted between the rotary pump and the turbomolecular pump to aid leak testing and system diagnostics. Gas dosing and air admittance were controlled by manually operated valves whilst process monitoring was facilitated by a viewport at the top of the chamber. All vacuum components were made

of stainless steel and all component interconnects were in the form of conflat flanges with single use copper gaskets.

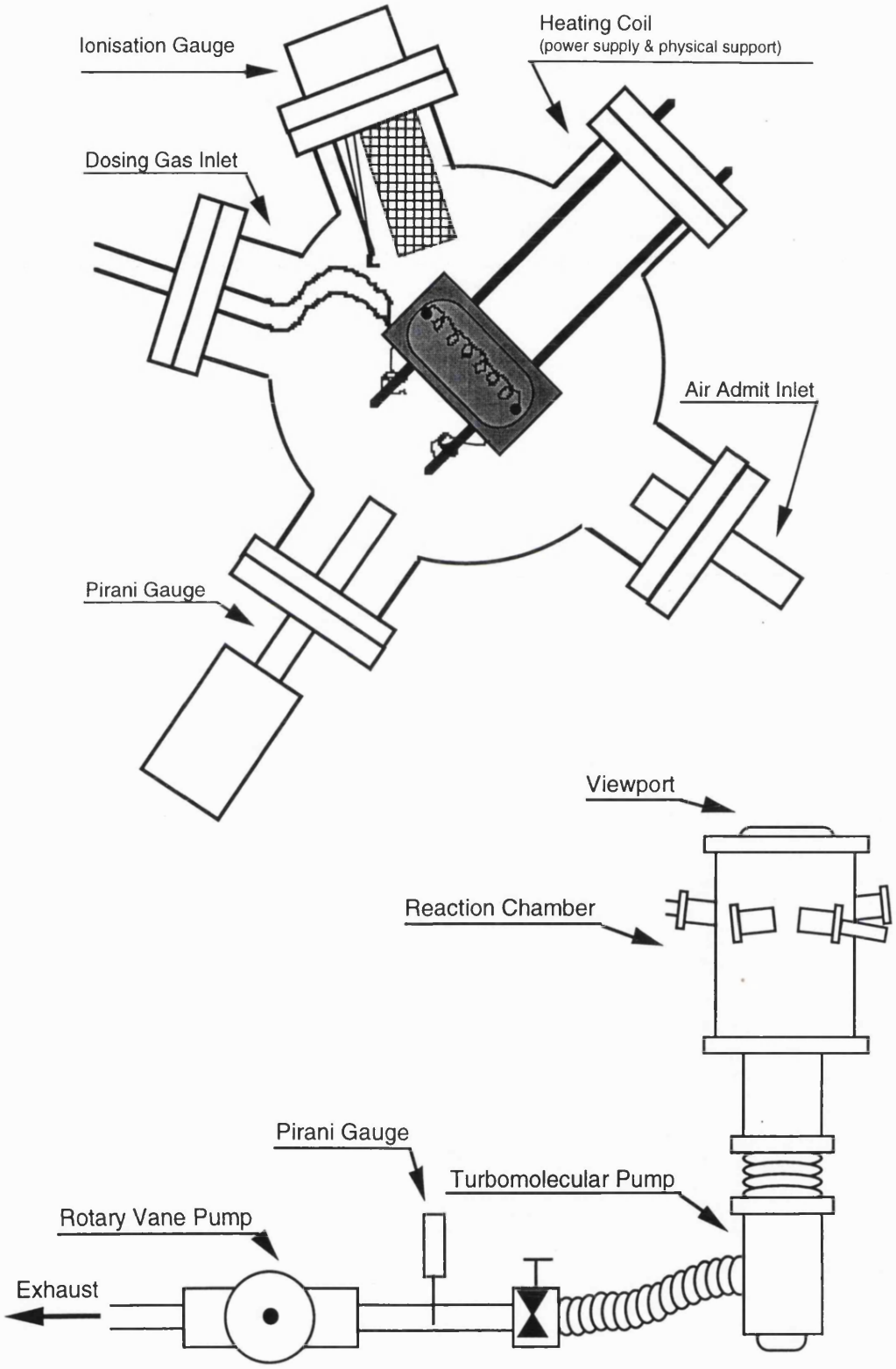

Figure 4.4: Schematic diagrams of the annealing system. TOP: the interior arrangement in plan view, outlining the relative positions of the sample heater, the gas inlets and the pressure gauges. BOTTOM: the exterior arrangement in side elevation outlining the pumping configuration.

Samples were heated by resistive heating of a coiled tantalum filament supported by a machined ceramic block. Heat transfer to the sample was achieved either by conduction via a heat spreader/attenuater or by radiation directly from the coil according to the temperature range required. For temperatures up to ≈700°C a small molybdenum plate supported above the heating coil acted as a heat spreader/attenuater. The sample was placed on this plate and a chromel-alumel thermocouple spot welded to the plate provided an approximate indication of the sample temperature. For heating samples above 700°C an alternative molybdenum plate was supported above the heating coil; this plate was drilled with a central aperture of diameter 4mm and was creased centrally along both its length and width, so that a single 4.2x4.2mm^2 CVD diamond tile could be supported above the coil for radiative heating whilst having minimal thermal contact with its means of support. This arrangement enabled samples to be heated to a temperature of >1100°C as measured by optical pyrometry.

Power was supplied to the heating coil by a pair of fully stabilised dual output current source units (Farnell PDD 3010A) with all four outputs wired in series to deliver a maximum power of ≈250W. Pressure and temperature were monitored manually during processing and input controls were operated as necessary to maintain the specified set-points for a given process.

4.3.2 Air Ambient Annealing

Annealing in air was carried out at atmospheric pressure using a barrel furnace. temperature feedback from a thermocouple was applied to a thermostatic controller (CRL 405) which supplied the furnace heating current via a thryristor unit to maintain automatically a programmed temperature. Samples were inserted using a molybdenum manipulator which was specifically designed to position the samples adjacent to the thermocouple within the furnace for optimum accuracy.

4.3.3 Header Mounting and Wedge Bonding

Completed devices which were scheduled for extensive or repeated testing were mounted on industry standard TO5 headers using a two part epoxy which was then cured at 140°C for 5 minutes. As a less robust alternative, cyanoacrylate (superglue) was occasionally used to facilitate demounting of devices (by soaking in acetone) if further processing or analysis was required.

Electrical contact to mounted devices was achieved by aluminium wedge bonding. Successful bonding was dependant primarily upon the roughness of the target surface and to a lesser extent upon the thickness of the contact metalisation. On rougher

surfaces, which yielded the stronger bonds, an industrial 'break strength' test indicated a typical breaking load of >7g, which matches the quality control requirement for commercial silicon devices. On smoother surfaces (small grain size and oriented/ aligned material) contact delamination precluded success by normal means, and satisfactory contacts could only be achieved by manual application of a conductive, silver loaded, epoxy (Epo-tek H20E). These bonds remained fragile and were not subjected to a break strength test.

4.4 Material Analysis

Investigation of the morphology, composition and structure of samples has been undertaken primarily by the techniques outlined in the following sections. In addition to the benefits and limitations of each approach as discussed in the paragraphs below and in the relevant results chapters, it must be noted generally that the results of any local probing technique applied to anisotropic, inhomogeneous material such as polycrystalline diamond films can only reflect the region of the sample which was subjected to analysis: an adjacent sector may yield different results under identical examination.

4.4.1 Scanning Electron Microscopy

The scanning electron microscope (SEM) is familiar as the workhorse imaging instrument for surface inspection beyond the resolving power of optical microscopy. The wavelength of visible light (390-770nm) fundamentally limits the best possible resolution and depth of field of optical systems to ≈250nm [4.11]. In the context of the rough sample surfaces typical of CVD diamond, this depth of field consideration leads to a maximum useful magnification of ≈x500. In contrast, electrons accelerated by an electric field to velocities where they have a De Broglie wavelength in the order of <0.01nm can be focused by electromagnetic lenses to a spot diameter of 10-20nm, enabling SEMs typically to offer magnification in the range x500-40,000 with a resolution of 2.5-10nm and a depth of field ≈500 times that of an optical system [4.12, 4.13].

The SEM is not however a direct analogue of an optical microscope in that the rastering of the electron beam over a sample surface causes the emission of secondary electrons. It is this secondary emission which is absorbed by a scintillator, re-emitted as optical photons and collected by a photomultiplier tube to create an electrical signal which can be displayed as an image on a cathode ray tube (CRT) [4.12]. This mode of operation is

known as 'secondary emission' and is the default form of SEM usage; some units support additional modes of analysis which allow elemental identification or which detect photons to yield cathodoluminescence spectra, these facilities were not available to the present study.

Electron microscopy for this project was performed by the author using a Hitachi S-800 SEM having a maximum resolution of 20nm and a specified magnification of x20-300,000. Samples were mounted for analysis on aluminium headers using silver loaded epoxy and were sputter coated with gold to render the surface conductive.

4.4.2 SIMS Depth Profiling

Secondary ion mass spectroscopy (SIMS) is a means of depth profiling the impurity content of a material. Ion beam sputtering with high energy (1-20keV) heavy ions, typically O^-, O_2^+ or Cs^+, removes material from the surface of the sample under investigation, resulting in the ejection of neutral atoms, molecules and a small fraction of ionised atoms (0.1-10%). A mass spectrometer analyses the secondary ion yield to identify elemental species and chemical concentrations, which can be plotted as a function of sputter time. The sputter time can in turn be correlated to a sputter depth by reference to calibrated standards, so that an impurity depth profile is obtained [4.13, 4.14].

SIMS is widely used in the semiconductor industry and is acknowledged as an effective and well characterised tool [4.11, 4.13, 4.15]. The main drawback of the technique is the fact that it is necessarily destructive, creating a crater $\approx$1mm diameter on diamond to analyse a region of diameter $\approx$10μm at the centre of the crater [4.16].

SIMS analysis for this project was undertaken by staff at AEA Technology, Harwell using a CAMECA IMS-3f system having a field of view of up to 400mm diameter and a spatial resolution of 1μm. The primary ion beam, typically 17.5keV being focused into a probe of 50μm diameter and rastered over an area of 500μm^2 to promote uniform sputtering [4.14].

4.4.3 Raman Scattering Spectroscopy

Raman scattering spectroscopy is a surface and near-surface probe which offers insight into the bonding energy of atoms within a sample. When monochromatic light, usually from a laser, is incident on a sample surface, a small proportion of the scattered light experiences an interaction with the lattice resulting in creation of an optical phonon and a consequent loss of energy known as the 'Raman effect' [4.11]. Corresponding to the

loss of energy, the scattered light exhibits a wavelength increase which is termed the 'Stokes' shift. Similarly, the subsequent relaxation of the lattice causes the phonon energy to be imparted to other scattered photons which exhibit a corresponding decrease in wavelength which is known as the 'anti-Stokes' shift.

In a typical experimental set-up, laser light is delivered to the sample through an optical microscope to facilitate operator selection of the region of the sample to be analysed at an instrument dependant spatial resolution of ≈1-100μm [4.11, 4.14]. The scattered light is then filtered and delivered to an optical multichannel analyser which can take the form of a spectrometer or monochromator combined with a photodiode array or charge coupled device. Scanning, collection and interpretation of the data under computer control allows rapid generation of spectra having a resolution of less than one wavenumber with the mode of operation (Stokes or anti-Stokes) being determined by the filtering regime of the optical system.

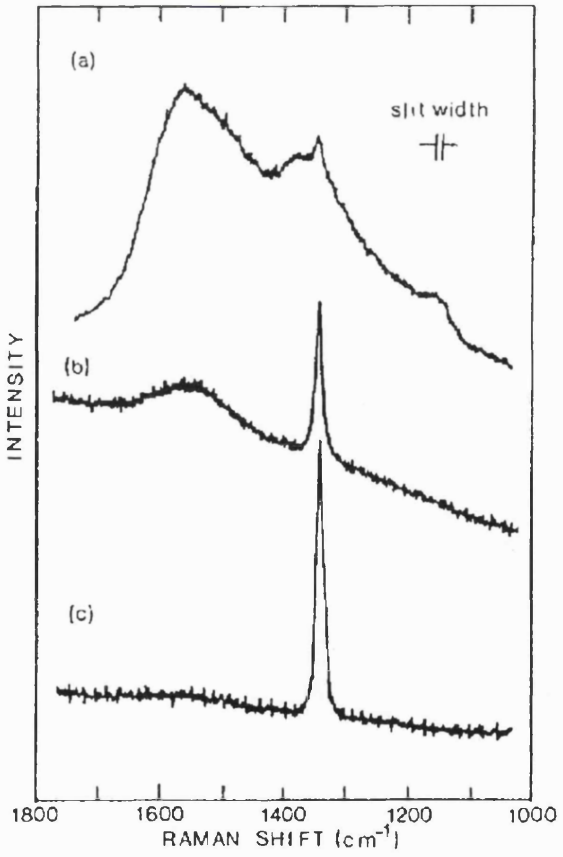

Figure 4.5: Raman spectra of carbon deposits on molybdenum substrates. (a) and (b) contain substantial proportions of non-diamond carbon as indicated by the broad peaks centred about 1500-1600cm^{-1} whilst (c) is good quality CVD diamond containing little non-sp^3 bonded material. [Reproduced from 4.17].

Raman scattering spectroscopy has been identified as a particularly useful technique for differentiating between different phases of carbon in CVD films [4.13, 4.16, 4.17]. This is due primarily to the characteristic single peak at 1333cm^{-1} attributable to purely sp^3 bonded carbon, which is clearly distinguishable from the broader non-diamond carbon features such as those shown at 1500-1600cm^{-1} in figure (4.5). Additional attractions of the technique are that it is non-destructive, requires little sample preparation and can be undertaken without the use of vacuum thereby enabling a rapid turn-around of samples [4.11]. The depth of material probed is related to the optical opacity of the target at the relevant wavelength such that only the surface of non-diamond carbon is analysed, whilst analysis of diamond reflects the structure of the near-surface region [4.14].

Raman scattering spectroscopy for this project was undertaken on the author's behalf at the Defence Evaluation and Research Agency, Malvern using a Renishaw 2000 system with 632.8nm He-Ne laser radiation.

4.4.4 Photoluminescence Spectroscopy

Photoluminescence (PL) spectroscopy yields information on the presence and nature of defect related sub-bandgap energy levels in a semiconductor [4.18]. Optical excitation of electron-hole pairs in a semiconductor is inevitably followed by recombination which can, amongst other processes, result in the emission of a photon of corresponding energy; if a carrier has been temporarily trapped prior to recombination then the wavelength of any photon emitted will indicate the energy level of that trap.

In a practical experiment the excitation, or 'pumping' illumination will usually be supplied by an ultraviolet laser which for most semiconductors would be energetic enough to ensure extensive excitation of electrons into trapping levels and the conduction band, from which carriers may then fall to additional trapping levels. The emitted luminescence is then detected by a computer controlled optical multichannel analyser and plotted as a spectral emission curve. In the case of diamond, the ultraviolet lasers in many general purpose PL analysis systems will be of a lesser energy than the bandgap. Because of this, the technique can be used to analyse only restricted system dependent regions of energy-space within the bandgap of the material, however this is not a serious limitation as PL spectra are rarely presented for broadband analysis, being more usually localised to the region of a known defect under investigation.

Photoluminescence spectroscopy for this study was undertaken using an argon ion laser to generate 476.5nm excitation. The source was mechanically chopped and the luminescence detected via a lock-in amplifier using an interference grating and calibrated photodiode assembly. All experiments were carried out at room temperature.

4.5 Electro-optic Analysis

4.5.1 Current-Voltage (*I-V*) Analysis

Most of the electrical characterisation described in this report was carried out using a combined voltage source and picoammeter unit (Keithley K487) connected to a personal computer for control and data logging by means of an IEEE 488 interface and simple BASIC routines. The voltage source was capable of providing an output potential of up to 500V, subject to its current limit of 2.2mA, and the picoammeter measured current in the range 0.01pA to 2.2mA. Electrical connections were made to contact pads on the samples either by bonding to a header (or by means of manually manipulated tungsten probes (Wentworth PRO109 head assembly, Signatone SE-T pins). The samples and probes were supported on a solid steel plate inside a grounded metal box to reduce noise generated by electromagnetic interference. Sample to system interconnects were via either co-axial or tri-axial low noise cables and BNC connectors. A small aperture in the lid of the sample enclosure allowed the sample to be illuminated if required.

Additional characterisation was carried out using another computer controlled voltage source/picoammeter (HP 4061A Semiconductor/Component Test System) which was similarly connected by low noise tri-axial cables to a Signatone probing station inside an earthed metal enclosure.

4.5.2 Photocurrent Analysis - Equipment

Photoresponse analysis of samples was effected by exposing the sample to narrow bandwidth (effectively monochromatic) illumination derived from a broadband 150W xenon arc lamp. A xenon source was selected because of its continuous output spectrum spanning the relevant infra red, visible and ultraviolet wavelengths.

Many xenon lamps are supplied as "ozone free", indicating that they have a glass sheath especially designed to absorb the more energetic deep UV light and thus prevent the generation of ozone when operated in an oxygen containing atmosphere. For this project a spectral range of 180 to 800nm was required, so it was important to ensure that the lamp used had a fused silica sheath which would transmit all the required wavelengths, as illustrated by figure (4.6). Ozone generation, which would attenuate the deep UV signal and present a carcinogenic hazard to the user, was prevented by continuously purging the lamphousing and optical path with flowing nitrogen.

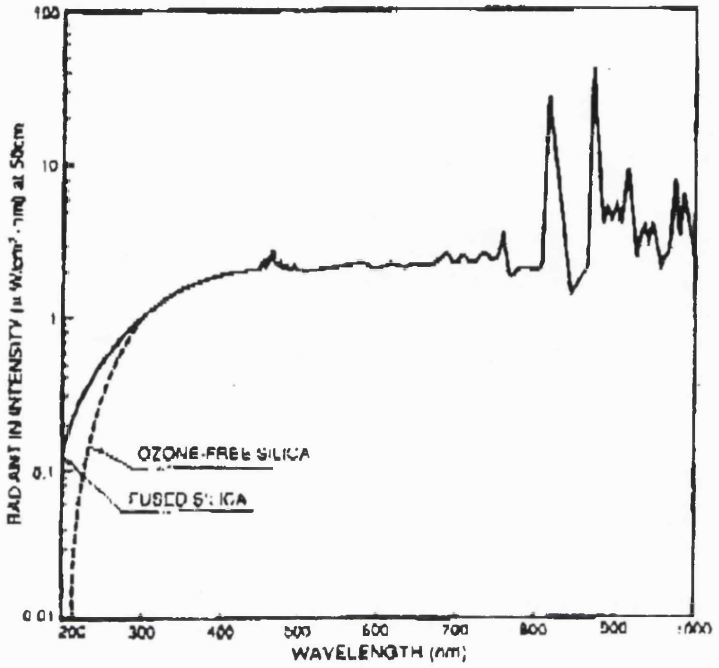

Figure 4.6: Spectral radiant intensity of standard ('ozone free') and fused silica 150W xenon arc lamps [Reproduced from 4.19].

The lamphousing (AMKO LTI A1000) used a parabolic reflector to achieve efficient collection and focusing of the broadband illumination without the attenuation that would occur if conventional lenses had been placed in the optical path. The focused broadband beam was delivered to a double grating monochromator (AMKO LTI 01-002) having a choice of two interchangeable 1200line/mm reflection gratings blaized at 500nm and 200nm, with the pass band under manual control via a sine drive mechanism. Micrometer adjusted entry and exit slits controlled the throughput/bandwidth trade-off and were generally configured to maximise throughput, with a setting of 5mm resulting in a pass band of ≈10nm. Higher order harmonics were eliminated from the specified pass band for a given grating position by means of a set of low-pass filters having cut-off wavelengths of 400nm and 630nm, the use of which is described below.

The sample under test was mounted and connected electrically as described above (§4.6.1); this system is illustrated schematically in figure (4.7).

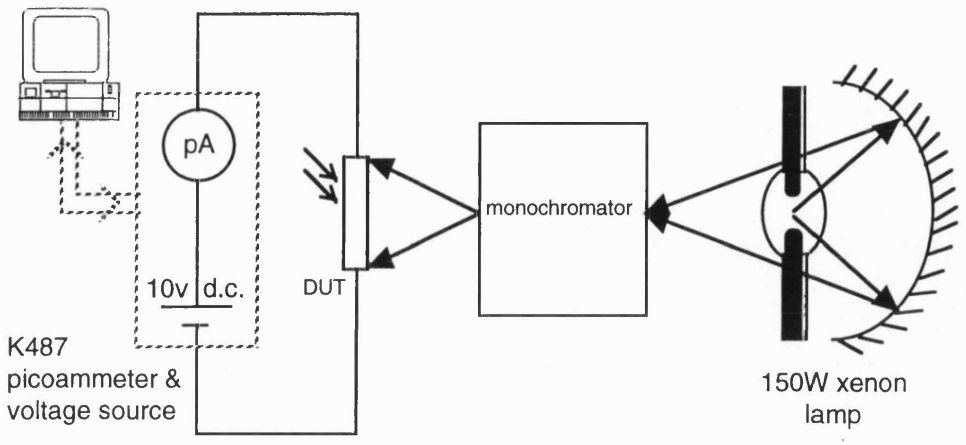

Figure 4.7: Schematic diagram outlining the deployment of the illumination system and picoammeter/voltage source unit for current-voltage and photocurrent analysis experiments.

4.5.3 Photocurrent Analysis - Procedure

The data required from photocurrent analysis experiments was the differential photocurrent response of a sample to a given wavelength, as discussed in §5. Thus for every wavelength (grating position) set on the sine drive of the monochromator two current readings were obtained: one in darkness and one under the selected illumination, so that the difference between these two values could be plotted as the response of the device to that excitation. The attraction and validity of reasserting the dark current at each wavelength in this way lies in the practical necessity to define what is meant by a working dark current. In §5.3 it is shown that the post-illumination conductivity decay of a photoconductor takes the form of an inverse exponential, and §3.2.2 demonstrated that the duration of this decay can be strongly influenced by the perfection and purity of the sample under test, such that the full decay time of the conductivity in a poor quality sample can be in the order of days [4.20]. To allow such a device to reset fully after each exposure would entail waiting perhaps a week between recording the response to each wavelength, meaning that a full responsivity spectrum could take months to obtain. Even if collecting such a data set were to be economically and logistically viable, its validity would be undermined over the extended time period by drift in the output of the light source and possible charging effects in the device itself.

A practical solution is to specify a fixed time interval between current readings, and to define the working dark current as being whatever the current has decayed to within this

allowed period. This is acceptable because the exponential decay format means that the initial period of turn-on or turn-off accounts for the most rapid part of the response characteristic: the part of the cycle which is ignored is the part during which least happens. Any systematic errors introduced in this way will tend to understate the response of a slow sample to the next exposure wavelength, so the risk of exaggerating a device's response due to residual conductivity from a previous exposure is avoided. A sampling interval of 1 minute per wavelength setting allows for 20s dark exposure, 20s light exposure and 20s reset time. This results in an overall experiment time of 38 minutes to obtain a complete spectral response curve, which is long enough to gain a reliable insight into the behaviour of the sample and short enough to be executed accurately and comfortably by a manual operator. When such an experiment is accompanied by dark current measurements and a speed of response test, as described elsewhere in this chapter, a complete picture of the sample's photoconductive properties will be obtained.

An additional complication in the process of obtaining photoresponse data over a wide range of wavelengths arises due to the nature of the grating optics which lie at the heart of the monochromator. When the grating angle is set to allow a pass band centred on a given wavelength λ_p, the 2^{nd}, 3^{rd}, 4^{th}.....n^{th} orders of the harmonics ($\lambda_p/2$, $\lambda_p/3$, $\lambda_p/4$.....λ_p/n) of that wavelength will also be present. Thus, if the passband is centred upon, for example, 800nm (to which intrinsic diamond has negligible sensitivity) the monochromator output will also contain diminished intensities of 400nm, 266nm and 200nm light, the last of which corresponds closely to bandgap illumination and so excites a significant increase in the conductivity of the sample. To avoid the erroneous conclusion that the sample is sensitive to 800nm excitation it is necessary to employ low (energy) pass filters to remove the unwanted harmonics.

The system constructed used a pair of filters with cut-offs of 400nm and 630nm along with an opaque shutter (equivalent to ∞nm cut-off) and the absence of any filter or shutter (equivalent to a 0nm cut-off). The procedure by which these filters were used is best described by reference to figure (4.8) in which the broadband light source is represented at the base of the diagram. Taking a vertical direction of photon flux, the polychromatic beam passes through one of the four available filters and is then incident upon the diffraction grating of the monochromator. The passband, as determined by the angle of incidence via the sine drive mechanism, is then projected through the exit slit of the monochromator and onto the target.

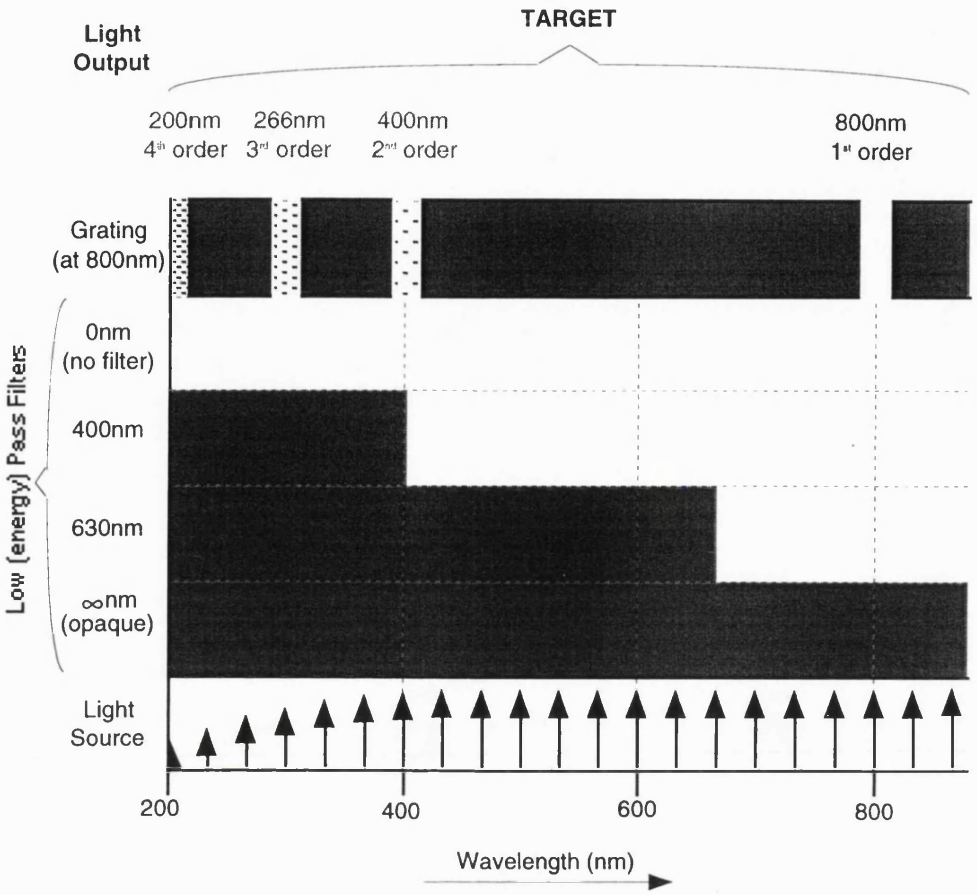

Figure 4.8: Schematic diagram outlining the use and function of filtering to remove unwanted harmonics from the light transmitted by the monochromator grating, see text for full description.

To obtain a full spectral responsivity curve the monochromator grating would be first set for a passband centred on 800nm. The two required current readings would be taken using the filter regime indicated by the heavy dotted box at the bottom right of the figure, ie: the dark current would be measured with the shutter closed (∞nm filter), this filter would then be replaced by the 630nm filter and twenty seconds later the photocurrent would be recorded. Following the measurement the shutter is returned and the device is allowed to reset for twenty seconds whilst the grating is rotated to select a passband centred on the next required wavelength, 780nm in this case. It can be seen from the diagram that under these conditions, the higher order passbands of the monochromator grating are excluded from both the dark and light exposure so that a true response current is obtained. For wavelengths in the range $400\text{nm} \leq \lambda_p < 630\text{nm}$ the filter regime is that indicated by the central dotted box on the diagram, and for $\lambda_p \leq 400\text{nm}$ the left hand boxed combination is used.

4.5.4 Photocurrent Analysis - Data Interpretation

The routine described above yields a data table of photoresponse current against wavelength. As previously noted in figure (4.6), the spectral intensity of the xenon light source is far from uniform, so a meaningful interpretation of the photoresponse data requires that it be corrected for the intensity of excitation applied.

A calibrated UV enhanced silicon photodiode was used to characterise the spectral output of the system; this device was supplied with spectral responsivity data expressed as amperes per watt of incident luminous intensity. By recording the spectral photocurrent response of the device, the incident optical intensity in watts was obtained for a given bandpass setting. This data set was then used as a calibration factor to convert device-under-test (DUT) photocurrent data into an ampere per watt value for each wavelength setting. This calibration process was both robust and straightforward, facilitating periodic routine recalibration of the system as well as specific recalibration exercises after system modifications.

For this project the calibrated spectral responsivity curve was adopted as a standard expression of device performance and it is the default format presented throughout this thesis. In certain contexts it is relevant also to analyse the absolute photocurrent response of a device: where this form of data is presented it is clearly identified as such.

4.5.5 Photocurrent Analysis - Gain Calculation

Photoconductive devices are capable of exhibiting current gain as discussed elsewhere (§5.3). Photoconductive gain, which is also known as External Quantum Efficiency (EQE) η_{ext}, is defined as the ratio of carriers detected in an external circuit n_{elec} to the number of photons absorbed by the detecting element n_{pho}:

$$\eta_{ext} = \frac{n_{elec}}{n_{pho}} \qquad (4.1)$$

The EQE is an experimentally measurable quantity, unlike the internal quantum efficiency η_{int} which is a measure of the number of absorbed photons which create photoexcited electrons and cannot be measured due to the inseparability of internal absorption, generation and recombination events. The magnitude of η_{ext} is a function of both device structure and operating conditions, and is therefore calculated separately for different experimental configurations as required in later sections of this thesis according to the following method.

n_{pho} is determined by measuring the current response I_{diode} of a commercial photodiode having active area A_{diode} which is calibrated to yield C_{diode} amperes per watt (A/W) of illumination at an unknown intensity P_{opt} of a specified wavelength λ_{pho} such that:

$$P_{opt} = \frac{I_{diode}}{C_{diode}} \tag{4.2}$$

Under steady state conditions P_{opt} represents an arrival rate of n_{pho} photons of quantised energy $E=(hc/\lambda)$ per second, so that in one second the number of incident photons per unit detector area is:

$$n_{pho} = \frac{P_{opt}\lambda_{pho}}{hc} = \frac{I_{diode}A_{diode}\lambda_{pho}}{C_{diode}hc} \tag{4.3}$$

where h is Planck's constant and c is the speed of light.

n_{elec} is determined from the device under test (DUT) by the current I_{DUT} and the active area A_{DUT} using the definition of current $Q=IT$ such that in one second:

$$n_{elec} = \frac{I_{DUT}A_{DUT}}{q} \tag{4.4}$$

where q is the electronic charge. Substituting (4.3) and (4.4) into (4.1) gives:

$$\eta_{ext} = \frac{A_{DUT}C_{diode}hc}{A_{diode}q\lambda_{pho}}\left(\frac{I_{DUT}}{I_{diode}}\right) \tag{4.5}$$

so that at a particular wavelength of interest η_{ext} can be found from a combination of known and measurable quantities. The expression outside the paranthesis is constant for a particular device structure and the configuration dependant incident photon flux is reflected by I_{diode}.

In the context of conventional photodiodes η_{ext} is always less than unity and is sometimes expressed as a percentage, whilst for devices capable of gain η_{ext} can be quite substantial and is usually stated as an absolute value. As η_{ext} is a ratio it is of course dimensionless.

4.5.6 Photoresponse Time Analysis

To facilitate investigation of the temporal evolution of the photoresponse of a sample, a removable shutter mechanism was installed between the output of the monochromator and the DUT. This was rendered necessary to minimise the shaping of the transient which was otherwise observed during experiments employing a manually operated shutter.

The shutter mechanism, derived from a single lens reflex (SLR) camera, could be configured to open and close upon manual triggering allowing arbitrarily long exposure periods bracketed by rapid transients, or alternatively to respond to a single stimulus by opening for a 10ms (nominal) fixed exposure. The current-voltage analysis equipment described in section 5.1 was unsuitable for recording these transients as the minimum sampling interval of the picoammeter was limited (by the embedded successive approximation and filtering routines) to >10ms for small values of current under investigation.

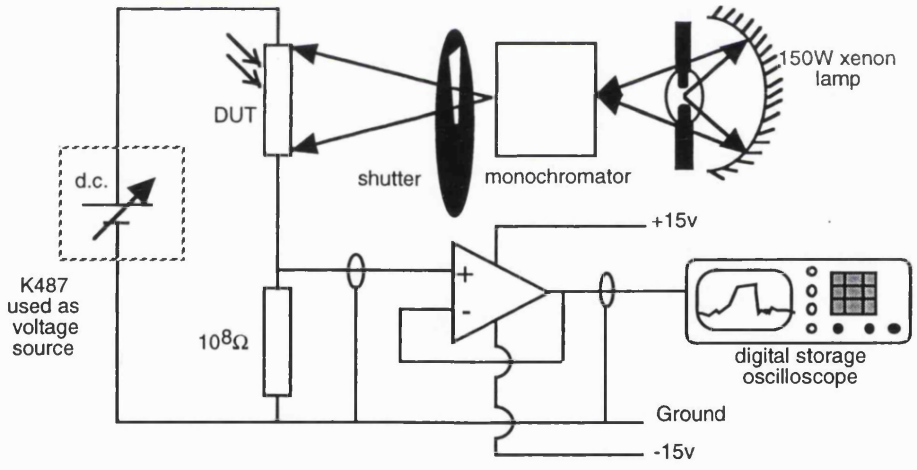

Figure 4.9: Schematic diagram outlining the deployment of light source, shutter, power supply and buffered digital oscilliscope for the capture and analysis of rapid transients.

Measuring rapidly changing small voltages can be readily achieved at low cost using an oscilloscope, by configuring the DUT as part of a voltage divider circuit. In the case of the undoped diamond samples presented for analysis, direct connection to the oscilloscope was precluded by the extremely low dark conductivity exhibited by many samples (in the order of 10's of GΩ) so a unity gain buffer was constructed using a high

input impedance operational amplifier of sufficient bandwidth to avoid deterioration of the measured signal (Harris Semiconductor CA3140). The oscilloscopes used were of the digital storage type (primarily a Hewlett Packard 54501A, additionally a Picoscope ADC50 PC based virtual instrument) to facilitate the capture of rapid events and subsequent data retrieval. This modified analysis system is outlined schematically in figure (4.9).

4.6 References

4.1 W. Kern, "Handbook of Semiconductor Wafer Cleaning Technology", Ed. W. Kern, Noyes Publications, New Jersey 1993, pp19.

4.2 G.S. Gildenblat, S.A. Grot and A. Badzian, Proceedings of the IEEE 79, 647 (1991).

4.3 F. Fang, C.A. Hewett, M.G. Fernandes & S.S. Lau, IEEE Transactions on Electron Devices 36, 1783 (1989).

4.4 S.A. Grot, G. Sh. Gildenblat, C.W. Hatfield, C.R. Wronski, A.R. Badzian, T. Badzian and R. Messier, IEEE Electron Device Letters 11, 100 (1990).

4.5 K. Das, V. Venkatesan, K. Miyata, D.L. Dreifus and J.T. Glass, Thin Solid Films 212, 19 (1992).

4.6 Y. Mori, H. Kawarada and A. Hiraki, Applied Physics Letters 58, 940 (1991).

4.7 B. Baral, S.S.M. Chan and R.B. Jackman, Journal of Vacuum Science and Technology A 14, 2303 (1996).

4.8 S.M. Sze, "Semiconductor Devices: physics and technology", Wiley, New York, 1985.

4.9 "AZ4620A Positive Photoresist for Thick Resist Film Applications", Data Sheet, Hoechst UK Ltd. Electronic Products Division, 56 Stewarts Road, Northants NN8 4RJ, UK.

4.10 W.S. Ruska, "Microelectronic Processing", McGraw-Hill, Singapore 1988.

4.11 P.E.J. Flewitt and R.J. Wild, "Physical Methods for Materials Characterisation", Institute of Physics Publishing, Bristol, 1994.

4.12 D. Clarkson, Electronics Today International 24(10), 12 (1995).

4.13 W. Zhu, "Defects in Diamond", in "Diamond: Electronic Properties and Applications", Ed. L.S. Pan and D.R. Kania, Kluwer Academic Press, Massachusetts, USA, 1995.

4.14 S.S.M. Chan, "Electronic Device Fabrication from Thin Film Diamond: surface preparation, patterning, metallisation and characterisation", PhD Thesis, University College, University of London, 1996.

4.15 S.P. Murarka, "Metallization: theory and practice for VLSI and ULSI", Butterworth-Heinemann, Massachusetts 1993.

4.16 M.S. Dresselhaus and R. Kalish, "Ion Implantation in Diamond, Graphite and Related Materials", Spriger-Verlag, Berlin, 1992.

4.17 S. Matsumoto, Y. Sato, M. Tsutsumi, N. Setaka, Journal of Materials Science 17, 3106 (1982).

4.18 J.I. Pankov, "Optical Processes in Semiconductors", Prentice-Hall International (1971) and Dover (1975).

4.19 Hammamatsu Photonics Data Sheet.

4.20 P. Gonon, S. Prawer, Y. Boiko and D.N. Jamieson, Diamond and Related Materials 6, 860 (1997).

5 DESIGNING A DEEP UV DIAMOND PHOTODETECTOR

5.1 Introduction

Based on the discussion of anticipated applications for diamond as an electronic material (§4) this chapter describes the design, prototyping and evaluation of a deep ultraviolet detector made from thin film diamond. The motivation to develop such a device arose through the fortuitous confluence of academic and commercial interests: the scientific desire to explore the electronic and electro-optic properties of CVD diamond being greatly eased by the emergence of a manufacturer wishing to extend its product range into deep UV and harsh environment sensing. As the difference between a photoconductivity experiment and a saleable device is in some cases a simple matter of packaging, a photodetector development programme was adopted as the vehicle with which to investigate the material.

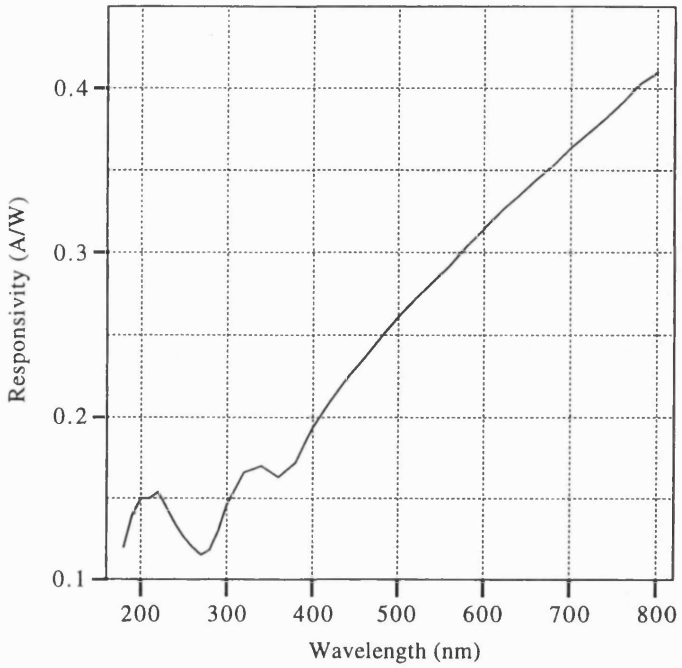

Figure 5.1: The spectral responsivity of a typical UV enhanced silicon photodiode. [Reproduced from 5.2].

5.2 Specification

A detailed discussion of the applications and end users of the devices described is presented in a later chapter (§11), however it is relevant to note that existing methods for detecting and quantifying deep UV primarily involve either a semiconductor photodiode or the combination of a photomultiplier tube and a vacuum photodiode. The latter arrangement is mechanically fragile, typically requires a bias potential of several hundred volts and usually offers broadband sensitivity from the infrared to the UV, depending upon the photocathode/glass envelope combination deployed [5.1]. Of semiconductor photodiodes available for deep ultraviolet detection, the most widely used are 'UV enhanced' silicon devices which differ little from standard photodiodes but instead of glass have a quartz or fused silica window to reduce the attenuation of shorter wavelengths.

The spectral responsivity of a typical UV enhanced silicon photodiode is reproduced as figure (5.1) and shows a broadband sensitivity in which the response to deep UV illumination at 200nm is ≈55% of the signal generated by a similar intensity of green

light at 500nm. The device has an active area of $1.2mm^2$ and is specified to operate at bias voltages of up to 5V with a dark current of 2pA at 10mV reverse bias, a peak d.c. current of 10mA, a maximum illumination intensity of $100Wcm^{-2}$ and a maximum soldering temperature of 200°C for 5 seconds [5.2]. The method of photodetection is optical excitation of an electron-hole pair in the reverse biased depletion region: the photogenerated carriers are rapidly separated and swept out of the depletion region by the built-in potential resulting in current flow in an external circuit. No amplification takes place resulting in an external quantum efficiency (§5.3) η_{ext} which in theory is ≤ 1 and in practice is always <1.

A diamond UV photodetector to complement the above devices was proposed which would exhibit the property of 'visible blindness' such that it would be relatively insensitive to visible wavelengths whilst responding strongly to the target excitation. Initial devices were specified to be sensitive only to wavelengths ≤225nm, which corresponds to the intrinsic bandgap absorption of diamond, with the intention that subsequent generations of device might be engineered to exhibit different absorption characteristics.

The operating voltage of the detector was required to be compatible with the microelectronic devices to which it was likely to be interfaced, resulting in a specification that satisfactory performance should be attainable at $V_B \leq 10V$. This would allow for direct connection to CMOS integrated circuits, popular op-amps and timers but excludes the less tolerant TTL regime.

In line with the silicon device, it was decided that the dark current should be in the order of picoamps. This not only provides for a large and therefore easily detectable change in current under illumination, but also minimises the current drawn by a device in the off-state, which is important for battery powered end user applications.

Given that the project aimed to investigate a wide range of device varients, and that commercialisation was an ultimate goal, it was agreed that commercially available CVD diamond should be used. Additionally, it was believed that attempts to grow custom material in-house would inevitably distract from the device development programme. Although small quantities of orientated aligned material as illustrated in figure (2.5) were obtained for evaluation purposes, such films were not available in quantity or at realistic prices at the commencement of the project, and remain relatively rare and expensive at the present time.

Additional requirements for practical detectors include factors such as speed of response, sensitivity, stability and manufacturability, however it was decided that these issues would be best addressed with the aid of data obtained from some preliminary experiments. On this basis a design operating on the principle of photoconductivity was generated to address the four primary specifications identified above and summarised in table (5.1).

Spec	Condition
1	to be sensitive only to wavelengths ≤ 225nm
2	satisfactory performance should be atainable at $V_B \leq 10V$
3	the dark current should be in the order of picoamps
4	commercially available CVD diamond should be used

Table (5.1): The four basic specifications against which a photoconductor design will be proposed.

5.3 Photoconductor Theory

5.3.1 Photocurrent

A photoconductor can be viewed as a resistor in which electrons are placed in the conduction band by optical excitation rather than the presence of ionised impurity atoms. An ideal sample of undoped diamond at low temperatures will contain no conduction electrons until it is exposed to light of a suitable wavelength as specified by equation (3.1), although no real sample is entirely free of defects or impurities so a dark current will always exist.

The current density J through a semiconductor sample of dimensions *wls* as sketched in figure (5.3) can be described using equation (2.4) which expressed the conductivity of a semiconductor, and the applied field E [5.3]:

$$J = \sigma E = q(\mu_n n + \mu_p p)E \qquad (5.1)$$

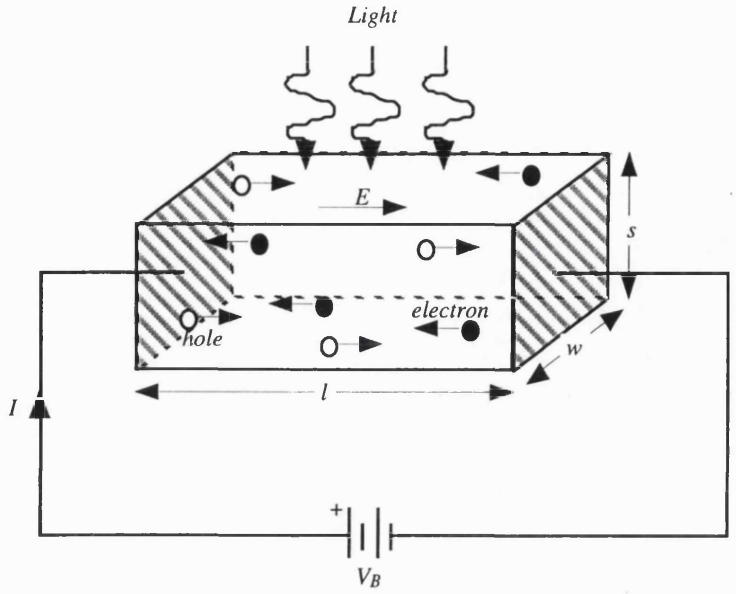

Figure 5.2: Schematic ouline of a basic bulk photoconductor. [Redrawn from 5.3].

In the context of a photoconductor, it is useful to describe the constitution of the carrier concentrations n and p in terms of the respective intrinsic thermal equilibrium components n_0, p_0 and the excess concentrations δn, δp due to optical excitation:

$$n = n_0 + \partial n \qquad\qquad p = p_0 + \delta p \tag{5.2}$$

such that the dark current density J_0 and the illuminated current density J_i are respectively:

$$J_0 = \sigma_0 E = q(\mu_n n_0 + \mu_p p_0)E \tag{5.3}$$

and

$$J_i = \sigma_i E = q\{\mu_n(n_0 + \delta n) + \mu_p(p_0 + \delta p)\}E \tag{5.3}$$

from which the photocurrent density ΔJ can be defined as $\Delta J \equiv J_i - J_0$. Multiplying by the detector cross sectional area $A = ws$ and expressing the field as a distributed potential $E = (V_B/l)$ enables the photocurrent ΔI to be stated as Ohm's law:

$$\Delta I = \Delta JA = q(\mu_n \delta n + \mu_p \delta p)\frac{A}{l}V_B \tag{5.4}$$

It is this spectrally dependant photocurrent ΔI which is plotted as responsivity in this thesis as discussed previously (§4.5.3, 4.5.4).

5.3.2 Photoconductive Gain

Under a given intensity of suitably energetic illumination P_{opt} the rate of carrier generation, provided s is sufficient to ensure complete absorption according to equation (3.2), is given by [5.3]:

$$G_0 = \eta_{eff} \frac{P_{opt}/E_g}{wls} \tag{5.5}$$

where the effective quantum efficiency $\eta_{eff}<1$ incorporates the unquantifiable internal quantum efficiency η_{int} and losses due to reflection.

The total density of mobile photogenerated electrons δn in the conduction band of the sample is given in terms of the steady state generation rate G_0 and the carrier lifetime τ_l by [5.4]:

$$\delta n = G_0 \tau_l \tag{5.6}$$

where it can be noted that $\delta p=\delta n$ as every excitation creates an electron-hole pair. In most semiconductors $\mu_n \gg \mu_p$ so the simplification $\mu=\mu_n$ is frequently applied [5.3] however in diamond $\mu_n \approx \mu_p$ (§2.4.3) so a more appropriate approximation is $\mu=2\mu_n$. Substituting this approximation and (5.6) into (5.4) yields:

$$\begin{aligned} \Delta I &= q(\mu_n + \mu_p) G_0 \tau_l \frac{A}{l} V_B \\ &\approx q 2\mu_n G_0 \tau_l \frac{A}{l} V_B \end{aligned} \tag{5.7}$$

Defining the transit time τ_T as the time taken for an electron to traverse the device length l at velocity v_n under a field according to the classical velocity, distance, time relationship [5.3]:

$$\tau_T = \frac{l}{v_n} = \frac{l}{\mu_n E} = \frac{l^2}{\mu_n V_B} \tag{5.8}$$

which can be substituted (5.7) so that ΔI becomes:

$$\Delta I = q(2G_0 lA)\frac{\tau_l}{\tau_T} \tag{5.9}$$

which is the total photocurrent in terms of the total number of carriers generated in the sample per second $2G_0 lA$, and τ_l / τ_T the ratio of the electron lifetime to the transit time. The significance of this expression is that whilst the generation of carriers can never be 100% efficient (η_{eff}<1), the expression τ_l / τ_T can be substantially greater than unity, giving rise to the property of photoconductive gain [5.3, 5.4, 5.5]. The above expression for gain can be restated in a particularly elegant way by returning to (5.5) and defining the primary current I_p due to photoexcited carriers as:

$$I_p = q\eta_{eff}\frac{P_{opt}}{E_g} \tag{5.10}$$

the photocurrent ΔI is:

$$\begin{aligned} \Delta I &= q\left(\frac{\eta_{eff} P_{opt}}{E_g}\right)\frac{\tau_l}{\tau_T} \\ &= I_p \frac{\tau_l}{\tau_T} \end{aligned} \tag{5.11}$$

which clearly shows that the gain, or EQE (§4.5.5) η_{ext} is given by:

$$\frac{\Delta I}{I_p} = \frac{\tau_l}{\tau_T} \tag{5.12}$$

A physical interpretation of photoconductive gain is that if $\tau_l >> \tau_T$ then a single charge carrier can makes several transits of the device during its lifetime; the electron does not of course actually go right round the circuit and back into the semiconductor, instead when it leaves the device a replacement is supplied at the opposite electrode by the circuit to maintain charge neutrality. The gain can be enhanced most obviously by applying a large bias potential to accelerate the electrons to a high or saturated velocity, thereby reducing τ_T as described by equation (5.8); a process to which diamond is extremely well suited due to its high carrier saturation velocity and large electric field breakdown strength (§2.4.4). Additional limitations which arise due to capacitative effects will be discussed in a later section (§7).

5.4 Implementation

5.4.1 Design Principles

The photoconductive mode of operation was selected in preference to a diode structure for three primary reasons:

i) Most semiconductors which are used for solid state photodetection, including silicon, exploit a reverse biased diode structure as a means of achieving a low dark current. Intrinsic diamond is highly resistive in the order of GΩ, so in the absence of photogenerated carriers the dark current should be extremely low rendering the creation of a rectifying contact unnecessary.

ii) The fabrication of reproducible rectifying contacts on thin film diamond is not yet a reliable technology (§2.6.2). The author had gained first hand experience of attempting to establish such contacts on diamond prior to the commencement of this project and was keen to avoid unwarranted complexity where possible, although insight developed over the intervening period may now make such devices a more realistic possibility.

iii) The photoconductive approach offered the prospect of exploiting photoconductive gain (§5.3.1) and the opportunities which exist for employing defect related centres for advantageous photoconductive device design, in contrast to the photodiode system where such defects are likely only to compromise detector performance.

The analysis of photoconductivity presented above indicates that device sensitivity will be improved by minimising the electrode spacing l as this will help to minimise the carrier transit time τ_T as illustrated by equation (5.4). An overriding factor when working on polycrystalline films however is that the material selection and electrode spacing should be considered in the context of carrier collection distances as discussed by Kania *et al.* [5.6]. It followed from this principle and from the results of Pan *et al.* [5.7] and Plano *et al.* [5.8] regarding the relative mobilities and collection distances observed in bulk and planar structures (§2.6.3) that in order to achieve optimal carrier transport properties, planar structures would be fabricated on the growth surface of films.

Despite the observation by Pan *et al.* [5.7](§2.6.2) that the mean carrier collection distance in early films was less than the mean crystallite dimension, it was felt that advances in film quality were likely to improve intra-crystallite carrier transport. It

therefore appeared likely that grain boundaries would become and remain the fundamental limiting factor on carrier collection distances. To minimise the loss of photogenerated carriers at grain boundaries it was decided that electrode spacing would be matched to mean crystallite surface dimensions in order to achieve a pseudo-single crystalline effect. This is illustrated schematically by figure (5.3) from which it can be appreciated that a carrier which is generated in one of the crystallites identified by white outline arrows will reach an electrode before it reaches a grain boundary.

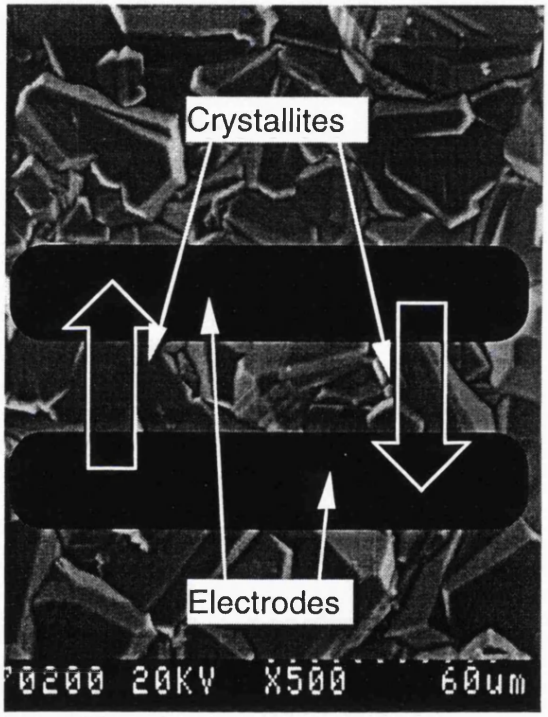

Figure 5.3: Schematic diagram illustrating the principle of close electrode spacing to achieve pseudo-single crystalline carrier transport.

Undoped diamond was selected for the first series of devices in order to meet the bandgap absorption requirement of specification (1) and the dark current requirement of specification (3). This meant that electrically the device would take the form of a dielectric between two conductors and the injecting contact regime would apply (§2.7.1), although the maximum bias level stipulated by specification (2) was unlikely to result in any injected current flow in the absence of photogenerated carriers. Consequently, the selection of contact metalisation was not influenced by work function considerations and thermally evaporated gold contacts were chosen for their stability and ease of processing. The adoption of a single layer metalisation ensured that both

lift-off and etching processes would be feasible, subject to any limitation caused by the nature of the diamond surface itself. The three design principles derived above are summarised in table (5.2).

Principle	Decision
1	planar structures would be fabricated on the growth surface of films
2	electrode spacing would be matched to mean crystallite surface dimensions
3	thermally evaporated gold would be used for the contact metallisation

Table (5.2): The three design principles which guided the design of the diamond photoconductor.

5.4.2 Material Selection

In contravention of specification (4), the material samples selected for the preliminary experiments were chosen to offer the greatest possible diversity in terms of quality and structure; the four films used were as follows.

Type A was randomly oriented freestanding ≈100μm thick MPACVD material as shown in figure (5.5 (a)) and also figures (2.5(c)) and (4.3) having a mean growth surface crystallite diameter of ≈20-40μm. It was colourless and optically transparent showing a strong Raman scattering feature at 1332cm^{-1} on a featureless background typical of good quality diamond as indicated in figure (5.4).

Type B was a 1mm thick silicon supported MPACVD oriented aligned film with partially coallesced crystallites having a wide variation of surface crystallite dimensions around a mean of ≈10μm as shown in figure (5.5(b)).

Type C was a thin, silicon supported randomly oriented film with a mean surface crystallite diameter of ≈1μm shown in figure (5.5(c)).

Type D was an optically smooth and transparent homoepitaxial film on a thin synthetic diamond substrate and is shown in figure (5.5(d)). Some outcrops of secondary nucleation were apparent around the perimeter of this sample.

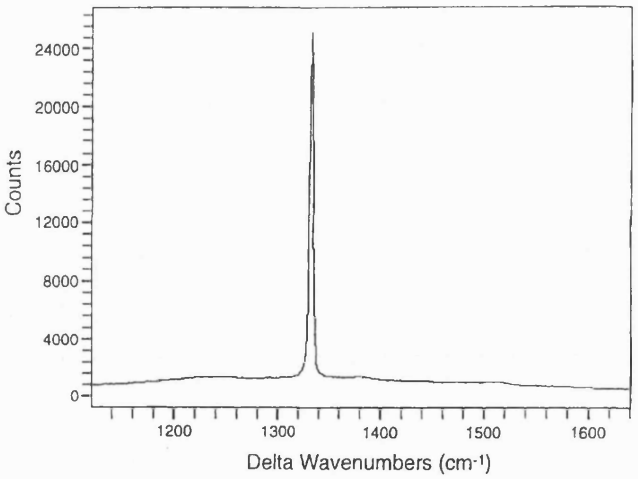

Figure 5.4: Raman scattering spectrum (632nm, HeNe light) of type A diamond film showing a strong single peak at 1332cm^{-1} on a featureless background typical of good quality diamond.

On the basis of the samples selected, an electrode spacing of 25μm was identified as meeting the requirements for pseudo-single crystallinity on type A film. A closer electrode spacing was considered in order to approach pseudo-single crystallinity on the other samples, however it was accurately anticipated that such a structure would be effectively impossible to fabricate on type A material. It was decided to interdigitate the electrode structure in order to maximise the optically active area of a sample within the restrictions of the close spacing requirement. A second hand mask was identified, repaired and modified through a series of lithographic processes to yield a set of 15 pairs of 25μm wide electrodes with an equal mark space ratio on a 100μm pitch.

5.4.3 Fabrication

Devices were fabricated on each sample type A-D according to the methods described in §4.2 and §4.3. An electron micrograph of a device on type A material is presented in figure (5.6) and shows the overall layout of the electrodes. This particular image reveals damage to the contact pads at the base of the picture where a failed attempt was made to achieve electrical bonding, and a short-circuit defect is visible in the lower centre region of the electrode array. A more detailed electron micrograph in figure (5.7) shows three electrodes on type A material indicating the extent to which the pseudo-single crystalline described in figure (5.3) has been achieved. The loss of the equal mark space ratio is an inevitable consequence of the specialist processing required to complete lithography on the type A surface. Figure (5.8) shows the connection of the 25μm aluminium bond wires to different diamond surfaces as labelled. A type A device which has been mounted on an industry standard TO5 header and is ready for

characterisation is pictured in figure (5.9) where the wires connecting the bond pads to the header pins are just visible.

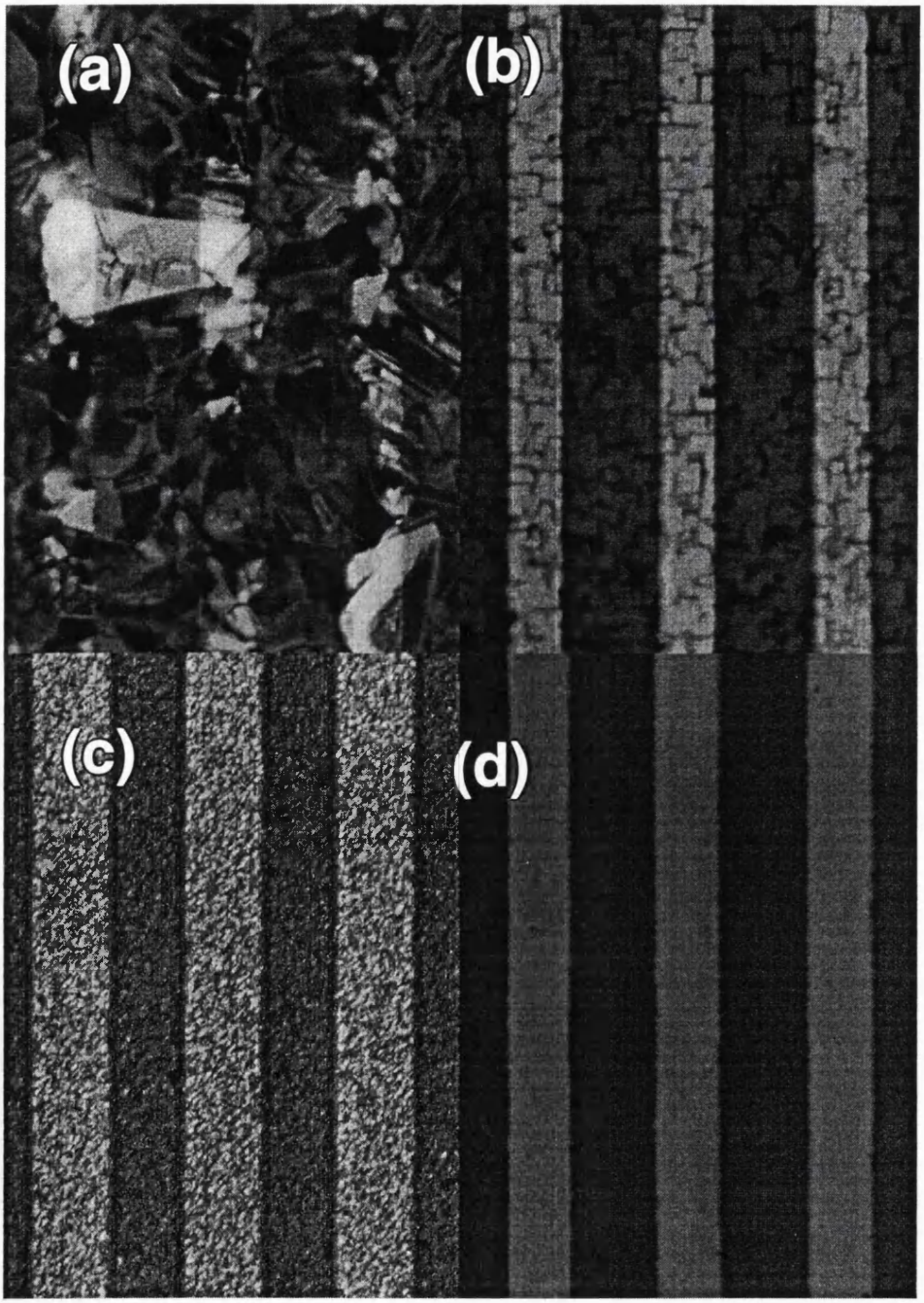

Figure 5.5: Optical micrographs of the four types of thin film diamond used for preliminary experiments; each electrode and gap is nominally 25μm wide, the distance between like points in each structure is exactly 50μm. (a) type A is ≈100μm thick randomly oriented freestanding film. (b) type B is silicon backed 1mm thick oriented aligned film. (c) type C is silicon backed small grain randomly oriented film. (d) type D is a homoepitaxial film on a single crystalline diamond substrate.

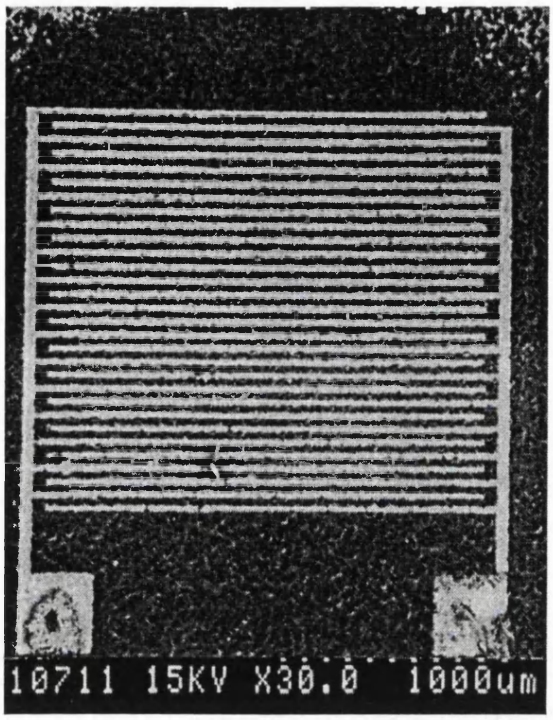

Figure 5.6 Electron micrograph of a photodetector on a type C diamond film. The electrode structure can be seen to consist of 25 pairs of 25μm wide electrodes with a (nominally) equal mark space ratio connected to two bonding pads by a pair of busbars.

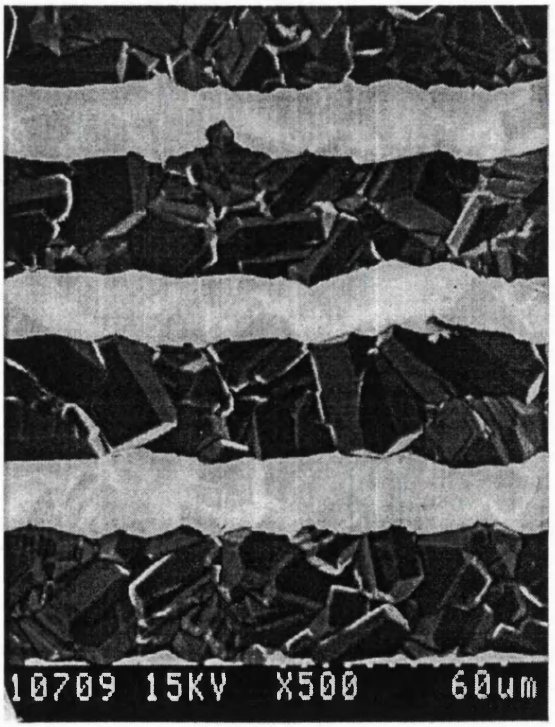

Figure 5.7: Electron micrograph of three electrodes (white) on the surface of a type A diamond sample. The successful implementation of the pseudo-single crystalline effect can be clearly seen.

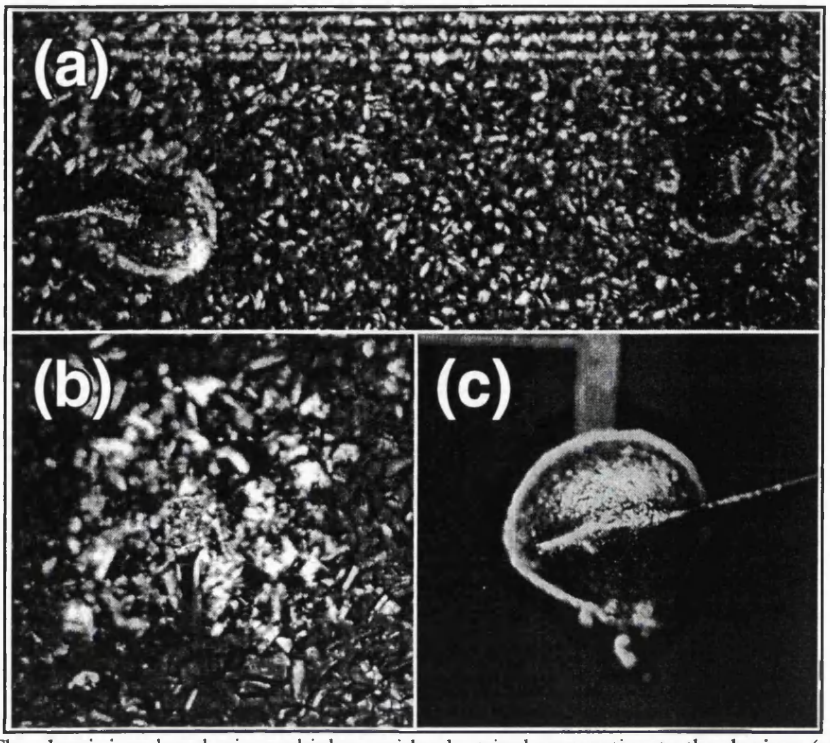

Figure 5.8: The aluminium bond wires which provide electrical connection to the devices (a) epoxy bond to type A diamond film. (b) ultrasonic bond to type A diamond film. (c) epoxy bond to type C diamond film.

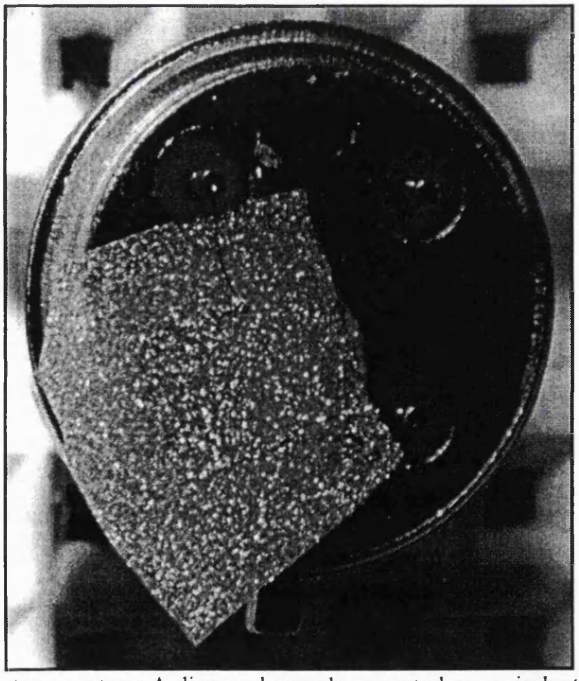

Figure 5.9: A photodetector on a type A diamond sample mounted on an industry standard TO5 header. The aluminium wires joining the bond pads to the header pins are just visible.

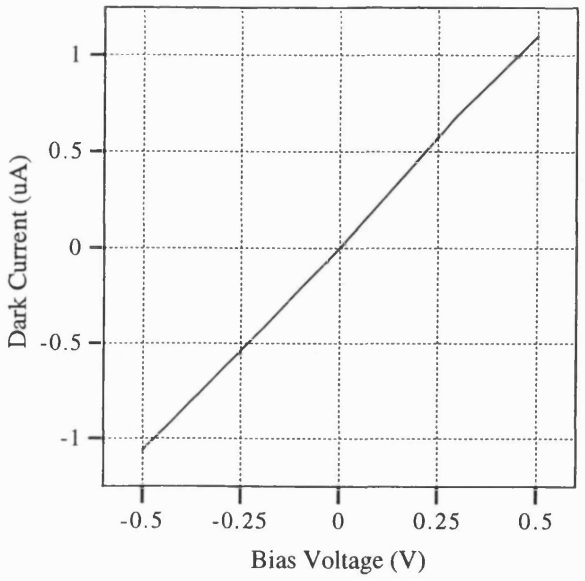

Figure 5.10: The *I-V* characteristic of a type A device as fabricated.

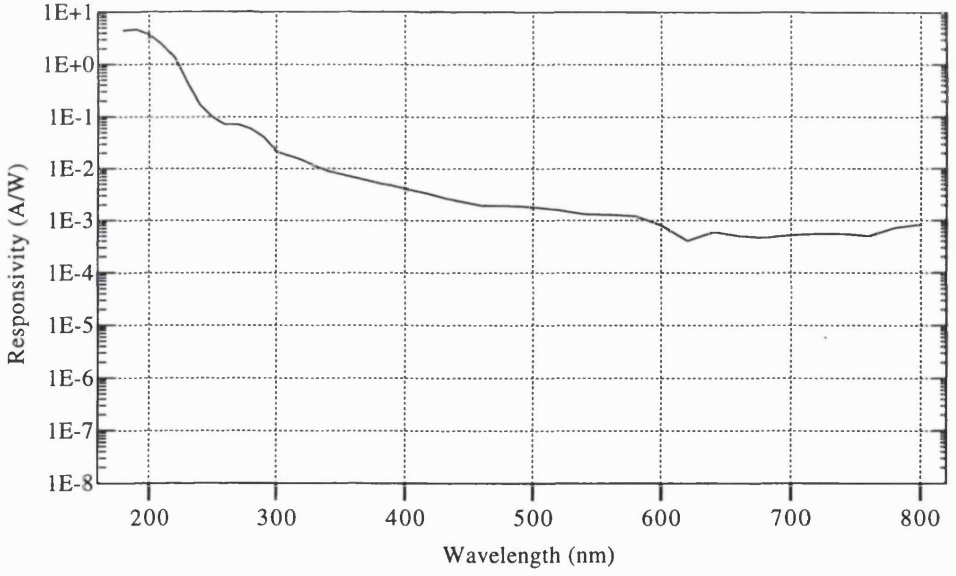

Figure 5.11: The spectral responsivity of a type A device as fabricated.

5.5 Results

Electrical and optical characteristaion of the samples was carried out as specified in §4.61-4, with the results presented here having been obtained from probed, rather than mounted devices.

The *I-V* characteristic of a type A device is plotted in figure (5.10) and shows a relatively high conductivity for undoped diamond, passing a current of ≈1μA at ±0.5V which fails specification (3). The spectral conductivity of the device plotted in figure (5.11) shows a greater sensitivity to deep UV than to the visible wavelengths, however the absence of a sharp cut-off in the response at ≈225nm is disappointing and fails to meet specification (1). The amplitude of the response suggests that gain is occuring even though the characteristic was obtained under a bias of 0.1V, well within specification (2), which was selected for compatibility with a type C device as will be discussed later.

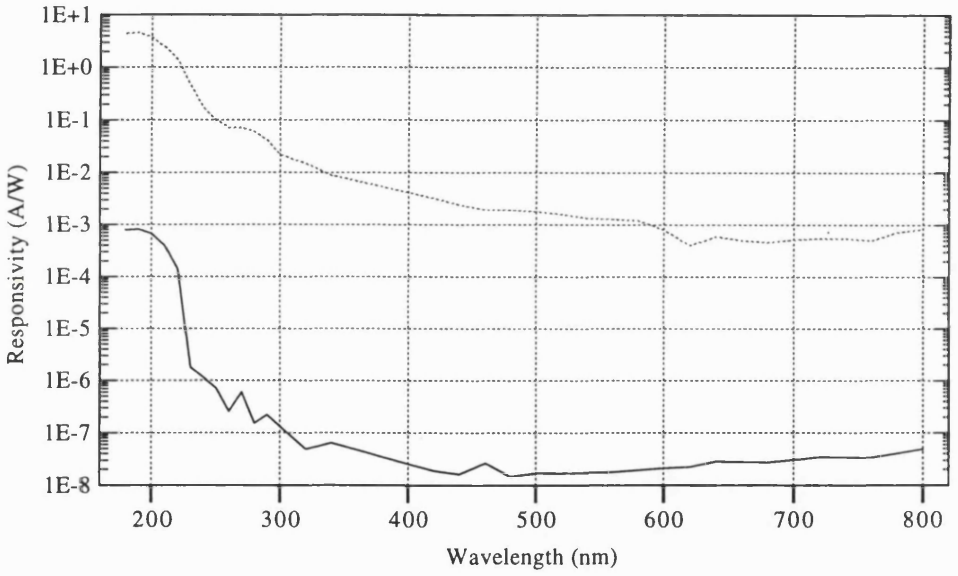

Figure 5.12: The spectral responsivity of a type B detector as fabricated. The response of a type A device is also shown (dotted) for reference.

No *I-V* characteristic is presented for a type B device as these devices were highly resistive and passed a dark current below the resolution of the analysis equipment at <0.04nA thereby satisfying specification (3) even at bias potentials well beyond the range of specification (2). The spectral response of a type B device is plotted in figure (5.11) and exhibits distinct wavelength selectivity satisfying specification (1) however the amplitude of the response is very low. The characteristic was obtained at a bias of 270V as no signal was detectable at lower levels indicating a failure to meet specification (2). The elevated bias across a nominal electrode spacing of 25μm resulted in a field of $1.08 \times 10^6 Vcm^{-1}$ which although below the level required to attain carrier saturation velocities (§2.4.4) could be expected to enhance the gain of the device as indicated by equations (5.8 & 5.9). The extremely low dark current and response

signals coupled with the clear photoconductivity threshold suggest that the crystallites may be locally pure and defect-free but that extensive grain boundary recombination compromises the macroscopic carrier transport properties of the material.

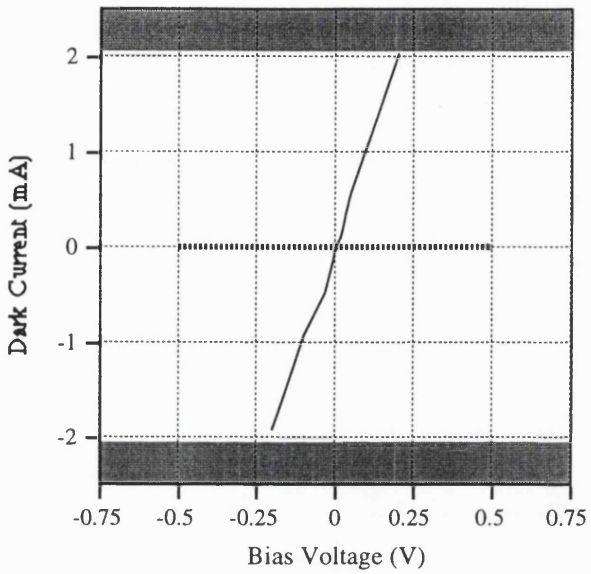

Figure 5.13: The *I-V* characteristic of a type C device as fabricated. The plot for type A is shown (dotted) for reference, and the current limits of the analysis system are indicated by shaded grey areas.

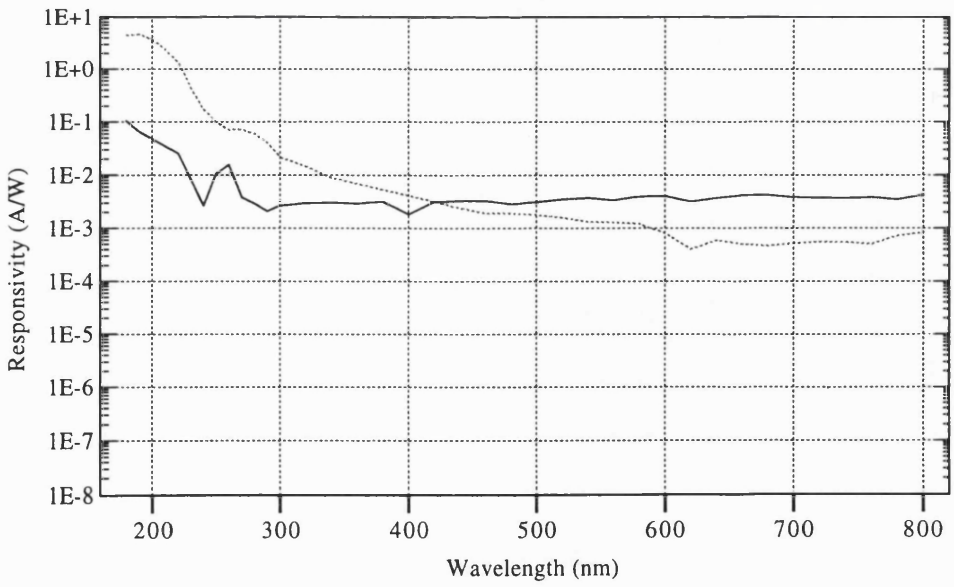

Figure 5.14: The spectral responsivity of a type C detector as fabricated. The response of a type A device is also shown (dotted) for reference.

The dark *I-V* characteristic of a type C device is plotted in figure (5.13) from which it can be seen that the device is highly conductive, saturating the analysis system with ±2.2mA at less than 250mV bias. It could perhaps be argued that this device satisfies the low voltages of specification (2) however this is evidently achieved at the expense of the dark current specification (3). The spectral response of the type C device shown in figure (5.14) indicates a small degree of wavelength selectivity but also significant response to all wavelengths which may really be a component of the excessive dark current.

No data at all is presented for device type D on the homoepitaxial film. Contrary to initial expectations, neither a dark current nor a response to illumination of any wavelength could be detected for this device at any bias level up to the equipment limit of ±500V. The experimental configuration was checked using a type A device and the type C was then re-examined but still failed to yield any detectable dark current or response data.

5.6 Conclusions

With reference to the published photoconducting detector characteristics discussed previously (§3.2.3), the shape of the spectral response curve of device type A can be considered to be broadly similar to that presented by Binari *et al.* [5.9], figure (3.3). It can be appreciated that the closer electrode spacing of the type A device permits comparable operation at one thousandth of the bias applied to the device of figure (3.3), which is an important consideration with respect to specification 2. The sharp spectral cut-off of the type B device surpasses anything previously published on CVD diamond and approximates the form of the IIb characteristic presented in figure (3.1), although some sub bandgap response is apparant in the region 230-320nm. The type B device is a valuable indicator that the best CVD films can approach the performance of good natural material. Significantly however, the large bias required to achieve this result fails specification 2, in addition to the acknowledged fact that the cost of a type B substrate fails specification 4. As a means of comparison, each device type has been scored (range 0-3) in table (5.3) against the specifications identified in table (5.1); for ease of interpretation the scores have been indicated by symbols as identified in the table caption.

Device	*Spec 1 wavelength*	*Spec 2 bias*	*Spec 3 dark current*	*Spec 4 cost*	*Score*
A	✗̸	✓̸	✗̸	✓	7
B	✓̸	✗	✓	✗	5
C	✗	✓̸	✗	✓	5
D	✗	✗	✗	✗	0

Table (5.3): Scoring the device types A-D with marks out of three for each of the specifications. ✗=0, ✗̸ =1, ✓̸ =2, ✓ =3.

From this semi-quantitative analysis it emerges that the type A device comes closest to meeting the overall specification, although the total score of 7/12 indicates only a 58% success. It is interesting to note that types B and C score equally at 5/12 but gain these scores against diametrically opposed specifications. The unexpected outright failure of the type D device demands further analysis of the sample, which has been undertaken and will be presented in a later chapter (§8). It is believed that the film must contain a high defect density resulting in very poor carrier transport properties: there can have been no failure to generate photoexcited carriers with the xenon lamp employed, from which it follows that the carriers were not available to the measurement system at the electrodes.

Based upon the preceeding discussion, it was decided to continue with the development of type A devices against a target of modifying their characteristics to meet the four stated specifications by means of material processing and/or optimised device geometry.

5.7 References

5.1 J.T. Verdeyen, "Laser Electronics" 3rd Edn, Prentice Hall, New Jersey, 1995.

5.2 "High Performance Silicon Photodetectors" Product catalogue: European Edition 2, Centronic Ltd., King Henry's Drive, CR9 0BG, U.K.

5.3 S.L. Chuang, "Physics of Optoelectronic Devices", Wiley, New York, 1995.

5.4 A. Rose, "Concepts in Photoconductivity and Allied Problems",Wiley Interscience, New York, 1963.

5.5 R.H. Bube, "Photoelectronic Properties of Semiconductors", Cambridge University Press, U.K., 1992.

5.6 D.R. Kania, M.I. Landstrass, M.A. Plano, L.S. Pan and S. Han, Diamond and Related Materials 2, 1012 (1993).

5.7 L.S. Pan, D.R. Kania, P. Pianetta, J.W. Ager III, M.I. Landstrass and S. Han, Journal of Applied Physics 73, 2888 (1993).

5.8 M.A. Plano, S. Zhao, C.F. Gardinier, M.I. Landstrass, D.R. Kania, H. Kagan, K.K. Gan, R. Kass, L.S. Pan, S. Han, S. Schnetzer and R. Stone, Applied Physics Letters 64, 193 (1994).

5.9 S.C. Binari, M. Marchywka, D.A. Koolbeck, H.B. Dietrich and D. Moses, Diamond and Related Materials 2, 1020 (1993).

6 IMPROVING THE WAVELENGTH DISCRIMINATION OF CVD DIAMOND PHOTODETECTORS

6.1 Introduction

This chapter describes the development and verification of an annealing regime which substantially modifies the device characteristics of photodetectors fabricated from polycrystalline CVD diamond films. The primary factors which influence the electronic properties of thin film diamond are considered in the context of the results presented in the previous chapter. A series of experiments is proposed with the aim of improving the carrier transport and wavelength discrimination characteristics of contemporary samples of the material. One particular annealing process is identified to cause an unprecedented enhancement of gain combined with a reduction in both dark current and sub-bandgap sensitivity.

6.2 Experimental Design

A meaningful attempt to improve the characteristics of device type A as presented in (§5.5) must begin by identifying the specific problems which will be addressed. Figure (5.10) indicated the dark current of a type A device to be in the order of a microamp which is substantially higher than could be expected for intrinsic diamond. Although the number of unknowns involved prevents accurate quantitative calculation of carrier parameters for such a primitive device, a 'ball-park' approximation of the carrier density required to pass such a dark current usefully indicates the scope of the problem and can be undertaken as follows:

Using equation (5.3) for the dark current, and assuming a single net carrier type, the experimentally determined carrier density n_{expt} can be expressed as:

$$n = \frac{I}{q\mu EA} \tag{6.1}$$

where: I, the measured current (§5.5) $\approx 1\text{x}10^{-6}$ A

q, the electronic charge [6.1] $\approx 1.6\text{x}10^{-19}$ C

μ, the carrier mobility (§2.4.3) ≈ 2000 cm^2/Vs

E, the applied field is 0.5 V over a nominal 25μm (§5.5) = 200 V/cm

A, the detector cross sectional area (c.s.a.) is approximated for a single finger pair by an overlapping finger length of 1800μm and an effective penetration/ device depth of 2μm [6.2]. The resulting area is multiplied by 29 to account for the fifteen intersecting finger pairs to yield an overall c.s.a. calculated as $(180\text{x}10^{-3})(2\text{x}10^{-4})(29) = 1.044\text{x}10^{-3}$ cm^2.

so that:

$$n_{expt} = \frac{(1x10^{-6})}{(1.6x10^{-19})(2000)(200)(1.044x10^{-3})} \approx 1.5x10^{10} / cm^3 \tag{6.2}$$

For comparison, it is possible to calculate the theoretical intrinsic carrier density for pure diamond at room temperature n_{theory}, given the effective carrier masses (§2.4.2) and the following expression [6.1]:

$$n_i = 4.9\times 10^{15}\left(\frac{m^*_{e,dos}m^*_{h,dos}}{m_0^2}\right)^{3/4} M_c^{1/2}T^{3/2}\exp\left(-E_g/2kT\right) \tag{6.3}$$

where: $m^*_{e,dos}$, the electron density of states effective mass is determined from equation (2.3) and the most recent theoretical data of table (2.1):

$$\begin{aligned}\frac{m^*_{e,dos}}{m_0} &= \left\{\left(\frac{m^*_{el}}{m_0}\right)\times\left(\frac{m^*_{et}}{m_0}\right)^2\right\}^{1/3}\\ &\approx \left\{(1.665)\times(0.290)^2\right\}^{1/3}\\ &\approx 0.519\end{aligned} \tag{6.4}$$

$m^*_{h,dos}$, the hole density of states effective mass is determined from equation (2.4) and the most recent theoretical data of table (2.1):

$$\begin{aligned}\frac{m^*_{h,dos}}{m_0} &= \left\{\left(\frac{m^*_{hh}}{m_0}\right)^{3/2}+\left(\frac{m^*_{lh}}{m_0}\right)^{3/2}\right\}^{2/3}\\ &\approx \left\{(0.614)^{3/2}+(0.208)^{3/2}\right\}^{2/3}\\ &\approx 0.692\end{aligned} \tag{6.5}$$

M_c, the number of equivalent minima in the conduction band [351] = 6

T, the absolute temperature ≈ 300K

E_g, the bandgap (§2.4.1) ≈ 5.5eV = 8.8x10^{-19}J

k, the Boltzmann constant [6.1] ≈ 1.38x10^{-23}J/K

so that:

$$\begin{aligned}n_{theory} &= 4.9\times 10^{15}(0.519\times 0.692)^{3/4}(6)^{1/2}(300)^{3/2}\exp\left(\frac{-8.8\times 10^{-19}}{2\times 300\times 1.38\times 10^{-23}}\right)\\ &\approx 2.02\times 10^{-27}\ /\ cm^3\end{aligned} \tag{6.6}$$

which is reasonably consistent with the value of <1x10^{-26}cm^{-3} cited elsewhere [6.3].

The result of calculation (6.2) indicates a dark carrier density approximately 10^{37} greater than is anticipated for pure diamond by calculation (6.6), yet it is known that the film was grown in an uncontaminated reactor so impurity doping is highly unlikely. Additionally, the film was pre-processed by high temperature acid bathing (§4.2.2) which is known to remove residual graphitic material from the exposed surface of a sample [6.4] and to dehydrogenate the near surface region, rendering surface conduction an unlikely mechanism to account for the large dark current.

A logical conclusion must therefore be that grain boundary conduction acts effectively as a short circuit path between the finger electrodes. The likely role of grain boundary regions is also indicated by the extensive sub-bandgap optical absorption exhibited by type A devices, and to varying degrees by types B and C as well. Fundamentally, such absorption cannot occur in pure diamond, which the Raman spectrum of figure (5.4) indicates the crystallites of type A material to be, from which it follows that the primary non-diamond portion of the detector is the cumulative bulk of the grain boundary regions.

Having deduced that the poor performance of the initial devices is attributable to a material factor, as opposed to a basic design flaw, it becomes relevant to consider the means by which the material may be modified in order more fully to achieve its device potential. Selection of the type of processing to be performed must take into account the requirement to act upon the non-diamond regions of the film without causing irreparable damage to the good quality diamond crystallites. Any processing must therefore be applied in such a way as to act only in the target regions: a stipulation which would be effectively impossible to meet by any active selection process, due both to the random distribution of grain boundaries and the vanishingly small surface cross-sections which they present.

Processes such as neutron irradiation (§3.3.2) and ion implantation (§9), which act uniformly across the entire exposed surface of a sample, were therefore deemed unsuitable for this part of the project. Gas ambient annealing however was identified as a suitable self-selecting process, which could be *applied* to a whole inhomogeneous sample but would *act* only on regions which were susceptible to the conditions applied. It was already known that annealing CVD diamond in air resulted in a reduced dark current [6.5, 6.6] believed to be due to oxidation, whilst hydrogenation would render the surface conductive (§2.5.4) and vacuum annealing is reported to have little effect up to temperatures of ≈1500°C unless the surface is contaminated with oxygen or a group VIII metal, both of which act as catalysts for graphitisation [6.5, 6.7]. No specific data

was available however on the outcome of annealing in methane, a component of the most widely used precursor mixture for thin film diamond growth (§2.3.3), which could potentially deliver either carbon or hydrocarbon radicals to receptive sites.

6.3 Experiment

A series of experiments was undertaken using replicates of the type A device with the dual aims of exploiting air annealing to reduce the dark current and investigating the unknown effects of annealing in methane. These treatments (§4.3.1, 4.3.2) were applied sequentially to samples labelled types E and F according to the processes described in table (3.1). A control sample type G was included on which process E was replicated with argon substituted for methane. In the light of initial results a second control type H was introduced, in which process E was again replicated but with nitrogen replacing air; a further cycle of air annealing was subsequently applied to samples of type H.

Sample	*Processing*
E	700°C, 1hr methane→ 430°C, 1hr air
F	430°C, 1hr air → 700°C, 1hr methane
G	700°C, 1hr argon→ 430°C, 1hr air
H	700°C, 1hr methane→700°C, 1hr nitrogen → 430°C, 1hr air

Table (6.1): The processing applied to sample types E to H.

Following each stage of processing, the dark current (§4.5.1) and spectral responsivity (§4.5.4) of each device was analysed. In some cases the characteristics of a sample type at a particular stage of processing prevented any meaningful data from being collected, usually because the devices were immeasurably conductive or resistive. All spectral responsivity data was obtained using a bias of 0.1V unless specified otherwise.

6.4 Results

6.4.1 Type E: Methane/Air

The dark current of a type E device is presented in figure (6.1). Figure (6.1(a)) plots the dark current in the as fabricated condition and is of the order of microamps, consistent with the type A structure of figure (5.10). After methane annealing, the dark current shown in figure (6.1(b)) was obtained, which can be seen to be almost 1000 times larger and caused the picoammeter to saturate at its current limit of ±2.2mA. After annealing in air however, the dark current dropped to the order of picoamps as indicated in figure (6.1(c)) which is somewhat erratic due to the autoranging feature of the instrument at this low level of current. Having established that the *I-V* characteristics were approximately linear under all conditions, the positive bias data was replotted in figure (6.1(d)) against a log scale for comparison.

The spectral responsivity of a type E device shown in figure (6.2) confirms the (§4) result that as fabricated the device exhibits a substantial sensitivity to sub-bandgap radiation. After methane annealing this characteristic deteriorates further as indicated by the dotted plot (b) which shows a reduced DUV response combined with an increased visible response, corresponding to the highly conductive condition illustrated by (6.1(b)). In plot (c) after air annealing the DUV response remains slightly over an order of magnitude less than in the unprocessed state of plot (a), but the sub-bandgap response has been significantly suppressed resulting in a sharp bandgap energy cut-off and a DUV-visible discrimination ratio of over six orders of magnitude.

6.4.2 Type F: Air/Methane

As fabricated, the dark current of the type F device illustrated in figure (6.3(a)) is in the order of microamps like the type A and E devices, but within this scale it is substantially larger indicating the variation which can occur between individual samples from a single diamond wafer. Annealing in air is seen in figure (6.3(b)) to reduce the dark current to the order of picoamps as in the case on the type E device and a subsequent anneal in methane is shown in figure (6.3(c)) to greatly increase the dark current to slightly above its initial value on the microamps scale.

Figure (6.4) presents the recordable spectral responsivity of the type F device. Plot (a) represents the device as fabricated and is essentially the same as for the type A and E devices. After air annealing however, when the device had become highly resistive in the dark, no photoresponse could be obtained under any conditions at any wavelength. Some degree of photoresponse was restored following the methane anneal, which

yielded plot (b) exhibiting a low sensitivity to bandgap excitation and very poor wavelength discrimination.

6.4.3 Type G: Argon/Air

The dark current of a type G device in the as fabricated condition is presented in figure (6.5(a)) and is substantially lower than the corresponding values for type E and F devices; this may reflect the fact that type G was from a batch fabricated on a different occasion to types E and F using another part of the same wafer. No data was recorded for the type G device after argon annealing, however after the air annealing stage the dark current was found to have increased by around three orders of magnitude to the order of tenths of a microamp.

Figure (6.6) presents the spectral responsivity data obtained from the type G device. Plot (a) represents the as fabricated condition showing a low overall level of response with substantial sub bandgap sensitivity including a particularly well defined feature between 250 and 320nm: this again indicates the variability of material across the wafer. After air processing the DUV response indicated by plot (b) has been enhanced by an order of magnitude with no suppression of the sensitivity to longer wavelengths.

6.4.4 Type H: Methane/Nitrogen/Air

The dark current of an as fabricated type H device is seen in figure (6.7(a)) to be so low that the characteristic was obtained over an extended voltage range of ±5V. Following methane and nitrogen processing figure (6.7(b)) indicates that the dark current saturates the picoammeter at a bias of ±0.2V. Although the characteristic appears asymmetric and is not shown to reach the -2.2mA limit it was observed that a V_B of -0.3V forced the analysis system into overload. Part (c) of the figure indicates that a subsequent air anneal only slightly reduced the dark current, which remained in the mA range.

The spectral responsivity of the type H device is presented in figure (6.8). Plots (a) and (b) were obtained in the as fabricated condition at V_B levels of 0.1V and 1.0V respectively. The similarity between plots (a) and (b) indicates that in this case a variation of an order of magnitude in the applied bias has little effect upon the form or level of the sensitivity of the device. Plot (c) represents the sensitivity after methane, nitrogen and air annealing and was obtained at a V_B of 0.01V due to the exceptionally high dark conductivity exhibited by the device in this condition. Despite the difference in applied bias, a comparison to the as fabricated characteristic shows that the overall response of the device to all wavelengths has increased uniformly so that the DUV-visible discrimination ratio remains poor.

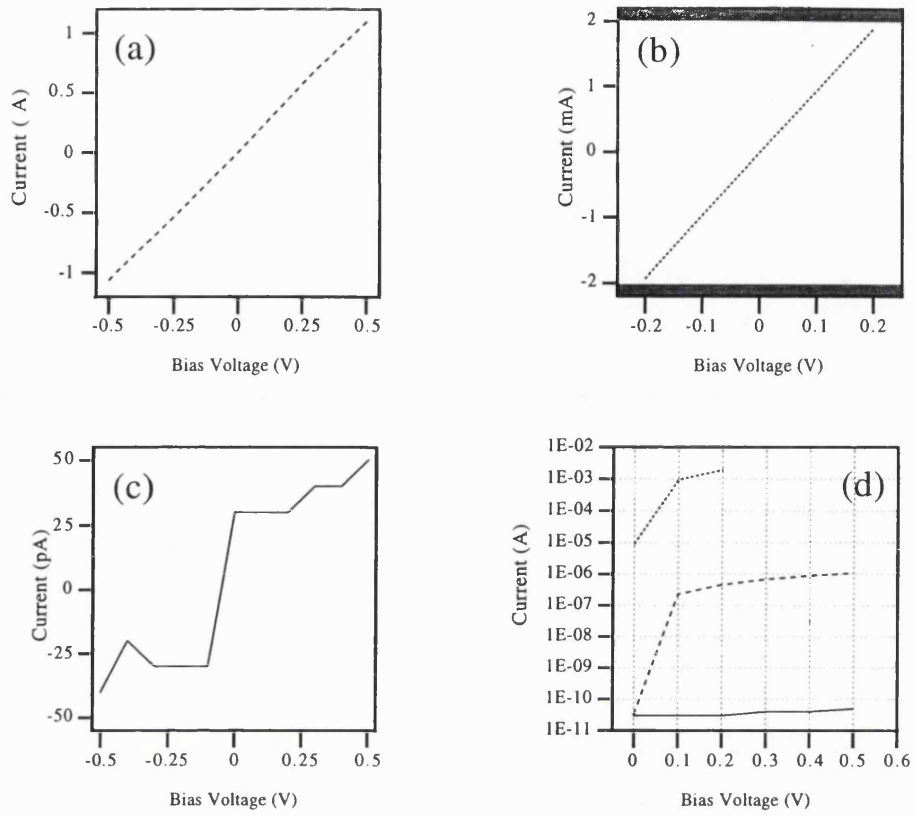

Figure 6.1: Dark current of a device type E at different stages of processing. (a) as fabricated. (b) after annealing in CH_4 for 1hour, shaded region indicates instrument current limit. (c) after annealing in air for 1 hour following (b). (d) data from (a, b and c) reproduced against a log scale; plot attributes as (a-c).

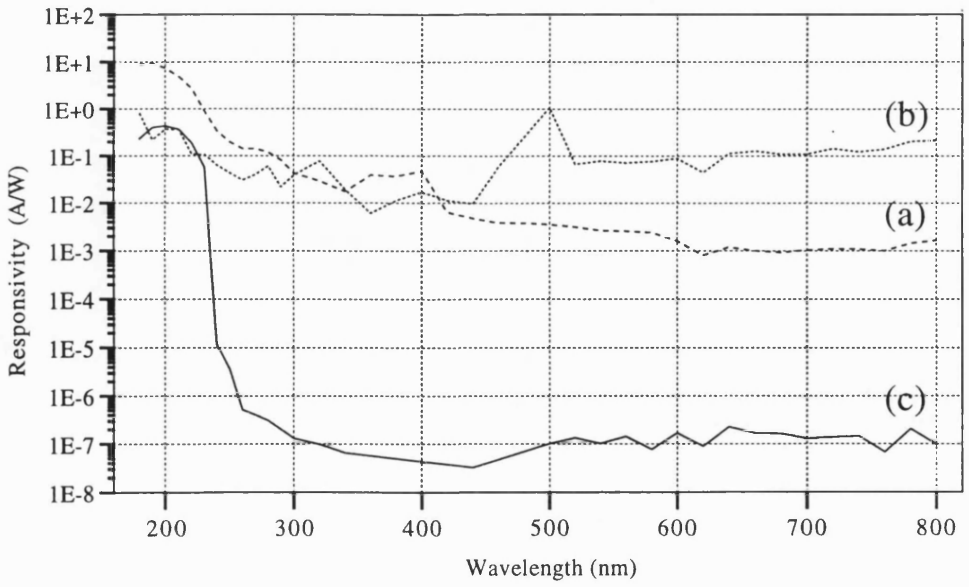

Figure 6.2: The spectral responsivity of a type E device. (a) as fabricated. (b) after methane annealing. (c) after methane and air annealing.

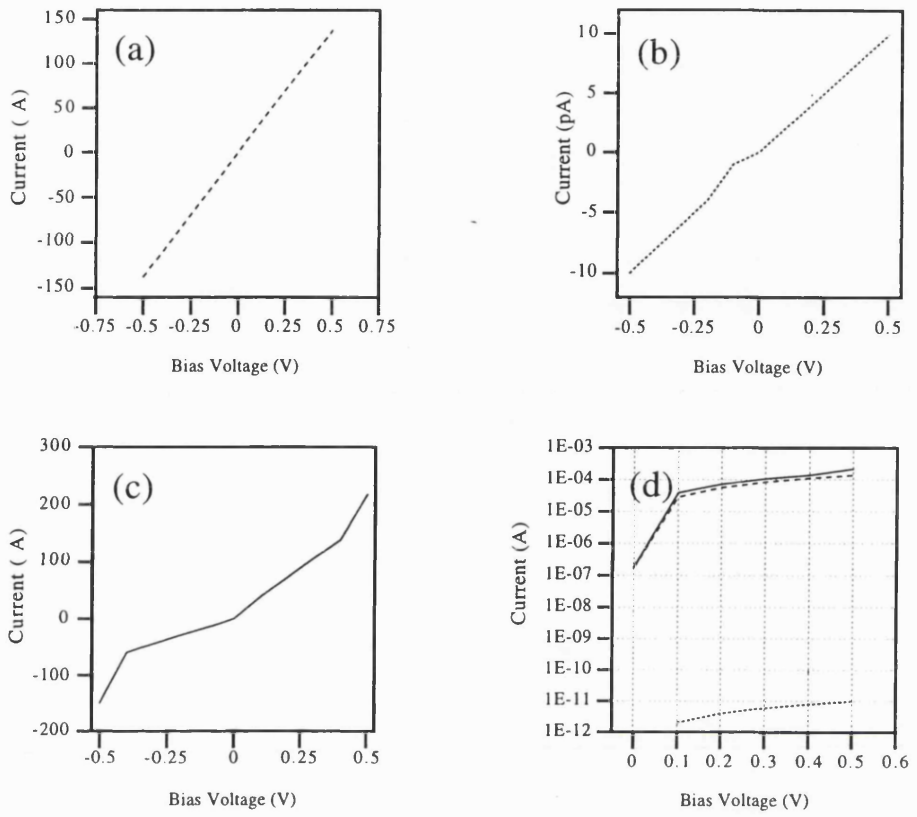

Figure 6.3: Dark current of a device type F at different stages of processing. (a) as fabricated. (b) after annealing in air for 1 hour. (c) after annealing in CH_4 for 1 hour following (b). (d) data from (a, b and c) reproduced against a log scale; plot attributes as (a-c).

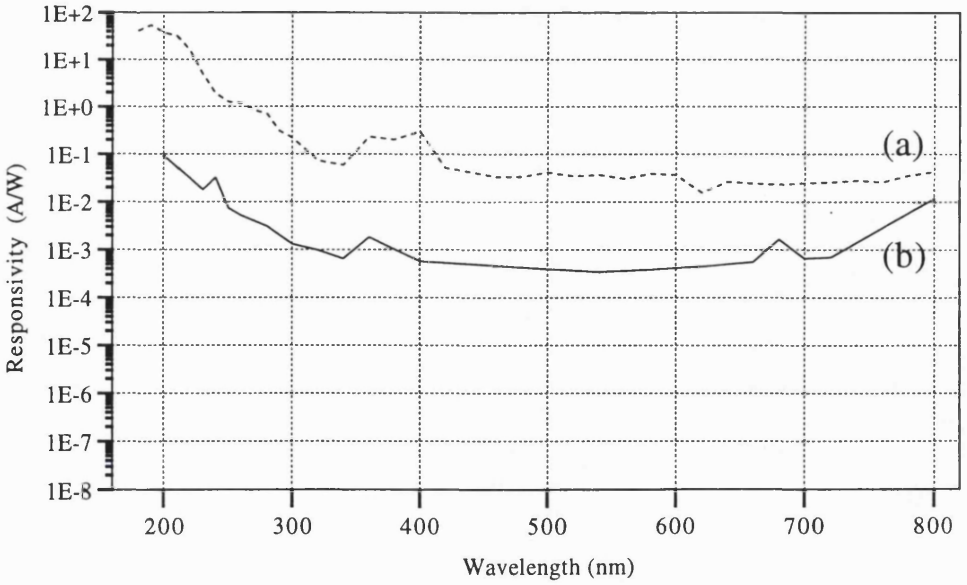

Figure 6.4: Spectral responsivity of a type F device (a) as fabricated. (b) after air and then methane processing.

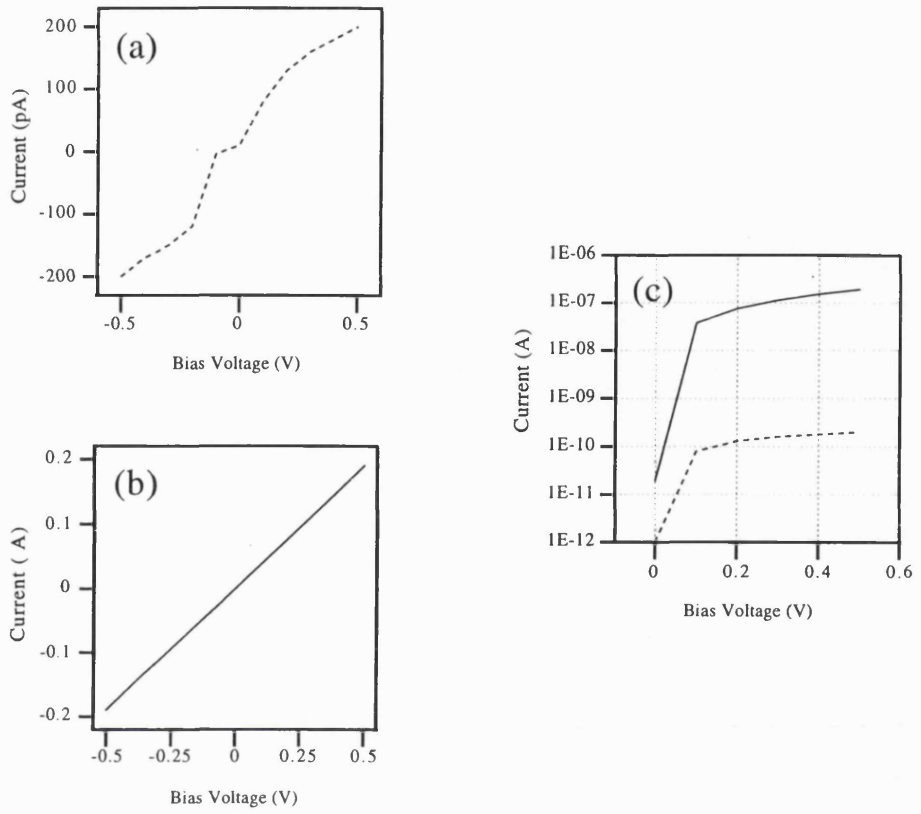

Figure 6..5: Dark current of a device type F. (a) as fabricated. (b) after annealing in argon and then air for 1 hour. (c) data from (a and b) reproduced against a log scale; plot attributes as (a) and (b).

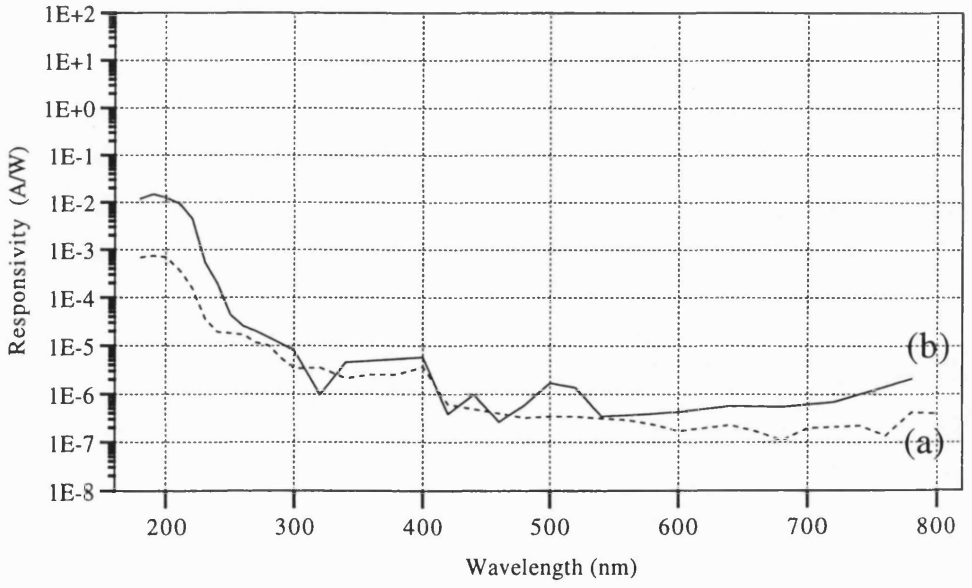

Figure 6.6: Spectral responsivity of a type G device. (a) as fabricated. (b) after argon and air annealing.

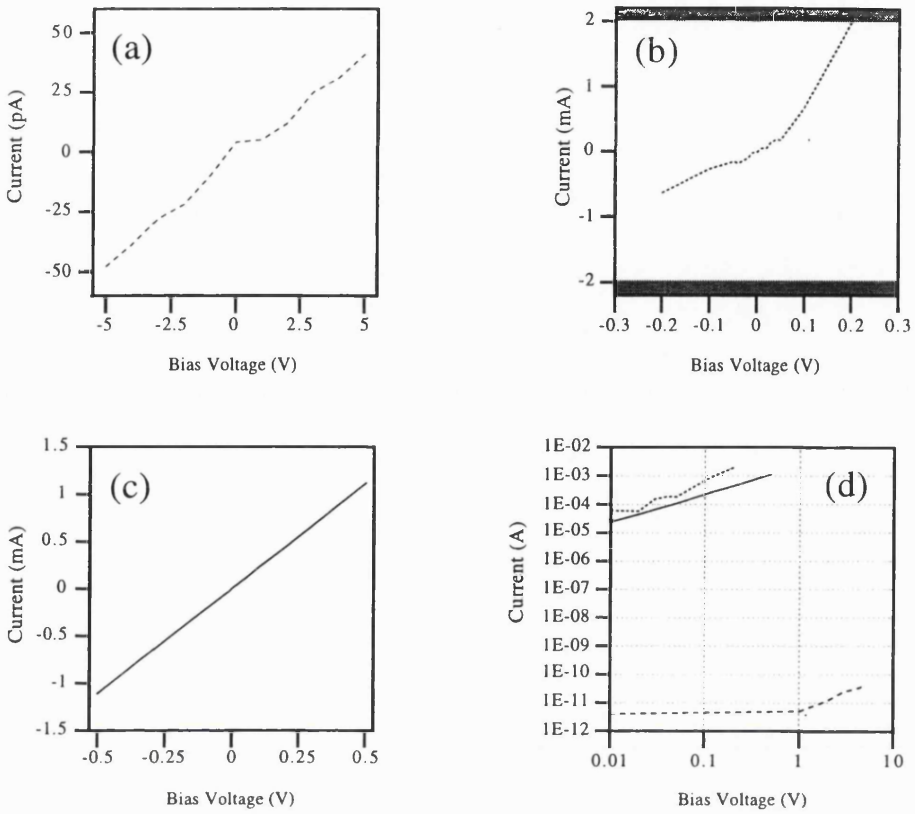

Figure 6..7: Dark current of a device type H. (a) as fabricated, note larger voltage scale. (b) after annealing in methane and then nitrogen. (c) after annealing in air for 1 hour following (b). (d) data from (a, b and c) reproduced against a log scale; plot attributes as (a-c).

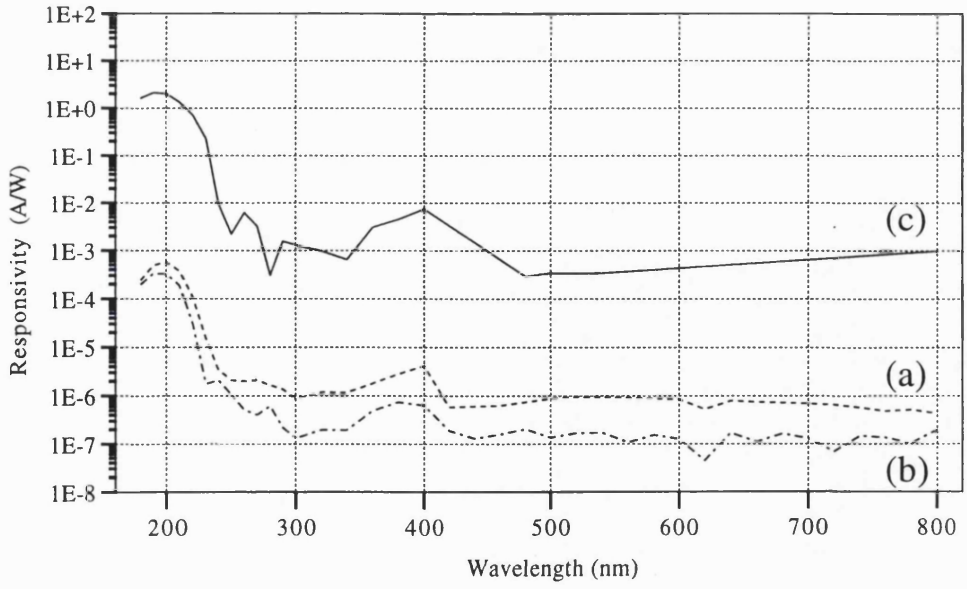

Figure 6.8: The spectral responsivity of a type H device (a) as fabricated with $V_B = 0.1$ V. (b) as fabricated with $V_B = 1.0$ V. (c) after methane, nitrogen and air annealing with $V_B = 0.01$ V.

6.5 Discussion

It is clear from the results presented above that annealing sequentially in methane and then air as described in table (6.1) causes a dramatic improvement in both the dark current and spectral photocurrent characteristics of the type E device. Repeated experiments have shown this effect to be reliable and reproducible over an extended time scale and several equipment configurations as indicated in figure (6.9).

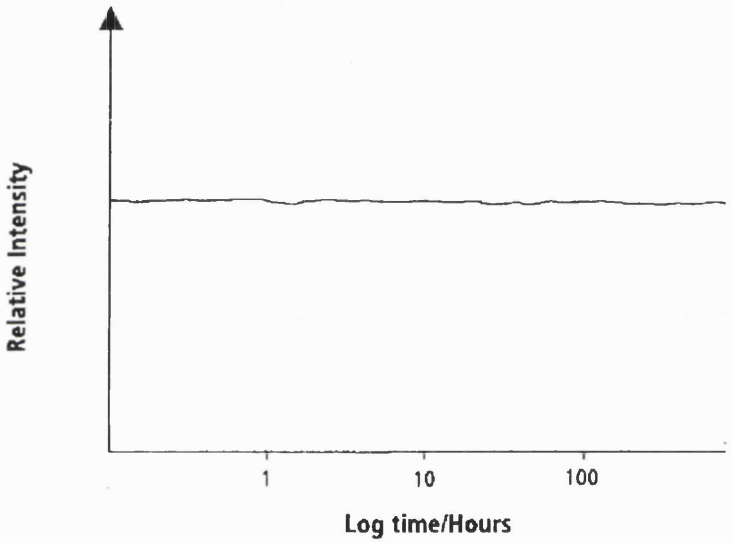

Figure 6.9: Stability of type E diamond detector response to excimer laser irradiation (193nm, 5W) over an extended time period. [Data from Centronic Ltd].

The results obtained for the type F device, which was subjected to a sequential air then methane annealing process, indicate that the order of processing is of critical importance. The data for the type G device confirms that the methane cannot be replaced by an inert species, indicating that a chemical or physical process is involved and that it is not sufficient simply to heat a device in an atmosphere which prevents oxidation and may reduce surface desorption. The characteristics of the type H device show that the correct steps taken in the correct order will fail if interrupted by a processing step which cannot itself be anticipated to significantly modify thin film diamond.

Together these experiments indicate that the methane interacts with the diamond resulting in a greatly increased conductivity. It is not clear whether the interaction takes

the form of a modification of the material at the pre-existing surface of the diamond, or the deposition of new material. The latter is thermodynamically more likely as the temperature involved is less than half that which would be required to break existing carbon-carbon bonds (§2.2). If deposition is occurring it might reasonably be assumed that the deposit is predominantly graphitic in nature as anticipated by figure (2.4); this is consistent with the noted conductivity of methane annealed samples. Graphite is known to oxidise readily at temperatures in excess of 350-400°C [6.8], from which it follows that air annealing after the methane treatment will result in the oxidation of graphitic deposits present on the surface, although this may not be the only process occurring at this time.

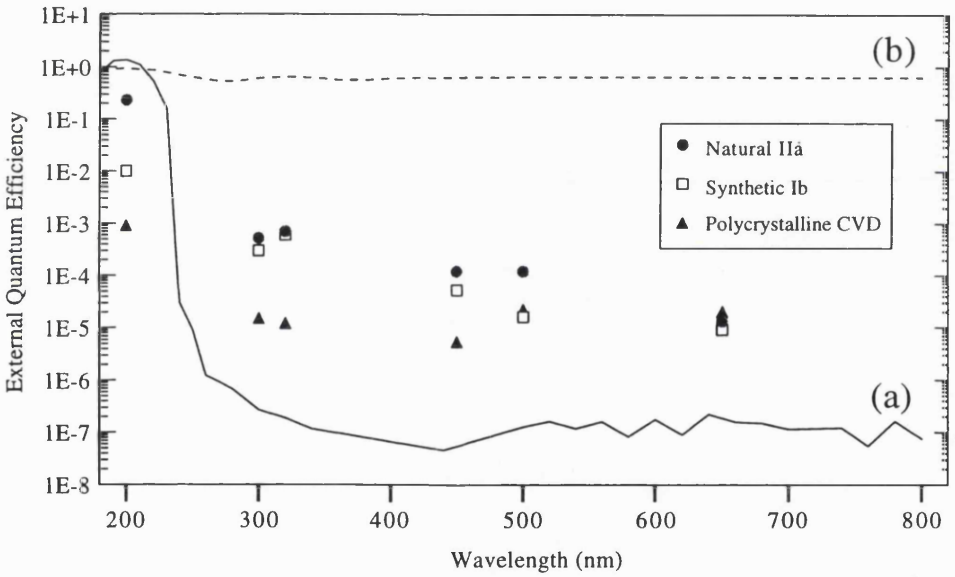

Figure 6.10: The gain (EQE) of different UV photodetectors. (a) fully processed type E device. (b) UV enhanced silicon photodiode. Natural, synthetic and CVD diamond detectors replotted from [6.6] as indicated (inset).

The photocurrent data for the fully processed E type device presented in figure (6.2(c)) has been inserted into equation (4.5) to obtain the photoconductive gain. Figure (6.10) shows this gain compared to the previously discussed results published by other researchers [6.9] (§3.2.3) for natural IIa, synthetic Ib and polycrystalline CVD diamond; the gain of a UV enhanced silicon detector measured under the same conditions is also shown.

In figure (6.10) it can be seen that both the gain and wavelength discrimination of the type E device exceed that of the best contemporary diamond detectors. The 200nm gain of the type E device is almost an order of magnitude greater than that of the natural IIa device and over three orders of magnitude greater than the CVD sample. Similarly, the 500nm (visible green) gain of the type E structure is respectively three and two orders of magnitude less than for the natural and CVD structures indicating highly effective rejection of sub-bandgap radiation by the type E detector. It is also evident that whilst the silicon photodiode is impressively efficient, it has a broadband response and cannot have an EQE that reaches or exceeds unity.

The favourable performance of the type E device compared to the best previously published results may be attributable to the optimised device geometry (§5.4.1), the post fabrication annealing process (§ 6.3) or a difference in the conditions under which the devices were tested. It is therefore informative to compare the devices in terms of established figures of merit, such as the effective mean carrier collection distance d (§2.6.2). Insertion of equation (5.8) into equation (5.12) to eliminate τ_T yields:

$$\mu\tau_l E = l\eta_{ext} \tag{6.7}$$

which is the same expression as equation (2.8), indicating that d may be calculated as the product of the gain η_{ext} and the electrode spacing l.

Values of d for the diamond detectors of figure (6.10) are presented below in table (6.2) from which it can be seen that the natural IIa device has a much greater mean effective collection distance than the other three structures. This can be interpreted as meaning that photocarriers travel further before recombination in the natural material than in the synthetic or CVD samples. The fact that the type E device achieves a substantially greater gain than the natural stone, despite having a lower d, indicates that the optimised structure of the former device more than compensates for the inferior quality of the thin film material in terms of overall carrier collection efficiency.

Sample	*Gain*	*E (V/cm)*	*l (μm)*	*$d=\mu_l\tau E$ (μm)*	*$\mu_l\tau(cm^2/V)$*
E	1.3486	200	25	0.33715	1.69×10^{-7}
Natural IIa	0.231	2857	350	80.85	2.83×10^{-6}
Synthetic Ib	0.001	2857	350	0.35	1.23×10^{-8}
Polycrystalline	0.0009	2857	350	0.315	1.10×10^{-8}

Table (6.2): The mean effective carrier collection distance d, $\mu_l\tau$ product and related parameters calculated at 200nm for the diamond photodetectors characterised in figure (9.10).

It will be noted however that the parameter d is substantially weighted by the applied electric field E which differs greatly between device structures. Elimination of E yields the mobility-lifetime ($\mu\tau$) product which is another widely accepted figure of merit used in the comparison of photodetecting materials [6.11]. The $\mu\tau$ products presented in table (6.2) show that whilst the natural diamond unquestionably possesses the best carrier transport properties of the tabulated samples, the type E processed device surpasses both the synthetic crystal and the previous best CVD sample by more than a factor of ten.

Having established that the type E process, combined with an optimised device geometry, will result in unprecedented performance from a thin film diamond detector in terms of dark current suppression, wavelength selectivity and the enhancement of gain, it becomes relevant to consider the maximum speed at which such detector can operate. A preliminary result presented as figure (6.11) indicates that as fabricated detectors are slow (plot (a)), to the extent that their practical applications would be severely limited. Plot (b) shows that after a type E treatment, the speed of response is dramatically improved to the extent that it becomes comparable to a natural IIa device of the type discussed above.

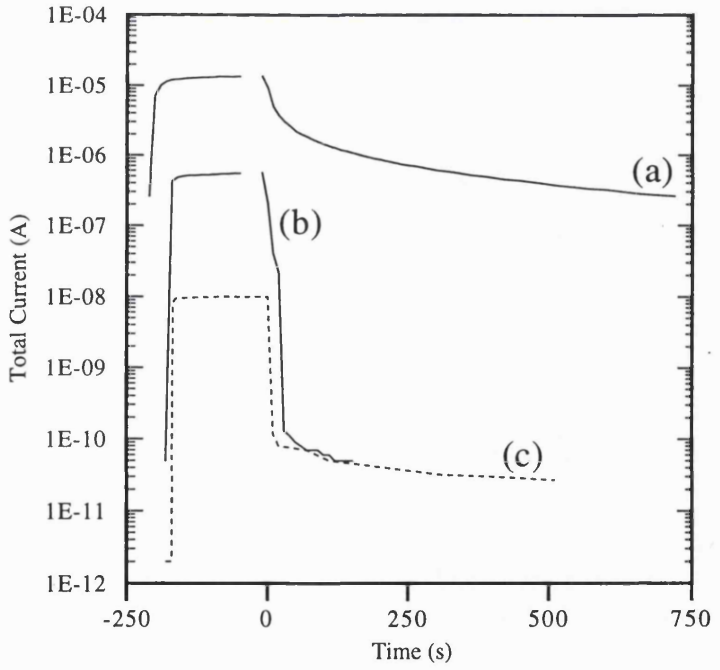

Figure 6.11: The speed of response of two diamond photodetectors under illumination at 200nm, 2.76×10^{-5} W/cm^2. (a) Type E device before any processing. (b) Type E device after methane-air processing. (c) Natural IIa device presented by Binari *et al.* [6.9].

A subsequent study undertaken in collaboration with another researcher [6.11] involved repeating the process using a range of methane pressures and air annealing times. It was found that following a type E methane anneal at 7mbar the visible response of a device could be further reduced by successive hours of air annealing up to three hours, after which although the visible response continued to diminish, there was a corresponding reduction in DUV sensitivity. When the methane annealing pressure was reduced to 1mbar the onset of reduced DUV response occurred after a single hour of air annealing, whilst a methane pressure of 0.1mbar led to a maximally suppressed sub-bandgap sensitivity after only fifteen minutes processing in air. These results indicate a clear relationship between the pressure of methane used during the first processing step and the air annealing time required to stabilise a device in the following process.

In a second collaborative investigation [6.12] it was found that the processing applied to device type E could also be used to effect an improvement in the characteristics of a type C device, although the enhancement was not as profound in this case. The dark current for a given bias potential was reduced by around two thirds, and an order of magnitude suppression was achieved in the photocurrent response at wavelengths in the range 250-800nm.

In terms of the specifications defined in (§5), a type E device represents a satisfactory level of performance, and indeed these structures have now been licensed to an industrial partner and are being sold commercially as discussed in a later section (§11). Further practical requirements can be defined however in relation to additional aspects of device performance such as sensitivity and speed, which will be addressed in the next chapter (§7). Further investigation is also required into the nature and mechanisms of the successful processing applied to device type E in order to optimise the deployment of this technique and determine its generality; this work is also undertaken in a later section (§8).

6.6 Conclusions

A sequential annealing process using methane and air has been identified which dramatically improves the dark current, speed and spectral response characteristics of DUV photodetectors made from polycrystalline thin film diamond, operating in the photoconductive mode. A dark current of <50pA has been demonstrated combined with a sharp wavelength cut-off at 225nm and a DUV-visible discrimination ratio of over six orders of magnitude. This level of performance from a device fabricated using

initially unpromising material surpasses all other known results, and has not been equalled by any outside laboratory since first publication by the author and co-workers (*Appl. Phys. Lett.* 67, 2117 (1995)). Further investigation is required to develop an insight into the mechanisms by which the process operates, approaches to which will be addressed in a later section (§8).

6.7 References

6.1 S.M. Sze, "Physics of Semiconductor Devices", Wiley, New York, 1981.

6.2 D.R. Kania, M.I. Landstrass, M.A. Plano, L.S. Pan and S. Han, Diamond and Related Materials 2, 1012 (1993).

6.3 D.L. Dreifus, "Passive Diamond Electronic Devices", in "Diamond: Electronic Properties and Applications", Ed. L.S. Pan and D.R. Kania, Kluwer Academic Press, Massachusetts, USA, 1995.

6.4 B. Baral, S.S.M. Chan and R.B. Jackman, Journal of Vacuum Science and Technology A 14, 2303 (1996).

6.5 P. Gonon, A. Deneuville, E. Gheeraert and F. Fontaine, Diamond and Related Materials, PRE-PRINT (1992).

6.6 K. Miyata and D.L. Dreifus, Japanese Journal of Applied Physics 33, 4526 (1994).

6.7 S. Evans, in "Properties and growth of Diamond" Ed. G. Davies, INSPEC, London, 1994.

6.8 H.O. Pierson, "Handbook of Carbon, Graphite, Diamond and Fullerenes: properties, processing and applications", Noyes Publications, New Jersey, 1993.

6.9 S.C. Binari, M. Marchywka, D.A. Koolbeck, H.B. Dietrich and D. Moses, Diamond and Related Materials 2, 1020 (1993).

6.10 R.H. Bube, "Photoelectronic Properties of Semiconductors", Cambridge University Press, U.K., 1992.

6.11 I. Davies, "An Investigation of UV Discrimination in Diamond Photoconductor Devices", MSc. Thesis, UCL, October 1995.

6.12 K.K. Soe, "Fabrication of Thin Film Diamond Ultraviolet Detectors", E740 3rd Year Project, Dept. Electronic & Electrical Engineering, UCL, May 1994.

7 IMPROVING THE SENSITIVITY AND SPEED OF CVD DIAMOND PHOTODETECTORS

7.1 Introduction

This chapter presents an investigation into ways in which the sensitivity and speed of photoconductive DUV detectors made from CVD diamond may be improved. Detectors which exhibit low dark current, wavelength selection and gain have previously been demonstrated (§6.5), and it has has been shown that annealing processes and an appropriate device geometry may be employed to overcome the non-ideal physical and electrical properties of contemporary diamond films. The inter-relationship between gain and bandwidth is discussed and experiments are undertaken to explore and illustrate this aspect of photoconductive device operation using a range of freestanding diamond films of varying crystallite dimensions.

7.2 Experimental Design

In the previous discussion of photoconductivity (§5.3.2) it was demonstrated through equations (5.9) and (5.12) that photoconductive gain is determined by the ratio of carrier lifetime τ_l to carrier transit time τ_T. It might therefore be assumed that material having a large value of τ_l will generally be preferred for photodetector applications.

The carrier lifetime, and hence the gain, can be enhanced by the use of material containing deep trapping centres [7.1]: because photoexcitation entails the creation of an electron-hole pair it is conceivable that one carrier type can become trapped whilst the other remains mobile. During the time that its 'partner' is trapped, the untrapped carrier will experience a reduced likelihood of recombination due to the reduced density of mobile opposite charges; it will therefore continue to traverse the device and circuit, contributing to the measured current flow. Once the trapped carrier is freed, the recombination probability reverts to the equilibrium value and the carrier pair will, on average, recombine after the balance of the trap-free lifetime has elapsed.

The above process has a profound impact on the transient response of a device because τ_l is the time constant which determines how long the photocarrier density will take to reach a steady state in response to a step change in illumination intensity. The filling and emptying of traps can be envisaged in terms of carriers being detained at defect centres for a mean trapping time τ_{trap} when illumination is first applied. Assuming that the excited photocarrier density exceeds the trap density, the traps will fill to a state of equilibrium at which point further trapping will occur only to replace thermally re-emitted carriers such that under constant illumination a steady state carrier density will be established. Following removal of the excitation, free carriers will recombine at their lifetime determined rate. Trapped carriers however will be released over a period controlled by τ_{trap} and will then decay over their free carrier recombination period resulting in a τ_l which has been extended by τ_{trap}. This process can cause a long, slow fall-off in photoresponse as exhibited by the CVD film described in figure (3.2).

In the simplest trap-free case of an intrinsic sample (ie: $\delta n=n$), the rate equation for carrier generation and recombination can be expressed as [7.2]:

$$dn/dt = G - n/\tau_l \tag{7.1}$$

where G is the generation rate and n/τ_l is the free carrier recombination rate.

When integrated with respect to time, equation (7.1) illustrates clearly the relationship between τ_l and the transient response of a photoconductor for both turn-on and turn-off [7.2]:

turn-on $$n(t) = G\tau_l\left[1 - \exp\left(-t/\tau_l\right)\right] \tag{7.2a}$$

turn-off $$n(t) = G\tau_l \exp\left(-t/\tau_l\right) \tag{7.2b}$$

from which it can be appreciated that any increase in τ_l by a period τ_{trap} will correspondingly increase the time taken for the device to switch on or off.

The above discussion leads to the concept of a 'gain-bandwidth' product such that an improvement in the sensitivity of a detector must result in a reduction in the fastest transient which the device can reproduce. The use of the term 'bandwidth' lends clarity to the discussion by treating the photodetector as a current amplifier. Under relatively low bias and illumination conditions as applied in the experiments presented to date, the precise value of this limit would be very difficult to anticipate theoretically. Both the carrier lifetime and the mobility are influenced by factors including the carrier density (and hence illumination intensity) and temperature as well as the quality of the material employed and device geometry. At high bias levels which approach the dielectric breakdown strength (§2.4.4), the creation of space-charge within the semiconductor leads to a capacitance related gain-bandwidth product which sets a fundamental upper limit for the material [7.1].

Despite the dramatic improvements in detector performance which can be effected by application of treatment E, a recalculation of equation (6.1) for the fully processed E type device of the previous chapter indicates an intrinsic carrier concentration of $\approx 3.7 \times 10^5 cm^{-3}$. This suggests that available films will be unable to sustain the anticipated maximum field of $\approx 10^7 V/cm$ quoted for diamond [7.3] and that attempts to determine the breakdown related gain-bandwidth product empirically are therefore unlikely to have a useful degree of generality at present.

Several approaches can be envisaged to improving the sensitivity (gain) and response speed of devices based around the type A format. Thicker films having a larger growth surface crystallite size could be expected to more closely approximate natural IIa material: such films would be anticipated to offer a larger $\mu\tau$ product as illustrated in the previous chapter, which could be combined with an electrically efficient electrode spacing to achieve a device exhibiting high gain but slow response. Conversely, a small

grained film, containing many defects, stacking faults and grain boundaries would be expected to facilitate extensive recombination resulting in a rapid response time but low gain.

Although the use of very high fields in existing devices is likely to lead only to catastrophic breakdown, equation (5.8) indicates that increasing the bias applied to a device will reduce the carrier transit time τ_T and may therefore increase the speed of operation of a low-trap density semiconductor. Any such improvement should be directly at the expense of the gain according to equation (5.9)

Figure (6.11) and the accompanying discussion (§6.5) offered a preliminary indication that type E processing could improve the switching speed of a device compared to the unprocessed case. On the basis of these initial results it is reasonable to conclude that further processing of the imperfect diamond film may lead to further passivation or repair of active defects and hence lead to further improvements in device performance.

7.3 Experiment

Photoconductors having standard 25μm gold surface electrodes were fabricated according to the previously described methods (§4.2) on three wafers of freestanding MPACVD diamond films to yield four device types labelled J, K, L and M as indicated in table (7.1). Optical micrographs of the three wafers bearing the interdigitated electrode structure are presented in figure (7.1) as labelled; in all cases Raman scattering (§4.4.3) showed a strong feature at 1332cm^{-1} on a featureless background similar to figure (5.3) indicating good quality diamond. All devices were subjected to type E processing (§6.3) after fabrication and before testing to reduce the dark current and improve both the gain and wavelength selectivity. Type L was serially subjected to four cycles of type E processing in order to accentuate any changes which might arise from such iterative treatment.

Sample	*Mean Grain Size*	*Thickness*	*Processing*
J	10-30	70	single type E
K	20-40	110	single type E
L	20-40	110	four cycles of type E
M	40-60	280	single type E

Table (7.1): The three types of MPACVD diamond wafer on which photodetectors were fabricated.

Dark current and photocurrent analysis (§4.5.1, 4.5.4) were undertaken at a range of bias potentials, and the speed of response was investigated using a mechanical shutter mechanism and a digital data store (§4.5.5). The shutter was triggered manually to expose the devices to twenty second periods of illumination at 200nm with the photoresponse current being recorded using the K487 unit (§4.5.1) operating in the fast data-logging mode to achieve a sampling interval of 100ms.

The crude experiment which had yielded the initial transient response of the previous chapter relied upon a manually operated sliding shutter which could not be easily opened and closed. Consequently, the results were believed to represent a convolution of the true detector response speed and the operator's reflex, leading to an understatement of the real switching potential of a diamond device. This view is supported by the unusual shaping which is apparent on both the pre- and post-processing 'off' transients presented. The precise switching speed of the shutter mechanism used for the present experiments could not readily be separated from the response speed of the electrical measurement system, however a calibration exercise using a fast silicon photodiode indicated the overall system response to be in the order of milliseconds and therefore negligible compared to the measured detector response and sampling interval.

Insertion of the shutter mechanism caused the DUT position for pulse response experiments to be 50mm further from the light source than for spectral response work. The incident light intensity was correspondingly scaled to ensure accuracy and consistency with previous gain calculations. The closer DUT site was treated as a point source radiating into a hemisphere of diameter 10mm from which surface the resited DUT collected photons over an active area of $2mm^2$.

A follow-up experiment was conducted in which a type L device was subjected to three further cycles of type E treatment and then evaluated under 10ms (nominal) pulses of 200nm excitation which executed automatically on a single trigger event. Data logging in this case was achieved using the buffered digital storage oscilloscope arrangement (§4.5.5).

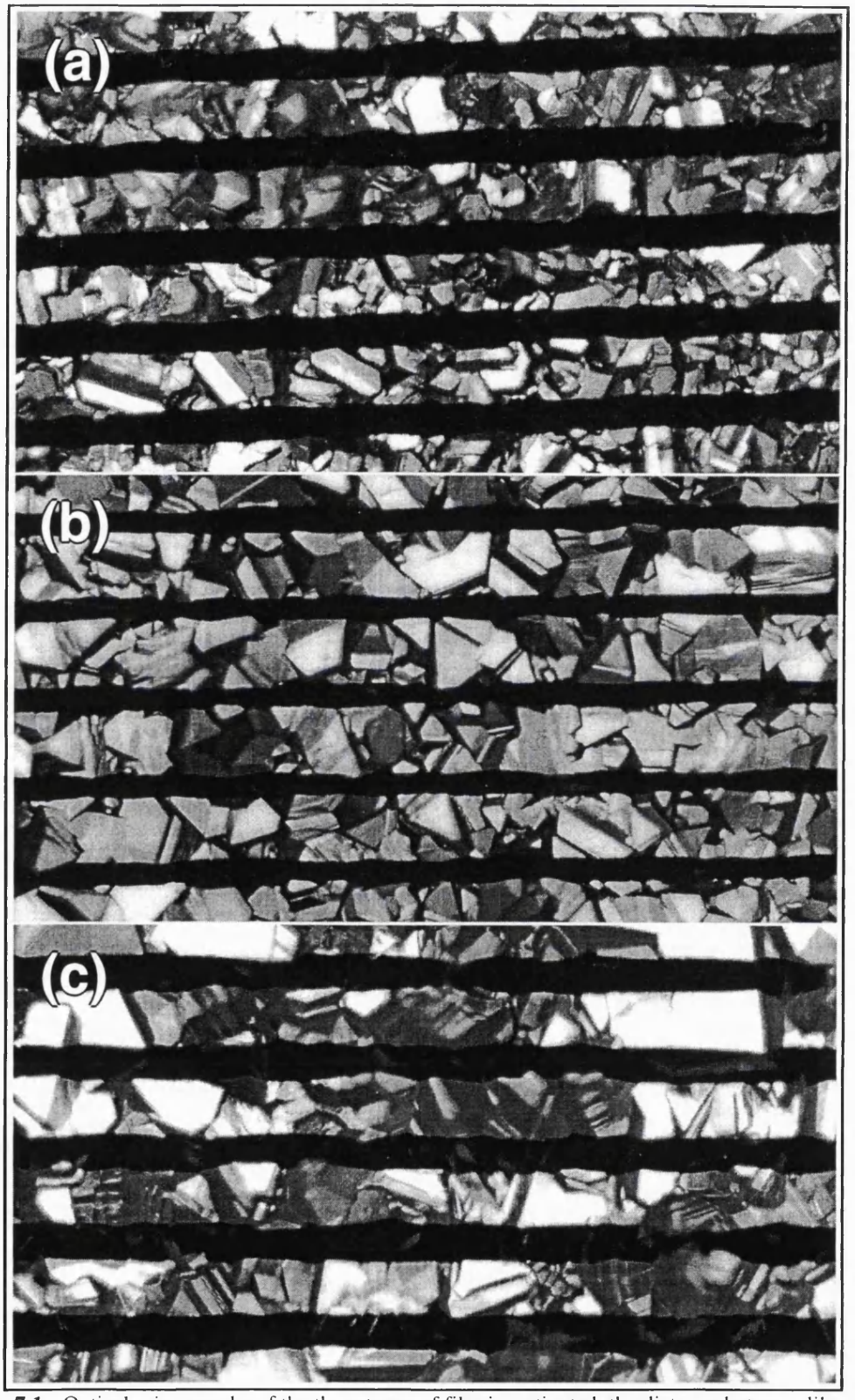

Figure 7.1: Optical micrographs of the three types of film investigated, the distance between like points in the gold electrode structure is 50μm. (a) Type J 'small' crystallites. (b) Types K and L 'medium' cxrystallites. (c) Type M 'large' crystallite size.

7.4 Results

After type E processing, all four device types yielded a large photocurrent under bandgap illumination and showed little response to longer wavelengths, consistent with the responsivity anticipated by figure (6.2) and equation (3.1). The dark current of each device type after full processing is shown in the log-log plot of figure (7.2). It can be seen that all device types exhibit very low conductivity and that at 10V the most conductive device has a resistance of >100MΩ.

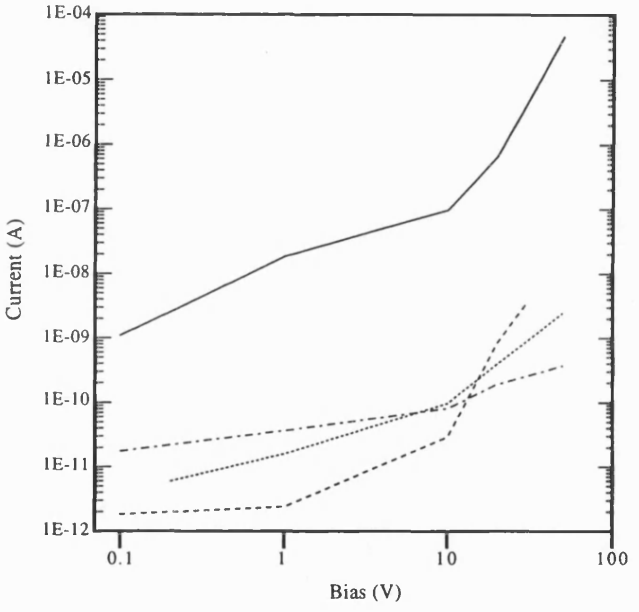

Figure 7.2: Dark current data for the four device types processed as described in table (7.1). Type J: dotted. Type K: dashed. Type L: dot-dashed. Type M: solid.

Surprisingly, the most conductive devices throughout this stage of the investigation were those on the large grain type M material, which were expected to be highly resistive on account of the low grain boundary density and known crystallite quality. Difficulties in achieving successful lithography on the type M material meant that small short circuits between finger electrodes had to be accepted during fabrication; these were subsequently broken by 'fusing' with a current of several amps. Although this technique created the open circuit required to continue the experiment, the resulting effective electrode spacing was much less than the specified 25 microns: this is believed to account for the higher than anticipated dark current.

Based on measurements of saturated (or near saturated) photoresponse current under 200nm illumination at a range of bias potentials, the gain of each device type determined using equation (4.5) is presented in figure (7.3). It is clear that each device type exhibits a linear relationship between gain and bias as fully anticipated (§5.3.1) by the model of a resistor which is conductivity modulated by the photoexcitation of carriers.

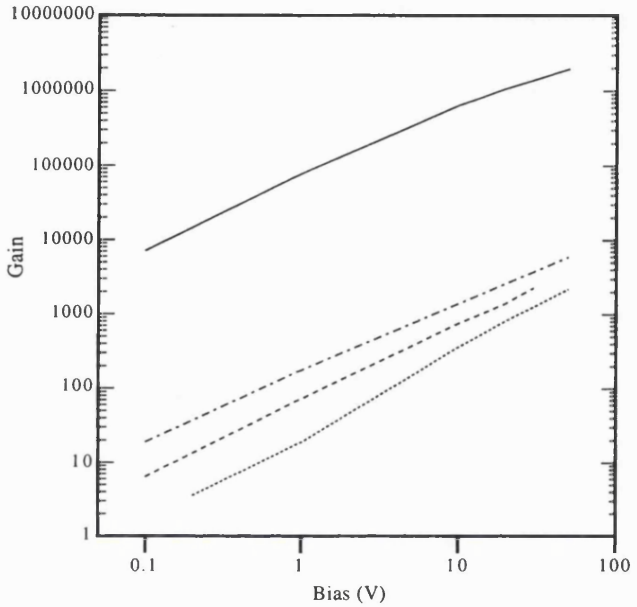

Figure 7.3: The bias dependant gain of the four device types processed as described in table (7.1). Type J: dotted. Type K: dashed. Type L: dot-dashed. Type M: solid.

Figures (7.4) to (7.7) illustrate the transient photocurrent response of a device of each type J, K, L and M respectively. In each case part (a) presents the true total current passed by the device, with log-lin axes serving to indicate the varying amplitudes of both dark and photocurrent and confirming the results of figures (7.2) and (7.3). The large current passed by the type M device is particularly clear from this form of plot. Part (b) of each figure represents the part (a) data as a normalised linear plot, facilitating a comparison of the shape of the transient characteristics. In the context of this study a device is 'on' when the photocurrent has reached 90% of the peak level attained during the 20 second exposure, and 'off' when the response has fallen to 10% of the peak value. Upper and lower deciles are marked, from which response times are derived in the following section (§7.5). The 10 ms response of the optimised type L device to a 10ms pulse of 200nm illumination is presented in figure (7.8) along with reference responses for the test system and a high gain type M device.

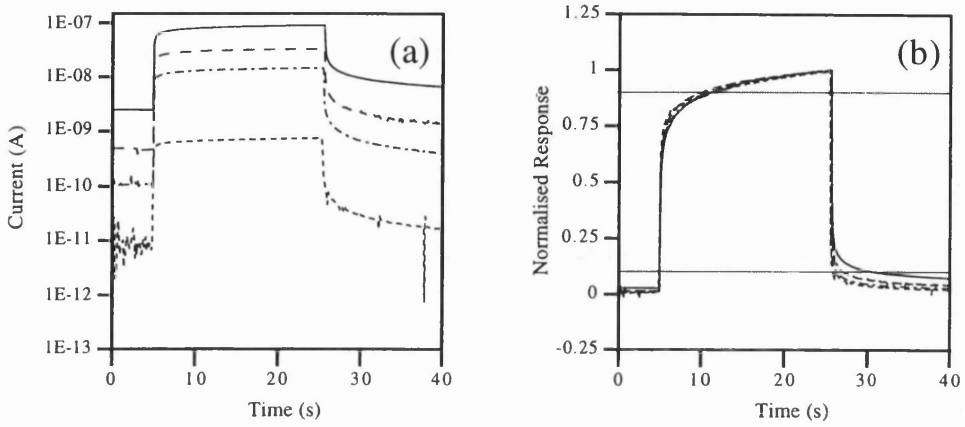

Figure 7.4: The temporal evolution of the photocurrent in a type J device under a 200nm, 20s excitation at a range of bias potentials (a) Total current. (b) Normalised current, upper and lower deciles marked. 1 volt: dashed. 10 volts: dot-dashed. 20 volts: course dashed. 50 volts: solid.

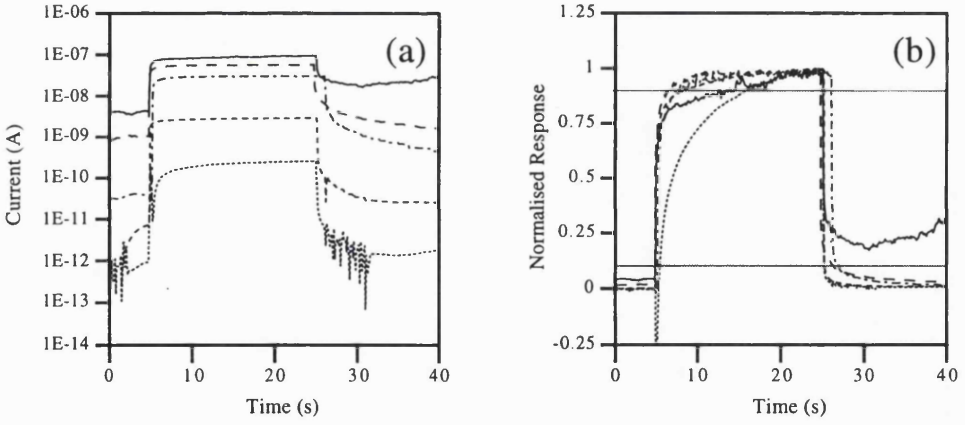

Figure 7.5: The temporal evolution of the photocurrent in a type K device under a 200nm, 20s excitation at a range of bias potentials (a) Total current. (b) Normalised current, upper and lower deciles marked. 0.1 volt: dotted. 1 volt dashed. 10 volts: dot-dashed. 20 volts: coarse dashed. 30 volts: solid.

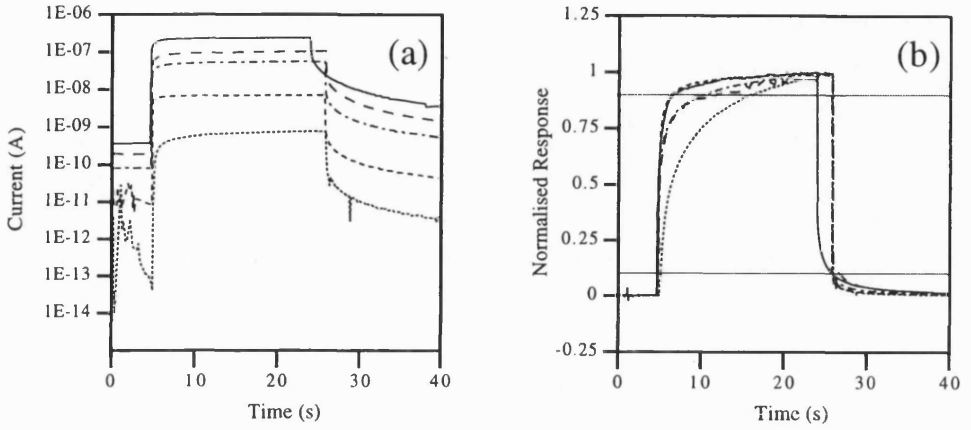

Figure 7.6: The temporal evolution of the photocurrent in a type L device under a 200nm, 20s excitation at a range of bias potentials (a) Total current. (b) Normalised current, upper and lower deciles marked. 0.1 volt: dotted. 1 volt dashed. 10 volts: dot-dashed. 20 volts: coarse dashed. 50 volts: solid.

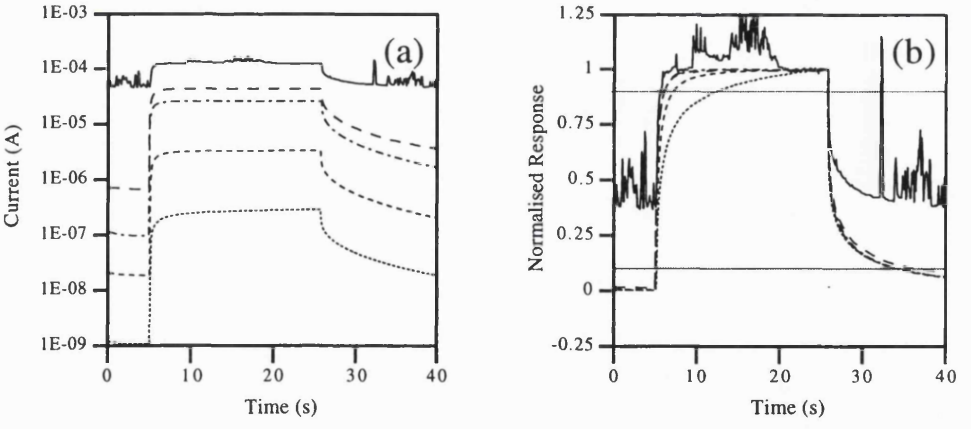

Figure 7.7: The temporal evolution of the photocurrent in a type M device under a 200nm, 20s excitation at a range of bias potentials (a) Total current. (b) Normalised current, upper and lower deciles marked. 0.1 volt: dotted. 1 volt dashed. 10 volts: dot-dashed. 20 volts: coarse dashed. 50 volts: solid.

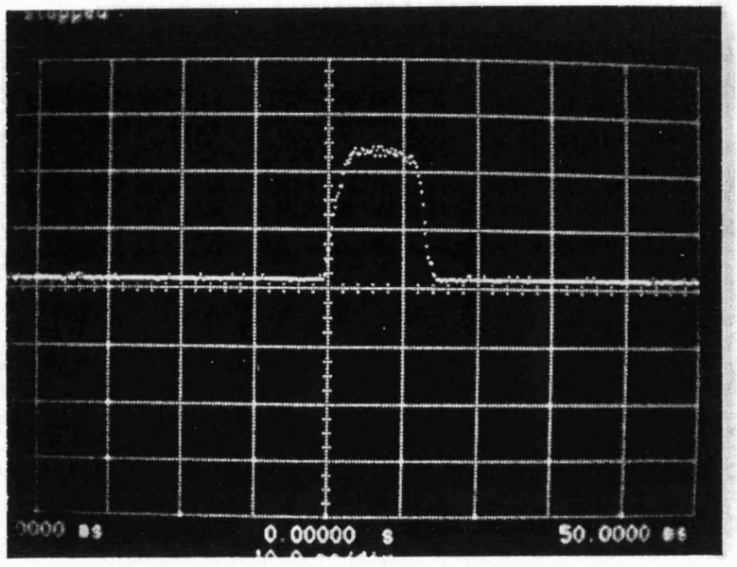

(a)

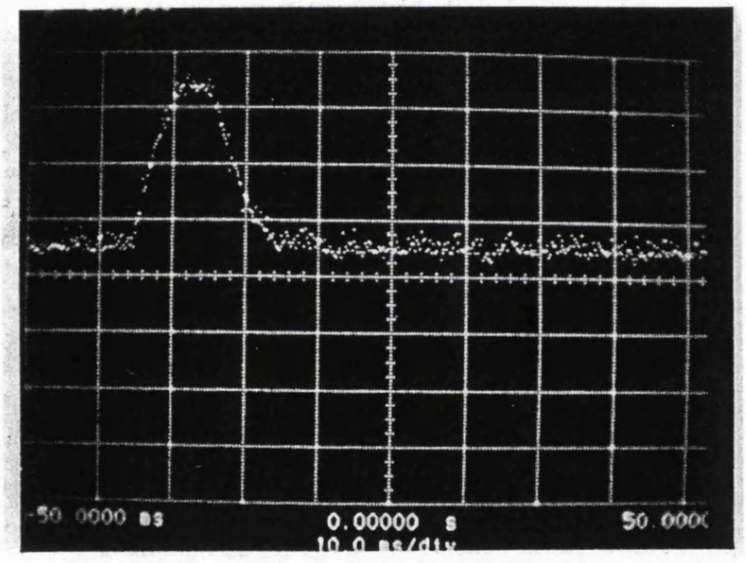

(b)

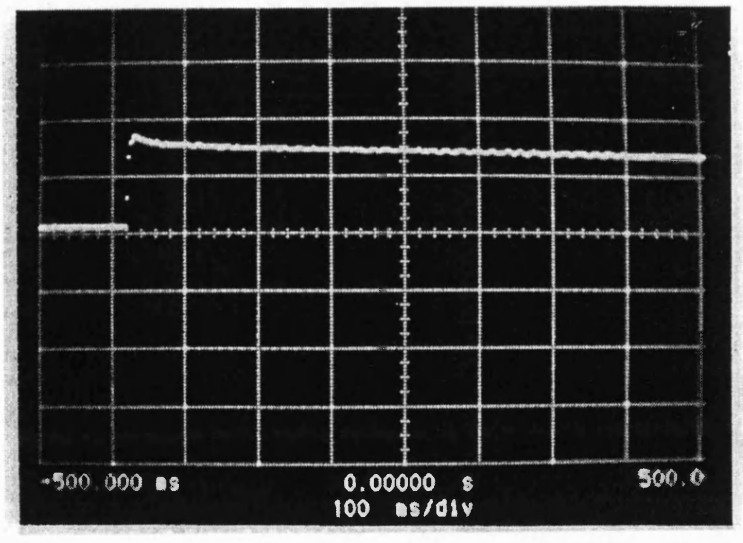

(c)

Figure 7.8: The temporal response of a type L device to 10ms (nominal) of 200nm illumination after a total of seven cycles of type E treatment. (a) System response. (b) Response of the optimised type L device. (c) Response of a high gain type M device.

7.5 Discussion

Reference to the dark current characteristics of figure (7.2) suggests that two separate conduction mechanisms operate at different bias levels. It may be surmised that under low bias conditions, grain boundary conduction is the controlling component of the total dark current, whilst at higher fields a combination of impurity conduction and space charge limited current become dominant. It will be noted that the onset of the high field conduction mechanism in the identically processed J, K and M device types occurs at around 10-20 volts, whilst the iteratively treated type L device exhibits a smaller low field conductivity and a lower threshold potential for onset of the higher current regime. This is consistent with the expectation that type E processing reduces the dark current by reducing surface and grain boundary conduction effects. The fact that at higher bias potentials the type L device passes a higher dark current than the corresponding singly processed type K device could indicate that the heat treatments have a cumulative effect of increasing or activating electrically active inter-grain impurities or defect centres. Such an effect would suggest that an optimum number of treatment cycles could be identified to achieve a maximum improvement in overall device performance.

Superficially, the gain characteristics plotted in figure (7.3) would appear to indicate a strong correlation between the sensitivity of a detector and the properties (grain size and processing) of the material from which it is made. Reference to figure (7.1) however indicates that device geometry must also be expected to exert an influence over sensitivity. Because the same nominal electrode spacing of 25μm was defined on each sample type regardless of grain size, it is clear that in terms of the pseudo single crystallinity effect (§5.4.1) a type L device will be more electrically efficient than a type J structure. Furthermore, it can be seen that the over-development and over-etching required to eliminate short circuits from the 'valleys' between electrodes has resulted in a loss of uniformity in the width of the finger electrodes on the different samples.

Concerted attempts at fabricating 10μm fingers having a 20μm pitch on type J and K samples were unsuccessful, indicating that processing considerations dictate a minimum mask resolution (and hence nominal device resolution) of 25μm for the diamond films which have been identified as being most suitable for photodetector fabrication (§5.6). As such, the devices presented can be described as having 'minimum practical electrode spacing', within which specification the type M device is clearly the most efficient at all bias levels investigated. It is also clear from figure (7.3) that the type L device exhibits greater gain at a given bias than the singly processed type K structure fabricated from

the same material. This indicates that repeated applications of the type E treatment to a sample can lead to incremental improvements in sensitivity, although this may be at the expense of dark current suppression as discussed above.

The transient response characteristics of figures (7.4) to (7.7) show considerable variations in switching time, both between device types and for a single device under different bias conditions. Whilst the true current data of part (a) in each figure indicates the sensitivity of the DUT in terms of the magnitude of the photoresponse current, the normalised data of part (b) offers a measure of switching speed and provides an insight into the switching characteristics that a detector could be expected to display if operated as a component in a suitably designed electronic circuit.

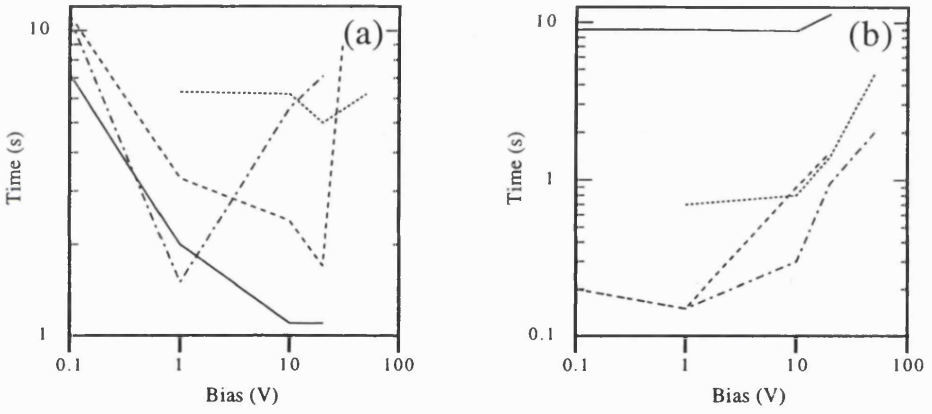

Figure 7.9: Speed of response: transition times between 10% and 90% of saturated value under 20s of 200nm excitation. (a) The turn-on time as a function of bias for each device type and (b) The turn-off time as a function of bias for each device type.
Type J: dotted. Type K: dashed. Type L: dot-dashed. Type M: solid.

It is clear from the (a) plots that in no device type at any bias level investigated did the photocurrent decay to its pre-excitation level within fifteen seconds of the optical excitation being removed. It is also evident that the only device configuration to saturate into the on condition during the 20 second exposure period was the type M device when biased at 10 volts or greater. The part (b) figures demonstrate that complete turn-off is not necessary for practical detection of a switching event as the 'tail' of persistent conductivity is seen to approach the noise level in a linear plot. This approximation cannot however be so generally applied to the slow turn-on of high trap density material exemplified by figure (7.4(b)), as deployment of the detectors for

quantitative analysis of the intensity of an excitation source requires that the amplitude of the output signal should rapidly reach a steady state level proportional only to the intensity of the applied illumination. The 10% to 90% transition periods have been extracted and plotted as functions of bias in figure (7.9) where turn-on time is plotted in part (a) and turn-off in part (b).

Together the pulse response and transition time graphs suggest that the generation and recombination of carriers in the devices investigated is not as simple as the process described by equations (7.2). In particular it will be noted that the evolution and decay of the photocurrent appear to occur over very different periods of time, with turn-off being much slower than turn-on, whereas theory anticipates that τ_l should be the controlling time constant in both cases. This disparity is believed to be due to re-trapping [7.2] during turn-off causing carriers to persist in the material for periods greatly in excess of the trap-free lifetime τ_l.

Figure (7.9(a)) shows that turn-on for all device types is slow under low bias conditions, indicating that the field is insufficient to achieve a rapid carrier transit time and that extensive spontaneous recombination reduces the free carrier density and hence retards the filling of traps to a steady state level; this view is supported by the relatively small gain exhibited under low bias as shown in figure (7.3). As the bias is increased in figure (7.9(a)) the turn-on time is seen to decrease, indicating efficient separation of electron-hole pairs and a reduced transit time, however further increases in bias potential lead to an increase in turn-on time. This deterioration may be attributable to induced space charge opposing the applied bias or increasing recombination, as the onset of the condition occurs for each device type at approximately the same potential at which the dark current was observed to increase in figure (7.2).

The turn-off times for each device type are seen in figure (7.9(b)) to be at their fastest under the low bias conditions which favour free carrier recombination, with the turn-off becoming slower as the increasing bias facilitates lifetime enhancement through retrapping. It therefore becomes apparant that a high bias level is required for high gain, rapid turn-on operation but that a low bias is required for rapid turn-off as the turn-off period in trap containing material is extended by the same conditions which enhance the gain and turn-on characteristics of the device.

To illustrate more clearly the trade-off between gain and switching speed in the devices investigated, the gain of each detector has been plotted as a function of inverse turn-off time in figure (7.10). This form of time axis has been selected to preserve the

convention that desired performance is represented in the sense of increasing location in the left-right direction. In the case of a single trapping level, an exponential curve could be fitted to the decay characteristic and the gain plotted against time constant [7.4], however attempts at curve fitting the present results indicate that the measured transient represents the superposition of several simultaneous processes involving different trapping centres which are only anticipated to be separable by intensive numerical methods disproportionate to the current requirement [7.5, 7.6].

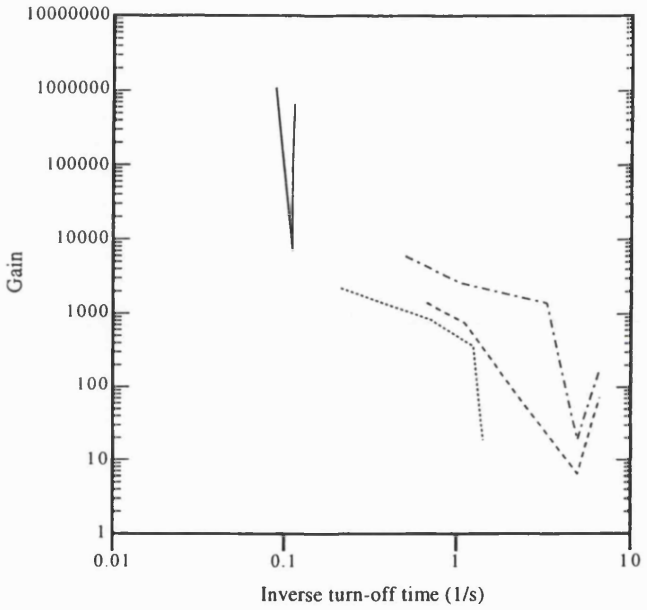

Figure 7.10: The gain of each device type plotted as a function of inverse turn-off time. Type J: dotted. Type K: dashed. Type L: dot-dashed. Type M: solid.

Reference to figure (7.10) confirms the discussion of (§7.2) which anticipated a trade-off between gain and speed of device operation. Although some recovery in gain appears to be possible at very high switching speeds in the K and L type devices, it should be noted that these results refer to low bias operation and cannot therefore be extrapolated to higher gain/t^{-1} values as the absolute response signal amplitude will become vanishingly small at ultra-low bias potentials.

The material hypothesis of (§7.2) is also confirmed in figure (7.10) which indicates that the small crystallite, high grain boundary density type J device is relatively fast but exhibits low gain whilst the mid grain size type K device is slower but more sensitive

and the large grain type M device is slow but very sensitive. This result demonstrates that diamond photodetector performance characteristics can be engineered through the careful selection of substrate material combined with a minimum practical electrode spacing and the application of type E processing.

The successful enhancement of a type K device by repetitive type E processing is clearly apparent in figure (7.10) which shows the type L structure to exhibit a higher gain for a given turn-off time than any other detector tested. The turn-off time achieved by this device of 0.3s at 10 volts compares favourably with the results reported by Vaitkus *et al.* [7.7] reproduced in figure (3.2) which took several minutes to turn off under a bias of 200 volts and a slightly lower illumination intensity than applied in the present study.

After further processing (§7.3) the response of the type L detector can be seen in figure (7.8(a)) to saturate fully on and off within a period of 18ms in response to a 200nm pulse of nominal duration 10ms. Under calibration conditions the detector system yielded the output shown in figure (7.9(b)) indicating a marked deviation from the ideal step response. This can be attributed to the fact that the shutter mechanism did not operate in a single open/close action but as a moving slit which travelled across the region of exposure, thereby 'spreading' the excitation pulse across the DUT in both space and time. Consequently the shaping of the diamond detector transient represents a convolution of the shutter characteristic and the device response and cannot usefully be analysed, however the overall response of the modified type L device can be seen to exceed the system response by only 3ms. Whilst the data can only strictly be read as indicating a response time of ≈10ms, the above discussion suggests that the response to a perfect step stimulus would be somewhat shorter.

Whilst the response times presented above are substantially longer that the 0.1ns response to sub-bandgap illumination reported by Aikawa et. al [7.8] reproduced in figure (3.5), the present work represents the fastest saturated response to date for a diamond detector under bandgap excitation. Although no verifiable data is available, and no result is therefore claimed, informal comment from a commercial user supplied with a type L device for evaluation purposes indicates that a response time of between 0.5 and 0.6ns has been measured for bandgap laser excitation. The author's successor is currently pursuing means of reproducing this work for release into the public domain.

7.6 Conclusions

The speed and gain of photodetector structures fabricated from polycrystalline CVD diamond films displaying differing grain sizes has been measured. After gas ambient processing devices on all samples were found to be visible blind and exhibit low dark current in the order of nA or less combined with bias and material dependent photoconductive gain of over 10^6. Devices displaying the highest levels of gain have the slowest turn-off times as expected, whilst devices having moderate gain ($\approx$100) have been found to exhibit fully turned on/off switching times of <10ms which is the fastest reported response of any thin film diamond detector to bandgap illumination. Such performance offers compatibility with contemporary imaging technology such as CRT displays which require a refresh rate of 50Hz (20ms).

In addition to careful selection of CVD material and device design, the repeated application of previously discussed (§6) gas treatments has been demonstrated to result in greatly enhanced device performance.

7.7 References

7.1 A. Rose, "Concepts in Photoconductivity and Allied Problems",Wiley Interscience, New York, 1963.

7.2 R.H. Bube, "Photoelectronic Properties of Semiconductors", Cambridge University Press, U.K., 1992.

7.3 M.W. Geis, Proceedings of the IEEE 79, 669 (1991).

7.4 N.V. Joshi, "Photoconductivity: Art, Science and Technology", Marcel Dekker Inc., New York, 1990.

7.5 N.V. Joshi and J.M. Martin, Physics Letters 113A, 318 (1985).

7.6 N.V. Joshi, Physical Review B 27, 6272 (1983).

7.7 R. Vaitkus, T. Inushima and S. Yamazaki, Applied Physics Letters 62, 2384 (1993).

7.8 H. Yoneda, K. Ueda, Y. Aikawa, K. Baba and N. Shohata, Applied Physics Letters 66, 460 (1995).

8 THE ORIGINS OF THE IMPROVEMENT ACHIEVED IN THE PERFORMANCE OF CVD DIAMOND PHOTODETECTORS

8.1 Introduction

This chapter presents an insight into the characteristics of the 'type E' process which was developed in the preceeding chapters (§6,7). The process is investigated in terms of the nature of the changes it induces in CVD diamond devices and the 'hardness' of these changes under conditions of elevated temperature and ionising radiation. The surface and near-surface spectroscopic techniques of photoluminescence and Auger electron spectroscopy are employed to gain information on the presence of signature-bearing defect centres and surface bonding characteristics respectively. On the basis of these observations, a possible mechanism is proposed by which the process may be operating.

8.2 Experimental Design

The type E process as described in table (6.1) was found in (§6.4.1) to be capable of effecting unprecedented improvements in the performance of a standard 25μm gold photoconductor (§5) on freestanding polycrystalline CVD diamond. After processing, the dark current passed by such a device was observed to decrease from ≈1μA at 0.5V to ≈50pA under the same bias. Simultaneously, the process was found dramatically to enhance the wavelength discrimination of the photodetector, substantially supressing the sensitivity to wavelengths corresponding to sub-bandgap absorption so that a discrimination ratio of more than six orders of magnitude is achieved between visible wavelengths and the 180-225nm bandgap response.

In (§7) the type E process was successfully redeployed to improve the 200nm sensitivity and speed of response of a similar detector, with evidence that repetitions of the process are capable of effecting further improvements in the performance of the target device.

Despite the evident success and utility of the process it remains unclear how, or indeed why, it should work as it does. There is no immediately obvious mechanism by which the conditions described in table (6.1) should lead to the dramatically improved device characteristics summarised above. It is not within the scope of the present study fully to characterise or explain the actions and mechanisms of the type E process: indeed a subsidiary research programme has recently been launched in which another researcher will conduct such an investigation over a three year timescale. Instead it is intended to investigate specific aspects of the nature of the treatment by evaluating samples which have been subjected to the processing, and thereby to build a picture of a likely mechanism of operation. It is anticipated that the proposed hypothesis may be tested by subsequent researchers using more sophisticated apparatus than is presently accessable to this author.

Based on the bonding and structure of diamond as discussed in (§2.2) it is unlikely that the moderate temperatures and gas ambients employed during process E could be capable of effecting any modification to regions of pure sp^3 bonded diamond within a target film. Equally, it is noted that the unwanted device characteristics which process E surpresses cannot be associated with good quality diamond: it has previously been demonstrated that high dark conductivity and sub-bandgap absorption are not exhibited by the pure material (§3.2.1 and §6.2). It is therefore apparent that the compromising regions of a device, and hence the regions upon which the type E process operates must

consist of non-diamond material. If they are not diamond then such regions must consist either of non-diamond bonded carbon phases (NDC) (§2.6.2) or of elements other than carbon. Some aspects of the latter case are considered in a later chapter which addresses the issue of impurity doped detectors (§9), however the films analysed to date have all been the products of known-clean reactor systems rendering NDC the most probable cause of compromised device operation.

Three regions within a freestanding polycrystalline diamond film can be anticipated to contain or consist of NDC; these are the nucleation region, the grain boundaries and the surface of the crystallites. Because of the design decisions taken in (§5.4.1) all the devices presented in this study have been fabricated on the growth surface of each film, using a planar electrode geometry. For this reason the presence of NDC at the nucleation surface can be discounted as a relevant factor in the present discussion. Some form of physical or chemical interaction is known to occur between the methane and the NDC as it has previously been demonstrated (§6.5) that the methane cannot be replaced by an inert species. The probable mechanism appears therefore to consist of either absorption or desorption at the exposed surface of the film or of in- or out-diffusion along the grain boundaries. The proposal that the improvements achieved by type E processing could arise due to surface effects leads to the question of how stable or 'hard' these improvements are. This issue is of particular importance because the surface of a device in use will typically be exposed to a wider range of conditions and more extreme enviroments than will ever be experienced by the bulk of a sample.

Taking the above discussion as a starting point, a series of experiments was proposed in which the nature and stability of the type E processing could be evaluated. The stability of samples which had been enhanced by the process was investigated by examining the variation in device performance when operated at elevated temperatures, and by exposing devices to an extended dose of ionising radiation. The latter experiment being intended also to serve the subsidiary purpose of determining the radiation hardness of CVD diamond devices for possible harsh environment operation (§3.3.2).

8.3 Experiment

8.3.1 Types of Experiment Undertaken

Replicates of the type E device were fabricated for electro-optic analysis using identical freestanding undoped polycrystalline CVD diamond tiles to those previously described (§5, 6), these were labelled type N as indicated in table (8.1). Additional samples of the same material were cleaned and/or subjected to type E processing but were not metallised as electrical contacts were not required for the spectroscopic studies. These samples were labelled as types P, Q and R as indicated.

Sample	*Acid Clean*	*Process E*	*Metalised*	*Description*
N_T	Yes	Yes	Yes	Spectral testing up to 300°C
N_R	Yes	Yes	Yes	Spectral testing before and after γ irradiation
P	Yes	No	No	Auger, photoluminescence
Q	Yes	Yes	No	Auger, photoluminescence
R	Yes	Methane only	No	Auger

Table (8.1): The processing applied to samples used to investigate the hardness and nature of the type E process.

8.3.2 Temperature Stability

Temperature testing of device type N_T was undertaken by attaching the device with a high temperature ceramic paste to a ceramic plate which supported a d.c. powered platinum heater strip. A chromel-alumel (type 'K') thermocouple was set into the paste to provide accurate temperature monitoring, whilst electrical contact to the mounted device was achieved by normal manual probing (§4.5.1). The spectral response of the device was recorded at room temperature, at 300°C and again at room temperature after cooling. The dark current of the type N_T device was also recorded at a range of temperatures. In total , the device was operated in excess of 400°C for over 5 hours.

8.3.3 Radiation Hardness

The radiation hardness of device type N_R was investigated by comparing the spectral responsivity and turn-off time of the device before and after exposure. The characterised device was exposed for 27 hours to a ^{60}Co source emitting equal quantities of 1.17MeV and 1.33MeV gamma radiation at a dose rate of 60kRad/hour.

This treatment was undertaken during a visit to CEA Saclay as part of an EU Alliance research collaboration in the field of diamond radiation sensors.

8.3.4 Auger Electron Spectroscopy

Auger Electron Spectroscopy (AES) was carried out in an Ultra High Vacuum (UHV) chamber using a Varian 981-2707 Cylindrical Mirror Analyser (CMA) and electron gun. An electron beam energy of 3kV was used throughout with a beam current of 1μA to minimise electron induced changes within the surface region.

8.3.5 Photoluminescence

Photoluminescence spectroscopy was undertaken as previously described (§4.4.4) using an argon ion laser operating at 476nm. Due to equipment limitations luminescence was recorded only in the spectral range 500-850nm (≈1.5-2.4eV) and therefore offered an insight into just under half the bandgap of diamond. This restriction was of little consequence however as other published works used later for comparison had investigated a similarly limited energy range.

8.4 Results

8.4.1 Temperature Stability

The dark current of device type N_T at room temperature and 150°C is presented in figure (8.1) which confirms that the device becomes more conductive at the higher temperature. Importantly however it is also clear that the after the device has been returned to room temperature the dark current is restored to a value very similar to its orginal level indicating that little or no permanent modification has occured. The differential spectral response (§4.5.3) of the device at room temperature, 150°C and 300°C is plotted in figure (8.2); whilst it has not been possible to calibrate this data into A/W, the arbitrary units employed are dimensionally the same as A/W (device current/illumination intensity) and differ only by a small linear multiplier. Subtle changes in the differential spectral characteristics can be observed between plot (a) obtained at room temperature, plot (b) obtained at 150°C and plot (c) obtained at 300°C and a small increase in photocurrent is apparent across all wavelengths; macroscopically however there is little material difference between the shape of the two plots. Plot (d) indicates that after returning to room temperature, the deep UV sensitivity of the device is unchanged from its initial condition. Some difference in the degree of rejection of longer wavelengths is evident on the log scale employed however

this is clearly not of the order of the sub-bandgap sensitivity exhibited by non process E devices as plotted in figures (5.11) and (5.12).

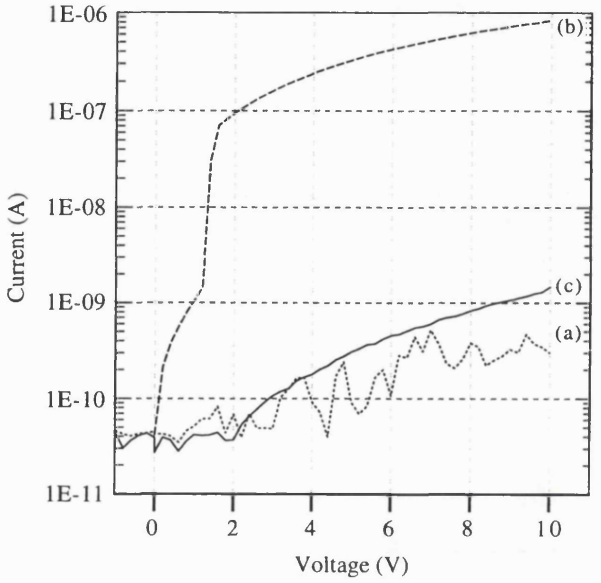

Figure 8.1: Dark current of a type N_T CVD diamond photoconductor fabricated by process E, operating (a) at room temperature, (b) at 150°C and (c) at room temperature following operation at 150°C.

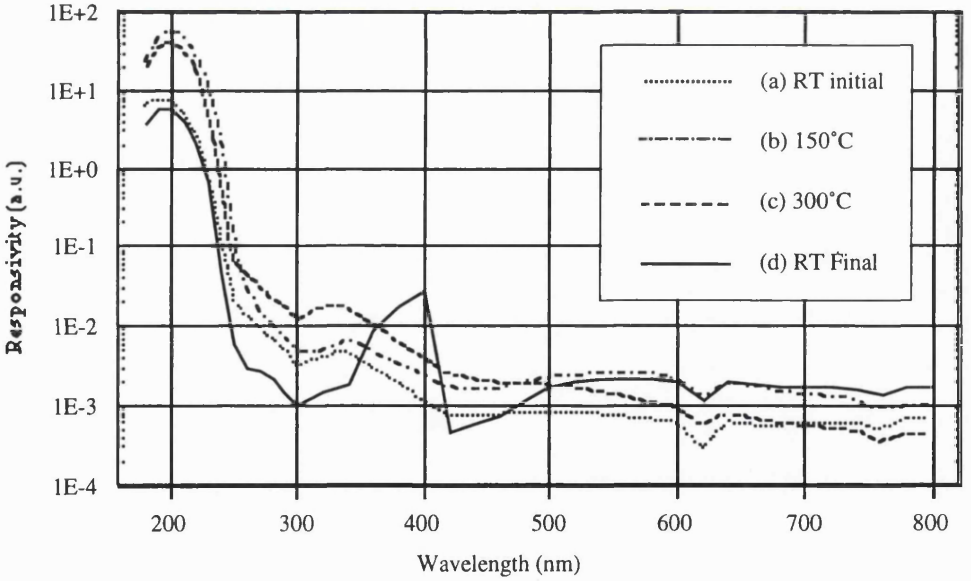

Figure 8.2: Spectral responsivity of a type N_T CVD diamond photoconductor fabricated by process E, operating (a) at room temperature, (b) at 150°C, (c) at 300°C and (d) at room temperature following operation at 300°C.

8.4.2 Radiation Hardness

The spectral response of device type N_R before and after exposure to an extended dose of gamma radiation is plotted in figure (8.3). It is clear that the major characteristics of sensitivity and UV selectivity exhibited by this device have not deteriorated as a result of the radiation dose applied. A small improvement appears to have occured in both the sharpness of the bandgap turn-on and the degree of sub-bandgap rejection exhibited. This may parallel the 'enhancement' of diamond device properties reported by Mainwood *et al.* [8.1, 8.2] (§3.3.2) following moderate doses of neutron irradiation however the differences reported here are too subtle to be regarded as significant without further repetitions of the work.

Further confirmation that the N_R device has not been significantly modified by the gamma radiation dose is evident in figure (8.4) which plots the turn-off time of the device in response to a pulse of 200nm UV illumination before and after exposure to the gamma source.

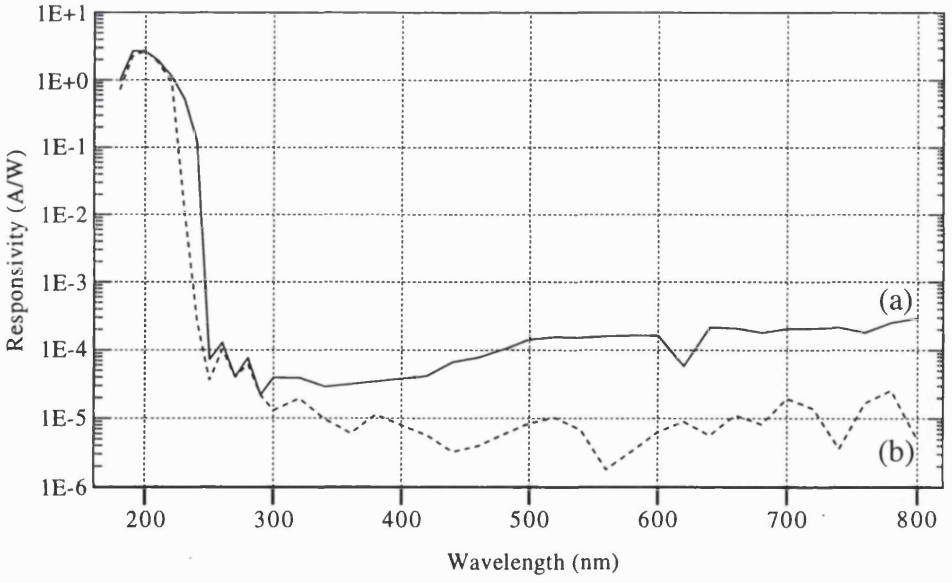

Figure 8.3: Spectral responsivity of a type N_R detector under 10V bias (a) before and (b) after exposure to a Cobalt 60 source emitting equal quantities of 1.17 and 1.33MeV γ rays to a total dose of 900KRad.

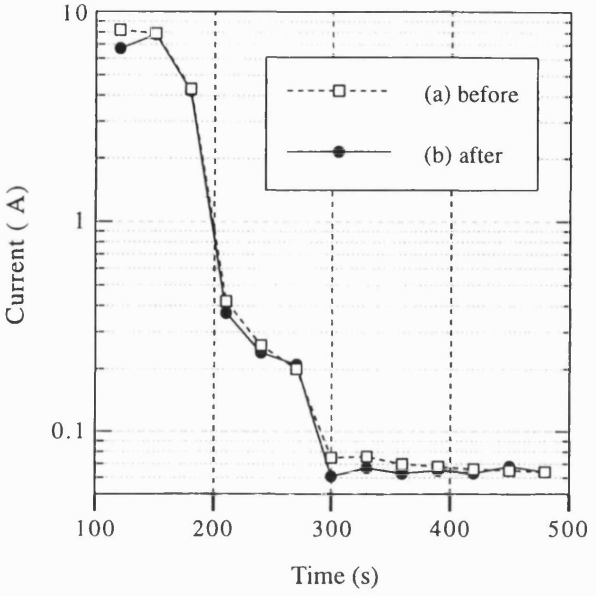

Figure 8.4: Speed of response to removal of a 200nm illumination source exhibited by a type N_R detector under 10V bias (a) before and (b) after exposure to a Cobalt 60 source emitting equal quantities of 1.17 and 1.33MeV γ rays to a total dose of 900KRad.

8.4.3 Auger Electron Spectroscopy

AES differential spectra recorded in the energy range 50-600eV (with a modulation of 5V) for the three sample types P, Q and R are shown in figure (8.5). In addition to a feature attributable to carbon at ≈270eV, another feature associated with oxygen at ≈514eV can be seen under some conditions. All 'as inserted' samples showed this peak however only on samples P and Q did the oxygen signal persist. On sample R which had only been methane treated it was significantly reduced after sample heating to 600°C *in vacuo*. Figure (8.6) shows higher resolution spectra recorded in the energy range 200-300eV (with a modulation of 2V) for each sample type following heat cleaning *in vacuo* prior to AES investigation. Significant variation in the structure of the peak attributable to carbon is evident. In the case of the untreated sample (spectrum (i)) a peak minimum occurs at 268eV with two peak maxima on the low energy side of the primary peak minimum. Similar structure is visible following type E processing (spectrum (ii)) but the higher energy of the two maxima is slightly decreased in intensity. The spectrum plotted as (iii) was recorded following methane treatment alone and is significantly different from (i) and (ii) in that the lower energy of the two maxima peaks is now the most intense and the primary peak minimum has shifted to 271eV. A new peak at 290eV is also apparent.

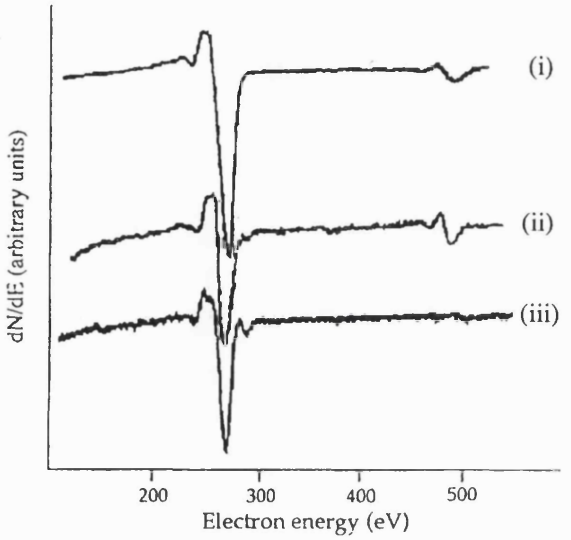

Figure 8.5: Auger electron specta of CVD diamond films treated as follows (i) type P acid cleaning only, (ii) type Q acid cleaning and type E processing and (iii) type R methane processing only.

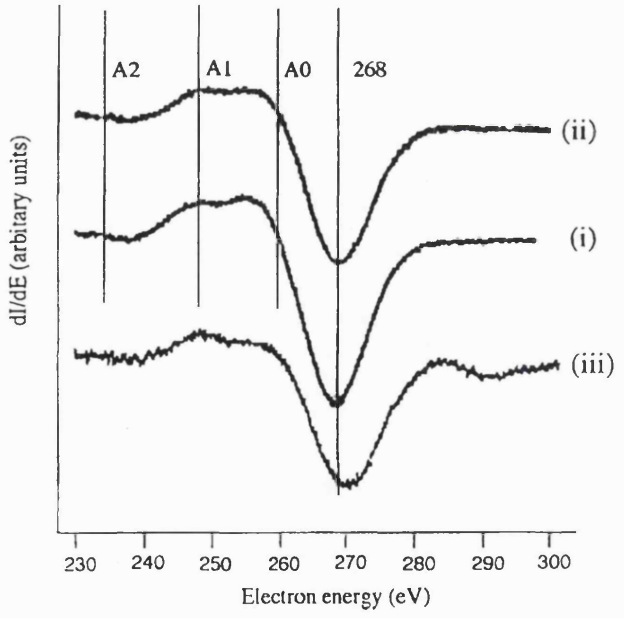

Figure 8.6: High resolution Auger electron spectra centred around the carbon KVV peak at ≈270eV of CVD diamond films treated as follows (i) type P acid cleaning only, (ii) type Q acid cleaning and type E processing and (iii) type R methane processing only.

8.4.4 Photoluminescence

Room temperature photoluminescence spectra for samples P and Q are presented in figure (8.7). For both samles a sharp feature centred at 1.68eV (737nm) is apparent along with a broad peak between x1.8 and 2.3eV (≈700-540nm). The 1.68eV peak has been identified in a number of studies of CVD diamond and attributed to a Si-vacancy defect [8.3, 8.4, 8.5, 8.6, 8.7, 8.8, 8.9]. The broad peak is commonly seen in PL studies of polycrystalline diamond films [8.3-8.9] but has not been clearly assigned. It is evident from figure (8.7) that type E processing has lead to a reduction in the 1.68eV peak height and a reduction and shift in the broad peak.

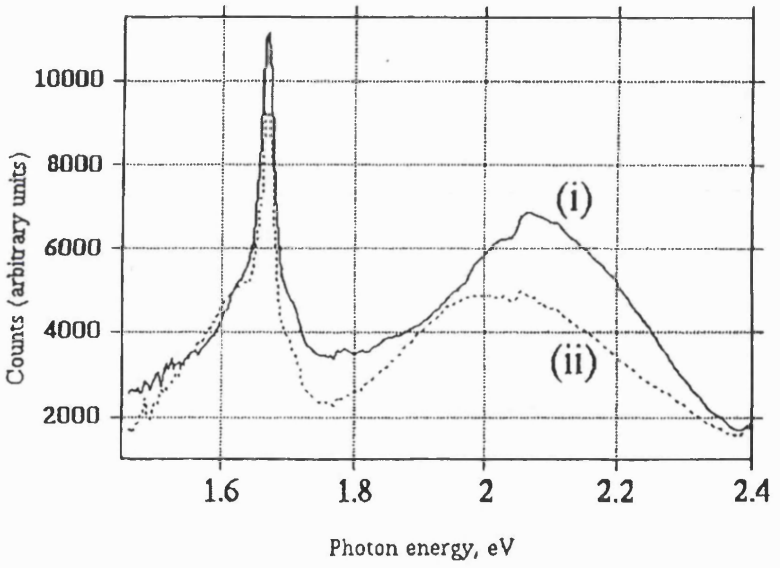

Figure 8.7: Photoluminescence spectra under 476.5nm laser excitation of freestanding CVD diamond films (i) type P untreated and (ii) type Q after type E treatment.

8.5 Discussion

8.5.1 Nature of the Effect of the Type E Process

The AES results provide some insight into how the surface of the diamond may be modified by the application of the type E process. The carbon peak arises from a KVV Auger process whilst the three maxima which arise in the valence band structure of diamond may give rise to a number of Auger processes with slightly differing energies. Peaks arising from from the two strongest, KV_1V_1 and KV_2V_2 transitions are

commonly observed along with surface and bulk plasmon losses from the Auger electrons of the primary (KV_1V_1) transition [8.10, 8.11]. The positions of A_0, A_1 and A_2, the three highest energy of these peaks observed by others are marked on figure (8.6). Close agreement is evident between these lines and the *N(E)* peak positions that can be predicted from the differential spectrum plotted for curves (i) and (ii). The CVD diamond film surfaces represented by these traces thus comprise good quality diamond over the probe depth of the AES technique (3-4 atomic layers [8.12]) and within the sensitivity of this technique (≈1% of a monolayer [8.12]). Spectrum (iii) in figure (8.6) shows the primary peak minima to be shifted to 271eV. This shift and the change in the nature of the fine structure on the low energy side of the peak is consistent with the presence of a graphitic surface [8.10]. In addition, a new peak with a minimum at an energy of ≈290eV is apparent. This feature has not been observed during studies on well defined graphite surfaces although Hoffman [8.13] reported a weak peak at 290eV for a type IIa natural diamond crystal whilst noting that a similar peak was not observed in AES spectra from CVD diamond films; no assignment was offered for this observation. the wide energy scan spectra of figure (8.5) indicate that the samples that had just been cleaned and those that had undergone both steps in the the type E process support a persistent surface oxide phase. The intensity of the peak suggests that this involves a sub-monolayer quantity of oxygen in both cases, but more oxygen is present on the treated surface than the cleaned one.

The oxygen peak which is evident on all 'as inserted' samples arises from simple air contamination and is readily removed by heating *in vacuo*, however the the type E process leaves the surface more heavily oxidised. The graphitic nature of the type R surface after methane treatment alone suggests that it is this oxidation that removes the graphitic phase during the second step of the type E process. This hypothesis is supported by the visual observation that a type R sample looks darker than an untreated sample, but that a fully processed type E sample is restored to a brighter appearance. A photograph of this effect is reproduced as figure (8.8), however the subtlety of the change, the subjectivity of its interpretation and the limitations of the printing process combine to prevent this image being offered as formal evidence - it is simply a supporting observation.

At the visible wavelengths explored in this study photoluminescence will emerge from the bulk of the diamond film, it can therefore be concluded that the strongly modified PL spectra recorded following type E treatment indicates that the processing acts upon more than just the outermost few atom layers of the material. The peak at 1.68eV has been observed in PL recorded for a number of types of thin film diamond. Fong and

Schwartz [8.3] found the peak to be strongly modified by the methane concentration used to grow films by MPACVD: increased methane concentrations, which are normally asssociated with decreasing diamond quality, led to a strongly reduced PL intensity at 1.68eV. These authors suggest that residual stress quenches the PL emission intensity but does not effect the peak position or half width. Vibronic bands associated with this peak were primarily due to lattice phonons. It was broadly concluded that this result agreed with earlier work which suggested that the peak was associated with Si impurities.

A study by Kania and Oelhafen [8.8] using MPACVD diamond films showed that the 1.68eV peak was stronger in randomly textured films than in (100) aligned ones, whilst Brown and Rand [8.7] have suggested that the defect responsible for this emission is (111) orientated. Bergman and co-workers [8.4, 8.6] found that isolated diamond nuclei grown by CVD emitted this PL band which was again attributed to Si defects. The strong 1.68eV peak evident in figure (8.7) is therefore to be expected even in high quality CVD diamond. Although recorded at room temperature, it is possible to identify the vibronic structure on the low energy side of the peak. The peak intensity is significantly reduced by the type E treatment (plot (ii)) but the peak position is unchanged: this implies that there is an increase in the stress level within the film.

Bergman *et al.* [8.4, 8.6] also studied broad band PL emission from CVD diamond films over a similar energy range to that presented in figure (8.7). The authors concluded that that amorphous material within the film, containing sp^2 bonding was responsible for the broad peak; it was proposed that a wide distribution of continuous in-gap states would result from the random nature of this form of defect. PL measurements made on amorphous hydrogenated carbon fims (DLC) have shown similar broad band characteristics over this energy range [8.14]. The fact that the type E treatment strongly modifies the intensity and position of this broad band implies that the nature of the amorphous material within the film is being changed.

In summary it can therefore be identified from the AES experiments that the type E process acts by donating carbon or a carbon containing species to the surface of the film whilst the subsequent oxidation step removes surface graphitic material. This model is supported by the earlier observation (§6.4.1) that the methane processed surface is highly conductive but that after oxidation the resistance is dramatically increased. The PL analysis suggests that increased stress and modified non-diamond carbon regions within the film may result from the treatment, and that the effects of the process must extend beyond the exposed and near surface regions of the film. As diffusion within

diamond grains is highly improbable at the temperatures involved, it would appear reasonable to anticipate a model involving transport of a carbon containing species along grain boundaries to achieve passivation of electro-optically active defects which are local to the grain boundaries.

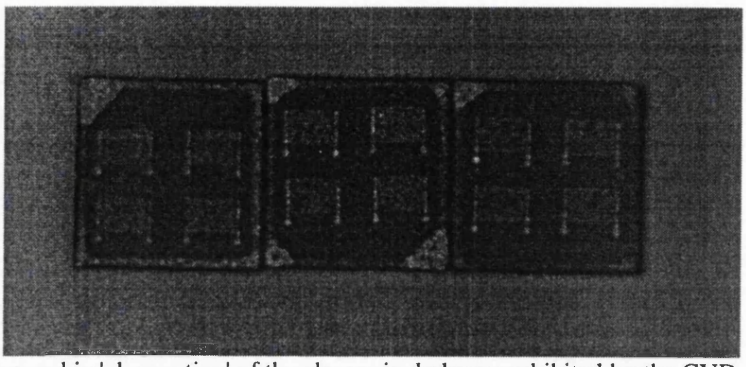

Figure 8.8: Photographic 'observation' of the change in darkness exhibited by the CVD diamond surface at each stage of type E processing. Left to right: untreated, methane only, methane and oxidation.

8.5.2 Permanence of the Type E Process

The results of the heat and radiation experiments together serve to indicate that the primary enhancements in device performance achieved by application of the type E process represent 'hard' or permanent changes to the material. Whilst the earlier results of iterative type E processing (§7.3) indicate that a single application of the treatment does not achieve an end point beyond which the material can change no further, the present results indicate that once a change has been effected it will not easily be reversed. The persistence of the process E induced properties (low dark current and high spectral discrimination) following elevated temperature operation supports the hypothesis of bulk material modification presented above by the PL analysis: if the methane step were simply donating carbon to deposit graphite on the diamond surface, and the oxidising step simply burning this off, then one might anticipate that an extended period of heating identical to the air oxidation step would result in some change in the dark current characteristics of the device, most probably in the form of a further reduction in the dark current. Instead it is seen in figure (8.1) that the dark current characteristic is almost exactly restored when the device is cooled to room

temperature after heating. From this one may speculate that whatever happens to the carbon containing species deposited during the first part of the process, it is apparently 'used up' within an hour of the standard air treatment.

The spectral result from the radiation hardness experiment indicates that whilst the primary characteristics of the type E process remained unchanged following the gamma dose, some enhancement of the spectral selectivity has occured. This could suggest that 'soft' (NDC) regions of the film which had not been modified by the type E process were affected by the radiation dose. If this is the case, then it may be reasonable to envisage a situation whereby transport of carbon containing species into the film occurs only to a limited depth or density, beyond which point the process is restriced either by lack of available mobile material or by a change in the prevailing transport conditions.

8.6 Conclusions

The nature of the material changes effected in polycrystalline CVD diamond by the type E process have been investigated by the surface analysis technique of Auger electron spectroscopy and the bulk analysis technique of photoluminescence spectroscopy. Additionally the permanance or 'hardness' of these changes has been investigated by exposing processed samples to elevated temperatures and high doses of ionising radiation.

The model which begins to emerge from these experiments is of a process in which carbon or hydrocarbon radicals are first donated to both the surface of the film and to the near surface bulk of the film, probably by transport along grain boundaries. The second stage of the type E process then entails the oxidation of the exposed surface of the film by which means the deposited non-diamond carbon material is removed from the exposed surface but not, or to only a lesser extent, from the bulk of the sample. The introduction of additional material into the bulk of the film is indicated by the photoluminescence experiment to result in an increase in strain within the film. If this increase in physical strain as opposed to chemical modification by the introduced material is the primary mechanism behind the optoelectronic effects of the process then a direct parallel may identified between the introduction of these carbon/hydrocarbon 'impurities and the mechanisms of the nitrogen related impurity centres previously reviewed (§2.5.2).

Based upon the results presented in this chapter, an extensive programme of further work can be recommended. An intuitive starting point for a comprehensive study of the nature and effects of the type E process would be to map the energy and density of defects which exist throughout the band structure of both unprocessed and fully processed films. Such a study would require the use of techniques capable of looking deeper into diamond's wide bandgap than the methods available to the present work. Happily, plans are now well advanced for a programme based around the use of Deep Level Transient Spectroscopy to be undertaken with the aim of correlating the energy levels identified both to known defect phenomena in diamond and to the results of transient photoresponse measurements undertaken using fast UV laser excitations.

8.7 References

8.1 A. Mainwood, L. Allers, J.F. Hassard, A.S Howard and A. Mahon, Proceedings of 187th Meeting of the Electrochemical Society, Reno, Nevada, USA, May 1995.

8.2 A. Mainwood, L. Allers, A.T. Collins, J.F. Hassard, A.S. Howard, A.R. Mahon, H.L. Parsons, T. Sumner, J.L. Collins, G.A. Scarsbrook, R.S. Sussmann and A.J. Whitehead, Journal of Physics D: Applied Physics 28, 1279 (1995).

8.3 T. Feng and B.D. Schwartz, Journal of Applied Physics 73, 1415 (1993).

8.4 L. Bergman, B.R. Stoner, K.F. Turner, J.T. Glass and R.J. Nemanich, Journal of Applied Physics 73, 3591 (1993).

8.5 T.S. McCauley and Y.K. Vohra, Physical Review B 49, 5046 (1994).

8.6 L. Bergman, M.T. McClure, J.T. Glass and R.J. Nemanich, Journal of Applied Physics 76, 3020 (1994).

8.7 S.W. Brown and S.C. Rand, Journal of Applied Physics 78, 4069 (1995).

8.8 P. Kania and P. Oelhafen, Diamond and Related Materials 4, 425 (1995).

8.9 S. Dannefaer, W. Zhu, T. Bretagnon and D. Kerr, Physical Review B 53, 1979 (1996).

8.10 B.B. Pate, Surface Science 165, 83 (1986).

8.11 P.G. Lurie and J.M. Wilson, Surface Science 65, 453 (1977).

8.12 P.E.J. Flewitt and R.J. Wild, "Physical Methods for Materials Characterisation", Institute of Physics Publishing, Bristol, 1994.

8.13 A. Hoffman, Diamond and Related Materials 3, 691 (1994).

9 EXTENDING THE WAVELENGTH RANGE OF CVD DIAMOND PHOTODETECTORS

9.1 Introduction

In this chapter methods for modifying the wavelength selectivity of diamond photodetectors are considered. Ion implantation is identified as a means of changing the material properties of thin film diamond both through the introduction of impurity species into the lattice and through modification (damage) of the lattice itself. Experiments are proposed and undertaken in which CVD diamond tiles are implanted with boron and nitrogen and subjected to a range of high temperature annealing processes prior to photodetector fabrication. Based upon extensive characterisation of these devices, conclusions are drawn as to the approaches which are most likely to result in reliable detection of sub-bandgap illumination by future devices.

9.2 Experimental Design

Whilst an early aim of this project was to minimise the sensitivity of thin film diamond photodetectors to sub bandgap illumination, the successful attainment of this goal (§5, 6) stimulates contemplation of a second generation of devices in which detector performance may be further modified, either through mode of operation or device engineering to meet a wider range of applications. In particular there is an industrial requirement for UV detectors which combine visible blindness with a strong sensitivity to wavelengths in the 250-300nm range (§11) Clearly the ultimate aim of such an investigation is to identify a 'toolbox' of techniques capable of engineering the cut-off wavelength of a detector to meet a given specification. In the first instance however a promising result would be the provision of evidence that a particular technique is capable of effecting a stable, reliable change of any type in detector performance.

9.2.1 Extrinsic Photoconductivity

Although pure diamond fundamentally cannot absorb light which has a longer wavelength than the 225nm bandgap excitation identified by equation (3.1), the presence of impurities or defects in the diamond lattice has been seen to facilitate extrinsic optical absorption as discussed in (§2.5 and 2.6) and illustrated by figures (2.8-2.10) and table (2.4). Whilst it was noted from the characteristics of the GR1 radiation induced defect centre reproduced in figure (2.11(b)), that extrinsic optical absorption does not necessarily lead to the generation of mobile charge carriers and hence photoconductivity, there are many examples in the literature of instances where imperfect diamond has been found to exhibit potentially useful extrinsic photoconductive properties.

Amongst the clearest examples of the type of effect one might wish to engineer into an advanced diamond detector is the sensitivity to sub-bandgap excitation observed by Denham *et al.* [9.1] in a natural type Ia stone. This characteristic, discussed in (§3.2) and reproduced as figure (3.1(c)), indicates that the peak sensitivity of that particular sample was observed at $\approx$4.6eV$\Leftrightarrow$270nm with the onset of 'visible blindness' occuring at $\approx$300nm. Further evidence of extrinsic photoconductivity in diamond has been provided by almost every thin film photoconductor result published in which wavelength selectivity data has been made available [e.g. 9.2, 9.3, 9.4, 9.5, 9.6, 9.7, 9.8], to which can be added the results of experiment types A, C, F, G and H presented in this thesis.

The main difficulties which arise when attempting to synthesise a particular extrinsic photoconductive response fall into two specific categories. Firstly, when a suitable characteristic has been observed in a particular sample, it is often unclear precisely what defect system has caused that effect. Secondly, even if the nature and extent of the defect system is accurately known, the insertion of controlled levels of impurity or damage into the crystalline lattice is particularly difficult in the case of diamond, due primarily to the same bonding characteristics which underwrite the material's most attractive properties.

Denham's result of figure (3.1(c)) is precisely the type of characteristic which one might wish to replicate in CVD diamond, however reference to the published details indicate that they serve as an example of both the above problems. Based on the authors' description of the stone as being type Ia, reference to table (2.3) indicates that such a sample is expected to contain nitrogen at a density of up to ≈3000ppm in the form of A or B centres (§2.5.2). This description, whilst accurate enough for gemmological classification, is inadequate when used as the 'recipe' for a photodetecting element in a semiconductor device. In addition to the label Ia leaving considerable doubt about the location, form and accurate atom density of nitrogen present, it will be noted that the wavelengts absorbed by the A and B centres represented by figures (2.8 (b) and (c)) offer a relatively poor match to figure (3.1(c)), leaving open the possibility that an unclassified defect state may be the real target for synthesis in this case.

Taking the carbon atom density in diamond of $\approx 1.8 \times 10^{23} cm^{-3}$ derived from [9.9], the impurity level of up to 3000ppm corresponds to a nitrogen density of $\approx 5.4 \times 10^{20} cm^{-3}$. This is an extremely high doping level by the standards of the semiconductor industry in general, and in the case of diamond can be placed in context by recalling the observation of Werner *et al.* [9.10] (§2.5.3) that boron doping at $8 \times 10^{20} cm^{-3}$ results in degenerate (metallic) conduction. Doping to such high levels must inevitably result in extensive disruption of the diamond lattice, however this is not necessarily a problem as such distortion is expected to be an essential aspect of the defect's influence (§2.5.2). A greater problem is that even if the target location were known, no currently available doping technology is capable of exerting the necessary degree of control over the ultimate lattice location of the dopant to ensure that the required defect type is created.

An alternative, and very different, target characteristic is shown in plot (a) of figure (9.1). This photoconductor consisted of standard interdigitated 25μm pitch electrodes on a silicon backed ≈6μm thick nominally undoped small grain (0.5-2μm) MPACVD polycrystalline diamond film, similar in appearance to figure (5.4(c)) but supplied by a

different manufacturer. The structure was fabricated on what was believed to be low-grade scrap material during development of a lift-off process for the fabrication of Ti/Au bilayer electrodes (§2.6.1); initially it exhibited a relatively high dark current so it was not submitted for photocurrent analysis. The high conductivity of the film had been attributed during earlier experiments to the possible incorporation of low levels of boron from a contaminated reactor during growth. Because of the suspected boron content, a sample of the film was used as the substrate for a photodiode structure reported elsewhere [9.11]. When the photodiode revealed unexpectedly good characteristics of low dark current (<2pA at 50V), little evidence of breakdown at 100V and the spectral characteristic plotted in figure (9.1(b)), the photoconductor was re-examined more carefully. During the interval between fabrication and testing, diffusion between the Ti and Au layers had occured causing the electrode structure to appear greenish-purple in colour; the dark current had also dropped, enabling a spectrum to be obtained.

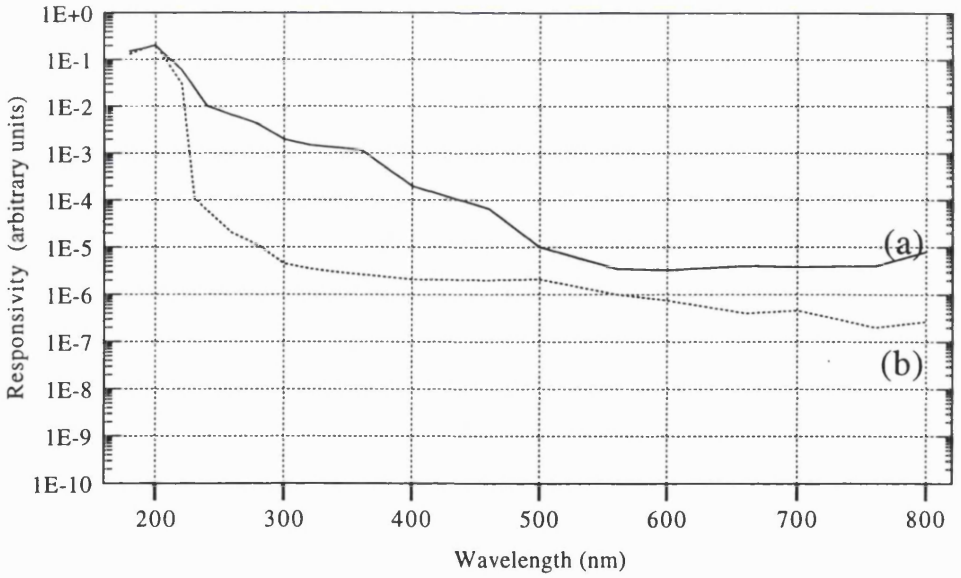

Figure 9.1: Photoresponse characteristics of structures on nominally undoped small grain polycrystalline diamond film (a) interdigitated photoconductor (Ti/Au) (b) Schottky diode (Au-Ti/Ag/Au).

Two points of particular interest can be noted from figure (9.1): firstly, it is clear that the photodiode and photoconductor structures fabricated on pieces of the same diamond wafer and tested using the same optical system exhibit very different spectral response characteristics. This could simply indicate that the film was highly inhomogeneous such that identical devices fabricated on adjacent chips of the wafer at the same time

would also display radically different properties, a view which is to some extent supported by an inability to faithfully reproduce the performance of either structure in subsequent experiments. An alternative explanation is that the different physical structures and modes of operation of the two device types may have caused, or emphasised, the difference in their characteristics. The purpose of introducing these two interesting but unstable devices is not however to analyse them in detail, but to observe and acknowledge the *form* of their spectral response curves, noting that these have been normalised for comparison so that the response amplitude is in uncalibrated arbitrary units.

The second point to be drawn from plot (9.1(a)) is that in addition to the clearly identifiable bandgap response, the sub-bandgap characteristic of the photoconductor consists of a series of regions of sensitivity which decrease in relatively well defined stages having thresholds at 280, 360 and 460nm. Recalling the work of Pace [9.7] and Salvatori [9.8] (§3.2.3) reproduced in figure (3.4), it may be postulated that the 360nm feature of the thin film device above may have a similar origin to the sensitivity thresholds in the region 340-350nm observed by these other researchers. Whilst neither author makes any specific claim as to the surface crystallite dimensions of the HFCVD and MPACVD films they employ, electron micrographs of the structures presented by these teams [9.12, 9.13] indicate the maximum crystallite dimension to be around 5μm diameter. It is also possible that Denham's 270nm centred broad peak and the highest energy sub-bandgap response of the thin film devices have a common lattice related cause, allowing that the shape of the peak in the CVD material may be somewhat masked by band tailing [9.14] attributable particularly to NDC regions and grain boundaries.

In summary therefore, it can be seen that the shape of the response spectrum of a diamond photoconductor can be modified by the presence either of impurities, or defects, or both - but that the form and nature of the imperfections exert a critical influence over the type of modification which is effected. From a device engineering perspective the question then arises as to how best one might attempt to introduce such imperfections into a potential detector substrate.

9.2.2 *In Situ* Doping of Diamond

As previously noted (§2.5), natural diamond invariably contains non-carbon impurities which are incorporated into the lattice during geological formation of the crystal [9.15]. Dopants can similarly be introduced into CVD diamond by provision of the required species to the deposition chamber, either in elemental form or as a constituent of a

larger 'carrier' molecule which is then broken down under the growth conditions to release the desired impurity for incorporation into the film.

Boron can be grown into diamond films from solid or vapour sources as discussed elsewhere (§2.5.3) and is the most extensively used dopant in diamond due to its ability to render the material p-type semiconducting. Other dopants which can be incorporated during growth include phosphorous [9.16, 9.17, 9.18, 9.19] (§2.5.4), silicon, tungsten and oxygen [9.20] where the latter three usually constitute unwanted contamination derived from the substrate, heating filament and carrier gases respectively where present.

Although nitrogen is present in almost all natural diamonds (§2.5.2) and has been incorporated into CVD diamond at densities of up to $1x10^{20}cm^{-3}$ [9.21], it has also been found strongly to influence the morphology and growth rate of films. Tsang *et al.* [9.22] deposited HFCVD diamond films using nitrogen N_2, ammonia NH_3, methylamine CH_3NH_2 or hydrogen cynanide HCN as the nitrogen carrier and found that the deposition rate depended critically upon the choice of C/N precursor used. After six hours of growth only the N_2 containing gas mixture yielded a continuous film and and the nitrogen incorporation level was commented to be very low. Another study investigated the influence of N_2 incorporation during MPACVD and concluded that the addition of nitrogen improved the quality of the diamond crystallites, reducing graphite content and outcrops of secondary growth, but that the nucleation density of diamond was also suppressed [9.23].

9.2.3 Ion Implantation into Diamond

Ion implantation is a widely used technique capable of introducing almost any impurity (ion species) into the near surface region of a solid; as such it is extensively employed for modifying the properties of semiconductor materials. This is usually effected by the insertion of electrically active dopant species but can also entail the deliberate creation of damage: in some semiconductor systems for example, backside implantation is used to create gettering centres and thereby effect passivation [9.24], or compensation of impurities which cannot be totally eliminated.

In the case of CVD diamond, ion implantation has been explored primarily as a means of achieving selective area doping with boron for electronic purposes [9.25, 9.26], however nitrogen doping has also been investigated recently with a view to enhancing the electron emission properties of diamond films [9.27]. Whilst the general features of

ion implantation technology are well documented elsewhere [9.28], Dresselhause and Kalish [9.29] have identified two specific properties of implantation into diamond:

(i) Because carbon is one of the lightest elements, most implants will either be comparable in mass or heavier. Specifically, nitrogen and boron, which are the two most widely considered implants for diamond, are of comparable mass to carbon and so meet the conditions for maximum momentum transfer.

(ii) Although diamond is usually regarded as an excellent insulator, it may transform on implantation into graphite which is a good conductor.

To the above comments it may added that because of diamond's metastability with respect to graphite (§2.2) and the generally low mobility of defects in diamond [9.36], the normally highly successful use of thermal annealing to repair implantation damage in other semiconductor systems does not have a direct analogue in diamond.

The greatest success to date in low damage boron implantation into diamond has been reported by Prins [9.30] and Fontaine *et al.* [9.31] who have developed processes based upon a Cold Implant Rapid Anneal (CIRA) cycle. In the CIRA process a specially developed substrate mounting facilitates implantation at -170°C followed by rapid heating *in situ* to ≈1000°C; annealing in a furnace at temperatures up to ≈1300°C was shown to further improve the electrical activation of the boron implant.

Kalish *et al.* [9.27] have recently demonstrated successful deployment of the CIRA technique for implantation of nitrogen into a type IIa diamond. A series of ten implantations at energies from 640 to 40keV resulted in a total implanted dose of $2.8 \times 10^{14} cm^{-2}$, yielding a nitrogen concentration of $\approx 4 \times 10^{18} cm^{-3}$ homogeneously distributed over a depth of 600nm. Subsequent *ex situ* annealing was undertaken to ≈1400°C for 10 minutes in a bell jar evacuated to 10^{-6} Torr having a residual atmosphere of argon and hydrogen. Following graphite removal by means of an acid etching step similar to that described in (§4.2.2), the sample was found to exhibit the same high resistance as had been measured prior to implantation, indicating little formation and/or complete removal of the graphite which usually forms during implantation and high temperature annealing. Luminescence and electron paramagnetic resonance (EPR) studies indicated that almost half the implanted nitrogen atoms occupied substitutional sites, with evidence that after the higher temperature annealing process, defects similar to those found in type Ib diamond (i.e. single substitional C centre, table (2.3) and (§2.5.2.3)) were found.

9.2.4 Design Decisions

Against the background presented above, it was concluded that very little data existed on prior attempts to modify the photoconducting threshold wavelength of thin film diamond for device applications. Whilst it was clear that the photoconductive characteristics of a sample could be modified by the presence of defects or impurities (§9.2.1) and that defects and impurities could be introduced by *in situ* doping (§9.2.2) or ion implantation (§9.2.3), there was a paucity of insight as to whether the latter techniques could be deployed with sufficient subtlety and control to achieve the former effects without damaging the material so extensively as to render it optoelectronically useless.

It was noted from the literature reviewed in (§9.2.1) that previously reported sub-bandgap photoconductivity in CVD films had generally arisen unintentionally, often as a consequence of poor quality thin film diamond substrates being employed. Given the widely acknowledged but not fully characterised effects which *in situ* doping is known to have on the nucleation, growth and quality of CVD diamond (9.2.2), coupled with the highly successful results previously obtained using the relatively large grain size undoped freestanding polycrystalline diamond of (§6-8), it was decided to conduct a series of experiments in which similar material to that previously employed would be implanted with various species and subjected to a range of annealing schemes to investigate ways in which the absorption characteristcs of the previously demonstrated devices could be modified. The species for implantation were chosen to be boron and nitrogen for the following reasons. Boron is known to be an electrically active acceptor but is anticipated by figures (2.8(e)) and (2.10) not to modify significantly the absorption threshold of diamond, whilst nitrogen should be an electrically inactive deep donor which would extensively modify the absorption properties of the material in a manner goverened by the type of post implantation annealing regime applied.

A parallel investigation was also proposed using a non-implanted silicon backed film which was to be nominally undoped and supplied against the specification 'as low grade as possible' in an attempt to gain insight into the characteristics of figure (9.1).

9.3 Experiment

A series of experiments was undertaken using two types of CVD diamond. Both films were grown on silicon in (different) clean MPACVD reactors. The thicker film ($\approx$100μm) was subsequently removed from its substrate to become freestanding; this

wafer was of identical specifications to the sample described by figures (5.3) and (5.4(a)). The thinner film (≈10μm) remained on its substrate and had a mean surface crystallite dimension of 2-5μm as shown in figure (9.2).

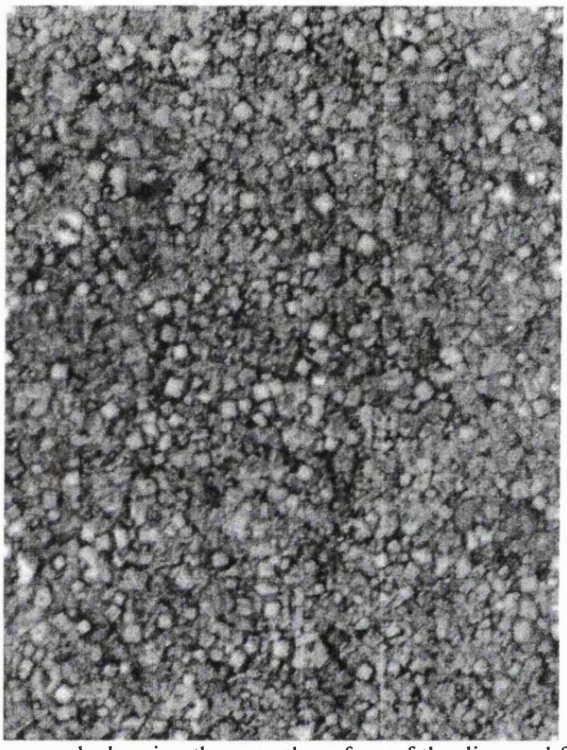

Figure 9.2: Optical micrograph showing the growth surface of the diamond film from which sample types U andV were fabricated.

Tiles cut from the freestanding film were implanted with either nitrogen or boron by staff at AEA Technology (Harwell) using the parameters outlined in table (9.1). A double nitrogen implant was used with the aim of doping the near surface region to a density of $\approx 3 \times 10^{19} cm^{-3}$, which approaches the accepted nitrogen density for type Ia stones such as that investigated by Denham, whilst maintaining the total implantation dose safely below the critical damage density of $\approx 5.2 \times 10^{15} cm^{-2}$ identified by Spits *et al.* [9.32]. Given the anticipated absorption depth of ≈2μm for bandgap radiation in pure diamond [9.33], it was initially proposed that a series of implants at different energies should be used in the manner of Kalish *et al.* [9.27] to create a relatively wide doped region. This was not deemed advisible however due to the imperative of avoiding the critical damage dose whilst attempting to create an order of magnitude higher doping density than achieved in the previous study. Instead it was proposed to concentrate the

dopant in the first 10% (200nm) of the absorption depth, as indicated by the TRIM (Transport of Ions in Matter) [9.29] simulation plotted as figure (9.3).

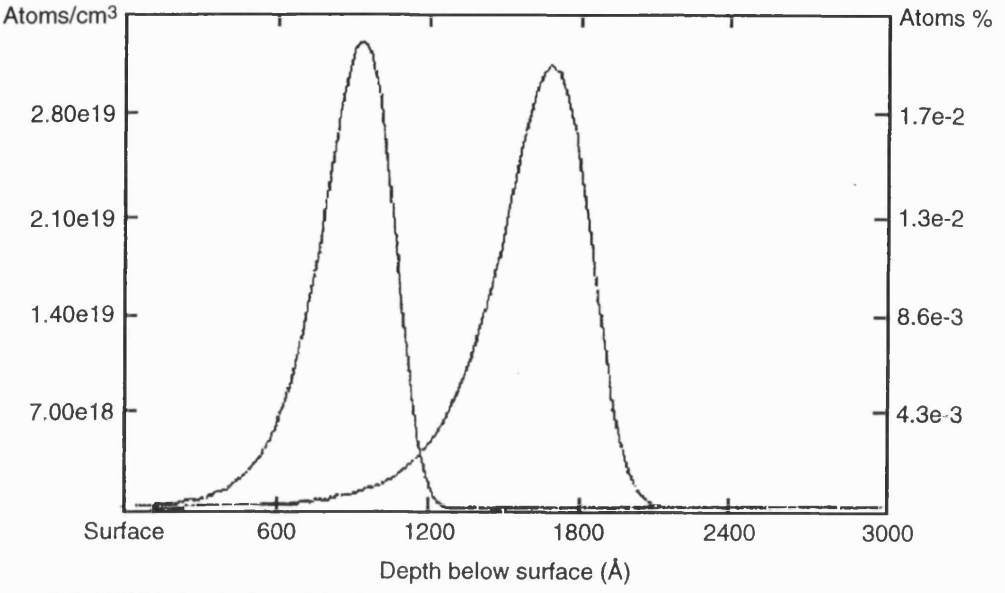

Figure 9.3: TRIM simulation of the impurity profile anticipated for the double nitrogen implant into CVD diamond.

The target doping density of the single boron implant was chosen to be in the order of $\approx 10^{18}cm^{-3}$ so that the 0.2% activation anticipated at room temperature [9.34] (§2.5.3) would result in a carrier density of $\approx 10^{15}cm^{-3}$. This is a relatively low activated carrier density by normal semiconductor device standards, and should therefore approximate the possible condition of a sample unintentionally doped by growth in a contaminated reactor. It was hoped that this approach would insert sufficient dopant or implantation damage to modify the optical absorption properties of the diamond without rendering it so heavily p-type conductive as to mask any changes within a greatly increased dark current. A TRIM simulation of the anticipated boron impurity profile corresponding to the conditions of table (9.1) is reproduced as figure (9.4). One tile containing each implant type was submitted for SIMS depth profiling (§4.4.2) to verify the integrity of the implantation process.

Implant	*Energy (keV)*	*Ion*	*Dose (ions/cm²)*	*Peak depth (nm)*	*Peak desity (atoms/cm³)*
N	90	$^{14}N^{+}$	$1.25x10^{14}$	100	$3.3x10^{19}$
	180	$^{14}N^{+}$	$1.5x10^{14}$	170	$3.1x10^{19}$
B	120	$^{11}B^{+}$	$5x10^{13}$	200	$8.7x10^{18}$

Table 9.1: The ion implantation parameters used and the target doping profile characteristics.

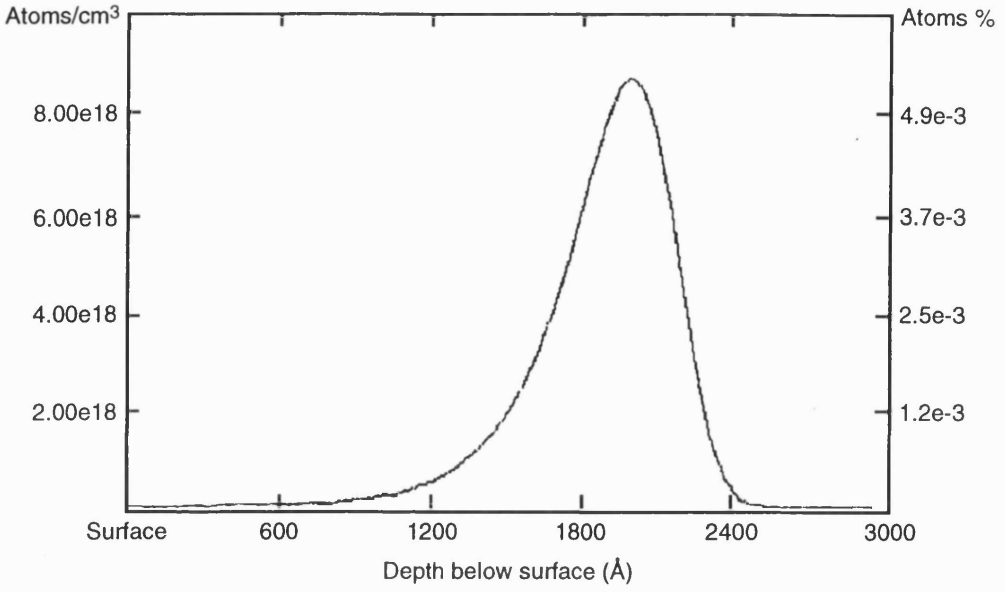

Figure 9.4: TRIM simulation of the impurity profile anticipated for the boron implant into CVD diamond.

Following implantation, a set of tiles containing nitrogen were labelled 'S' and subjected to one of three forms of annealing process as outlined in table (9.2). A control sample S_I received no post-implant anneal whilst sample types S_{II} and S_{III} were annealed *in vaccuo* (base pressure $\approx 10^{-6}$ Torr) at 800°C and 1100°C respectively using the apparatus of (§4.3.1). A parallel series of boron doped tiles were processed and labelled type 'T' as tabulated. It was observed on sample types S_{III} and T_{III} after annealing, that a darkened region had appeared on the nucleation surface of each sample as illustrated by figure (9.5). This indicated that graphitisation had occured on the surface of each tile which had been closest to the heat source; the circular shape of the graphitised region corresponds to the aperture in the molybdenum plate which supported the tile above the heating element. After annealing, standard 25μm interdigitated electrode structures were fabricated from gold on all sample types, including chips from the thin film labelled 'U', using the established procedures of (§4.2.2 and 4.2.3). Procedure (§4.2.2) was modified slightly in that the graphitised samples were subjected to two cycles of acid cleaning in order to achieve more extensive removal of the excess non diamond carbon material. All samples were analysed for dark current and spectral response characteristics (§4.5.1-4.5.4) using a 10V bias unless stated otherwise, treated with a type E process (§6) and then tested again.

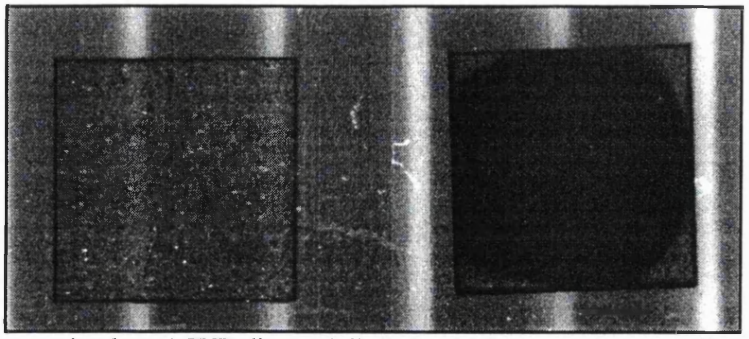

Figure 9.5: A nitrogen implanted CVD diamond tile before high temperature annealing (LEFT) and after annealing at ≈1100°C for 1 hour (RIGHT); extensive graphitisation is clearly visible.

Based upon observations which will be discussed in the following sections, two further experiments were undertaken. A series of samples labelled V_I, V_{II} and V_{III} from the undoped silicon backed wafer were prepared as gold photoconductors according to the methods of (§4.2.2 and 4.2.3) with variations in the maximum temperature of the acid bath to 170, 220 and 250°C respectively. Additionally two sample types from the nitrogen implanted tiles, labelled W_I and W_{II} were prepared as photoconductors having had no post-implant anneal, but with acid bath temperatures of <170°C and >250°C respectively.

Sample	*Film*	*Implant*	*Processing*
S_I	80μm Freestanding	N	none → test → type E → test
S_{II}	80μm Freestanding	N	800°C anneal → test → type E → test
S_{III}	80μm Freestanding	N	1100°C anneal → test → type E → test
T_I	80μm Freestanding	B	none → test → type E → test
T_{II}	80μm Freestanding	B	800°C anneal → test → type E → test
T_{III}	80μm Freestanding	B	1100°C anneal → test → type E → test
U	10μm Si backed	none	none → test → type E → test
V_I	10μm Si backed	none	acid bath to 170°C
V_{II}	10μm Si backed	none	acid bath to 220°C
V_{III}	10μm Si backed	none	acid bath to 250°C
W_I	80μm Freestanding	N	acid bath <170°C
W_{II}	80μm Freestanding	N	acid bath >250°C

Table 9.2: The nature and processing of the samples prepared for evaluation in this chapter.

9.4 Results

The SIMS depth profile for the boron implanted material is reproduced as figure (9.6). This profile shows a very good correlation to the TRIM simulation of figure (9.4), indicating a peak boron concentration of $\approx 2.5 \times 10^{18}$ atoms/cm^3 at a depth of ≈230nm. Figure (9.7) reproduces the best attempt at obtaining SIMS data from a nitrogen implanted sample. It should be noted that the raw data presented is not calibrated, having an intensity signal (counts/second) plotted vertically against sputtering time on the horizontal axis. The 12amu carbon secondary ion signal, followed as a matrix line and plotted at the top of the figure, is clear and remains steady throughout the profile, however the 14amu nitrogen profile (middle trace) is very low and fails to show clear intensity peaks where they would be expected from the TRIM simulation of figure (9.3). The reason for this is thought to be the poor detection limit of nitrogen when compared to boron using SIMS; from work carried out on implants into silicon, nitrogen has been found to have a relative sensitivity factor around 1000 times less than for boron [9.35]. As it is likely that a similar relationship exists in diamond, it is unsurprising that having measured a signal from the boron of ≈1000 counts/second, the nitrogen signal is almost indistinguishable from the background level.

The photoresponse characteristics of the non-annealed photodetectors on implanted tiles are reproduced in figures (9.8) and (9.9) for the nitrogen and boron dopants respectively. In each case the dotted plot marked (a) indicates the characteristic before application of the type E process, whilst the solid (b) line represents the response after treatment. Two features of these graphs are particularly striking: the lower overall sensitivity of both device types to bandgap radiation compared to standard type E structures, and the fact that the characteristics of both S_I and T_I devices as fabricated are almost identical. This will be discused in the following section.

Figure (9.10) shows the spectral photoresponse of a device fabricated on a type S_{II} nitrogen sample after 800°C annealing. This sample type was highly conductive, causing the picoammeter to current-limit (I_{max}=2.2mA) when biased at 10V so the presented data corresponds to a bias of 1V. After treatment with a type E process the type S_{II} sample became too conductive to analyse and no plot is available for the device in this condition. After 1100°C annealing a nitrogen containing type S_{III} sample exhibited a dark current higher than the non-annealed S_I tile but lower than its 800°C annealed type S_{II} counterpart.

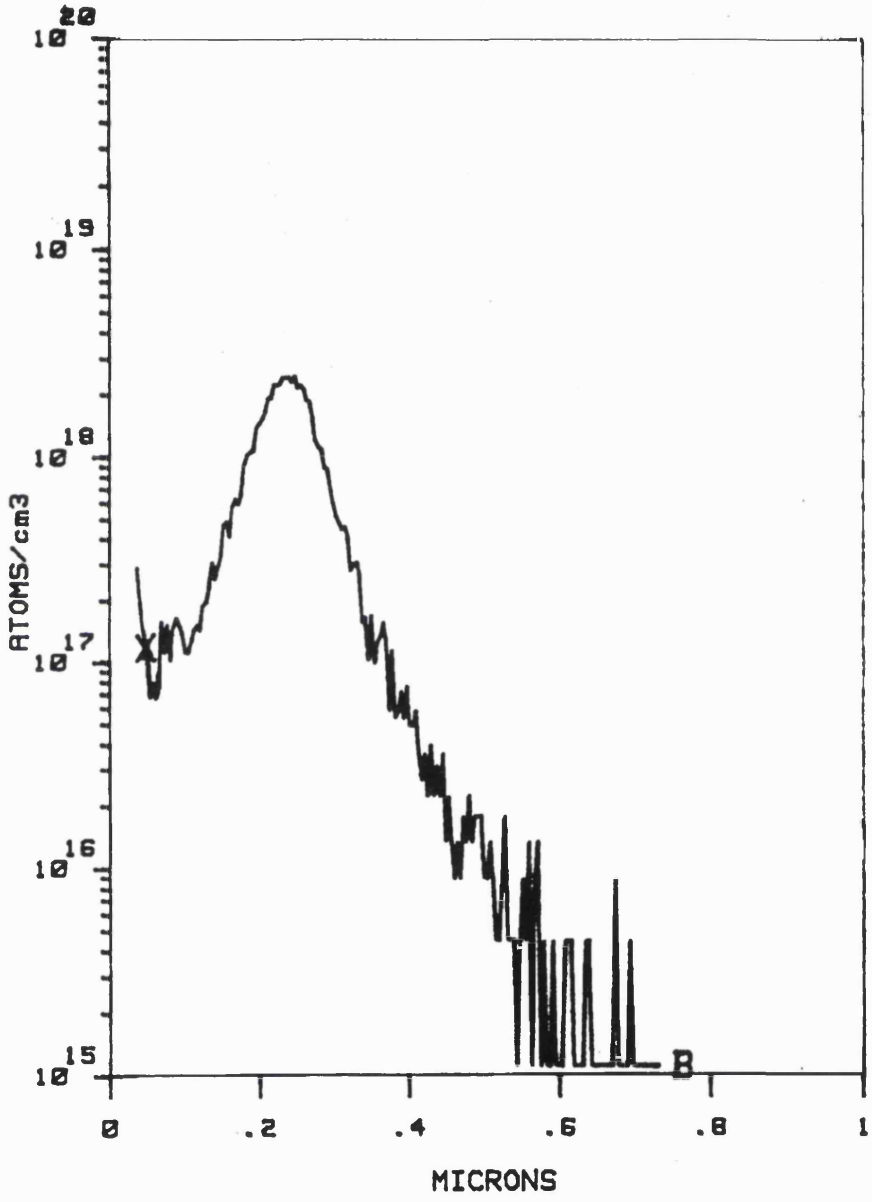

Figure 9.6: SIMS depth profile for boron implanted CVD diamond tile (type 'T').

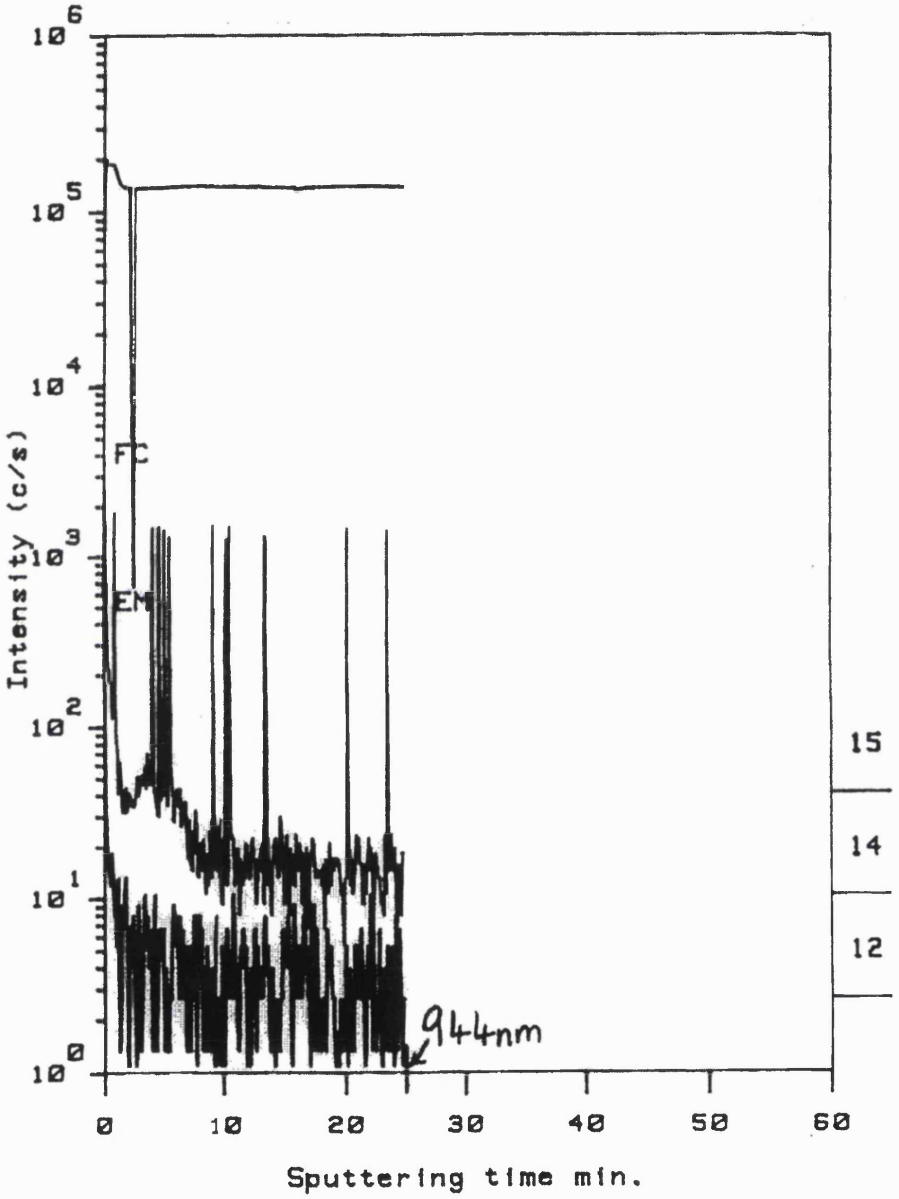

Figure 9.7: SIMS profile for nitrogen implanted CVD diamond tile (type 'S'). Not calibrated for depth.

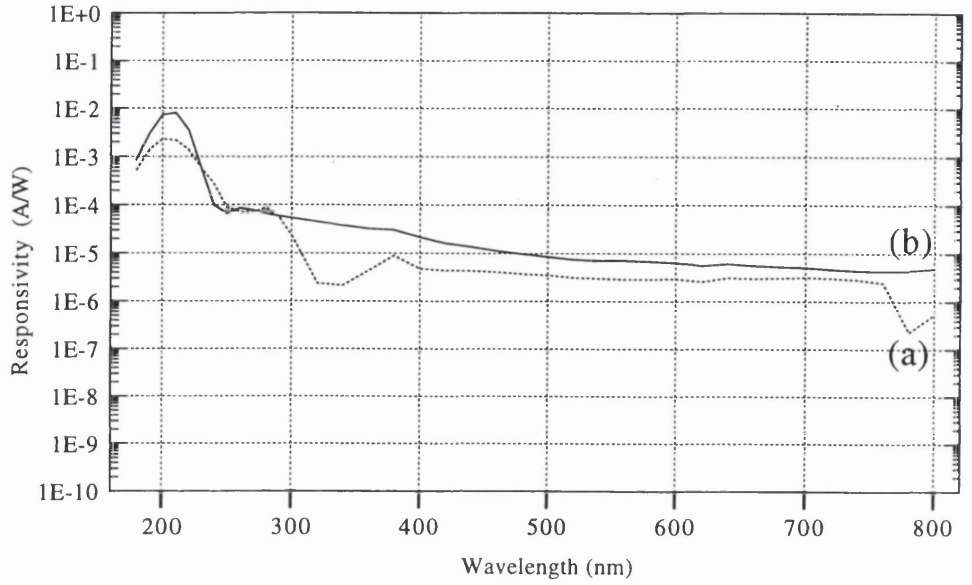

Figure 9.8: Photoresponse characteristics of S_I structures on nitrogen implanted freestanding diamond film (a) as fabricated (b) after a 'type E' treatment.

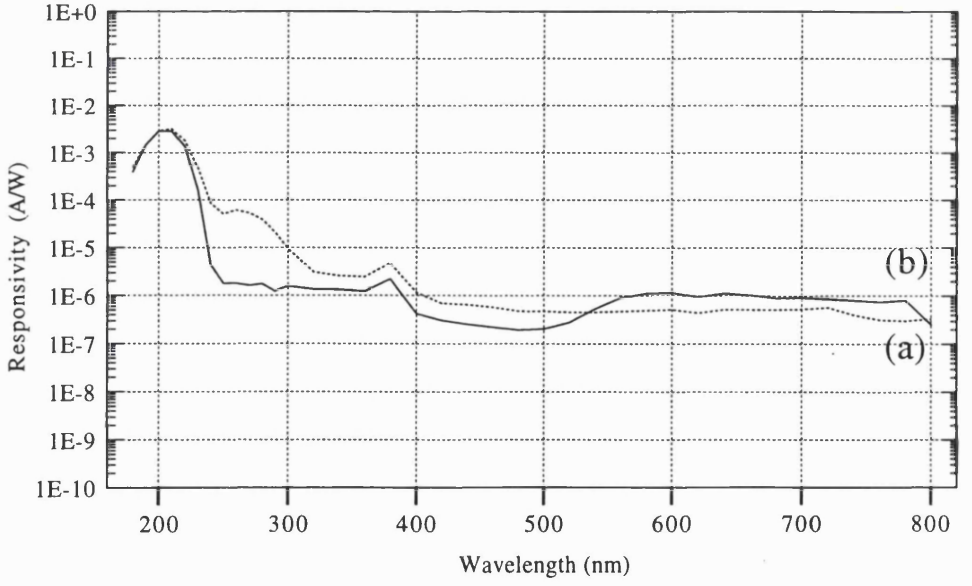

Figure 9.9 : Photoresponse characteristics of T_I structures on boron implanted freestanding diamond film (a) as fabricated (b) after a 'type E' treatment.

The spectral response of the as fabricated S_{III} device shows a fairly uniform sensitivity to all wavelengths in the range 350-800nm as indicated by plot (b) of figure (9.10), however at shorter wavelengths approaching the bandgap no response characteristic is shown on the log scale employed. This is because the differential photocurrent (§4.5.3) of this device in the spectral region 350-180nm is *negative*, indictating that the absorption of higher energy photons is promoting an emptying of traps previously filled either thermally or by absorption of longer wavelengths of light. Treating this device type with a type E process is shown by plots (c) and (d) of figure (9.10) to restore the DUV response of the detector to the condition of a type E processed S_I (N implanted, non-annealed) detector. The IR-visible characteristic of the E-treated S_{III} device type is however highly erratic, as exemplified by the two plots (c) and (d) obtained consecutively in a single analysis session. It is clear that whilst the dramatic DUV activated detrapping of plot (b) no longer occurs after E-treatment, a memory effect is exhibited whereby the response to a given wavelength of excitation may be highly dependent upon the previous illumination history of the sample.

Figure (9.11) charts the dark current passed by this series of nitrogen implanted devices under 10V bias as a function of annealing treatment. The current through the type S_I device approaches a microamp and is moderately *increased* by type E processing, contrary to the observed characteristic of the process on non-implanted diamond. As previously noted, the dark current of the S_{II} device type is very high causing the analysis system to overload at 10V, both before and after E-processing, indicated in figure (9.11) by the solid arrows. The 1100°C annealed S_{III} device is initially more conductive than the non-annealed sample, but after E-treatment becomes highly resistive, indicating that the process has had the passivating/restorative effect that would be anticipated from prior deployments.

For the boron doped samples T_{II} and T_{III} no spectral data is presented, however the dark current is characterised in figure (9.12). T_{II} as fabricated exhibited a noise dominated current during spectral testing, whilst in all other conditions the boron samples are seen to have been too conductive to characterise.

The characteristics of a type U device (silicon backed, non-implanted diamond) are presented in figure (9.13). It can be seen that in the as fabricated condition, the device exhibits an extensive continuum of sub-bandgap sensitivity as anticipated by the discussion of (§9.2) however the 'target' features of figure (9.1) have clearly not been replicated. Furthermore, the application of a type E process to this sample has led to a deterioration in wavelength discrimination and an increase in dark current (not plotted) to the order of microamps at 10V.

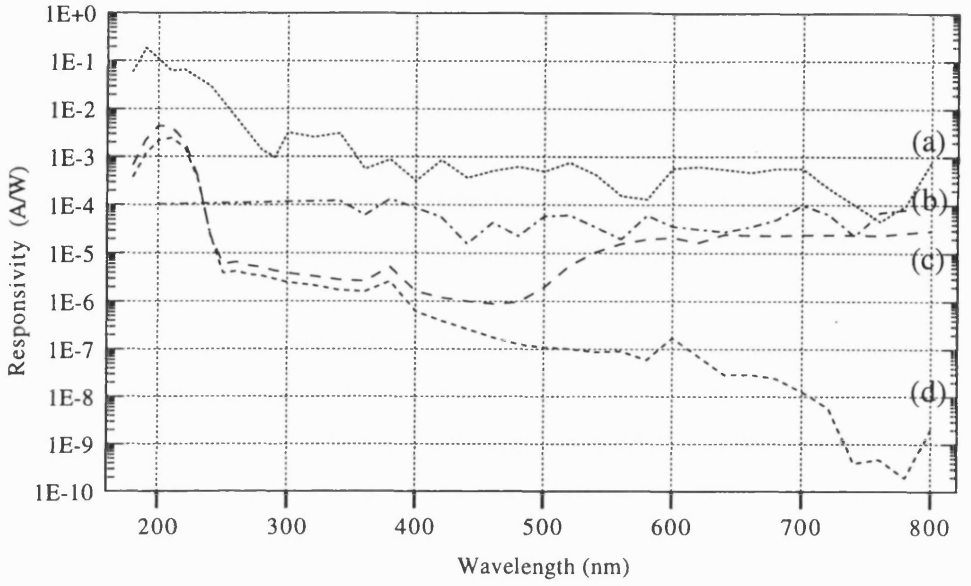

Figure 9.10: Photoresponse characteristics of structures on nitrogen implanted freestanding diamond film (a) S_{II} after 800°C anneal (b) S_{III} after 1100°C anneal (c) & (d) S_{III} after 1100°C anneal and E process.

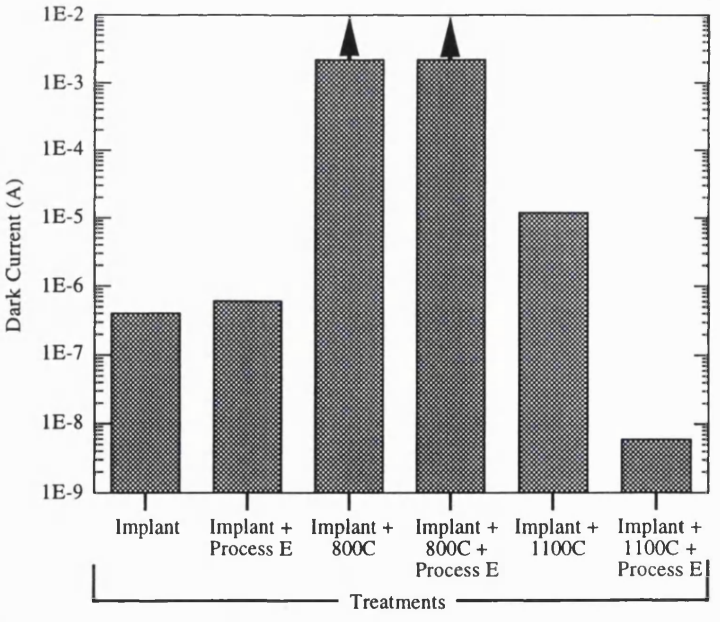

Figure 9.11: Dark current under 10V bias of photoconductors on nitrogen implanted freestanding thin film diamond as a function of processing. Arrow indicates test system driven out of range.

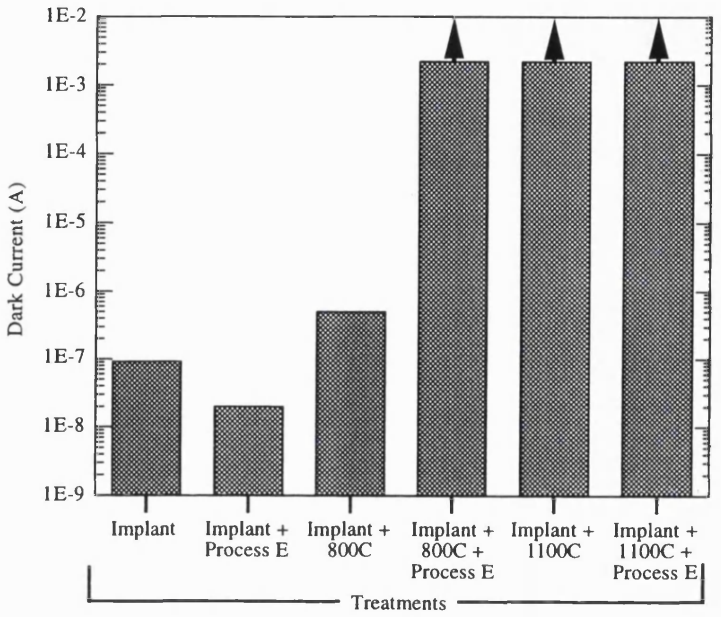

Figure 9.12: Dark current under 10V bias of photoconductors on boron implanted freestanding thin film diamond as a function of processing. Arrow indicates test system driven out of range.

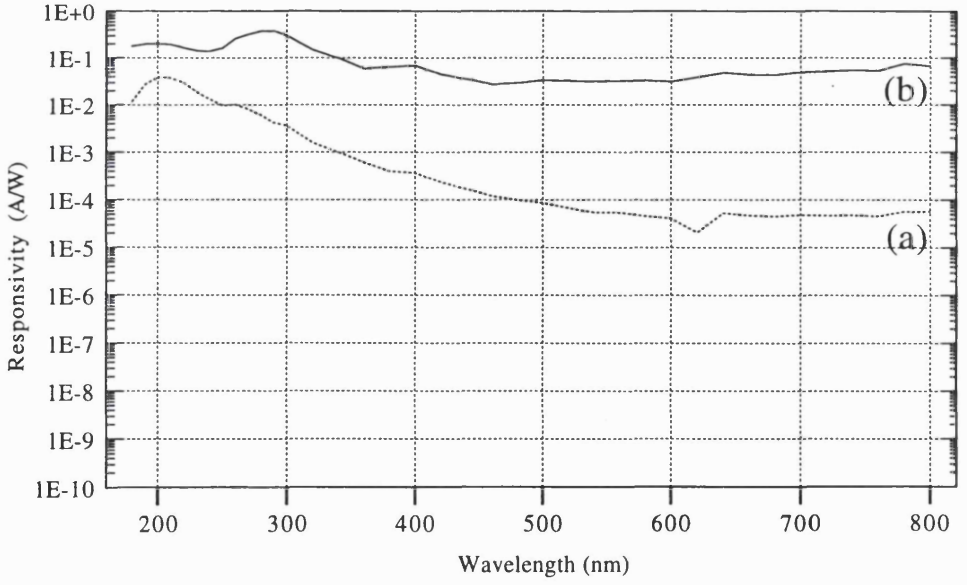

Figure 9.13: Photoresponse characteristics of U structures on undoped polycrystalline silicon backed diamond film (a) as fabricated (b) after a 'type E' treatment.

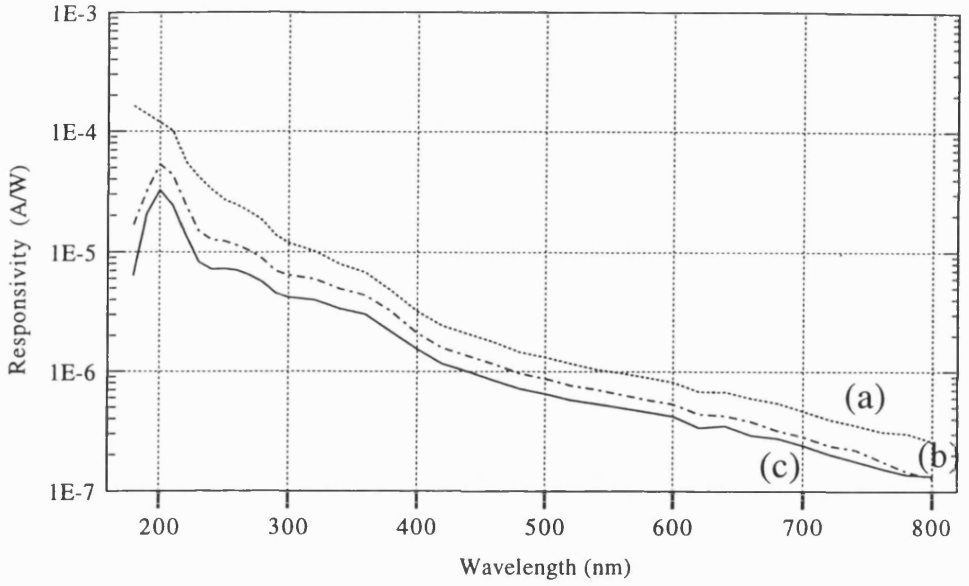

Figure 9.14: Photoresponse characteristics of V structures on undoped polycrystalline silicon backed diamond film after acid cleaning at a range of temperatures (a) 170°C (b) 220°C and (c) 250°C.

During a series of attempts to produce replicates of the type U devices, systematic variations were identified in the characteristics of each batch. Careful evaluation of the equipment configuration and processing conditions deployed suggested that the precise temperature of the acid bath process was the most likely cause of the observed inconsistencies. It is for this reason that an upgraded heating system was acquired and the type V devices were fabricated, the spectral response characteristics of which are presented in figure (9.14). It is clear from figure (9.14) that under the more carefuly controlled conditions, subtle thresholds of sensitivity can be seen in the characteristics of the V type devices. There also appears to be a direct relationship between the temperature at which a type V device is acid bathed and both the shape and amplitude of its spectral response. The extent of the modifications effected by temperature is however small, as might be expected from a non-optimal device geometry (no pseudo-single crystalline effect (§5.4)), on specifically low grade material.

A further brief experiment was therefore performed in which the S_I device type was reproduced as a W type on which the acid bath was performed at temperatures in the range <170°C and >250°C. The result of this study is plotted in figure (9.15) where the higher temperature W_{II} treatment is represented by plot (a) and the lower temperature W_I characteristic by plot (b). It can be seen that whilst the cool processed W_I sample exhibits a sub bandgap response having a clearly discernable threshold, this feature is missing from the characteristic of the W_{II} device.

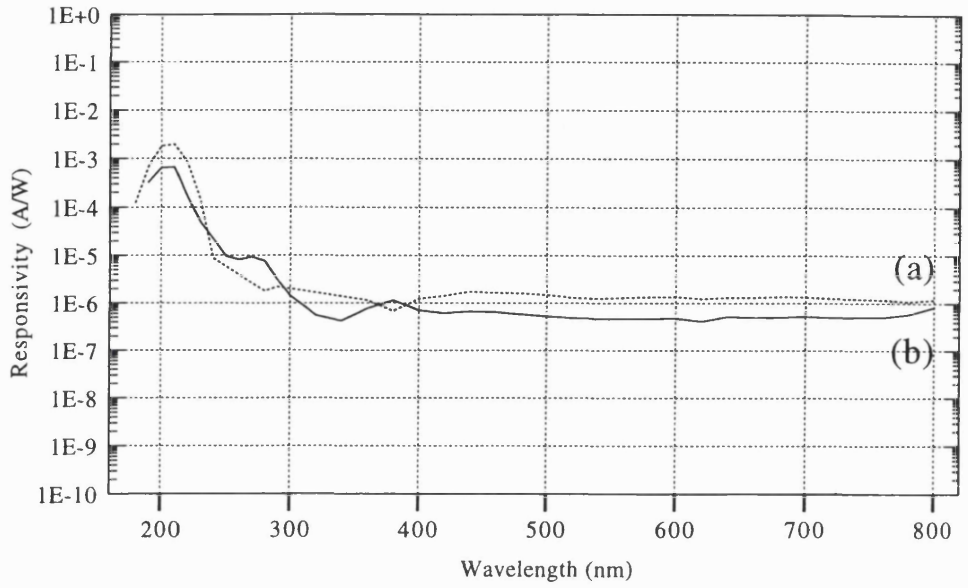

Figure 9.15: Photoresponse characteristics of W structures on nitrogen implanted freestanding diamond film after acid cleaning at (a) >250°C (b) ≤170°C.

9.5 Discussion

It is clear from the results presented above that none of the fabricated structures match the characteristics of the sample targets discussed in (§9.2.1). This is unsurprising and does not in any way undermine the value of the experiments. On the contrary, several informative trends can be identified which combine to help ameliorate the shortage of information previously identified as limiting the options of device designers working with CVD diamond (§9.2.4).

Regarding the implanted films, it has been noted that the characteristics of the as fabricated S_I and T_I device types in figures (9.8 and 9.9) are almost identical. As these samples contain different densities of different impurity species, it must be concluded that the sub-bandgap absorption observed cannot be attributed to either of these factors. Instead the common property of both non-annealed samples is that they are expected to contain extensive implantation damage with many of the implanted impurities located as interstitials, it is therefore proposed that the observed characteristics of these devices should be attributed to implantation damage rather than impurity doping.

After type E processing the characteristics of the two device types become markedly different. The nitrogen implanted S_I loses wavelength discrimintion whilst this is gained by the boron containing T_I sample; throughout this work the bandgap response of both device types remains substantially lower than for the non-implanted devices reported in previous chapters (§6,7). The deduction of implantation damage can be extended to suggest that the heavily implanted S_I sample contained extensive damage, providing a multiplicity of sites onto which carbon or hydrocarbon species could attach in a number of configurations during the type E process, giving rise to a continuum of defect states with corresponding absorption energies. This view is supported by the increase in dark current exhibited by the device after E type processing. In contrast the T_I sample experienced a lower implantation dose and so sustained less extensive damage; the type E process was therefore effective in achieving passivation, resulting in supression of the defect related absorption and a reduction in the dark current.

Although the 800°C anneal applied to sample types S_{II} and T_{II} was anticipated to be insufficient to promote repair of implantation damage or redistribution of the implanted impurity [9.27], it is clear from its effects that it is not benign. The dark current of the nitrogen containing S_{II} is seen in figure (9.11) to be dramatically increased following the anneal and to persist in an enhanced state after type E processing, whilst the (low bias) as fabricated photoresponse showed a broadening of the sensitivity near the bandgap and a deterioration in the rejection of all longer wavelengths. These results may indicate that limited reordering of the damaged material is taking place at this temperature but that the outcome is detrimental to device performance. Based on the suggestion that vacancies and interstitials will both be mobile at temperatures above ≈600°C [9.15] (§2.6.2), it could tentatively be suggested that defects are being redistributed throughout the near implant region, but that insuficient energy is available for lattice repair or the bonding of an impurity into a substitutional site. This explaination may be consistent with the characteristics of the boron containing T_{II} sample which, as fabricated, exhibited a higher dark current than its non-annealed counterpart and under illumination exhibited randomly changing wavelength independent positive and negative currents indicative of extensive filling and emptying of shallow traps. After type E processing the T_{II} sample exhibited a very high conductivity, for which two possible explainations can be offered. Either the E process compounded the redistribution effected by the 800°C anneal by attaching carbon or hydrocarbon species to defect sites, or the cumulative heating effect of the anneal followed by the type E process was sufficient to migrate some of the boron into substitutional locations resulting in p-type conductivity.

There can be little doubt that the 1100°C anneal which was applied to the boron doped T_{III} samples resulted in effective migration and relocation of the dopant, as these conditions mirrored the anneal employed by Kalish *et al.* [9.27] and the devices were found to be highly conductive both before and after type E processing. It is also clear that the nitrogen implanted S_{III} samples were extensively modified by the1100°C anneal as the dark current of these devices was over an order of magnitude greater than for the non-annealed equivalents whilst extensive emptying of traps was observed under illumination in the range 180-35nm. This may indicate that the form of the implantation damage has been changed by the anneal, but that the material remains highly electro-optically defective. After type E processing, the dark current of the S_{III} type device can be seen in figure (9.11) to have have been reduced to the order of nanoamps, which is comparable to some non-implanted detectors on identical material after type E treatment (§6,7). The fact that the improvement in dark current is accompanied by a notable, but less extensive improvement in photoresponse characteristic is indicated in figure (9.10). This would seem to suggest that although the 1100°C anneal and the type E treatment have together enhanced the electronic properties of the sample, the optical properties remain non-ideal.

It is notable that whilst the fully annealed boron implanted samples exhibit a conductivity consistent with the presence of an electrically active dopant, and some nitrogen implanted samples display damage related optical absorption characteristcs, there is no evidence of nitrogen promoted modifications to the photocurrent characteristics of any of the devices analysed. This result, which deviates from the previously discussed (§9.2.1) literature based picture of nitrogen containing diamond may be attributable to one or both of the following problems. It is possible that an insufficient quantity of nitrogen was implanted to create a detectable density of optical absorption centres, however a higher doping density would have led to an unacceptable degree of implantation damage. Alternatively, it is possible that the implanted nitrogen failed to migrate onto lattice sites and persists in the sample primarily as an interstitial impurity. This view may be supported by the combined low dark current and sub-bandgap snsitivity of E-treated S_{III} samples, as these characteristics could indicate distortion of the lattice consistent with a high density of interstitials. In either case, it is not immediately apparent that alternative implantation conditions or annealing steps could be chosen to yield a different outcome, from which it follows that *in situ* doping appears to be a more likely prospect for the creation of heavily nitrogen doped diamond films. The author's successor is currently investigating this possibility, within the previously identified constraints (§9.2.2) imposed upon the CVD growth conditions by the presence of nitrogen.

Thin film device type U offered little of interest in its initial photoresponse characteristic, however the deterioration in performance caused by type E treatment serves to confirm that this kind of processing cannot universally improve all types of defective diamond. The value of this result is that it lends weight to the proposal above, that 1100°C annealing of the S_{III} samples resulted in a modification of the defects into a form which could be effectively treated by the type E process. An interesting further experiment, which was not carried out due to time constraints, would be to investigate the outcome of 1100°C annealing type U material prior to device fabrication and E processing.

The dependence of the photoresponse characteristics of theV and W type devices on the precise temperature at which they were acid bathed confirms that both films have a considerable NDC content, as it is this material which the acid bath is known to remove (§4.2.2). Conversely, it may be proposed that the spectral response characteristic of a diamond photodetector may be modified by the deliberate insertion, creation or deposition of carefully controlled NDC regions. In essence, this perspective has already been acknowleged throughout the chapter, in that the discussion of damage related absorption is in effect NDC absorption by a different name. The value of the V and W results however is to suggest that the wavelength discrimination of a given NDC containing substrate can be to some degree 'tuned' by variation of the processing temperature, potentially offering a cheap and simple method of creating a wide range of device characteristics to order from a simple and limited library of substrates. To determine the practicality of this approach, a series of further investigations should be undertaken to establish the 'hardness' of the modifications introduced into the device, and to identify specific forms of NDC which could be related to particular absorption characteristics.

9.6 Conclusions

Investigations have been undertaken to explore the potential for modifying the wavelength sensitivity of photodetectors on freestanding undoped CVD diamond by the introduction of impurities using ion implantation. It was found that identical characteristics could be obtained from samples implanted with boron and nitrogen in different doses, indicating that the changes observed were due to implantation damage rather than the the creation of impurity related extrinsic photoconductivity phenomena.

It is believed that the failure of nitrogen implanted CVD tiles to exhibit the absorption characteristics reported elsewhere for Ia diamond was due either to an insufficinet doping density, or a failure of the implant to migrate to substitional lattice sites when annealed. it is therefore proposed that future work should include an investigation of the photoconductive properties of *in situ* nitrogen doped films.

Results obtained from both low quality undoped diamond film and implantation damaged freestanding tiles, indicated that precise control of the NDC content could be achieved by variation of the temperature of the acid cleaning step commonly employed in the fabrication of diamond electronic devices. A demonstrable degree of control was exerted over the sub-bandgap photoresponse characteristrics of defective diamond films in which the NDC content had been varied by means of the processing discussed above.

9.7 References

9.1 P. Denham, E.C. Lightowlers and P.J. Dean, Physical Review 161, 762 (1967).

9.2 S.F. Kozlov, R. Stuck, M. Hage-Ali and P. Siffert, IEEE Transactions on Nuclear Science 22, 160 (1975).

9.3 C.P. Beetz Jr. and S.H. Tan, SPIE 1759, 156 (1992).

9.4 R. Vaitkus, T. Inushima and S. Yamazaki, Applied Physics Letters 62, 2384 (1993).

9.5 L. Allers and A.T. Collins, Journal of Applied Physics 77, 3879 (1995).

9.6 Y. Aikawa, K. Bab, N. Shohata, H. Yoneda and K. Ueda, Preprint presented at "Diamond Films '95", Albufiera, Portugal, proceedings published as Diamond and Related Materials (1996).

9.7 E. Pace, F. Galluzzi, M.C. Rossi, S. Salvatori, M. Marinelli and P. Paroli, Nuclear Instruments and Methods in Physics Research A 387, 255 (1997).

9.8 S. Salvatori, E. Pace, M.C. Rossi and F. Galluzzi, Diamond and Related Materials 6, 361 (1997).

9.9 H.O. Pierson, "Handbook of Carbon, Graphite, Diamond and Fullerenes: properties, processing and applications", Noyes Publications, New Jersey, 1993.

9.10 M. Werner, O. Dorsch, H.U. Baerwind, E. Obermier, L. Haase, W. Seifert, A. Ringhandt, C. Johnston, S. Romani, H. Bishop and P.R. Chalker, Applied Physics Letters 64, 595 (1994).

9.11 M.D. Whitfield, S.S.M. Chan and R.B. Jackman, Applied Physics Letters 68, 290 (1996).

9.12 M.C. Rossi, Oral presentation at EMRS Spring Meeting, Strasbourg June 1996.

9.13 S. Salvatori, Oral presentation at Diamond Films '97, Heriot Watt University, Edinburgh, UK August 1997.

9.14 J.I. Pankov, "Optical Processes in Semiconductors", Prentice-Hall International (1971) and Dover (1975).

9.15 J. Wilks and E. Wilks, "Properties and Applications of Diamond", Butterworth-Heinemann, Oxford, 1991.

9.16 T.H. Borst and O. Weis, Private communication: pre-print distributed at 5th European Conference on Diamond, Diamond-like and Related Materials, Il Ciocco , Italy, 25-30th September 1994, but not included in proceedings.

9.17 K. Okano, H. Kiyota, T. Iwasaki, Y. Nakamura, Y. Akiba, T. Kurosu, M. Iida and T. Nakamura, Applied Physics A 51, 344 (1990).

9.18 T. Nishimori, K. Nakano, H. Sakamoto, Y. Takakuwa and S. Kono, Applied Physics Letters 71, 945 (1997).

9.19 S. Koizumi, M. Kamo, Y. Sato, H. Ozaki and T. Inzuka, Applied Physics Letters 71, 1065 (1997).

9.20 W. Zhu, "Defects in Diamond", in "Diamond: Electronic Properties and Applications", Ed. L.S. Pan and D.R. Kania, Kluwer Academic Press, Massachusetts, USA, 1995.

9.21 J.A. Freitas Jr, K. Doverspike, P.B. Klein, Y.L. Khong and A.T. Collins, Diamond and Related Materials 3, 821 (1994).

9.22 R.S. Tsang, C.A. Rego, P.W. May, M.N.R. Ashfold and K.N. Rosser, Diamond and Related Materials 6, 247 (1997).

9.23 H. Chatei, J. Bougdira, M. Remy, P. Alnot, C. Bruch and J.K. Krüger, Diamond and Related Materials 6, 505 (1997).

9.24 S.M. Sze, "Physics of Semiconductor Devices", Wiley, New York, 1981.

9.25 A.T. Collins and E.C. Lightowlers, Physical Review 171, 843 (1968).

9.26 R. Kalish, C. Uzan-Saguy, A. Samoiloff, R. Locher and P. Koidl, Applied Physics Letters 64, 2532 (1994).

9.27 R. Kalish, C. Uzan-Saguy, B. Philosoph, V. Richter, J.P. Lagrange, E. Gheeraert, A. Deneuville and A.T. Collins, Diamond and Related Materials 6, 516 (1997).

9.28 S.M. Sze, "Semiconductor Devices: physics and technology", Wiley, New York, 1985.

9.29 M.S. Dresselhaus and R. Kalish, "Ion Implantation in Diamond, Graphite and Related Materials", Springer-Verlag, Berlin, 1992.

9.30 J.F. Prins, Material Science Reports 7, 271 (1992).

9.31 D. Masse, J. Bouchard, J-L. Picolo, N. Coursol, J.P. Torre, J.W. Zhou, N. Coron, P. de Marcillac, J. Leblanc and H. Stroke, Nuclear Instruments and Methods in Physics Research A 339, 131 (1994).

9.32 R.A. Spits, J.F. Prins and T.E. Derry, Nuclear Instruments and Methods in Physics Research B 85, 347 (1994).

9.33 D.R. Kania, M.I. Landstrass, M.A. Plano, L.S. Pan and S. Han, Diamond and Related Materials 2, 1012 (1993).

9.34 A.T. Collins, Semiconductor Science and Technology 4, 605 (1989).

9.35 N. Montgomery and C. Johnston, "Boron and Nitrogen Implants into Diamond Films", Commercial Report, AEA Technology plc, July 1997.

9.36 D.L. Dreifus, "Passive Diamond Electronic Devices", in "Diamond: Electronic Properties and Applications", Ed. L.S. Pan and D.R. Kania, Kluwer Academic Press, Massachusetts, USA, 1995.

10 THIN FILM DIAMOND DEVICES FOR THE DETECTION OF ALPHA PARTICLE RADIATION

10.1 Introduction

There are many anticipated advantages to using diamond as a solid state detector of alpha particle radiation. As discussed in the review chapter (§3) particular importance is attached to diamond's hardness to gamma and neutron irradiation (§3.3) and its resistance to physical and chemical attack in hostile environments.

This chapter describes the investigation of thin film diamond alpha particle detectors having two distinctly different geometries: the standard bulk configuration as used for silicon and germanium particle detectors is compared to a surface planar device based upon the ultraviolet photodetector structures presented in previous chapters.

10.2 Experimental Design

Solid state alpha particle detectors fabricated from conventional materials such as silicon suffer extensive damage and consequent degradation of performance when exposed to relatively low levels of radiation (<100 kRad). Diamond is considerably more resilient although the extent of its radiation hardness has not yet been fully quantified and has long been considered a promising material for radiation detector applications (§3.3.3). The recent emergence of chemical vapour deposition (CVD) techniques for the growth of thin films of diamond (§2.3.3) has made the fabrication of diamond radiation detectors commercially and technically interesting, however the polycrystalline nature of contemporary films which compromises the performance of all existing thin film diamond devices is particularly relevant in the field of radiation detection. This is because the alpha events to be detected are likely to lead to the creation of much smaller and more rapidly evolving charge clouds than the optical absorption of bandgap radiation. It is therefore relevant to investigate whether the careful device design (§5) and material treatment (§6) which has enabled high performance UV photodetectors to be realised may also be applied to diamond alpha particle detectors. Thin film diamond alpha particle detectors have previously been reported elsewhere although to date poor collection efficiencies and hence poor sensitivities have been demonstrated [10.1, 10.2].

At the outset of the experimental design, it is necessary briefly to review the anticipated mode of operation of the diamond detector and the type of output which will be required from the device. Alpha particle detectors, like other nuclear radiation sensors, are required to furnish answers to one or more of a series of questions depending upon the particular application. The three modes of deployment for alpha particle detectors are outlined in table (10.1) in the form of three basic questions, the reason for asking each question and the means by which a sensor typically provides the required answer.

Within a particular application it is not uncommon for combinations of different detectors to be used in order to achieve the required coverage of the three detection modes tabulated. Often for example, detection takes place in a controlled environment which can only contain one or two known isotopes so that spectroscopy is not required. A large area device may be used for detection of contaminated material during a screening process (perhaps on a conveyor belt) whilst a pulse counting detector may record the activity of static samples selected from the conveyor when the initial detector has been triggered. In many cases the practical constraints of an application prevent complete collection of data from all three device operating modes: spectroscopy for

example cannot be undertaken if the emitting species is embedded or suspended in another material as this will attenuate the alpha particle energy to some depth dependent extent and thereby mask the true energy of the emission.

Semiconductor radiation detectors made from germanium or silicon (drift compensated with lithium) are available commercially, but suffer from the disadvantages previously discussed. Diode structures (both bipolar and Schottky) are used in a reverse biased configuration to minimise dc leakage and typically take the form of a parallel-electrode bulk device as sketched in figure (10.1) [10.3].

Mode	*Question*	*Physical Interpretation*	*Sensor Output*
Detection	Is a source in view?	Is contaminated material being detected?	Signal on/off (pulses or no pulses)
Pulse counting	How active is the source?	How much contaminated material is present?	Signal rate/unit time (pulses/second)
Spectroscopy	How energetic is the source?	What is/are the contaminating species?	Signal amplitude (pulse height)

Table 10.1: Characteristic modes of operation and application of nuclear radiation detectors

Whilst the high intrinsic resistivity of diamond means that a diamond alpha detector need not be rectifying to achieve low dark current, early diamond devices for alpha particle detection have mimicked the parallel-electrode structure of the existing solution [10.1, 10.4]. It may be anticipated however from reference to figure (4.3) and the discussion of (§5.4.1) that such a geometry implemented in contemporary thin film diamond will be very inefficient in terms of charge carrier collection. It is therefore proposed that a planar structure as used for the photodetectors previously presented in this thesis may offer the prospect of a sensitive and more efficient alpha detecting device.

The performance of a solid state alpha detector is strongly controlled by the efficiency with which carriers are sensed in or removed from the diamond film. Consequently it is desirable to engineer devices such that the mean carrier drift length is increased; this can be achieved by improving carrier mobility (μ) and lifetime (τ) values since the drift distance is the product of these terms multiplied by the electric field strength (§2.6.3). For high performance detectors this distance should be larger than the active region of

the device in order to allow maximum charge collection. For state-of-the art CVD material a value of ~200μm has been reported for beta particles at minimum ionising energy impinging on a 1mm thick film [10.5]; this represents a drift distance of around 20% of the thickness of the detector. However, drift distances within typical CVD films are reported to be in the range 1-20μm [10.6].

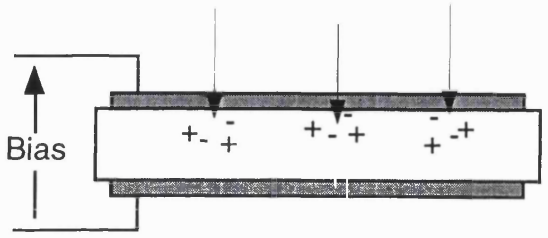

Figure 10.1: Schematic of bulk semiconductor particle detector using a parallel-electrode geometry. [After 10.3].

An alternative method for improving the performance of CVD diamond detectors is to reduce the separation between the device electrodes with the aim of better matching detector dimensions to the mean free drift distances that can be achieved. In the context of a bulk device this suggests the use of very thin diamond membranes, however such material is unlikely to offer useful electronic characteristics: if an inherently thin film is grown then it will be dominated by the highly defective nucleation region, whilst a thick film which has been mechanically thinned will be electronically damaged as discussed elsewhere (§5).

Considering instead an interdigitated surface planar geometry, it will be appreciated that a detector may benefit from closely spaced electrodes on the unmodified surface of the better quality growth region of a film. A trade-off can be anticipated in that the rough nature of the diamond surface coupled with a penetration depth of alpha particles in diamond of ≈15μm [10.7] will lead to considerable anisotropy of the electric field within the sensitive volume of the planar detector. This variation in the field will lead to non-uniform detection of charge clouds within the material so that spectroscopy by means of pulse height analysis will not be possible with such a device. This limitation is not however a severe one in the light of the preceding discussion on the operating mode requirements of different applications. It may additionally be noted that even a bulk diamond detector will support an inhomogeneous field due to the thickness variations caused by the roughness of the growth surface, however in this instance the

inhomogeneity will be proportionally much smaller than in the case of the surface planar device.

10.3 Experiment

To investigate the possible benefits of using a surface planar (photodetector style) device geometry for alpha particle detection, three samples of freestanding undoped polycrystalline MPACVD diamond tiles identical to those previously described (§5, 6) were prepared as summarised in table (10.2). All three were subjected to standard cleaning processes (§4.2.1, 4.2.3) prior to metalisation. Continuous gold electrodes (≈50nm) were deposited by thermal evaporation onto both the nucleation and growth surfaces of device type X and onto the nucleation side of device type Z whilst a thicker deposition of ≈500nm was made onto the growth surfaces of device type Y and Z. Device types Y and Z were lithographically patterned with a standard interdigitated electrode structure on the growth surface (§4.5.3) to yield samples having the characteristics indicated in figure (10.2). The type E process (§6.3) was then applied to all three samples.

Sample	*Acid Clean*	*Electrode Geometry*	*Process E*
X	Yes	Parallel plates	Yes
Y	Yes	Surface planar	Yes
Z	Yes	Parallel plates (rough is patterned)	Yes

Table 10.2: The preparation of samples used to investigate the alpha particle detection capabilities of bulk and planar CVD diamond devices. Electrode geometries are shown schematically in figure (10.2).

Devices were characterised *in vacuo* by exposure to 5.5MeV alpha particles from a 0.34μCi ^{241}Am source which emitted 1.369×10^4 α/second into a hemispherical volume. Standard NIM (Nuclear Instrumentation Module) electronics were used to monitor detector response and co-axial cables were used for all experiments to minimise the pick-up of noise. The device under test was connected to an Ortec 142C charge sensitive pre-amp for signal collection and application of the bias voltage from an HV supply module. The pre-amp output was conditioned by a shaping amplifier (typical gain ≈500, shaping constant 2μs) and then presented to both an oscilloscope for general

signal confirmation and a PC controlled MCA (Multi Channel Analyser) for pulse height monitoring. This system is outlined schematically in figure (10.3).

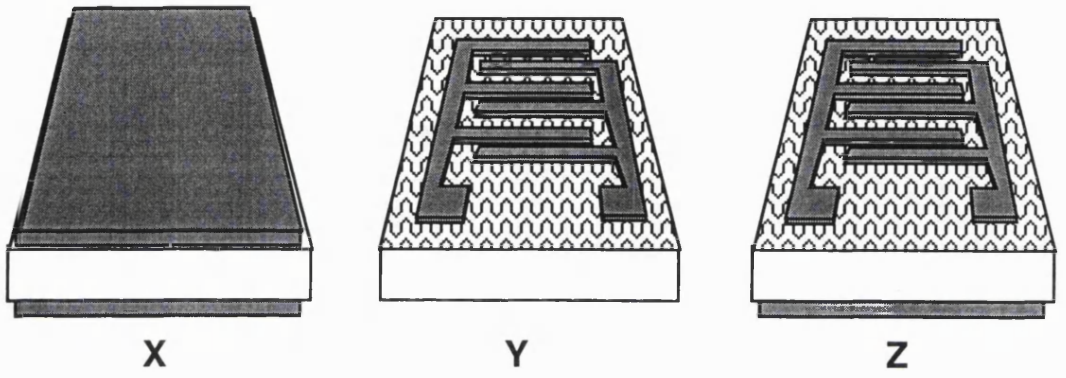

Figure 10.2: Schematic representations of the three device geometries fabricated for diamond alpha particle detector experiments.

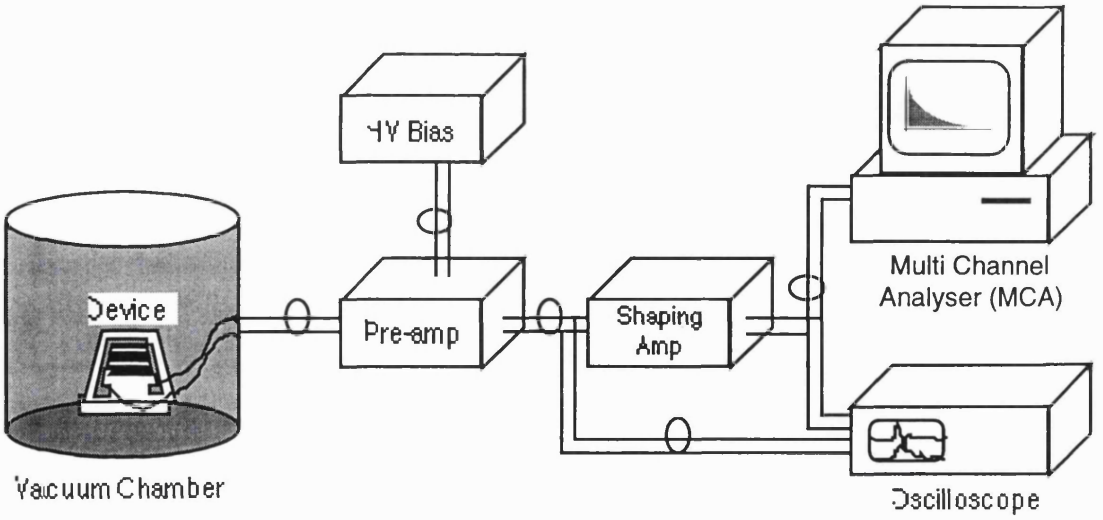

Figure 10.3: Schematic of the experimental arrangement for alpha particle detection using thin film diamond sensors and standard NIM signal processing equipment.

10.4 Results

A typical pulse response obtained from device type Y operating in the planar mode under 60 volts d.c. bias is presented in figure (10.4). The pre-amp output is shown as channel 1 (upper trace) and it is clear that on detection of an alpha particle this signal rises rapidly and then falls steadily. The rising transient represents the real-time evolution of the charge cloud whilst the decay is a function of the amplifier electronics [10.8].

The lower trace of figure (10.4) shows the output of the shaping amplifier where the temporal evolution data from the pre-amp response has been discarded to yield an amplified pulse, the height of which is directly proportional to the quantity of charge created in the device by a single alpha absorption event. As an alpha particle carries a fixed quantity of energy, in this case 5.5MeV, it might be anticipated that each absorption event will lead to an identical number of electron-hole pairs being created in the detector volume and hence to an identical pre-amp output pulse. For this ideal condition the shaping amplifier output will then consist of a train of pulses having an identical amplitude which is directly proportional to the energy of the monoenergetic source.

In the present experiment the ideal case may not be achieved for several reasons. An experimental artefact arises in the form of the decay time constant of the preamp input circuit which can cause pulse 'pile-up'. This condition occurs when the peak from a newly detected event is superimposed upon the decaying tail of the previous event with the result that the new peak amplitude will not accurately reflect the size of the charge cloud in the detector. Pulse pile-up is illustrated in figure (10.5) for a type Y detector operating under a 30μCi ^{241}Am source.

The counts-energy characteristics as recorded by the MCA for both the type X and Y detectors under identical electric fields of 1.5×10^4 V/cm are plotted in figure (10.6). It is clear from the population of channels beyond 500 within the MCA spectrum that the planar device Y presents pulses of considerably greater amplitude to the MCA than is achieved by the sandwich device X.

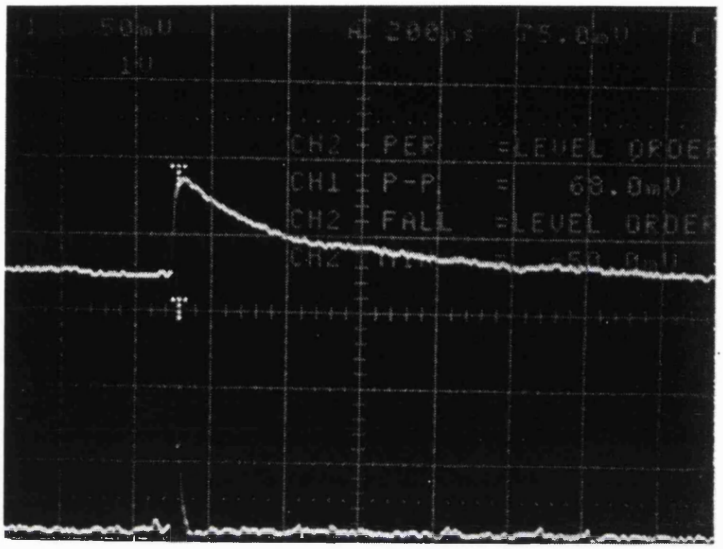

Figure 10.4: Oscilloscope plots of preamp (top) and shaping amp (bottom) output when an alpha particle is detected in a diamond sensor

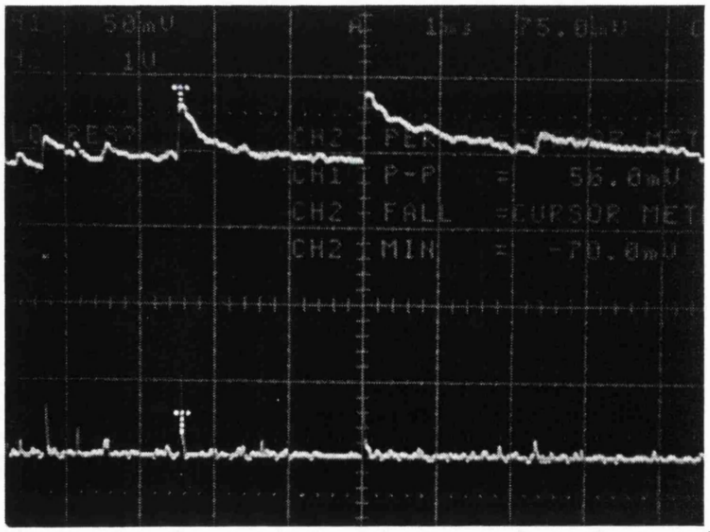

Figure 10.5: Oscilloscope plots of preamp (top) and shaping amp (bottom) output when several alpha particles are detected by a diamond sensor.

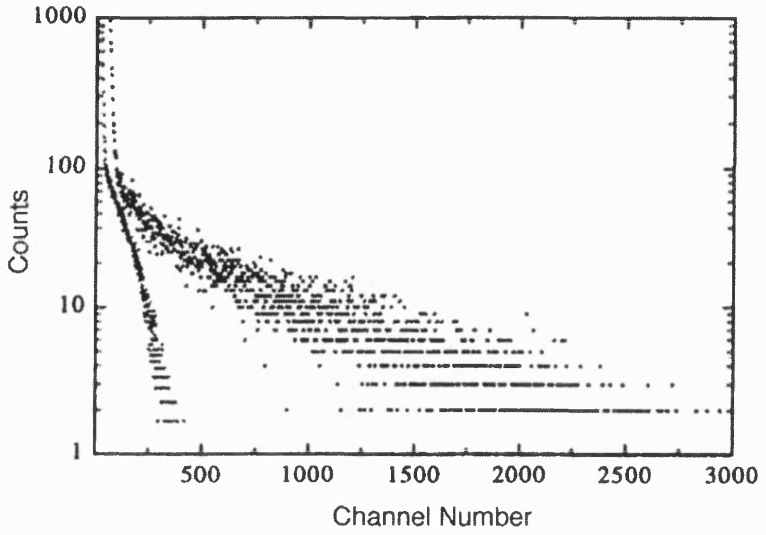

Figure 10.6: MCA spectrum ('counts-energy curve') for a type X sandwich diamond detector (left hand plot) and a type Y planar diamond detector (right hand plot) exposed to a ^{241}Am source *in vacuo* at a bias field of 1.5×10^4 V/cm.

Separate MCA spectra for the planar and bulk configurations of the type Z device are presented in figures (10.7) and (10.8) respectively. As can be expected, figure (10.7) confirms the device Y result indicating that a planar electrode structure enables a greater number of high energy pulses to be recorded whilst figure (10.8) confirms the device X characteristic of detecting pulses over a more narrow energy range. An interesting feature of figure (10.8) is the emergence of a peak in the counts-energy curve which is clearly separate from the low energy noise signal.

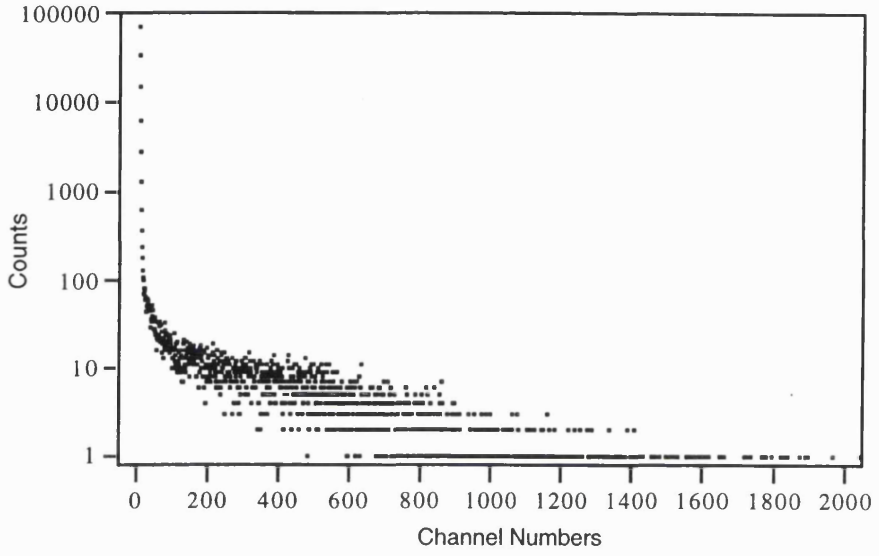

Figure 10.7: MCA spectrum for a type Z device operated in planar mode under exposure to 5.5MeV ^{241}Am alpha particles and a detector bias field of 2.4x10^4 V/cm.

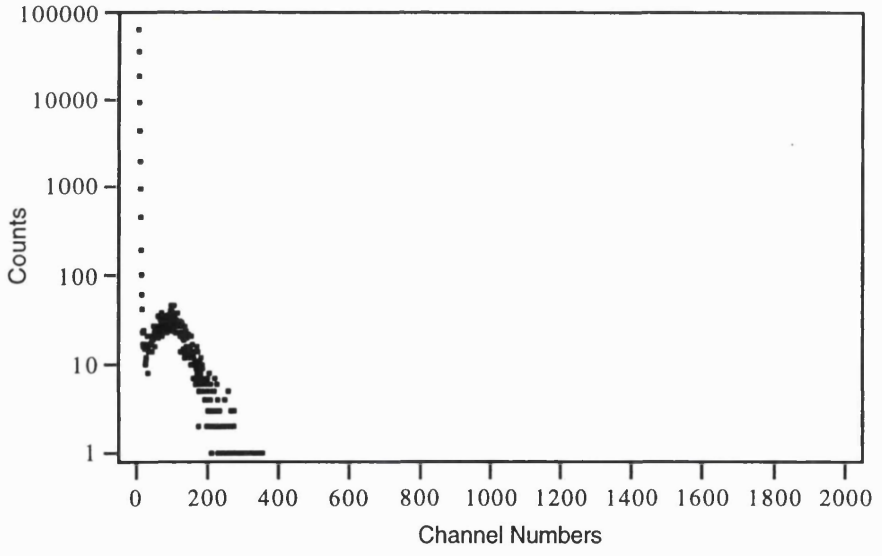

Figure 10.8: MCA spectrum for a type Z device operated in sandwich mode under exposure to 5.5MeV ^{241}Am alpha particles and a detector bias field of 2.4x10^4 V/cm.

10.5 Discussion

The counts-energy curves for device types X and Y presented in figure (10.6) show no clear peaks, thereby confirming the expectation of (§10.2) that charge clouds created by monoenergetic radiation will not be uniformly detected by polycrystalline diamond devices. Although pulse-pileup as presented in figure (10.5) is an acknowledged phenomenon affecting detector performance, it is unlikely that this is the main cause of the peakless spectra as this example was obtained for illustrative purposes by use of a source 100 times as active as the standard experimental source. Instead, it is more likely either that some of the mobile charges were lost through near-instantaneous recombination before they could be detected, indicating poor electrical transport properties in the detector material, or the charges were deposited into a region of the detector which was devoid of electric field, indicating poor detector design.

The fact that the charge collection efficiency of these detectors is found to vary for identical excitations leads to a reassertion that the devices will not be suitable for spectroscopic applications. If instead the devices are to be useful for pulse counting applications it becomes relevant to consider the detection efficiency of the structures. This is quantified by expressing the number of counts (regardless of energy) recorded in each detector as a proportion of the number of alpha particles which have been incident upon (and therefore absorbed in) the detector during the experiment.

Calibration of the detected charge compared to that created within the detector indicates an efficiency of 40% for the planar type Y device compared to 10% for bulk type X device. A doubling of the bias field to 3.2×10^4 V/cm raised the efficiency of the type Y device to 70% whilst that of the type X device showed little improvement beyond 10% as the potential field applied was increased. The important implication of this result combined with the counts-energy curve of figure (10.4) is that whilst the bulk detector offers a more uniform pulse amplitude response, the planar electrode pattern sees four to seven times as many alpha events during a given exposure as can be recorded by the bulk geometry.

Considering now the characteristics of the planar and bulk operating modes of the type Z device shown in figures (10.7) and (10.8), it is informative to calibrate the horizontal axes in terms of the effective energy which corresponds to a given channel number. Using a pulser to simulate the deposition of 0.5MeV alphas into silicon results in a peak appearing at channel 420; allowing that 3.6eV is required to create an electron-hole pair

in a silicon detector compared to 13eV in diamond, this indicates that a peak at channel 420 would represent 1.8MeV alphas being detected in diamond. Correspondingly, in a tottally efficient device absorbing 5.5MeV alphas the peak would be expected to appear at channel 1283.

There is clearly no peak on the counts-energy plot of figure (10.7) at any channel number, however the fact that channels right up to number 2048 are populated indicates that some (few) events appear to be giving rise to more than the theoretical maximum number of charge carriers. There is no comprehensive explanation for this observation however it is possible that some form of gain mechanism similar to the previously discussed photoconductive gain (§5.3.2) may be taking place. It is most probable however that the effect is a result of the field distribution within the device - this will be analysed in more detail later in this section.

The peak visible on figure (10.8) is centred about channel number 98 and can be used to estimate the carrier collection efficiency of the material used in this device. As every incoming alpha had energy of 5.5MeV every charge cloud will have been of the same amplitude. According to the preceding calibration exercise, if each of these charge clouds had been efficiently collected the resulting pulses would all have appeared on channel 1283, instead however the modal pulse amplitude is centred about channel 98. This suggests that on average, most of each 1283 sized pulse will be lost through recombination so that by the time it is detected it appears only to be a 98 sized pulse. The carrier collection efficiency within the detector is therefore a relatively low (98/1283)*100=7.64%. This result should not be too surprising however as it must be remembered that carriers collected in this mode of operation must pass through the highly defective nucleation region of the film where extensive recombination is anticipated.

To summarise the above discussion, it can be said that the bulk structure achieves a low detection efficiency of ≈10% which is independent of applied field whilst the planar structure records a higher detection efficiency of 40-70% depending upon bias. The poor bulk detection efficiency may be related to the relatively low carrier collection efficiency of 7.6% however the lack of a modal pulse amplitude from the planar device prevents a comparison of carrier collection efficiencies between the two geometries.

Whilst the electric field distribution in the bulk device structure is relatively straightforward, it can be anticipated that a more complex situation operates within the planar device. Using a finite element simulation code [10.9], the field distribution

profile within the planar device has been studied and is shown in figure (10.8) to vary substantially both across the surface of the detector and with increasing depth beneath the surface. This two-dimensional variation in field has been extracted from the colour coded plot of figure (10.8) and is presented as the third axis in figure (10.9).

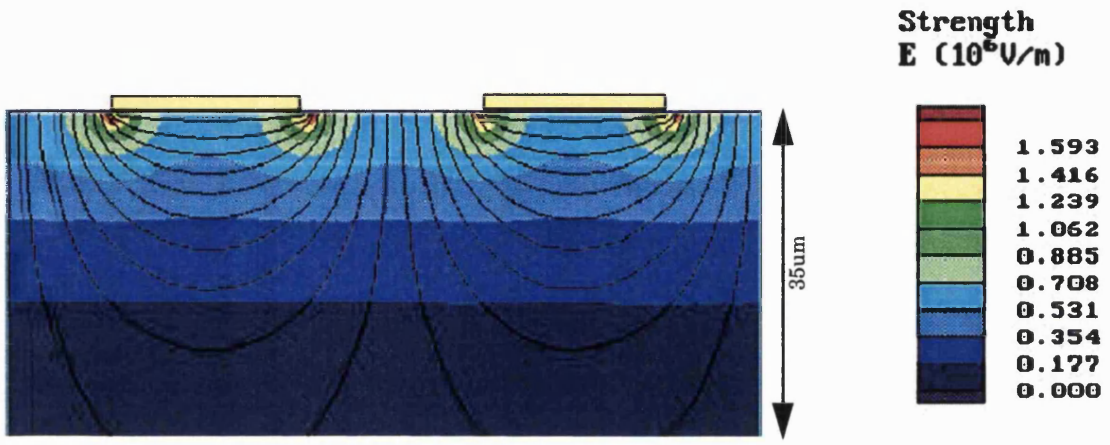

Figure 10.9: Finite element simulation of electric field strength and equipotential lines within a device having surface planar electrodes 20μm wide on a 40μm pitch.

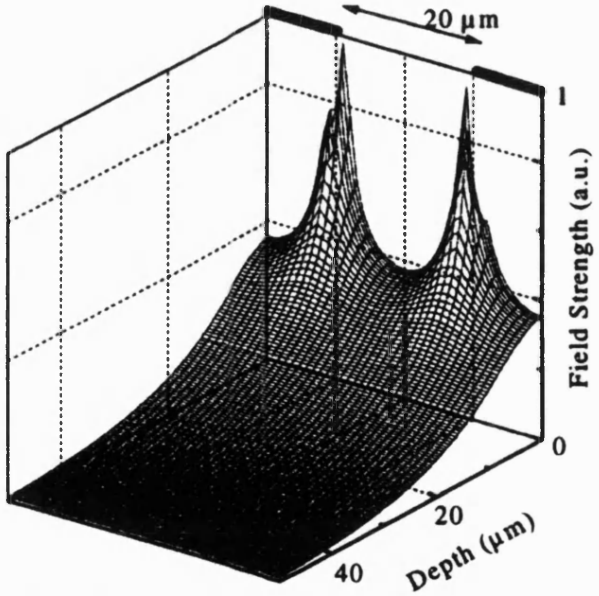

Figure 10.10: Electric field strength with respect to electrode spacing and detector depth extracted from the finite element simulation of a planar detector structure presented in figure (10.9)

The inhomogeneity of the field within the detector is clear as it varies by up to 62% across the surface of the device and by more than 87% between the peak surface value and the minimum value encountered one electrode depth (20μm) beneath the surface. although the energy deposited by an incoming alpha particle (and therefore the charge creation) is weighted towards the final ≈5μm of travel as described by the Bragg curve [10.8], when this field variation is taken into account we see a greater relative contribution from charge created in the surface region. This is the origin of the higher signal strengths seen in the planar device and therefore any system that maximises this effect would be desirable.

For a given detector area a significant proportion of the bulk of the device exists at very low field strengths and it becomes relevant to consider how this situation may be improved to achieve maximum and more uniform fields throughout the active region of the detector. One possibility is to explore the option of physically rearranging the electric field within the device by recessing the electrode structures into the surface of the detector. This approach has been simulated for recess depths of both 5μm and 10μm and the resulting field strength profiles are presented in figures (10.11(a) and (b)) respectively.

The simulations indicate that the recessed structures could offer two distinct advantages over the simple surface planar electrode format. The greater uniformity of field between electrodes indicated most clearly in figure (10.11(b)) could be anticipated to greatly enhance the uniformity of carrier collection within the sensitive region of the device. This would result in a greater pulse height uniformity and could therefore render such devices suitable for spectroscopic functions in addition to the present possibility of pulse counting applications. The second advantage indicated by both simulations of recessed electrodes is the greater amplitude of the field strength shown for the bulk of the region between each set of electrodes. Whilst the surface planar arrangement showed regions of greater peak field, particularly due to edge effects, a consequence of dropping the electrodes into the bulk of the diamond film is to move these edges away from the main sensitive region and allow a greater field to apply across most parts of the device where detection is required to occur.

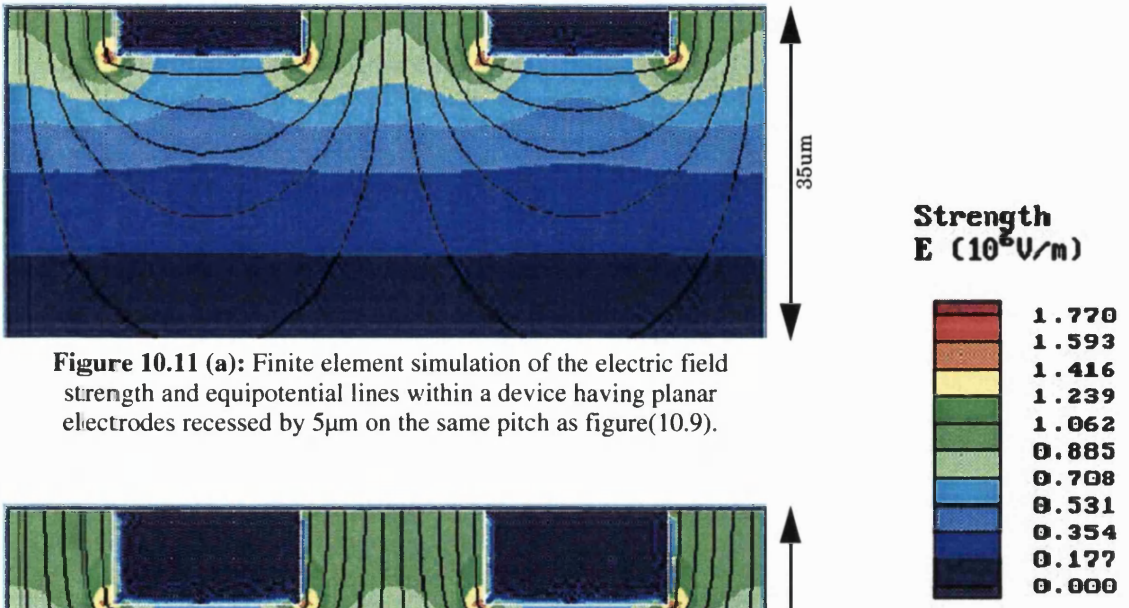

Figure 10.11 (a): Finite element simulation of the electric field strength and equipotential lines within a device having planar electrodes recessed by 5μm on the same pitch as figure(10.9).

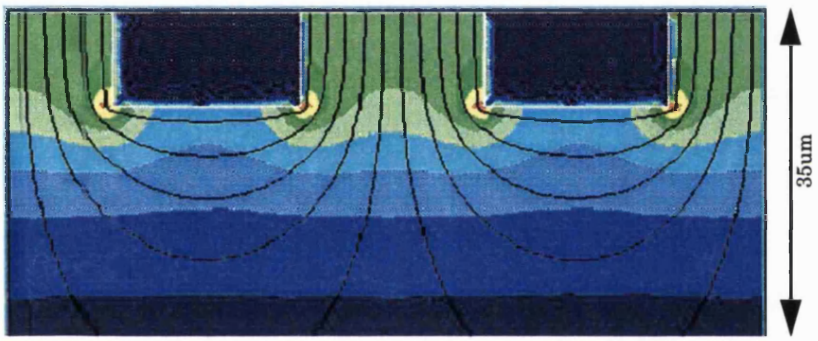

Figure 10.11 (b): Finite element simulation of the electric field strength and equipotential lines within a device having planar electrodes recessed by 10μm on the same pitch as figure(10.9).

10.6 Conclusions

The response of thin film diamond detectors to monoenergetic alpha particle irradiation has been investigated using both the traditional bulk geometry and the novel surface planar structure previously developed for UV photodetector applications. It has been shown that the planar device design achieves a detection efficiency of 40-70% which greatly surpasses the value of 10% recorded for the bulk structure under an identical bias field. The electric field strength distribution within the planar structure has been investigated by simulation and the insights gained from this analysis have been used to propose an enhanced recessed electrode format with the aim of combining the high sensitivity of the surface planar design with the uniformity of field previously observed in the bulk geometry.

Simulation of the new device design has indicated that electrodes recessed by ≈10μm can be anticipated to offer both a high detection efficiency and the prospect of spectroscopic device operation due to the uniformity of the fields and the shifting of edge effects to less dominant regions of the device. A follow-up project in which devices having this geometry will be fabricated by the dual means of excimer laser patterning and reactive ion etching is being undertaken by another researcher.

10.7 References

10.1 F. Foulon, T. Pochet, E. Gheeraert and A. Denueville, IEEE Transactions on Nuclear Science 41, 927 (1994).

10.2 T. Pochet, A. Brambilla, P. Bergonzo, F. Foulon, C. Jany and A. Gicquel, Italian Physical Society Conf. Proc. (Eurodiamond '96) 52, 111 (1996).

10.3 A. Edward Profio, "Experimental Reactor Physics", Wiley, New York, 1976.

10.4 C.P. Beetz, B. Lincoln, D.R. Winn, K. Segall, M. Vasas and D. Wall, IEEE Transactions on Nuclear Science 38, 107 (1991).

10.5 A. Mainwood, oral presentation at Diamond '97 meeting, Edinburgh UK, August 1997.

10.6 M.I. Landstrass, M.A. Plano, M.A. Moreno, S. McWilliams, L.S. Pan, D.R. Kania and S. Han, Diamond and Related Materials 2, 1033 (1993).

10.7 S.F. Kozlov, R. Stuck, M. Hage-Ali and P. Siffert, IEEE Transactions on Nuclear Science 22, 160 (1975).

10.8 G.F. Knoll, "Radiation Detection and Measurement", Second Edition, Wiley, New York, 1989.

10.9 Quickfield 3.4, Tera Analysis, http://www.quickfield.com.

11 CONCLUDING REMARKS

The preceding chapters have demonstrated a series of sensor devices made from thin film diamond which exhibit outstanding performance in terms of sensitivity, speed, radiation hardness and elevated temperature operation. It is important however to recall the comments of chapter 1 in which it was noted that technical performance alone is not sufficient to ensure the successful adoption by industry of a new electronic material system. Having stated the intention to explore the potential of diamond sensors in application areas where they represent an enabling technology, it is now relevant to assess the extent to which this has been achieved.

Although there are many conventional and wider bandgap materials which are now being explored for use as deep UV photodetectors, it is important to recall that most of these developments represent complementary as opposed to competing solutions. This is clearly indicated in the graph presented as figure 11.1, from which it can be seen that a range of sensor technologies is now emerging which will combine to offer full coverage of the UV wavelengths beyond the region normally associated with silicon sensors. In terms of product maturity, diamond and silicon carbide are both available commercially, but presently each is offered only by a single manufacturer: Centronic for diamond photoconductors and Cree for SiC photodiodes. Gallium Nitride will undoubtedly find applications which could overlap with those of diamond in the high temperature and harsh environment arenas, however material growth remains problematic for this material at present.

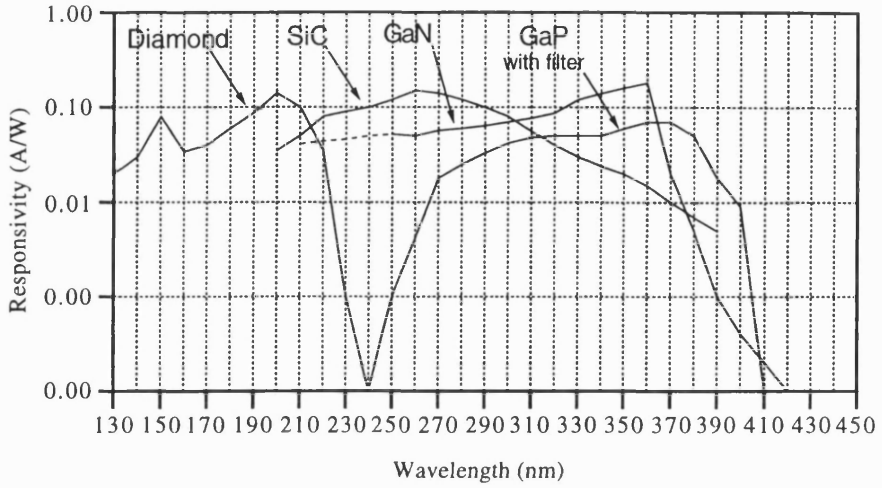

Figure 11.1: The spectral responsivity of diamond, SiC, GaN and GaP ultraviolet photodetectors as offered commercially in recent publicity material from the Boston Electronics Corp., USA.

Allowing that diamond is unchallenged at deep UV wavelengths by other semiconductor detectors, it is necessary to question whether a new sensor is required for a spectral region which has been served for many decades by photomultiplier tubes. Cost is the simplest answer to this question, although probably not the most important one. A typical UV optimised photomultiplier tube is presently offered at a price which is substantially more expensive than the volume prices offered by Centronic Ltd. for generic diamond devices similar to the type described in this thesis. More important practical considerations include the photomultiplier tube's bulk, fragility, failure modes and the requirement for a high voltage power supply.

Assuming that diamond is therefore the detector of choice for the <225nm spectral region, it remains to be established that there is a requirement for sensors to operate at these wavelengths. The main market drivers identified by Centronic Ltd. are the fields of industrial processing (including plasmas and combustion), semiconductor processing, excimer lasers and pollution control, all of which are sectors which are considered to be pushing for improved systems utilising deep UV sensors. Processing industries such as water purification are moving to deuterium light sources and need to monitor 200nm wavelengths so that organic matter in water can be removed. Photolithography processes for the semiconductor industry are now developing systems based around 193nm excimer lasers in order to achieve finer resolution and higher transistor densities.

Pollution monitors use deep UV measurements to accurately quantify H_2S and SO_x emissions again via the use of deuterium light sources.

Taking as an example the photolithographic equipment market, the potential growth in demand for deep UV sensors is indicated by the data in table 11.1. The global market for these machines is ≈2000 units per year (1998) and growing at 8% pa. Each machine will require up to 16 sensors and by 2005 only 193nm machines will still be in production. Diamond at present is the only sensor solution that is available to the designers of these machines and it is projected by Centronic Ltd. that this business alone will be worth in excess of £1m pa within 18 months.

Lithographic System	1998	1999	2000	2001
i-Line (300nm)	50%	45%	25%	15%
deep UV (248nm)	50%	55%	70%	70%
deep UV (193nm)			5%	10%

Table 11.1: Anticipated market share of photolithographic technologies supplied by Centronic Ltd.

If as appears likely, contemporary diamond sensors are capable of meeting the requirements outlined above, the next logical step is to anticipate future generations of detectors in order to focus further research upon subjects of greatest need. Whilst crystal ball-gazing is hardly the stuff of an engineering thesis, it seems reasonable to anticipate that future applications will place increasing demands upon the resolution offered by diamond detectors. In order to make smaller sensors, the roughness of the polycrystalline surface will need to be addressed. In the absence of heteroepitaxial growth processes, smoothing or polishing techniques will need to be developed which avoid or minimise damage to the near surface region of the film. Mechanical polishing to date has not achieved this and it remains to be seen what results will be offered by laser smoothing processes. Once surface morphology has been controlled and device resolution improved it will be a natural next step to implement imaging arrays in one and two dimensions.

Further applications for a radiation hard semiconductor will inevitably be an important field of diamond device development. The lack of a suitable existing solution suggests that neutron dosimetry may be an early example of this work.

Aside from the applications, much new insight into the properties and management of diamond films themselves can be anticipated for the next few years. Not only is it hoped that current studies will throw further light on the mechanisms of the type E process, it is also inevitable that growth processes will continue to improve - possibly to the extent that the basic type E process will eventually become obsolete.

The control, doping and modification of the electronic properties of diamond can be expected to progress, although present indications are that the novel hydrogen conductivity mechanisms will offer equal or greater potential for device applications than the traditional bulk impuritiy doping techniques for some time to come. Instead bulk impurity doping may be hoped to show its potential for modifying the optical properties of the material as tentatively explored here in chapter 9.

In short, there is much still to be done in this field and I wish luck, good fortune and pleasure to all who participate in it. I hope that I will continue to myself.

PUBLICATIONS

List of publications related to this thesis

1. Diamond based electromagnetic radiation detectors.
   R.B. Jackman, S.S.M Chan and R.D. McKeag, European patent application 9511802.2 (June 1995).

2. Polycrystalline diamond photoconductive device with high UV-visible discrimination.
   R.D. McKeag, S.S.M. Chan and R.B. Jackman, Applied Physics Letters 67, 2117 (1995).

3. UV photodetectors from thin film diamond.
   S.S.M. Chan, R.D. McKeag and R.B. Jackman, Physica Status Solidi A-Applied Research 154, 445 (1996).

4. Thin film diamond UV photodetectors: photodiodes compared with photoconductive devices for highly selective wavelength response.
   M.D. Whitfield, R.D. McKeag, L.Y.S. Pang, S.S.M. Chan and R.B. Jackman, Diamond and Related Materials 5, 829 (1996).

5. Photoconductive properties of thin film diamond.
   R.D. McKeag, R.D. Marshall, B. Baral, S.S.M. Chan, and R.B. Jackman, Diamond and Related Materials 6, 374 (1997).

6. High collection efficiency thin film diamond particle detectors.
   P. Bergonzo, F. Foulon, R.D. Marshall, C. Jany, A. Brambilla, R.D. McKeag and R.B. Jackman, in "Semiconductors for room-temperature radiation detector applications" Vol. 487, Ch. 93, pp. 441-446, Eds R.B. James, T.E. Schlesinger, P. Siffert, W. Dusi, M.R. Squillante, M. OConnell and M. Cuzin, Materials Research Society.

7. High collection efficiency CVD diamond alpha detectors.
   P. Bergonzo, F. Foulon, R.D. Marshall, C. Jany, A. Brambilla, R.D. McKeag and R.B. Jackman, IEEE Transactions on Nuclear Science 45, 370 (1998).

8. Diamond UV photodetectors: sensitivity and speed for visible blind applications.
R.D. McKeag and R.B. Jackman, Diamond and Related Materials 7, 513 (1998).

9. High performance diamond UV photodetectors.
R.D. McKeag, oral presentation at "Diamond and Diamond-like Carbon Growth at Low Pressures: Fundamentals to Applications", Institute of Physics Congress, Brighton, March 1998.

10. Diamond ultraviolet photodetectors.
R.D. McKeag, oral presentation at Rank Prize Fund mini-symposium on "Optoelectronic Materials for the Next Millenium", Ambleside, UK, October 1998.